

Cover Page



Universiteit Leiden



The handle <http://hdl.handle.net/1887/79194> holds various files of this Leiden University dissertation.

**Author:** Bosman, A.D.

**Title:** Uncovering the ingredients for planet formation

**Issue Date:** 2019-10-08

# Uncovering the ingredients for planet formation

Proefschrift

ter verkrijging van  
de graad van Doctor aan de Universiteit Leiden,  
op gezag van Rector Magnificus prof. mr. C.J.J.M. Stolker,  
volgens besluit van het College voor Promoties  
te verdedigen op woensdag 8 oktober 2019  
klokke 16:15 uur  
door

Arthur Daniel Bosman

geboren te 's Gravenhage, Nederland  
in 1992

Promotiecommissie

Promotores: Prof. dr. E. F. van Dishoeck  
Prof. dr. A. G. G. M. Tielens

Overige leden: Prof. dr. H. J. A. Röttgering  
Prof. dr. B. R. Brandl  
Prof. dr. E. A. Bergin University of Michigan  
Dr. J. R. Najita National Optical Astronomy Observatory  
Dr. K. M. Pontoppidan Space Telescope Science Institute

ISBN: 978-94-028-1688-4

**Front cover:**

Mock JWST spectra of a protoplanetary disk.  
Illustration by Anouk van Schie.

# CONTENTS

<b>1</b>	<b>Introduction</b>	<b>1</b>
1.1	Star and planet formation . . . . .	1
1.1.1	The initial stages of star formation . . . . .	3
1.1.2	Disk formation and evolution . . . . .	4
1.1.3	Disk structure . . . . .	5
1.1.4	Dust evolution . . . . .	8
1.1.5	Planet formation . . . . .	10
1.2	Astrochemistry . . . . .	11
1.2.1	Gas-phase chemistry . . . . .	11
1.2.2	Grain surface chemistry . . . . .	12
1.2.3	Chemistry in disks . . . . .	12
1.3	Infrared spectroscopy . . . . .	13
1.3.1	Energy levels and transitions . . . . .	14
1.3.2	Line formation . . . . .	14
1.3.3	Observational challenges . . . . .	17
1.4	Disk modelling . . . . .	19
1.5	This thesis . . . . .	19
1.5.1	Future outlook . . . . .	21
<b>2</b>	<b>CO destruction in protoplanetary disk midplanes: inside versus outside the CO snow surface</b>	<b>23</b>
2.1	Introduction . . . . .	25
2.2	Methods . . . . .	27
2.2.1	Parameter space . . . . .	27
2.2.2	Chemical network . . . . .	28
2.2.3	CO destruction routes . . . . .	31
2.3	Results . . . . .	34
2.3.1	Physical parameter space . . . . .	34
2.3.2	Chemical parameter space . . . . .	40
2.4	Discussion . . . . .	42
2.4.1	When, where and how is CO destroyed within 3 Myr . . . . .	43
2.4.2	Implications for observations . . . . .	45
2.4.3	Observing chemical destruction of CO . . . . .	46
2.4.4	Interactions with disk dynamics . . . . .	47
2.5	Conclusions . . . . .	47
	Appendix . . . . .	49
2.A	Dali protoplanetary disk models . . . . .	49
2.B	Chemical model . . . . .	49

2.B.1	Initial abundances . . . . .	52
2.B.2	H <sub>2</sub> formation rate . . . . .	53
2.B.3	Calculation of grain-surface rates . . . . .	53
2.B.4	Implications of modelling assumptions . . . . .	54
<b>3</b>	<b>CO<sub>2</sub> infrared emission as a diagnostic of planet-forming regions of disks</b>	<b>57</b>
3.1	Introduction . . . . .	59
3.2	Modelling CO <sub>2</sub> emission . . . . .	62
3.2.1	Vibrational states . . . . .	62
3.2.2	Rotational ladders . . . . .	62
3.2.3	Transitions between states . . . . .	64
3.2.4	CO <sub>2</sub> spectra . . . . .	65
3.2.5	Dependence on kinetic temperature, density and radiation field	68
3.3	CO <sub>2</sub> emission from a protoplanetary disk . . . . .	68
3.3.1	Model setup . . . . .	70
3.3.2	Model results . . . . .	71
3.3.3	Line-to-continuum ratio . . . . .	83
3.3.4	CO <sub>2</sub> from the ground . . . . .	84
3.3.5	CO <sub>2</sub> model uncertainties . . . . .	86
3.4	Discussion . . . . .	87
3.4.1	Observed 15 μm profiles and inferred abundances . . . . .	87
3.4.2	Tracing the CO <sub>2</sub> iceline . . . . .	91
3.4.3	Comparison of CO <sub>2</sub> with other inner disk molecules . . . . .	94
3.5	Conclusion . . . . .	94
	Appendix . . . . .	95
3.A	Collisional rate coefficients . . . . .	95
3.B	Fast line ray tracer . . . . .	97
3.C	Model temperature and radiation structure . . . . .	97
3.D	Model fluxes $g/d_{\text{dust}}$ . . . . .	98
3.E	LTE vs non-LTE . . . . .	98
3.F	Line blending by H <sub>2</sub> O and OH . . . . .	102
3.G	<i>Spitzer</i> -IRS spectra . . . . .	104
<b>4</b>	<b>Efficiency of radial transport of ices in protoplanetary disks probed with infrared observations: the case of CO<sub>2</sub></b>	<b>107</b>
4.1	Introduction . . . . .	109
4.2	Physical model . . . . .	111
4.2.1	Gas dynamics . . . . .	111
4.2.2	Dust growth and dynamics . . . . .	112
4.2.3	Model parameters . . . . .	115
4.2.4	Boundary conditions . . . . .	116
4.3	Chemical processes . . . . .	116
4.3.1	Freeze-out and sublimation . . . . .	116
4.3.2	Midplane formation and destruction processes . . . . .	118
4.3.3	Simulating spectra . . . . .	123
4.4	Results . . . . .	123
4.4.1	Pure viscous evolution . . . . .	123
4.4.2	Viscous evolution and grain growth . . . . .	125

4.4.3	Viscous evolution and CO <sub>2</sub> destruction . . . . .	127
4.4.4	Viscous evolution, grain growth and CO <sub>2</sub> destruction . . . . .	129
4.4.5	Model spectra . . . . .	129
4.5	Discussion . . . . .	134
4.5.1	Chemical processes . . . . .	134
4.5.2	Physical processes . . . . .	136
4.6	Summary and conclusions . . . . .	142
	Appendix . . . . .	144
4.A	UV dust cross sections . . . . .	144
4.B	Chemical modelling . . . . .	144
4.B.1	Gas-phase only models . . . . .	144
4.B.2	Grain surface chemistry between the H <sub>2</sub> O and CO <sub>2</sub> icelines . . . . .	146
4.C	Viscous evolution and grain growth . . . . .	147
<b>5</b>	<b>Probing planet formation and disk substructures in the inner disk of Herbig Ae stars with CO rovibrational emission</b>	<b>153</b>
5.1	Introduction . . . . .	155
5.2	Data overview . . . . .	159
5.3	Slab modelling of the vibrational ratio . . . . .	160
5.3.1	Analytical line ratios . . . . .	161
5.3.2	RADEX models . . . . .	164
5.3.3	LTE vs non-LTE . . . . .	165
5.3.4	Absolute fluxes . . . . .	165
5.3.5	Physical conditions in the CO emitting region . . . . .	169
5.4	DALI modelling . . . . .	169
5.4.1	Model setup . . . . .	169
5.4.2	Model results . . . . .	173
5.4.3	Disk surface emission . . . . .	176
5.4.4	$T_{\text{gas}} \approx T_{\text{dust}}$ . . . . .	179
5.5	Discussion . . . . .	180
5.5.1	Implications for sources with low $v_2/v_1$ at small radii . . . . .	184
5.5.2	Implications for high $v_2/v_1$ at large radii . . . . .	188
5.5.3	Comparison to T-Tauri disks: distribution of UV flux matters . . . . .	189
5.5.4	Predictions for future observations . . . . .	191
5.6	Conclusions . . . . .	192
	Appendix . . . . .	193
5.A	CO molecule model . . . . .	193
5.A.1	Rovibrational . . . . .	193
5.A.2	Electronic . . . . .	193
5.B	Excitation tests . . . . .	194
5.C	Line profiles . . . . .	196
5.D	Near-infrared excess . . . . .	196
5.D.1	CO as tracer of the inner disk radius . . . . .	196
5.E	Lowering the flux of the outer disk . . . . .	201
5.F	Thermal dissociation of CO . . . . .	203

---

<b>6 The dry and carbon poor inner disk of TW Hya: evidence for a gigantic icy dust trap</b>	<b>205</b>
6.1 Introduction . . . . .	207
6.2 Methods . . . . .	208
6.3 Results . . . . .	209
6.4 Discussion . . . . .	212
6.4.1 Constraining the inner disk chemical structure . . . . .	212
6.4.2 Hiding C and O carriers? . . . . .	212
6.4.3 Implications of uniform depletion . . . . .	213
Appendix . . . . .	214
6.A DALI model . . . . .	214
<b>Bibliography</b>	<b>214</b>
<b>Nederlandse samenvatting</b>	<b>231</b>
<b>List of Publications</b>	<b>237</b>
<b>Curriculum Vitae</b>	<b>239</b>
<b>Acknowledgments</b>	<b>241</b>

# 1 | INTRODUCTION

The ground under our feet is something that is so taken for granted, that most of humanity has literally been built on it. Because our familiarity with the earth most people will think of the planet Earth as typical. A quick look at our neighbouring planets, Mars and Venus, which have similar compositions, seems to confirm that view. However, when we look further in our solar system, bodies mostly made up of a mixture of silicates and iron become rare. Mercury’s composition is dominated by iron, while the other four planets, Jupiter, Saturn, Uranus and Neptune have a composition that is dominated by gas,  $\text{H}_2$  and He instead of solids. Furthermore, apart from Venus, there is no object that has a mass roughly similar to that of the Earth.

Going further afield, looking at planets around other stars, it seems that the diversity in planet sizes and compositions is even bigger than the diversity already seen in our solar system (Udry & Santos 2007; Lissauer et al. 2014; Winn & Fabrycky 2015; Sing et al. 2016; Dawson & Johnson 2018, see also Fig. 1.1). These studies show that if there is any planet that is typical, it is the super Earth. Planets with a mass a few times that of the Earth. Many of these objects are thought to have a composition that is dominated by a mixture of iron and silicates, but some of planets these might have large reservoirs of liquid water (“water worlds”), graphite (“diamond planets”) or an extended gaseous envelope (“sub-Neptunes”).

## 1.1 Star and planet formation

Within our galaxy the major reservoir of solid material is interstellar dust grains. This reservoir of grains is the material from which all future planets will draw their solid component. These grains are small,  $<1 \mu\text{m}$  (e.g. Mathis et al. 1977; Weingartner & Draine 2001; Zubko et al. 2004). The cores of these grains consist of much of the same material as our Earth, iron and silicates, with an added component of amorphous carbonaceous material. Collecting many of these grains into a planet will thus not result in something that looks like the Earth as the Earth has very little carbon (Allègre et al. 2001; Bergin et al. 2015). This means that to understand how the Earth came to be, one does not need to only look at the physics, but also look at the chemistry that happens during this journey from grain to planet. This thesis focusses on the chemical environment in which planets form. What is the composition of gas and dust during the planet formation process?



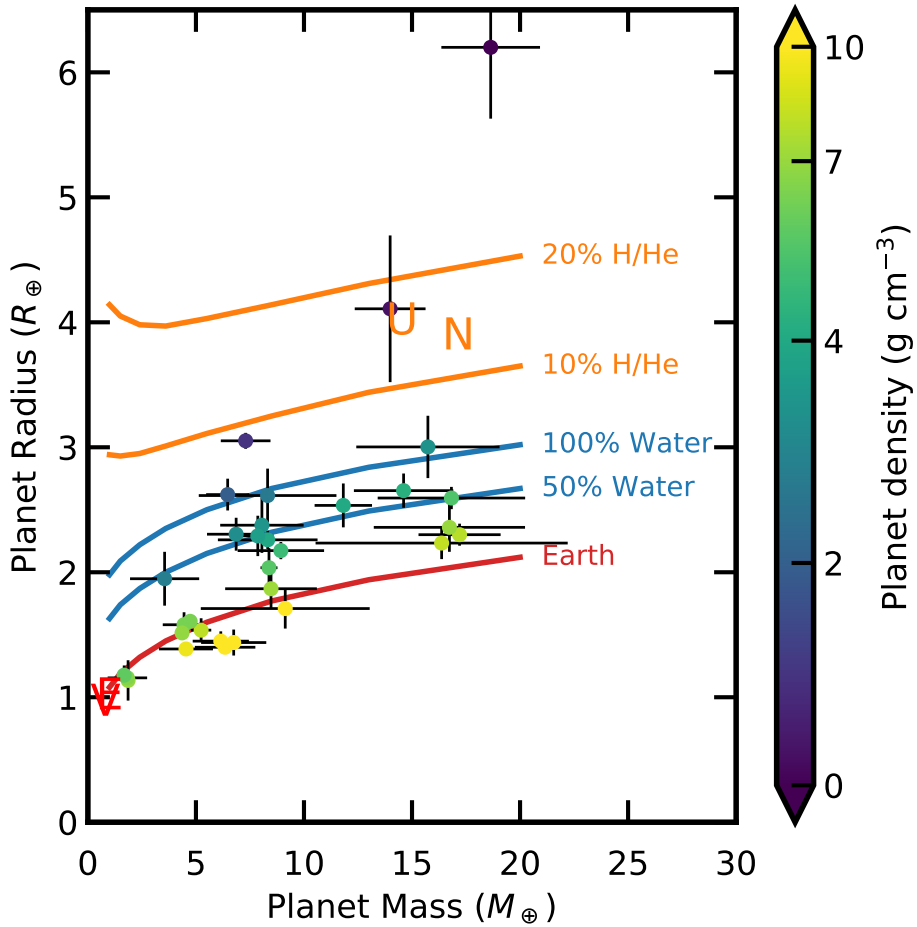


**Figure 1.1:** Planet masses and planet sizes for a set of exoplanets with masses less than 20 Earth masses with data taken from Han et al. (2014); Lopez & Fortney (2014); Lissauer et al. (2014). Solid lines show theoretical curves for different planet compositions. The letters V, E, U and N denote the locations of Venus, Earth, Uranus and Neptune respectively. The color of the exo-planet points indicates the average density. These exo-planets have a larger diversity in bulk composition than that of the solar system.



**Figure 1.2:** 360 degree panoramic view of the Milky Way at visible wavelengths. Dark lanes can be seen where dust obscures the stars behind it. Credit: ESO/S. Brunier

### 1.1.1 The initial stages of star formation

From an astronomical viewpoint, the process of planet formation is just a small part of a much bigger and more violent process, the process of star formation. This means, that before we can talk about planet formation proper, it is necessary to have a rough understanding of star formation. Star formation in our galaxy happens in giant molecular clouds. These clouds consists of molecular gas, mostly  $\text{H}_2$ , He, CO and  $\text{N}_2$  and dust, small ( $0.005 - 1 \mu\text{m}$ ) particles of silicate and carbonaceous material in a 100:1 gas-to-dust mass ratio (Draine 2003). Nearby clouds can be seen as dark lanes against the stars of the Milky Way (Fig. 1.2).

Density fluctuations in the cloud lead to the formation of cores, objects ( $\sim 0.1$  parsec, few solar masses) that are bound by their own gravity (for a review, see Ward-Thompson 2002; André et al. 2014). Some of these cores slowly contract with the supporting magnetic field leaking out until the support in the central region of the core is not enough to balance the contracting forces of gravity. At this point the core collapses inside-out, forming one to a handful of proto-stars in the center (Shu 1977). Over the course of the next few  $10^5$  yr the star will be fed by gas from the remnant of the core, or proto-stellar envelope. This does not go without problems, however. Due to the dynamic nature of clouds, cores formed in these clouds have some internal motions, leading to a small amount of net rotation, and thus angular momentum in the core.

This angular momentum has to be conserved during collapse. The gas will thus not fall in straight towards the star, but it will spiral with an increasing angular velocity the closer it gets to the star. A high angular velocity will act as an outward force, slowing down gas that moves perpendicular to the angular momentum axis. Gas can still freely fall in the direction parallel to the angular momentum axis. This leads to the creation of flattened, rotating and infalling structure in the plane perpendicular to the angular momentum axis, a pseudo disk (Terebey et al. 1984; Galli & Shu 1993). Around the same time, the proto-star itself can only have so much angular velocity or

momentum, as accretion of too much angular momentum will lead to the proto-star spinning itself apart. To stop this from happening, part of the accreting material, and most of the angular momentum, is ejected through bipolar outflows or lost through magnetic breaking on the core scale (Bachiller & Tafalla 1999).

### 1.1.2 Disk formation and evolution

At some point the gas falling towards to proto-star will have so much angular momentum that it can no longer accrete directly onto the proto-star. Gas falling from large radii will have high enough angular momentum that it will reach a stable orbit before accreting onto the star. At this point the pseudo disk transforms into a mostly rotationally supported, or Keplerian, disk (e.g. Cassen & Moosman 1981; Terebey et al. 1984). At this point the infall of gas no longer determines the speed at which the star accretes, instead it is the speed at which the gas in the disk can lose angular momentum that sets the timescale for accretion onto the star. The disk can lose angular momentum in multiple ways. In the inner regions, the bipolar outflow and gas flows launched by magnetic forces at the disk surface (disk winds) can expel gas and extract angular momentum, driving accretion. At larger radii other processes have to be invoked to lose, or more accurately, transport angular momentum.

Disk accretion, for most of the time, is thought to happen through a viscous process (Shakura & Sunyaev 1973). The viscosity transports angular momentum outward, making the disk more spread out, allowing most of the gas to accrete inward. This transport of material inward, and angular momentum outward, happens due to shear forces in the disk. The angular velocity of the gas is not constant, but increases towards to star. This velocity gradient induces velocity shear. This shear transports angular momentum outward, as the gas will try to catch up to the gas within its orbit, increasing its velocity. The efficiency of this process depends on the viscosity of the gas. This viscosity is normally very low for laminar flows of molecular gas, but if the gas is turbulent it has a higher effective viscosity.

The accretion onto the star due to disk processes will most likely be slower than the infall of the envelope onto the disk. As such the disk will become more and more massive. At some point the disk may become so massive that its own gravity dominates the gravity of the star and its own thermal support (Kratte & Lodato 2016). This gravitational instability leads to the creation of overdensities in the disk, such as spiral density waves or spherical clumps of gas. The movement of these overdensities steer up the gas and the gravitational pull of the overdensities allows for the transport of angular momentum. As such, when the disk becomes unstable, the accretion rate unto the star increases until the disk has lost enough mass to be gravitationally stable again. This leads to a variable accretion rate of gas onto the star and the gravitationally unstable episodes dominate the transfer of mass from disk to star when the envelope is still present.

For low mass stars, at some point after  $\sim 4 \times 10^5$  yr, the gaseous envelope around the proto-star is gone, accreted onto the disk, or blown away by outflows and winds (Dunham et al. 2014). This leaves a mostly naked star-disk system that we call a proto-planetary disk. The star dominates the mass budget in the system, containing at least 90% and most of the times more than 99% of the mass of the system. The disk contains the rest of the mass, which it funnels onto the star over a period of  $\sim 3 \times 10^6$  yr (Haisch et al. 2001; Cieza et al. 2007). This is the final, and longest stage in the

star formation process. It is in this stage of star formation where gas giants need to accrete their gas and in which planetesimals need to be formed and herded into position so planetary bodies can be formed. The longevity and geometric simplicity of the proto-planetary disk allows for detailed studies of these systems and the physical and chemical processes that they under go.

### 1.1.3 Disk structure

An overview of a general disk structure is given in Fig. 1.3. Gas and dust are rotating around the central star in a slightly flared disk. All of the heating in the disk is caused by the irradiation of the central star, except for maybe the  $< 1$  AU where the release of gravitational energy during accretion heats up the gas. This causes a (dust) temperature structure that increases both inwards and upwards, in the directions of higher flux. Vertically, the disk is in hydrostatic equilibrium. The density is generally assumed to be vertically distributed like a Gaussian, although the vertical temperature gradient indicates that, for the disk to be in hydrostatic equilibrium, the density distribution needs to slightly deviate from a true Gaussian. The density distribution of the gas is generally parametrized as (Chiang & Goldreich 1997):

$$\rho_{\text{gas}}(r, z) = \frac{\Sigma(r)}{\sqrt{2\pi}H(r)} \exp\left[-\frac{1}{2} \frac{z^2}{H(r)^2}\right], \quad (1.1)$$

with  $\Sigma(r)$  the surface density and the scaleheight

$$H(r) = H_c \left(\frac{r}{R_c}\right)^\psi, \quad (1.2)$$

with  $H_c$  the scaleheight at reference radius  $R_c$  and  $\psi$  the flaring angle. Radially the surface density of the gas decreases outward as is generally parameterized by (Lynden-Bell & Pringle 1974):

$$\Sigma(r) = \Sigma_c \left(\frac{r}{R_c}\right)^{-\gamma} \exp\left[-\left(\frac{r}{R_c}\right)^{2-\gamma}\right], \quad (1.3)$$

$\Sigma_c$  is the surface density at  $R_c$  and  $\gamma$  is the power law slope. This slope is generally shallow enough that most mass is at large radii.  $R_c$ , the radius beyond which the gas start to drop exponentially, differs strongly between disks (e.g. Tazzari et al. 2016).

Observations have shown that many disks do not have as smooth of a gas distribution as Eq. 1.3 proposes. The most obvious of these are the transition disks (e.g. Espaillat et al. 2014). These objects show a cavity that is strongly depleted in gas and dust with gas cavities smaller than dust cavities (van der Marel et al. 2016). High resolution ALMA observations of large dust grains have shown more subtle substructures suggesting that, at least all large disks, have substructures in the dust, which indicates that there are also substructures in the gas (ALMA Partnership et al. 2015; Andrews et al. 2016, 2018). These substructures have been observed to levels that correspond to gas surface density deviations of tens of percent. Finally, high resolution near-infrared observations that trace the small dust and thus the gas-scale height also show rings and gaps, indicating that the scale-height is not a constantly increasing function of radius (e.g. Avenhaus et al. 2017).

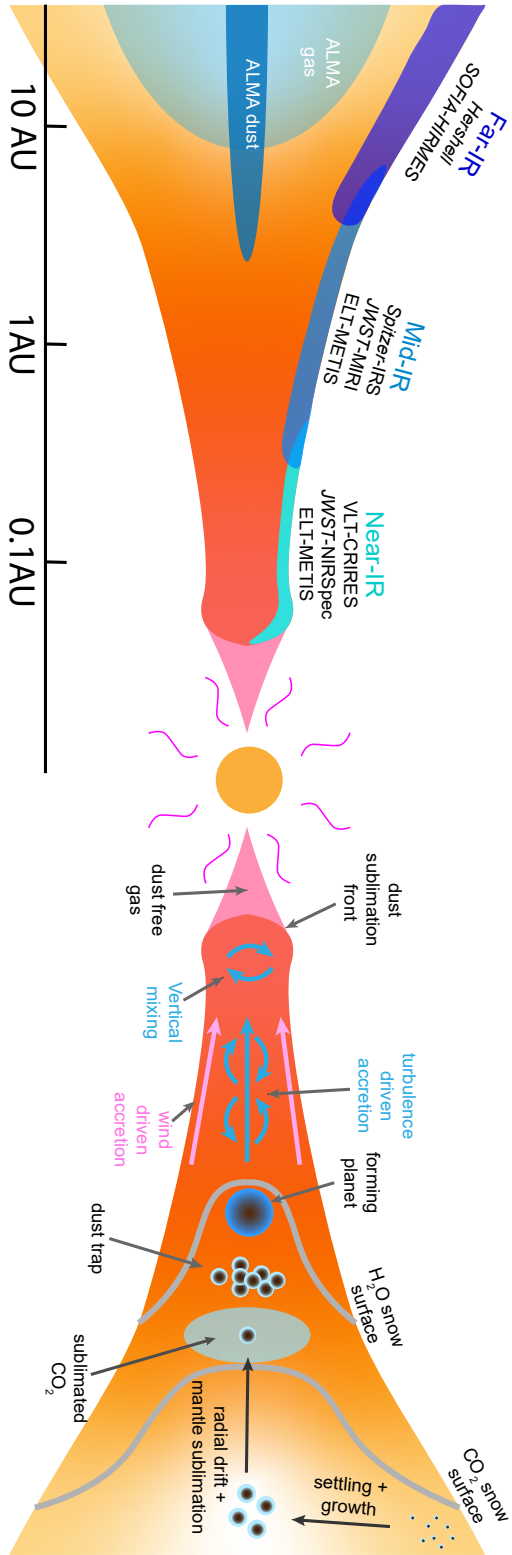


**Figure 1.3:** Overview of the structure of the inner disk. The left side shows which regions can be probed with which instruments, the right side shows the location of the snow surfaces of H<sub>2</sub>O and CO<sub>2</sub> as well as some physical processes.

The large differences in physical conditions set by the disk structure have a large impact on the chemical composition of the gas. One of the strongest effects is due to the radial temperature gradient. The different freeze-out temperature of abundant molecules such as  $\text{H}_2\text{O}$ ,  $\text{CO}_2$ ,  $\text{CO}$  and  $\text{N}_2$  create steps in the elemental composition of the gas at the locations that they freeze-out (known as icelines Öberg et al. 2011, see Fig. 1.4). These icelines have a direct impact on the molecules that we can observe. For example, the  $\text{N}_2\text{H}^+$  ion can only exist in gas that is rich in  $\text{N}_2$  but strongly depleted in  $\text{CO}$  (Aikawa & Herbst 1999; van 't Hoff et al. 2017).

Physical and chemical processes in the disk complicate this picture, however. Chemical evolution can turn very volatile species, like  $\text{CO}$ , into more species that are more tightly bound to the grains, such as  $\text{CO}_2$ , this can have a large effect on the elemental composition of the gas (Eistrup et al. 2016). The reverse can also happen, turning very tightly bound species such as  $\text{H}_2\text{O}$  and  $\text{CO}_2$  into  $\text{O}_2$  and  $\text{CO}$ . The exact effect is hard to generalize, and depends strongly on the physical and chemical assumptions (Eistrup et al. 2018). Furthermore, as will be discussed later, the gas and dust in the disk are not perfectly coupled. This allows for the transport of ices through the disk, and across icelines. As dust generally moves in faster than the gas, the region within an iceline can be enriched by evaporating ices (Ciesla & Cuzzi 2006; Schoonenberg & Ormel 2017; Booth et al. 2017).

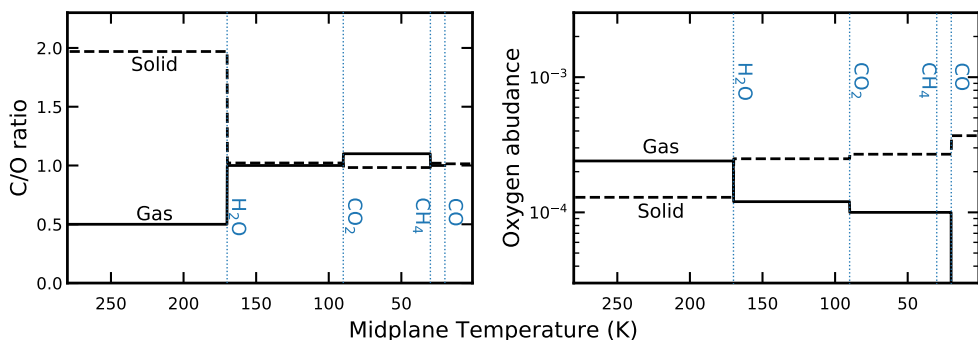


**Figure 1.4:** Elemental C/O ratio (left) and O/H (right) ratio plot for both the solids (dashed line) and the gas (solid line). The lines show just the effects of the  $\text{H}_2\text{O}$ ,  $\text{CO}_2$ ,  $\text{CH}_4$  and  $\text{CO}$  icelines (blue, dotted vertical lines). icelines significantly change the elemental composition of both the solids (dashed line) and the gas (solid line).

Close to the star, the gas and dust are hot enough that the dust itself sublimates. This happens at  $\sim 1500$  K and is generally seen as the inner edge of the disk. Gas within this radius is not shielded from UV irradiation and is thus likely dominated by atomic and ionized gas.

There are also vertical variations in the physical conditions, with lower densities, higher temperatures, and higher UV radiation fields higher up in the disk. The temperature structure leads to a two-dimensional sublimation front, generally called snow surfaces, with the classical iceline located at the point the snow surface crosses the disk midplane (see Fig. 1.3, right side). Furthermore, due to the different conditions, the surface layers have a very different chemistry from the more shielded midplane, this is discussed in more detail in Sec. 1.2.3.

The different temperatures cause parts of the disk to strongly emit at different wavelengths. Hot gas and dust ( $> 500$  K) from the inner few AU emits mostly in the 1-5  $\mu\text{m}$  range while cooler gas and dust (100–500 K) within  $\sim 10$  AU has emission peaking in the mid and far-infrared 5 – 100  $\mu\text{m}$ . The coldest gas and dust at radii larger than 10 AU emit in the (sub-)millimeter regime ( $> 0.1$  mm). This correlation allows for observations targeting specific scales in the disk without spatially resolving these scales in the disk.

#### 1.1.4 Dust evolution

During most of the star formation process grains tightly follow the gas. Small grains are coupled with the gas through gas-grain collisions. The high densities of the circumstellar disk allow for the growth and evolution of the grains. Initially, gentle collisions between small dust grains allow for the growth of grains from microns to millimeters (Blum & Wurm 2008). During this growth process, grains become large enough to decouple from the gas (Weidenschilling 1977). At this point the grains no longer feel the pressure of the gas. This means that grains will settle towards the mid-plane, as the pressure gradient that supports the gas no longer supports the large grains. This leads to disk surface layers that are poor in dust and a mid-plane that is enriched especially in large dust (Dubrulle et al. 1995). The high dust densities in the midplane lead to more growth. However, the decoupling of grains from the gas increases the relative velocities of grains. High speed collisions will not result in growth, but in bouncing and fragmentation, depending on the relative sizes, limiting the maximal grain size to a few millimeters for purely silicate particles (Blum & Wurm 2008; Brauer et al. 2008). These processes are known as the bouncing barrier and the fragmentation barrier. These barriers are one of the greatest puzzles in planet formation. If you cannot grow beyond a millimeter, how do you build something that is thousands of kilometres across?

The fragmentation and bouncing barriers are not the only barrier to grain growth. Another barrier is the radial drift or meter-sized barrier. Whereas in the inner, denser regions of the disk, fragmentation and bouncing strongly restrict growth, in the more tenuous outer regions of the disk radial drift will limit the growth of grains (e.g. Weidenschilling 1977). Radial drift is the more subtle brother of vertical settling. The gas has a negative pressure gradient in the radial direction. This gradient is shallow, but it is not negligible. It allows the gas to have a stable orbit around the star at a velocity that is slightly less than the Keplerian velocity. Large decoupled grains in a stable orbit need to move with the Keplerian velocity. They thus move faster than the gas they reside in.

This means that the grains feel a headwind and thus slowly lose (angular) momentum and need to move closer to the star to get back into a stable orbit where the same process pushes it further inward. The speed at which this orbital decay happens depends strongly on the properties of the gas and the mass and porosity of the grains. Very small or very porous grains are full coupled to the gas and thus do not decay. Very large, very compact bodies have enough mass that the momentum lost due to the headwind is very small compared to the total momentum and thus the orbital decay is very slow. In between, there are bodies that are too large to be supported by the gas pressure but do not have enough momentum to plough through the gas. These bodies are generally called pebbles, about 1 mm in size at radii  $> 20$  AU and they

are the particles mostly transported by radial drift (Brauer et al. 2008; Birnstiel et al. 2010). At 1 AU the dust size at which the drift speed is maximal, is about a meter, therefore the name "meter-sized" barrier.

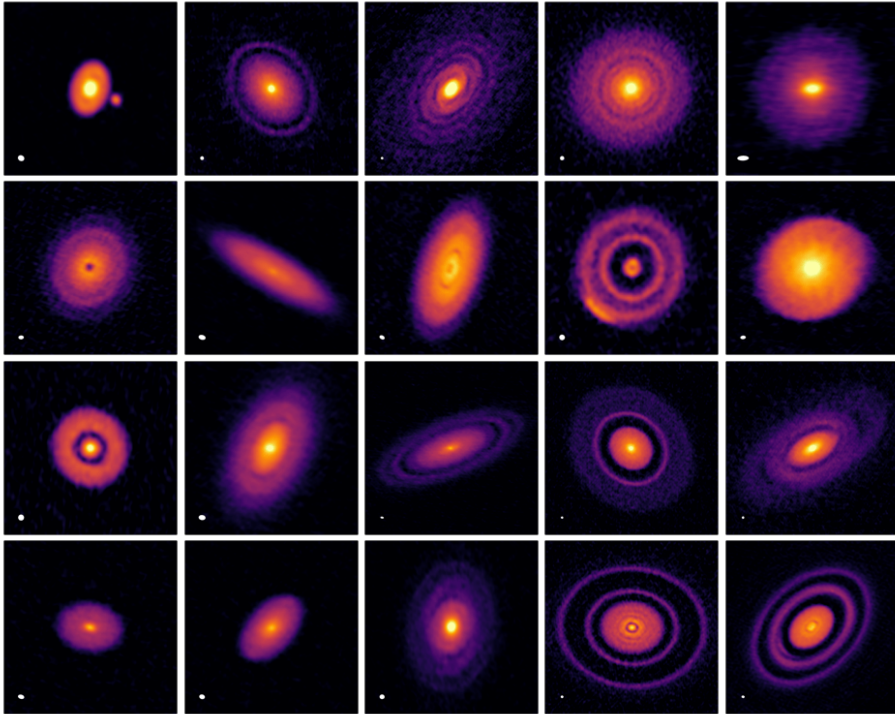


**Figure 1.5:** High resolution ALMA continuum observations of a sample of bright disks (Andrews et al. 2018). All of the disks in this sample show some substructure, with the most common being dust rings indicative of pressure maxima halting radial drift.

In the inner regions of the disk, fragmentation will make it hard to ever reach dust sizes that efficiently drift. In the outer regions the sizes for efficient radial drift are smaller. This leads to a large flux of solids coming from the outer disk, where most of the mass is, through the inner disk, to be accreted into the star. Models predict that in some cases this can be so efficient that more than 90% of the dust is accreted onto the star in the same time that 10% of the gas accretes, leaving a very dust depleted disk. There is little evidence of these very dust poor, or gas rich disks, leading us to question the actual speed of radial drift. The large amount of substructures that have been observed in proto-planetary disks can be very efficient in reducing the radial drift speed if they are caused by variations in the gas pressure (see Fig. 1.5 Pinilla et al. 2012b; ALMA Partnership et al. 2015; Andrews et al. 2016, 2018). To explain these substructures, (proto)-planets are generally invoked (e.g. Zhang et al. 2018), seemingly creating a chicken and egg problem. We need the substructures to keep the dust and form planets, but we need planets to make substructures.



### 1.1.5 Planet formation

Theoretically it seems to be very hard to make large bodies in any disk, but observations show that on average every star has a planetary companion, with many stars having diverse planetary systems (e.g. Winn & Fabrycky 2015). The existence of many gas giants further implies that large bodies are formed in gas-rich disks. Nature thus has ways around our theoretical barriers. The planets themselves might contain clues as to how nature overcomes the growth barriers. One interesting clue would be in where these planets are actually formed. Rocky planets capture only the solid component of the disk which includes the ices. The atmospheric composition of giant planets should be influenced by the location where they accrete their gas as well as the exact amount of solids that they accrete during this stage. Especially the location of the planet relative to the iceline leaves a strong impact on the composition (Fig. 1.4).

At early stages of disk formation it is possible to directly form planets during the episodes that the disk is gravitationally unstable (Kratte & Lodato 2016). These gravitationally instability (GI) planets are expected to be massive gas giants. They should form in the outer parts of the disk, where collapse is easier. The composition of these planets should be the same as that of the star. After the GI planet has formed it will open a gap in the gas and dust disks, and cut off its own accretion. Afterwards there is a period of a few Myr that the planet can migrate through the disk, so it can still end up close to the star (Paardekooper & Mellema 2006; Chambers 2009; Paardekooper & Johansen 2018; Dawson & Johnson 2018).

The other planet formation paradigms, core accretion and pebble accretion, are invoked for all sorts of planets. Both core accretion and pebble accretion need one or more seeds to start of planet formation. One of the few ways to make these seeds, or planetesimals, is through the streaming instability (Youdin & Goodman 2005; Johansen et al. 2014). In the core accretion paradigm, these seeds grow by collisions with each other. In the pebble accretion paradigm, planetesimals initially grow by accretion from the pebble flow that passes the orbit of the planet (Ormel & Klahr 2010; Johansen & Lambrechts 2017). This is more efficient than simply sweeping up the material in the orbit of the planet as the accretion cross section for pebbles is larger and the pebble mass reservoir can be far larger. If a planetesimal or planetary core gets big enough, about 10 Earth masses, the core starts accreting directly from the gas and dust disk and is on its way to become an ice or gas giant (Ikoma et al. 2000). The composition of the gas and solids that is accreted in this stage is critical for the final atmospheric content of the planet. As with the GI planets, these ice and gas giants can then migrate through the disk, ending up at a location far from where they accreted most of their atmosphere. In both paradigms, planetesimals that do not grow quickly enough during the protoplanetary disk stage to start gas accretion are either concentrated into rocky bodies after the disk disperses, or ground to dust by repeated collisions and ejected from the system.

Planet formation, thus, is a complex process. Some of the formation history is imprinted in the composition of the planet, which is a better preserved quantity than, for example, the location at which a planet is found. To be able to use this information a good understanding of the physical and chemical conditions during planet formation is needed.

## 1.2 Astrochemistry

The chemical composition of molecular gas contains a wealth of information on the physical conditions. To be able to extract that information it is necessary to understand the chemistry that happens in the extreme and diverse conditions in space. Since the detection of the first molecule in space (Swings & Rosenfeld 1937), astronomers and chemists have worked together towards an understanding of interstellar chemistry. This is an interdisciplinary effort combining results from astronomical observations, quantum chemical calculations, modelling of full chemical networks and laboratory experiments.

When studying the astrochemistry during star formation the focus is mostly on the volatile species, as these are easily observed and identified. Volatile molecules are molecules that do not freeze-out or form solids at temperatures above the freeze-out temperature of  $\text{H}_2\text{O}$ , which is between 120 and 150 K depending on density. The most abundant of these molecules are made up of H, C, O and N. The study of the chemistry of volatiles is generally split up in two lines of research, gas-phase chemistry and grain-surface chemistry. An understanding of both is needed to be able to explain the chemical complexity that is observed.

### 1.2.1 Gas-phase chemistry

Gas-phase chemistry, as the name implies, is chemistry that happens in the gas-phase. For any chemistry to happen, collisions between molecules need to occur. As such, it is not the reaction that is energetically most favourable, but the reaction that happens first that sets the chemical composition. Astrochemistry is thus mostly a study of chemical kinetics. To be able to calculate the kinetics, reaction cross sections and barriers have to be known.

Reactions that involve ions and molecules with large dipole moments will generally be faster than reactions involving molecules without a far-reaching magnetic or electric field as they have a large reaction cross section that is nearly independent of temperature. The low temperature in most molecular environments strongly suppresses reactions with barriers and almost completely quenches endothermic reactions. This means that reactions between two closed shell molecules are almost non-existent at low temperature.

As nearly all reactions happening in space will be exothermic, there is a final consideration that needs to be taken into account, the conservation of energy. This is especially a problem for reactions of the kind  $\text{X} + \text{Y} \longrightarrow \text{XY}$  as the final product will contain enough energy to break the newly formed bond, without any efficient way to release this energy. In dense environments there will generally be a 3rd body to take that energy from the molecule and convert it to kinetic energy, but in low density environments, that energy will need to be released through emission of a photon before the molecule breaks apart again. Photon emission is slow compared to the timescales in the molecule, as such, reactions of this type are strongly suppressed in favour of reactions of the type:  $\text{AB} + \text{C} \longrightarrow \text{A} + \text{BC}$ . This severely limits the diversity of molecules that can be made in the gas-phase. Gas-phase chemistry can efficiently create molecules such as CO,  $\text{O}_2$ , HCN and carbon chains, but abundant molecules, like  $\text{H}_2\text{O}$ ,  $\text{NH}_3$ ,  $\text{CH}_3\text{OH}$  and  $\text{H}_2$  are almost impossible to make in the gas-phase, especially at temperatures below 300 K.

Over decades, astrochemists have been collecting reaction data, resulting in databases like UMIST (McElroy et al. 2013) and KIDA (Wakelam et al. 2015) containing thousands of reactions and their rate coefficients. These databases draw from a wide range of studies, theoretical work of critical reactions, experimental studies, astronomically derived rates and expert guesses.

### 1.2.2 Grain surface chemistry

To be able to form hydrogen rich molecules, such as  $\text{H}_2$ ,  $\text{H}_2\text{O}$ ,  $\text{NH}_3$  and  $\text{CH}_3\text{OH}$ , grain surface chemistry is needed. The surface of grains is a place where atoms, molecules and radicals can concentrate allowing for more efficient chemistry. Moreover, the bulk of the grain is able to quickly absorb the energy that is released in the chemical reactions making reactions of the type  $\text{X} + \text{Y} \longrightarrow \text{XY}$  possible. The high abundance of atomic hydrogen and its reactivity in these reactions allows for the efficient formation of hydrogenated species on the ice.

Most reactions on the grain, especially at very low temperatures, are thought to take place through the Langmuir-Hinshelwood mechanism (see, e.g. Cuppen et al. 2017, for a review). It assumes that species on the surface are capable of diffusion over the surface, this allows for species to meet and react. The speed at which this hopping happens is thought to be dependent on the desorption energy of a species. This means that the highly volatile H-atom is mobile, on the ice, down to 10 K. At 10 K larger radicals and other atoms are not mobile, but at slightly higher temperature radicals like HCO,  $\text{CH}_2$  and  $\text{CH}_3$  become more mobile and larger, multicarbon species can be formed on the grain surface (e.g. Chuang et al. 2017). As the temperature comes close to 20 K, CO can very efficiently diffuse over the grain surface, allowing for the formation of species like  $\text{CO}_2$ , even under high density ( $n > 10^8 \text{ cm}^{-3}$ ) conditions.

Another pathway for reactions to happen on the grain surface, is the Eley-Rideal mechanism. Reactions that take place with this mechanism start with a reactant in the gas-phase and a reactant on the grain-surface. The gas-phase species collide with the grain at the location of the other reactant and a reaction takes place. For most reactions and conditions Langmuir-Hinshelwood is more efficient, but if surface coverages and gas-grain collision rates are high Eley-Rideal can dominate (Ruffle & Herbst 2001).

### 1.2.3 Chemistry in disks

The chemistry in proto-planetary disks can roughly be separated in three regimes. The high temperature chemistry, photon dominated chemistry and the cosmic-ray driven chemistry (Aikawa et al. 2002). High temperature chemistry happen in the inner few AU of the disk away from the surface layers. The high temperatures force all volatiles to be sublimated and, in combination with high densities, allow for chemistry that approximates the chemistry happening here on Earth, with molecular abundances close to chemical equilibrium. The most abundant molecules aside from  $\text{H}_2$ ,  $\text{N}_2$  and CO are expected to be  $\text{H}_2\text{O}$ ,  $\text{CH}_4$ ,  $\text{NH}_3$  and HCN (Agúndez et al. 2008; Walsh et al. 2015; Najita & Ádámkóvics 2017; Agúndez et al. 2018). This region in the disk, near the mid-plane is very hard to probe, only very sensitive observations at long wavelengths can detect molecules in this region of the disk (Bruderer et al. 2015; Notsu et al. 2016).

In the surface layers of the disk the chemistry is dominated by UV and X-ray photons. These photons dissociate and ionize molecules. The molecules that are abundant

are those that can form rapidly at high temperatures or are hard to dissociate.  $\text{H}_2$ , CO and  $\text{N}_2$  all have both of these properties. All are bi-atomic, which means that they need less collisions to form than larger molecules. They also share a UV absorption spectrum that is dominated by narrow lines. This means that only a small fraction of the UV flux can dissociate these molecules allowing them to survive in regions of harsh UV fields when these dissociating photon have been absorbed; this process is known as self-shielding (van Dishoeck & Black 1988; Visser et al. 2009; Li et al. 2013; Heays et al. 2014).  $\text{H}_2\text{O}$  is more easily dissociated than  $\text{H}_2$ , CO and  $\text{N}_2$  (e.g. Heays et al. 2017). However this molecule can form fast, especially in regions of high temperature that are due to heating by UV photons.  $\text{H}_2\text{O}$  formation is only a two step process, starting from the abundant O atom and the even more abundant  $\text{H}_2$ :  $\text{O} + \text{H}_2 \longrightarrow \text{OH} + \text{H}$  followed by  $\text{OH} + \text{H}_2 \longrightarrow \text{H}_2\text{O} + \text{H}$ . The high temperatures ( $> 300$  K) make the barriers that are involved surmountable. HCN is a molecule that, in its own way, is hard to destroy. While HCN can easily be dissociated by UV photons, the resulting CN radical is more robust against UV photons. In warm molecular gas, CN quickly reacts with  $\text{H}_2$  or other H carrying molecules, like  $\text{CH}_4$ ,  $\text{C}_2\text{H}_6$  or  $\text{NH}_3$ , to form HCN. This makes CN and HCN good tracers of temperature and UV field in the surface layers of disks (e.g. Visser et al. 2018; Cazzoletti et al. 2018; van Terwisga et al. 2019).

The final chemical regime is the cosmic-ray dominated regime. This describes the chemistry in the cold ( $\lesssim 100$  K), shielded regions in the disk. With these low temperatures and without the formation of radicals due to UV photons, the chemistry should settle into a state in which no changes should happen, even on the 10 Myr timescale of the disk. However, in most astrophysical environments there are cosmic-ray or other highly energetic particles that drive the chemistry. The high energy of the particles ( $\gg \text{GeV}$ ) gives them great penetration depth, reaching regions that X-rays and UV photons cannot (Umebayashi & Nakano 2009).

Collisions of these energetic particles with  $\text{H}_2$  create  $\text{H}_2^+$  as well as a high energy electron. The  $\text{H}_2^+$  reacts with  $\text{H}_2$  to form  $\text{H}_3^+ + \text{H}$ , and  $\text{H}_3^+$  can initiate ion molecule chemistry generally ending with the creation of another H atom. The energetic electron collides with other  $\text{H}_2$  molecules exciting electronic transitions that relax and produce a local, weak UV field (Prasad & Tarafdar 1983). These UV photons produce more radicals, making them available for chemical reactions.

In the coldest gas, the production of hydrogen atoms, together with CO residing on the grains, leads to hydrogenation reactions forming  $\text{CH}_3\text{OH}$  (Watanabe & Kouchi 2002; Cuppen et al. 2009). At higher temperatures, OH radicals formed from the dissociation of  $\text{H}_2\text{O}$  in the ice can react with CO forming  $\text{CO}_2$  on the grain surface. Cosmic ray impacts also produce  $\text{He}^+$ , above 20 K collisions of  $\text{He}^+$  with CO produce  $\text{C}^+ + \text{O} + \text{He}$ .  $\text{C}^+$  and O will generally end up in  $\text{CH}_4$  and  $\text{H}_2\text{O}$  respectively.

### 1.3 Infrared spectroscopy

Infrared observations are an efficient tool to study the inner regions of protoplanetary disks. As mentioned before, infrared emission is coming from the warm regions in the disk and thus carries information on disk scales that are hard to resolve with any current instrument except by infrared interferometry. Observations of gas lines in the near-(1–5  $\mu\text{m}$ ) and mid-infrared (5–25  $\mu\text{m}$ ) carry a wealth of information. The comparative line strengths of different molecules contain information on the abundance

of the observed molecules. The large amount of lines of a single molecule that can be captured in a single observation can also be used to constrain physical conditions. The formation of IR lines is a complex process, so to derive the physical and chemical environment of the line forming regions, a good understanding of this process is necessary.

### 1.3.1 Energy levels and transitions

Many near- and mid-infrared molecular lines come from vibrational transitions. These transitions change the vibrational energy that the molecule carries. Figure 1.6 shows the energy level structure and the radiative transitions for a simple case: CO. CO only has one vibrational mode. This means that there is only one fundamental vibrational band, around  $4.7 \mu\text{m}$ . In the example this band is made up of two transitions,  $v = 1 - 0$  ( $v1$ ) and  $v = 2 - 1$  ( $v2$ ), in practice all bands with  $\Delta v = 1$  will be around the same wavelength, but the emission decreases with the vibrational excitation, at least up to excitation temperatures of 3000 K.

Poly-atomic molecules will have more than one vibrational mode, leading to multiple vibrational bands. Examples of this can be seen in Bruderer et al. (2015) and Chapter 3, Fig. 3.1. Depending on the vibrational band, the rovibrational spectrum can be divided up into two or more parts. The CO  $v1$  spectrum between  $4.5$  and  $5 \mu\text{m}$  is composed of two wings, the short wavelength  $R$ -branch ( $v = 1, J + 1 \rightarrow v = 0, J$ ) and the longer wavelength  $P$ -branch ( $v = 1, J - 1 \rightarrow v = 0, J$ ). Other vibrational bands show three components. The CO<sub>2</sub>  $15\mu\text{m}$  band shows the  $R$ -branch and  $P$ -branch wings, as well as a  $Q$ -branch ( $v = 1, J \rightarrow v = 0, J$ ) feature between them. This feature is typically a blend of many lines and as such is easy to detect with low resolution spectroscopy (Carr & Najita 2008; Salyk et al. 2011b).

### 1.3.2 Line formation

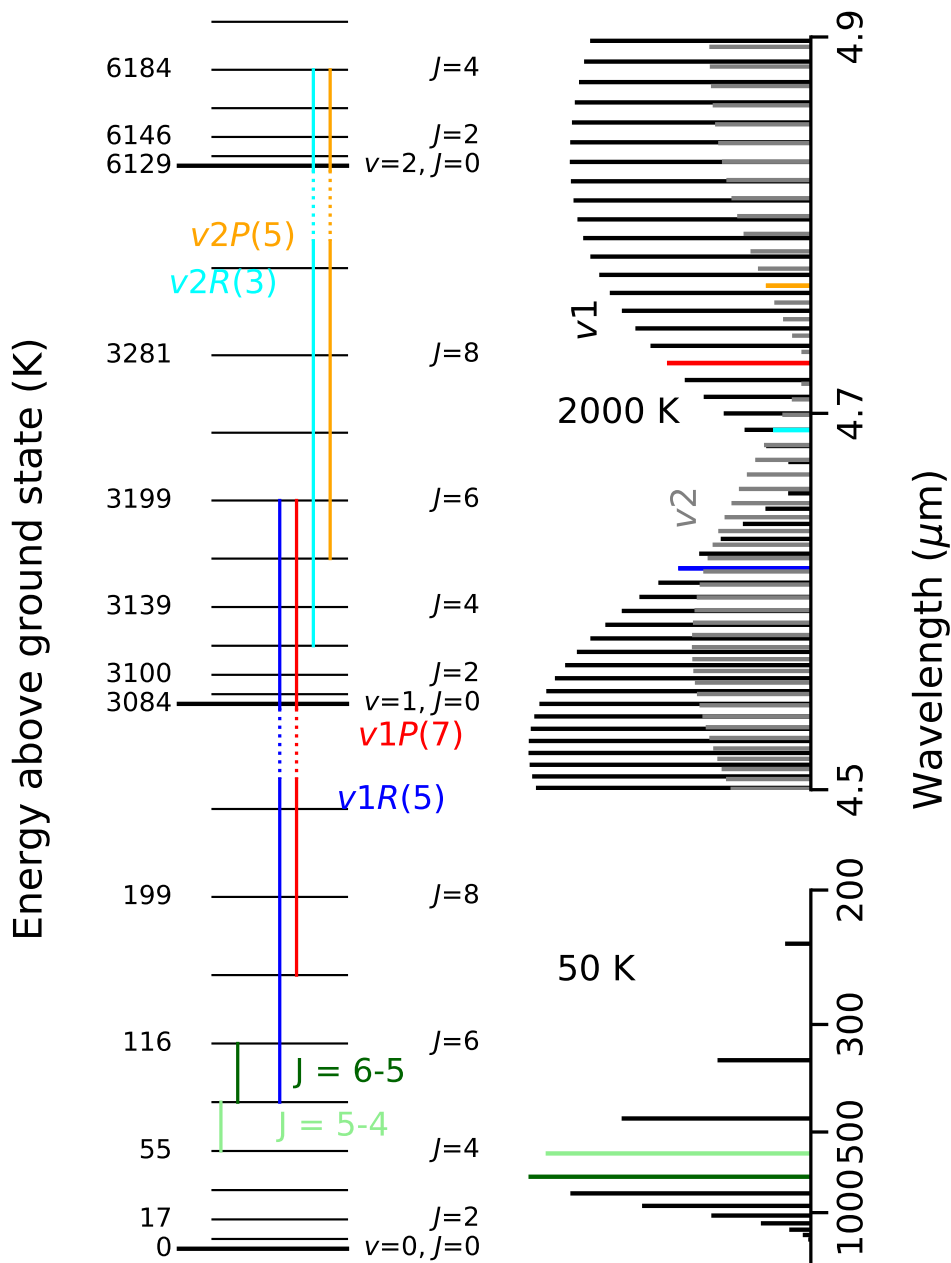
#### Local thermal equilibrium

Figure 1.6 clearly shows that the line density in the vibrational band in the infrared is a lot higher compared to the rotational transitions at sub-millimeter wavelengths. In local thermal equilibrium (LTE) the population ratio between two levels,  $n_u/n_l$  depends on the degeneracy of the levels,  $g_i$ , the difference in level energy,  $E_i$ , and the local temperature ( $T_{\text{kin}}$ ):

$$\frac{n_u}{n_l} = \frac{g_u}{g_l} \exp \left[ -\frac{(E_u - E_l)}{k_b T_{\text{kin}}} \right]. \quad (1.4)$$

The flux emitted in a given transition depends on the population of the upper level of the transition and the inherent strength of the transition, which is expressed through the Einstein  $A$  coefficient,  $A_{ul}$ , the frequency at which a level decays. Einstein  $A$  coefficients for a variety of molecules and atoms can be found in databases such as HITRAN (Rothman et al. 2013), EXOMOL (Tennyson et al. 2001), JPL (Pickett et al. 1998) and CDMS (Endres et al. 2016).

As the (ro-)vibrational lines come from levels with many different level energies, the relative strength of these lines is dependent on the excitation temperature of the molecule as is illustrated in Fig. 1.7. Both the relative strengths of rovibrational lines in a given vibrational transition as well as the relative strength of two different



**Figure 1.6:** Energy levels (left) and spectrum (right) of CO. For each vibrational level, only up to  $J = 9$  is shown, and the spacing between rotational levels has been exaggerated by a factor 10. Spectra are presented for 50 K (sub-millimeter) and 2000 K (infrared).

vibrational transitions can be used to estimate the local gas temperature (e.g. Najita et al. 2003; Salyk et al. 2011b; van der Plas et al. 2015, Chapter 3 of this Thesis).

While this can also be done for rotational transitions at longer wavelengths, the large spacing between lines for simple and common molecules like CO, CN and HCN generally necessitates multiple observations or wide band, low spectral resolving power observations, which leads to a lower line sensitivity. The strength of the infrared observations comes from the ability to observe tens of lines within a single observation, with some instruments also having the spectral resolving power to measure the line profile. The other option is to use transitions of more complex molecules as CH<sub>3</sub>CN, NH<sub>3</sub>, H<sub>2</sub>CO or SO<sub>2</sub>. While these molecules have many temperature sensitive lines, their emission is generally a lot weaker making it hard to use these temperature probes in more evolved disks.

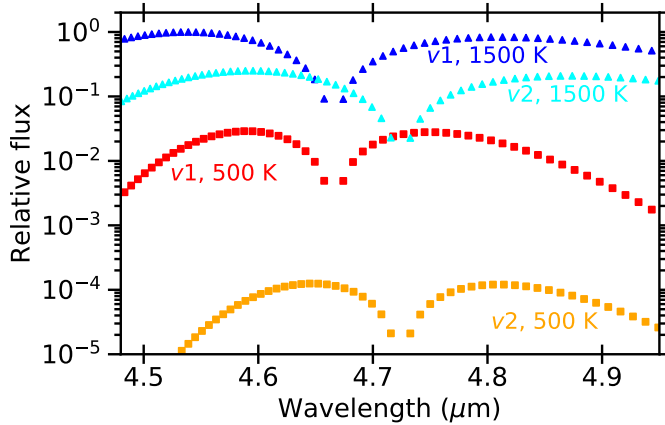


**Figure 1.7:** Flux of the CO  $v_1$  and  $v_2$  bands at two different temperatures. Increasing the excitation temperature increases the total flux in each band, with the fluxes at large  $J$  being increased more than at low  $J$ . At the same time the  $v_2$  band flux increases more with temperature than the  $v_1$  band. All these features can be used to determine the temperature of the gas a molecule is emitting from.

### Non-LTE effects

The LTE approximation is a useful tool for the analysis of infrared spectra, however, the LTE approximation does not necessarily hold in the surface layers of disks. A molecule is said to be in LTE if collisions with the gas have equilibrated the internal energy of the molecule with the kinetic energy of the gas. All molecules will try to lower their internal energy through the emission of photons. Collisions thus have to redistribute energy in the molecule faster than photon emission removes it.

In the high density environments ( $n > 10^8 \text{ cm}^{-3}$ ) that rovibrational lines generally arise from in disks, this might be true for the rotational excitation, but the vibrational excitation is not necessarily fully coupled by collisions. This is a mixed blessing, on the one hand it makes interpreting observations more difficult, on the other hand, because the excitation is not completely set by the temperature, other physical conditions can now be inferred from the spectra. The de-excitation rate of a molecular

level  $u$  to level  $l$  through collisions with species X is given by  $n_X k_{ul}$ , where  $n_X$  is the abundance of species X and  $k_{ul}$  is the collisional rate coefficient. These collisional rate coefficients are challenging to measure or calculate, as such they are known for fewer levels and molecules than the Einstein A coefficients. The Leiden Atomic and Molecular DATabase (LAMDA) and BASECOL database collect these collisional rate coefficients for species of astronomical interest. Even so, the lack of data forces astronomers to extrapolate or estimate collision rate coefficients (e.g. Bruderer et al. 2015, Chapter 3). A pair of levels is generally in LTE if the density of the main collision partner is higher than the critical density,  $n_{\text{crit}} = A_{ul}/k_{ul}$ . Below this density the population in the upper level is less than expected from LTE and the molecule will, in the absence of other sources of excitation, be sub-thermally excited.

Interactions between a molecule and photons can also change the excitation of a molecule. If a photon has the same energy as needed for a transition two things can happen, stimulated emission and absorption. Stimulated emission is the process that is used in lasers. For stimulated emission to happen, a photon has to interact with a molecule that is excited. If a transition exists at the right energy the incoming photon interacts with the excited molecule, de-exciting it through the emission of a photon identical to the incoming photon.

Absorption is the opposite process in which a photon gets absorbed and excites the molecule. In proto-planetary disks, where a strong infrared field is generated in the inner disk, this is a common process in the layers of the disk where the density is lower than the critical density. The excitation of a molecule in this way is called (infrared-)pumping. Infrared-pumping is a driving force setting the emitting region of infrared lines, and can thus have a large impact on the observed line profiles and line fluxes (Bruderer et al. 2015).

### 1.3.3 Observational challenges

Observing near- and mid-infrared lines is challenging. Many of the common molecules in space are also present in our atmosphere, for example  $\text{H}_2\text{O}$ ,  $\text{CO}$ ,  $\text{CO}_2$  and  $\text{CH}_4$ . The strongest transitions that we would like to observe, are also present in the Earth's atmosphere as the bands responsible for the greenhouse effect.  $\text{CO}_2$  is unobservable from the ground with current facilities and to observe  $\text{H}_2\text{O}$  one needs to go to lines with very high rotational excitation ( $E_{\text{rot}} > 3000$  K) to escape atmospheric absorption (Salyk et al. 2008; Pontoppidan et al. 2010; Banzatti et al. 2017).  $\text{CO}$  is a bit easier as the atmospheric lines of this molecule are strong, but narrow. This means that, with well timed observations, it is possible to use the motion of the Earth around the Sun to Doppler shift the astronomical line out of the atmospheric absorption line (e.g. Brown et al. 2013).

While technically challenging, doing observations from the ground has a few distinct advantages over the generally more expensive observations at high-altitude or from space. The first is that any observatory that has to leave the ground has strong size and weight constraints. These constraints are less present for Earth-based observatories. This means that mirrors can be bigger, yielding higher resolution and a larger light collecting surface. It also means that instruments can be bigger and more complex. Finally, ground based instruments are serviceable, allowing both day-to-day maintenance as well as full instrument upgrades without having to build and launch a complete observatory. As a result ground based instruments such as VLT-VISIR, VLT-



CRIFES(+), IRTF-iSHELL, Gemini-TEXES and Keck-NIRSpec(2.0) have a high resolving power ( $R = \lambda/\Delta\lambda = 20000\text{--}100000$ ) as well as a good wavelength coverage. The high resolving power helps by resolving both the atmospheric absorption lines as well as resolving line profiles of the astronomical target.

The line profile shape is dominated by the coherent motion of the gas which, for most disks, is Keplerian rotation. With stellar mass and inclination known, it is possible to infer the radial location of the emitting gas. The strong lines of CO are perfect to do these tests, as CO is a good tracer of  $\text{H}_2$  as both molecules are robust against photodissociation. Studies of this kind have revealed a sequence of gap opening in disks with CO that coincides with a change in physical conditions, for disks around both T-Tauri and Herbig sources (Pontoppidan et al. 2008a; Salyk et al. 2011b; Brown et al. 2013; van der Plas et al. 2015; Banzatti & Pontoppidan 2015; Banzatti et al. 2018). Detailed studies of line profiles from some T-Tauri disks reveal that not all the CO is moving in Keplerian orbits. Very peaked profiles provide evidence for disk winds (e.g. Bast et al. 2011) and this is supported by spectro-astrometric measurements, implying that the emitting area is very small (Pontoppidan et al. 2011a).

For a few of the brightest objects, the line profiles of other molecules,  $\text{H}_2\text{O}$ , OH,  $\text{C}_2\text{H}_2$  and HCN have also been measured (e.g. Salyk et al. 2011b; Mandell et al. 2012; Najita et al. 2018). The line profiles of HCN at  $3\ \mu\text{m}$  and  $12.5\ \mu\text{m}$  are very similar, while the physical conditions to excite these lines are very different (Mandell et al. 2012; Bruderer et al. 2015; Najita et al. 2018). This indicates that something interesting is happening with either the physical or chemical structure of the disk to forcing the emitting regions of these lines to overlap completely.

As many IR lines are simply not accessible from Earth, multiple space missions have been dedicated to observations in the near- and mid-infrared such as *IRAS*, *ISO* and *Spitzer*. For proto-planetary disks, *Spitzer* was transformational as it was the first instrument that could determine the composition of the planet formation regions of proto-planetary disks (Carr & Najita 2008; Salyk et al. 2008, 2011b). The low spectral resolving power meant that only strong lines or transitions made up of many lines, such as ro-vibrational  $Q$ -branches could be detected. However, the large spectral coverage meant that many different molecules were captured in a single observation.

*Spitzer* showed that  $\text{H}_2\text{O}$ ,  $\text{CO}_2$ , HCN and  $\text{C}_2\text{H}_2$  are abundant in the surface layers of disks around T-Tauri stars (Carr & Najita 2008; Pontoppidan et al. 2010; Salyk et al. 2011b; Carr & Najita 2011). Observations of disks around more massive Herbig, however, did not show such rich spectra (Pontoppidan et al. 2010; Salyk et al. 2011b). *Spitzer* data, combined with sub-millimeter fluxes, also show an interesting trend in the  $\text{H}_2\text{O}$  to HCN emission ratio, with brighter, more massive disks, showing high HCN/ $\text{H}_2\text{O}$  flux ratios, while less massive disks show lower HCN/ $\text{H}_2\text{O}$  flux ratios. This indicates that the abundances in the inner disks are influenced by processes happening at larger radii (Carr & Najita 2011; Najita et al. 2013). This indicates that the inner disk and the outer disk are intrinsically linked.

In a few years, hopefully in early 2021, the *James Webb Space Telescope (JWST)* will be launched. It will host a range of instruments, allowing for imaging and spectroscopy between  $0.6$  and  $28\ \mu\text{m}$ . The spectral resolving power of *JWST*-NIRSpec ( $0.6\text{--}5\ \mu\text{m}$ ) and *JWST*-MIRI ( $5\text{--}28\ \mu\text{m}$ ) of  $1200\text{--}3000$  is  $2\text{--}5$  times higher than that of *Spitzer* allowing for the individual measurements of CO,  $\text{C}_2\text{H}_2$ , HCN and  $\text{CO}_2$  lines (Bruderer et al. 2015; Woitke et al. 2018, Chapter 3). This, in turn, allows for more accurate determinations of the abundances of these molecules, as well as better

characterisation of the physical conditions in the regions these lines emit from.

## 1.4 Disk modelling

Many efforts have gone into modelling or simulating disks around young stars (Armitage 2011). Dealing with processes from disk formation (Visser & Dullemond 2010) and dust growth and evolution (see, e.g. Birnstiel et al. 2010; Testi et al. 2014; Krijt & Ciesla 2016) to planet formation (see, e.g. Morbidelli & Raymond 2016) and disk dispersal (see, e.g. Owen 2016; Ercolano & Pascucci 2017). All these examples deal with the physical evolution of the disk. Disks, however, are relatively long lived and most of the physical evolution happens on Myr time-scales. As such, there are many cases in which the disk can be modelled as a static object.

These models are used to understand the physical structure of the disk that we observe. Continuum radiative transfer codes, such as RADMC-3D (Dullemond et al. 2012), TORUS (Harries et al. 2019) and Hyperion (Robitaille 2011) model the dust temperature structure. Various chemical codes use these or analytical temperature structures to calculate the chemical structure of the disk (e.g. Aikawa et al. 2002; Semenov & Wiebe 2011; Walsh et al. 2015; Najita & Ádámkóvics 2017; Agúndez et al. 2018; Furuya & Aikawa 2014). These temperature and chemical structures can then be post-processed by excitation and ray-tracing codes, for example LIME and RADLite (Brinch & Hogerheijde 2010; Pontoppidan et al. 2009), to simulate observations. Coupling multiple codes allows for the modelling of disks starting with a density structure and producing observables (e.g. Cleaves et al. 2015, 2017). Line formation, molecular composition, molecular excitation and the heating cooling balance are all coupled and gas temperatures can be different from dust temperatures (e.g. Jonkheid et al. 2004; Kamp & Dullemond 2004). Therefore codes have been developed to do the physics and chemistry internally consistent, these are called thermo-chemical codes. Examples of these are Dust And Lines (DALI, Bruderer et al. 2012; Bruderer 2013), Accretion disk with Dust Evolution and Sedimentation (ANDES, Akimkin et al. 2013), Protoplanetary Disk Model (ProDiMo, Woitke et al. 2009) and the codes presented by Gorti & Hollenbach (2008) and Du & Bergin (2014). Globally these codes are very similar, but each code has particular focus points on physical and chemical processes. Some thermo-chemical codes, specifically DALI and ProDiMo use a simpler chemical network, or a network tuned to the question at hand (e.g. Miotello et al. 2014; Kamp et al. 2017; Visser et al. 2018; Woitke et al. 2018). This allows for shorter computation times as well as the evaluation of large grids of models.

## 1.5 This thesis

The road to understanding the formation and composition of the Earth is still long and filled with mysteries. Understanding the physical conditions under which planets form in proto-planetary disks, through the emission of molecules will allow us to walk further on this road and unravel some of the mysteries of planet formation. For the formation of the Earth especially the conditions in the inner few AU from the star are important. Infrared lines are the best tool available to trace this region. However, the inner disk is not a separate entity as the conditions in the outer disk can influence the inner disk and should thus not be neglected. This thesis focusses on interpreting

molecular observations using physical and chemical models of varying complexity. The main goal is to increase our understanding of the chemical and physical processes that are (or are not) responsible for the emission that we observe.

Chapter 2 of this thesis takes a detailed chemical look into the question of CO sub-millimeter emission from disks as a whole. CO is often used as tracer for H<sub>2</sub> and a tracer of total gas mass. However emission from CO is very weak in disks and inconsistent with other disk mass tracers. This indicates that the chemistry of CO might be more complex. This would have an impact not just on our measurements of disk gas masses, but also on our predictions of planets formed here. Chapter 2 investigates the chemical processes that can happen in the main mass reservoir of proto-planetary disks near the midplane, looking at the cosmic-ray driven chemistry in both the gas-phase and on the grain surface.

Chapter 3 and 4 of this thesis investigate CO<sub>2</sub> in proto-planetary disks. CO<sub>2</sub> is an abundant carrier of both carbon and oxygen and a critical ingredient in understand the carbon and oxygen budget in disks. Chapter 3 investigates the line formation processes in disks. This knowledge is used to derive abundances from *Spitzer*-IRS observations and to make predictions for *JWST* observations. Chapter 4 discusses and models the effect of transport of material from the outer to the inner disk, focussing on CO<sub>2</sub> and its potential to be a tracer of the transport of ice material through the disk.

Chapter 5 deals again with CO, but this time in the inner regions of Herbig Ae disks. Near-infrared spectroscopy of CO rovibrational lines in Herbig disks shows different trends than for T-Tauri disks. The excitation and line formation of CO rovibrational lines are investigated and the observed trends are put into the context of the physical structures that are causing them.

Chapter 6 focusses on the inner (0.3–2.3 AU) of TW Hya. Archival *Spitzer* data including H<sub>2</sub>O and H<sub>2</sub> lines and VLT-CRIRES data of CO lines are compared to a detailed thermo-chemical model, tailored to TW Hya. By varying the elemental abundances, the carbon and oxygen budget of the inner disk of TW Hya is constrained.

The main conclusions of this thesis are:

- Chemical processes in the outer disk will lower the CO abundance. These processes will mostly produce molecules that are hard to observe because they are either strongly bound to the ice (CH<sub>3</sub>OH, H<sub>2</sub>O), do not emit in the sub-millimeter (CH<sub>4</sub>) or both (CO<sub>2</sub>). However, to lower the CO abundances to the observed levels by pure chemical processes, high cosmic-ray ionisation rates or efficient ionisation by other types of radiation are needed. Under these conditions of fast processing, midplane ices are predicted to be very rich in CO<sub>2</sub> and CH<sub>3</sub>OH, while hydro-carbons, CH<sub>4</sub> and C<sub>2</sub>H<sub>6</sub> dominate the carbon budget in both the ice and gas of the disk atmosphere.
- Gaseous CO<sub>2</sub> is more than two orders less abundant in the inner disk than it is in interstellar ices. This indicates that inner disk chemistry has a strong impact on the abundance of CO<sub>2</sub>. The higher resolving power of *JWST*-MIRI will allow for the detection of individual *R* and *P* branch lines as well as the <sup>13</sup>CO<sub>2</sub> *Q*-branch. This will enable the detection of the variation of the CO<sub>2</sub> abundance with radius. In these determinations, it is critical to properly take into account infrared pumping, as it allows CO<sub>2</sub> to emit from far larger radii, than predicted from pure LTE models.
- Transport of icy grains from the CO<sub>2</sub> rich outer disk, to the CO<sub>2</sub> poor inner disk

is efficient, and can strongly impact the CO<sub>2</sub> abundance of the inner disk. In disks with only gas accretion, the bulk CO<sub>2</sub> abundance within the CO<sub>2</sub> iceline should equilibrate with the outer disk icy CO<sub>2</sub> abundance within 1 Myr. If radial drift is included, the bulk CO<sub>2</sub> abundance within the CO<sub>2</sub> iceline will be even higher. These abundances are inconsistent with current observations, and no chemical pathway is fast enough to destroy CO<sub>2</sub> in the midplane. A strong vertical gradient in the CO<sub>2</sub> abundance could solve this problem, with low CO<sub>2</sub> abundances in the surface layers, and high CO<sub>2</sub> abundance near the mid-plane. Observations of <sup>13</sup>CO<sub>2</sub> with *JWST*-MIRI might be able to observe this gradient. It provides a warning that surface abundances may not be representative of the midplane.

- Velocity resolved near-infrared observations of CO contain a wealth of information on the inner regions of disks and Herbig Ae disks in particular. In the dust free inner regions and in the sublimation zone of Herbig disks the conditions are so harsh, with high temperatures and UV fields, that CO cannot survive in high enough abundance to be detected. CO emission in disks that have dust in the inner  $\sim 5$  AU comes only from the disk surface, not from the inner wall. For most of these disks the extent of the rovibrational CO emission is truncated, indicating disk substructure on a few AU scale, possibly linked to substructures seen in the highest resolution sub-millimeter images. Disks that lack dust in the inner  $\sim 5$  AU, are also strongly depleted in gas ( $\delta_{\text{gas}} < 10^{-5}$ ) in this region. The region from which the lines are emitted is rich in gas, with dust depleted by at least two orders of magnitude. This pattern fits well with giant planets in the cavities in these disks.
- The inner disk of TW Hya appears to have a similar underabundance of elemental carbon and oxygen as the outer disk. This indicates that the transport of icy grains over icelines, especially the H<sub>2</sub>O iceline, is restricted. This is most likely due to a strong dust trap at the location of the bright sub-millimeter ring at 2.3 AU.

### 1.5.1 Future outlook

The *James Webb Space Telescope* has been on the horizon for quite a while, and when it starts observing, should revolutionize the study of the inner regions of proto-planetary disks. For *JWST* to have the full impact it can have, more detailed models will be necessary. The data that *JWST* will give us contain information on the temperature, density and chemical structure of the inner few AU of the disk, exactly the information that is necessary for planet formation models. However, to extract this information, fitting rotational temperatures and molecular column densities will not be enough. Exploiting the dependencies of the chemistry on the physical conditions, it will be possible to measure the elemental ratios, as well as measure constraints the absolute density of gas in the surface layers. *JWST* will be able to measure the elemental oxygen and carbon contents of the inner disk atmosphere directly.

These measurements constrain not only the composition but also the size of the gas reservoir that feeds giant planets in the inner disk. This full census of molecular gas in the inner disk can then be put into the molecular context of the full disk as well as in the context of disk evolution. Ground based infrared spectroscopy will have a big role

to play in the *JWST* era, providing velocity resolved line profiles and as such, spatial information on the emitting gas. This information will be crucial for understanding *JWST* spectra and connecting the physical conditions (temperature, density) with radial location. ALMA has only just started revolutionising our understanding of the outer disk, there are also opportunities for the inner disk. ALMA probes deeper into the disk with the sub-millimeter radiation than is possible with infrared emission. As some energy levels can only be populated in the inner most regions of the disk it is possible to probe the inner few AU with ALMA without resolving this region by choosing the right lines to observe. This allows for the measurement of the H<sub>2</sub>O midplane snowline location, and, when combined with infrared observations provides 2D information on the inner disk. Without an upgrade in line sensitivity (or a large drop in over-subscription rate), this might only be possible in a handful of disks.

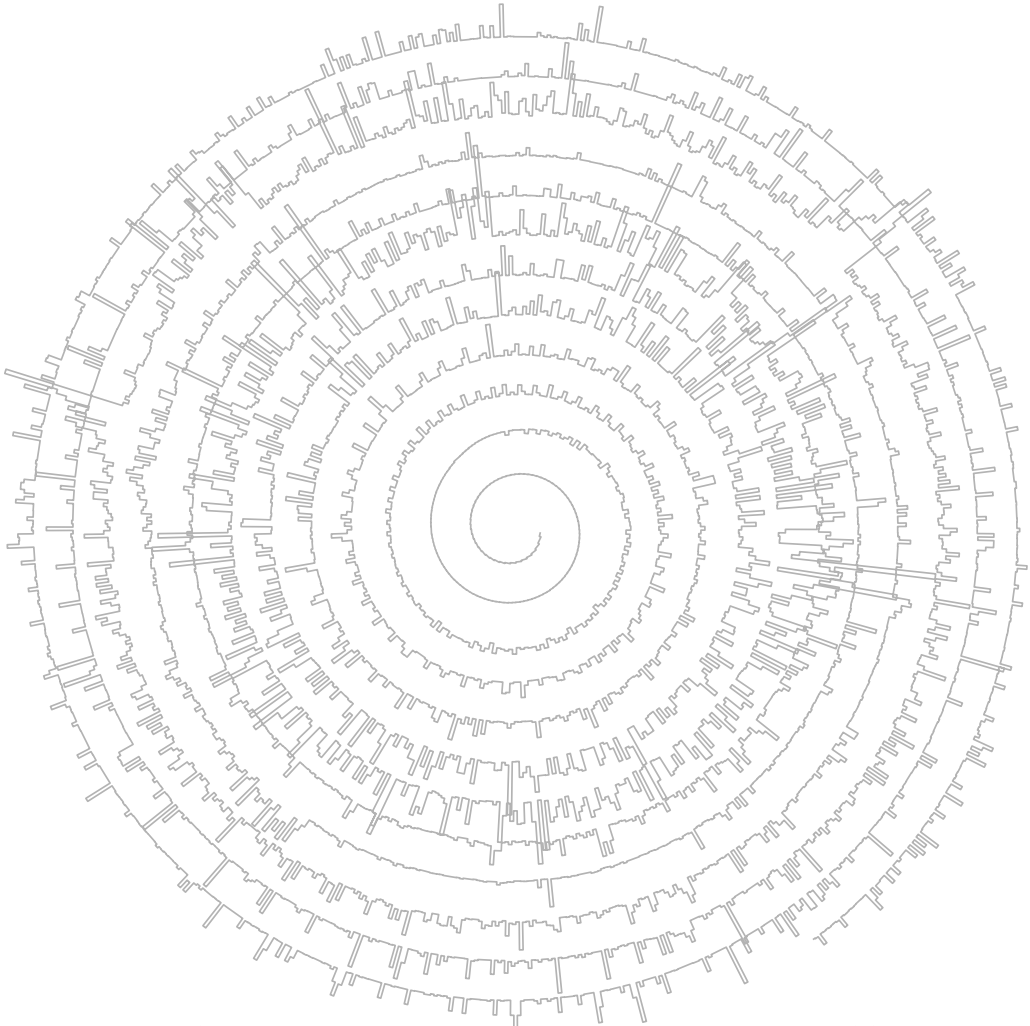
Looking beyond *JWST*, there are more observatories to be excited about. The Extremely Large Telescope (ELT), a 39 meter telescope built by ESO, will host Mid-Infrared E-ELT Imager and Spectrograph (Metis, Brandl et al. 2014). METIS will have IFU capabilities at near and mid-infrared wavelengths at high resolving power (R=100000). This allows for diffraction limited imaging of velocity resolved gas emission, providing resolved kinematic information for many disks. The HIRMES instrument on SOFIA, as well as the proposed Space Infrared Telescope for Cosmology and Astrophysics (SPICA) and Origins Space Telescope (OST) will provide velocity resolved spectra at mid- and far-wavelengths. Data from these telescopes can fill in the gap between the hot inner disk probed with *JWST* and the colder, outer disk as probed with ALMA, a critical region for building planets.

Both the advent of *JWST* as well as the success of ALMA has given modellers an impulse towards more intricate, and more complete models of proto-planetary disks. ALMA observations show that disks are, in many cases not smooth and to understand the effects of these substructures, they need to be included in the models. It has become clear that the strategy of modelling only one physical aspect of the disk (e.g. dust evolution, gas dispersal) or modelling purely the chemical evolution in a static disk is no longer enough to understand the observations. More and more effort will be put into combining the effects of the physical and chemical evolution, and interactions that they have. Here, it is not the goal to have a model that includes everything, or a model that can fit all observations, but that we learn why a process is important and what the implications are of a model that can explain the observations.

*JWST* will further challenge our models. *JWST* spectra will contain information of a range radii in the disk. This convoluted information can only be extracted using models that properly include line formation processes. This is somewhat problematic at this point, as CO, H<sub>2</sub>O and HCN are the only molecules for which we have proper collisional rate coefficients. To get everything we can out of *JWST*, the collisional rate coefficients need to be calculated for the other abundant inner disk species, such as CO<sub>2</sub>, CH<sub>4</sub>, C<sub>2</sub>H<sub>2</sub> and NH<sub>3</sub>. Fortunately, some of this work is underway as part of the Dutch Astrochemistry Network II. Finally, as in the inner disk, all timescales are shorter, it is even more important to understand the interaction between physical processes, such as vertical mixing, dust growth and settling and the spectra that we observe.

# 2

## CO DESTRUCTION IN PROTOPLANETARY DISK MIDPLANES: INSIDE VERSUS OUTSIDE THE CO SNOW SURFACE



A. D. Bosman, C. Walsh and E. F. van Dishoeck, 2018, *A&A*, 618 182

## Abstract

**Context:** The total gas mass is one of the most fundamental properties of disks around young stars, because it controls their evolution and their potential to form planets. To measure disk gas masses, CO has long been thought to be the best tracer as it is readily detected at (sub)mm wavelengths in many disks. However, inferred gas masses from CO in recent ALMA observations of large samples of disks in the 1–5 Myr age range seem inconsistent with their inferred dust masses. The derived gas-to-dust mass ratios from CO are 1-2 orders of magnitude lower than the ISM value of  $\sim 100$  even if photodissociation and freeze-out are included. In contrast, *Herschel* measurements of HD line emission of a few disks imply gas masses in line with gas-to-dust mass ratios of 100. This suggests that at least one additional mechanism is removing CO from the gas-phase.

**Aims:** Here we test the suggestion that the bulk of the CO is chemically processed and that the carbon is sequestered into less volatile species such as CO<sub>2</sub>, CH<sub>3</sub>OH and CH<sub>4</sub> in the dense, shielded midplane regions of the disk. This study therefore also addresses the carbon reservoir of the material which ultimately becomes incorporated into planetesimals.

**Methods:** Using our gas-grain chemical code we perform a parameter exploration and follow the CO abundance evolution over a range of conditions representative of shielded disk midplanes.

**Results:** Consistent with previous studies, we find that no chemical processing of CO takes place on 1–3 Myr timescales for low cosmic-ray ionisation rates,  $< 5 \times 10^{-18} \text{ s}^{-1}$ . Assuming an ionisation rate of  $10^{-17} \text{ s}^{-1}$ , more than 90% of the CO is converted into other species, but only in the cold parts of the disk below 30 K. This order of magnitude destruction of CO is robust against the choice of grain-surface reaction rate parameters, such as the tunnelling efficiency and diffusion barrier height, for temperatures between 20 and 30 K. Below 20 K there is a strong dependence on the assumed efficiency of H tunnelling.

**Conclusions:** The low temperatures needed for CO chemical processing indicate that the exact disk temperature structure is important, with warm disks around luminous Herbig stars expected to have little to no CO conversion. In contrast, for cold disks around sun-like T Tauri stars, a large fraction of the emitting CO layer is affected unless the disks are young ( $< 1 \text{ Myr}$ ). This can lead to inferred gas masses that are up to two orders of magnitude too low. Moreover, unless CO is locked up early in large grains, the volatile carbon composition of the icy pebbles and planetesimals forming in the midplane and drifting to the inner disk will be dominated by CH<sub>3</sub>OH, CO<sub>2</sub> and/or hydrocarbons.

## 2.1 Introduction

The total gas mass is one of the most fundamental parameters that influences protoplanetary disk evolution and planet formation. Interactions of the gas and dust set the efficiency of grain-growth and planetesimal formation (e.g. Weidenschilling 1977; Brauer et al. 2008; Birnstiel et al. 2010; Johansen et al. 2014), while interactions of planets with the gaseous disk leads to migration of the planet and gap formation (see, e.g. Kley & Nelson 2012; Baruteau et al. 2014, for reviews). Significant amounts of gas are needed to make giant Jovian-type planets. All of these processes depend sensitively on either the total amount of gas or the ratio of the gas and dust mass. Dust masses can be estimated from the continuum flux of the disk, which is readily detectable at sub-millimeter (mm) wavelengths. However, the main gaseous component  $\text{H}_2$  does not have any strong emission lines that can trace the bulk of the disk mass, so that other tracers need to be used. Emission from the CO molecule and its isotopologues is commonly used as a mass tracer of molecular gas across astronomical environments (for reviews see, e.g. van Dishoeck & Black 1987; Bolatto et al. 2013; Bergin & Williams 2017). CO is resistant to photodissociation because it can self-shield against UV-photons and is thus a molecule that can trace  $\text{H}_2$  in regions with low dust shielding (van Dishoeck & Black 1988; Viala et al. 1988; Lee et al. 1996; Visser et al. 2009). CO also has, in contrast with  $\text{H}_2$ , strong rotational lines, coming from states that can be populated at 20 K, the freeze-out temperature of CO. In most astronomical environments, CO is also chemically stable due to the large binding energy of the C–O bond. This chemical stability means that CO is usually the second most abundant gas-phase molecule and the main volatile carbon reservoir in molecular astronomical environments. Thus, the recent finding that CO emission from protoplanetary disks is very weak came as a big surprise and implies that CO may be highly underabundant (Favre et al. 2013; Bruderer et al. 2012; Du et al. 2015; Kama et al. 2016; Ansdell et al. 2016). Is CO transformed to other species or are the majority of disks poor in gas overall?

By extrapolating the chemical behaviour of CO from large scale astronomical environments to protoplanetary disks it was expected that only two processes need to be accounted for in detail to determine the gaseous CO abundance throughout most of the disk: photodissociation and freeze-out of CO (Dutrey et al. 1997; van Zadelhoff et al. 2001, 2003). This was the outset for the results reported by Williams & Best (2014) who computed a suite of disk models with parametrised chemical and temperature structures, to be used for the determination of disk gas masses from the computed line emission of CO isotopologues. This method was expanded by Miotello et al. (2014, 2016) who calculated the temperature, CO abundance and excitation self-consistently using the thermo-chemical code DALI<sup>1</sup> (Bruderer et al. 2012; Bruderer 2013). Miotello et al. (2016) used a simple gas-grain network that includes CO photodissociation, freeze-out and grain-surface hydrogenation of simple species, but no full grain surface chemistry. DALI also computes the full 2D dust and gas temperature structure, important for determining the regions affected by freeze-out and emergent line emission. Because emission from the main CO isotopologue  $^{12}\text{C}^{16}\text{O}$  is often optically thick, most observations target the rarer CO isotopologues. These do not necessarily follow the highly abundant  $^{12}\text{C}^{16}\text{O}$  as  $^{12}\text{C}^{16}\text{O}$  can efficiently shield itself from photodissociating UV radiation at lower  $\text{H}_2$  column densities compared with

---

<sup>1</sup><http://www.mpe.mpg.de/~facchini/DALI/>



the less abundant isotopologues. As such, the rarer isotopologues are dissociated over a larger region of the disk, an effect known as isotope-selective photodissociation (see, for example Visser et al. 2009). The combined effects of the different temperature structure and isotope-selective photodissociation change the emission strengths of the CO isotopologues by up to an order of magnitude compared with the predictions of Williams & Best (2014).

When either of these model predictions including photodissociation and freeze-out are applied to ALMA observations of large samples of disks, still low gas masses are determined: inferred gas masses are close to, or lower than, the calculated dust mass from the same observations instead of the expected 100:1 ratio (Ansdell et al. 2016; Miotello et al. 2017; Pascucci et al. 2016; Long et al. 2017). While it is possible that these disks are indeed very gas depleted, independent determinations of the gas masses such as from far-infrared HD data (see, e.g. Bergin et al. 2013; McClure et al. 2016; Trapman et al. 2017) and mass accretion rates (Manara et al. 2016b) imply that the CO/H<sub>2</sub> abundance ratio is likely much lower than expected, at least in the CO emitting part of the disk.

Multiple mechanisms have been proposed to explain this low CO abundance, both chemical and physical. A physical argument for the low CO abundances comes from the vertical mixing of the gas together with settling of dust. Kama et al. (2016) argued that the low CO abundance in the upper emitting layers of the outer disk can be explained by the constant vertical cycling of gaseous CO. Every vertical cycle some CO will freeze-out onto grains that have grown and settled below the CO snow surface. These larger grains do not cycle back up again to the warmer regions where CO can be returned to the gas. They show that the CO abundance can be significantly lowered over the disk lifetime. This mechanism also predicts a strong anti-correlation between age and measured CO abundance. The mechanism can explain the destruction of CO in the warm layers, such as reported by Schwarz et al. (2016) and at the same time explain the lower than expected H<sub>2</sub>O abundances found in the outer disk of TW Hya and other disks by Hogerheijde et al. (2011) and Du et al. (2017). However this mechanism cannot explain the low abundance of CO inside of the CO iceline, the radial location of the snow surface at the midplane, as inferred by Zhang et al. (2017) for TW Hya.

Alternatively, there are various chemical mechanisms that destroy CO, sometimes referred to as “chemical depletion”. Some of the proposed chemical pathways start with the destruction of gaseous CO by He<sup>+</sup>, leading to the formation and subsequent freeze-out of CH<sub>4</sub> (Aikawa et al. 1999; Eistrup et al. 2016) or, when computed at slightly higher temperatures, the gas-phase formation of C<sub>2</sub>H<sub>2</sub> and subsequent freeze-out and further chemical alteration on the grain-surface (Yu et al. 2016). Another pathway to destroy CO is the reaction with OH to form CO<sub>2</sub>, either in the gas-phase (Aikawa et al. 1999), or on the grain-surface (Furuya & Aikawa 2014; Reboussin et al. 2015; Drozdovskaya et al. 2016; Eistrup et al. 2016; Schwarz et al. 2018). The formation of CO<sub>2</sub> through the grain-surface route seems to be most efficient at temperatures around 25 K, just above the freeze-out temperature of CO. A third pathway to destroy CO is the hydrogenation of CO on the dust grain-surface forming CH<sub>3</sub>OH (Cuppen et al. 2009; Yu et al. 2016; Eistrup et al. 2018). All of these models start with a high abundance of CO and modify the abundance through chemical processes. Alternatively there are models that do not have CO initially as they assume that, due to some reset process, the gas is fully ionised or atomic at the start of the calculation (Eistrup et al.

2016; Molyarova et al. 2017). Due to the high abundance of OH during the transition of atomic to molecular gas, CO<sub>2</sub> can be efficiently formed. At low temperatures (< 50 K) CO<sub>2</sub> becomes the most abundant carbon bearing species.

All of these CO destruction processes are driven by dissociating or ionising radiation, either UV photons, X-rays or cosmic-rays. In regions where UV photons and X-rays are not able to penetrate, cosmic-rays drive the chemistry, so that the chemical timescales of CO processing are strongly dependant on the cosmic-ray ionisation rate (Reboussin et al. 2015; Eistrup et al. 2018). Indeed, Eistrup et al. (2016) show that chemical evolution during the disk lifetime in the dense midplane is negligible if the only source of ionisation is provided by the decay of radioactive nuclides. In line with these results, Schwarz et al. (2018) find that even in the warm molecular layers either a cosmic-ray ionisation rate of  $10^{-17} \text{ s}^{-1}$  or a strong X-ray field is needed to significantly destroy CO. High cosmic-ray ionisation rates are not expected if the proto-stellar magnetic field is sufficiently strong to deflect galactic cosmic-rays (Cleeves et al. 2015).

The goal of this paper is to study the chemical pathways that can destroy CO in those regions of the disk that are sufficiently shielded from UV photons such as that near the disk midplane. The effectiveness and timescale of CO destruction pathways as functions of temperature, density and cosmic-ray ionisation rate are investigated for comparison with the increasing number of ALMA surveys of CO in disks in the 1-10 Myr age range. We also study the effect of the assumed grain-surface chemistry parameters, in particular the tunnelling barrier width and the diffusion-to-binding energy ratio. To be able to do this study in an as general sense as possible we do not restrict ourselves to any specific disk structure but instead perform a parametric study of temperature, density and cosmic-ray ionisation rate over a range representative of a significant portion of the disk mass.

## 2.2 Methods

### 2.2.1 Parameter space

To constrain the amount of chemical processing of CO in shielded regions of disks, a grid of chemical and physical conditions typical for disk midplanes inside and outside the CO iceline is investigated. The explored parameter range is given in Table 2.1. The disk midplane is assumed to be shielded from stellar and interstellar UV-photons. As such, cosmic-ray induced photons are the only source of UV photons included in the model. The region is also assumed to be shielded from the most intense fluxes of stellar X-rays. The effects of moderate X-ray ionisation rates are similar to the effects of scaled up cosmic-ray ionisation rates (Bruderer et al. 2009).

There are two steps in this parameter study. First a grid of chemical models for different physical conditions are computed. Temperatures, densities and cosmic-ray ionisation rates typical for cold, shielded regions of protoplanetary disks are used. For these models typical chemical parameters were used. In particular the tunnelling barrier width ( $a_{\text{tunnel}}$ ) and diffusion-to-binding energy ratio ( $f_{\text{diff}}$ ), characterizing surface chemistry (see Sec. 2.2.2), were kept constant at 1 Å and 0.3 respectively.

For typical T-Tauri and Herbig disks, the physical conditions probed by our models are shown in Fig. 2.1. The exact specifications of the models are presented in Appendix 2.A. Both models assume a tapered power-law surface density distribution

and a Gaussian vertical distribution for the gas. The dust and gas surface densities follow the same radial behaviour with an assumed global gas-to-dust mass ratio of 100. Vertically there is more dust mass near the mid-plane, to simulate dust settling. The temperatures and densities that are included in the chemical models are shown in orange in the bottom panel in Fig. 2.1. The dark orange regions are those that are also completely shielded from VUV radiation. The gas is considered shielded if the intensity of external UV radiation at 100 nm is less than  $10^{-4}$  times the intensity at that wavelength from the Draine ISRF (Draine 1978; Shen et al. 2004). Our models are however more broadly applicable to other parts of the disks due to dynamical mixing, as described below.

As the T-Tauri disk model is colder (because of the less luminous star) and more compact compared to the Herbig disk model, there is more mass in the region of the disk probed by our models for that disk. The exact extent and location of the region probed by our chemical models strongly depends on the chosen parameters of the disk model. In the Herbig model the temperature never drops below 20 K, as such CO is not frozen out anywhere in that disk model.

For selected points in the physical parameter space an additional grid of chemical models is explored (see Sec. 2.3.2).

### 2.2.2 Chemical network

The chemical network used in this work is based on the chemical model from Walsh et al. (2015) as also used in Eistrup et al. (2016, 2018). The "RATE12" network from the UMIST Database for Astrochemistry forms the basis of the gas-phase chemistry (McElroy et al. 2013)<sup>2</sup>. RATE12 includes gas-phase two-body reactions, photodissociation and photoionisation, direct cosmic-ray ionisation, and cosmic-ray-induced photodissociation and ionisation. Three-body reactions are not included as they are not expected to be important at the densities used in this work. Photo- and X-ray ionisation and dissociation reactions are included in the network but their contribution is negligible because we assume the disk midplane is well shielded from all external sources of X-ray and UV photons.

Freeze-out (adsorption) onto dust grains and sublimation (desorption) of molecules is included. Molecules can desorb either thermally or via cosmic-ray induced photodesorption (Tielens & Hagen 1982; Hasegawa et al. 1992; Walsh et al. 2010, 2012). Molecular binding energies as compiled for Rate12 (McElroy et al. 2013) are used, updated with the values recommended in the compilation by Penteado et al. (2017), except for NH, NH<sub>2</sub>, CH, CH<sub>2</sub> and CH<sub>3</sub>. For NH and NH<sub>2</sub> we calculate new estimates using the formalism proposed by Garrod & Herbst (2006) and the binding energy for NH<sub>3</sub> (3130 K, Brown & Bolina 2007). For the CH<sub>x</sub> radicals the binding energy is scaled by the number of hydrogen atoms with the CH<sub>4</sub> binding energy of 1090 K as reference (He & Vidalí 2014). A list of all the binding energies used in this work is given in Table 2.8. The binding energy used for H<sub>2</sub>, 430 K, predicts complete freeze-out of H<sub>2</sub> at temperatures up to 15 K at densities of  $10^{12}$  cm<sup>-3</sup>. However, at similar densities, H<sub>2</sub> freezes-out completely at much lower temperatures (Cuppen & Herbst 2007). The binding energy used here is the H<sub>2</sub> to CO binding energy, whereas the H<sub>2</sub> to H<sub>2</sub> binding energy is expected to be much lower (Cuppen & Herbst 2007). As such we modify the binding energy of H<sub>2</sub> such that it is 430 K as long as there is less

<sup>2</sup>Which is available at: <http://www.udfa.net>

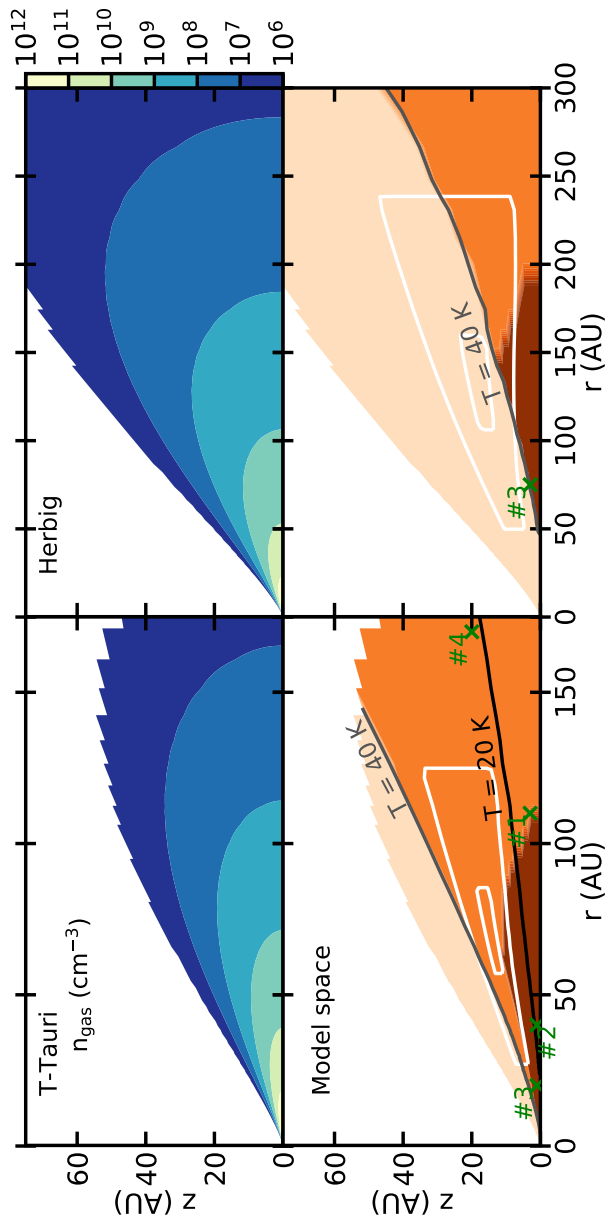


**Figure 2.1:** Number density (*top*) and region of the disk included in the parameter study (*bottom*) for a typical T-Tauri ( $L = 0.3 L_{\odot}$ ) (*left*) and Herbig ( $L = 20 L_{\odot}$ ) (*right*) disk model (see App. 2.A for details). The part of the disk that is included in the physical models is shown in dark orange and is bound by the highest temperature included (40 K) and the restriction that the UV is fully shielded. Light orange denotes the region with temperatures and densities probed by our models but with some low level of UV. White contours show the regions contributing to 25% and 75% of the emission from the  $\text{C}^{18}\text{O}$  3-2 line. The green crosses numbered #1, #2, #3 and #4 are approximate locations of the representative models of Sec. 2.3.1.

than one monolayer of H<sub>2</sub> ice on the grain. Above two monolayers of H<sub>2</sub> ice we use the H<sub>2</sub> on H<sub>2</sub> binding energy of 100 K. Between these two regimes, the binding energy of H<sub>2</sub> is linearly dependant on the coverage of H<sub>2</sub> ice. This is a different approach compared to that described in Hincelin et al. (2015) and Wakelam et al. (2016) but it has a similar effect on the H<sub>2</sub> ice abundance. In all cases  $E_{\text{diff}} = f_{\text{diff}} \times 430\text{K}$  for the diffusion of H<sub>2</sub>.

Experimentally determined photodesorption yields are used where available (see, e.g. Öberg et al. 2009c,b,a), specifically  $2.7 \times 10^{-3}$  CO molecules per photon is used from Öberg et al. (2009c). We note that a large range of CO photodesorption yields, between  $4 \times 10^{-4}$  and 0.25 CO molecules per photon, are available in the literature due to the significant effects of experimental conditions (Öberg et al. 2007, 2009c; Muñoz Caro et al. 2010; Fayolle et al. 2011; Chen et al. 2014; Muñoz Caro et al. 2016; Paardekooper et al. 2016). Fayolle et al. (2011) show that temperature and the wavelength of the incident photon strongly influence the photodesorption yield. For all species without experimentally determined photodesorption yields, a value of  $10^{-3}$  molecules photon<sup>-1</sup> is used. The sticking efficiency is assumed to be 1 for all species except for the atomic hydrogen that leads to H<sub>2</sub> formation.

The formation of H<sub>2</sub> is implemented following Cazaux & Tielens (2004) (see Appendix 2.B.2 for a summary). This formalism forms H<sub>2</sub> directly out of gas-phase H. This fraction of atomic hydrogen is not available for reactions on the grain surface. About 50% of the atomic hydrogen is used to form H<sub>2</sub> in this way. The remaining atomic hydrogen freezes-out on the grain surface and participates in the grain surface chemistry. Using this formalism ensures that the abundance of atomic H does not depend on the adopted grain-surface parameters. The balance between H<sub>2</sub> formation and H<sub>2</sub> destruction by cosmic-rays produces an atomic H abundance in the gas that will always be around  $1 \text{ cm}^{-3}$  independent of the total H nuclei abundance.

For the grain-surface reactions we use the reactions included in the Ohio State University (OSU) network<sup>3</sup> (Garrod et al. 2008). The gas-phase network is supplemented with reactions for important chemicals, e.g. the CH<sub>3</sub>O radical, that are not included in RATE12. The destruction and formation reactions for these species are taken from the OSU network. The grain-surface network also includes additional routes to water formation as studied by Cuppen et al. (2010) and Lamberts et al. (2013). The grain-surface reactions are calculated assuming the Langmuir-Hinshelwood mechanism. Only the top two layers of the ice are chemically "active" and we assume that the chemically active layers have the same composition as the bulk ice. No reaction-diffusion competition for grain-surface reactions with a reaction barrier is included (Garrod & Pauly 2011). The exact equations used to calculate the rates can be found in Appendix 2.B.3.

The rates for the grain-surface reactions greatly depend on two quantities, the tunnelling barrier ( $a_{\text{tunnel}}$ ) and the diffusion-to-binding energy ratio ( $f_{\text{diff}}$ ).  $a_{\text{tunnel}}$  is usually taken to lie between 1 and 1.5 Å (Garrod & Pauly 2011; Walsh et al. 2015; Eistrup et al. 2016), and we test the range between 0.5 Å to 2.5 Å. The diffusion-to-binding energy ratio is generally taken to range between 0.3 and 0.5 (Walsh et al. 2015; Cuppen et al. 2017), although recent quantum chemical calculations predict values as low as  $f_{\text{diff}} = 0.15$  for H on crystalline water ice (Senevirathne et al. 2017). On the other hand, recent experiments suggest fast diffusion rates for CO on CO<sub>2</sub> and H<sub>2</sub>O ices (Lauck et al. 2015; Cooke et al. 2018). The range tested here,  $f_{\text{diff}} = 0.1$  to

<sup>3</sup><http://faculty.virginia.edu/ericherb/research.html>

**Table 2.1:** Physical and chemical parameters explored

Parameter	Symbol	Range	Fiducial value
Temperature	$T$	10 – 40 K	–
Density	$n$	$10^6 - 10^{12} \text{ cm}^{-3}$	–
Cosmic-ray ionisation rate	$\zeta_{\text{H}_2}$	$10^{-18} - 10^{-16} \text{ s}^{-1}$	–
Tunnelling barrier width	$a_{\text{tunnel}}$	0.5 – 2.5	1 Å
Diffusion-to-binding energy ratio	$f_{\text{diff}}$	0.1 – 0.5	0.3

**Table 2.2:** Symbol overview for the rate equations

Symbol	Parameter	Value [Unit]
$R_{X+Y}$	X + Y reaction rate	$[\text{cm}^{-3} \text{ s}^{-1}]$
$n_{X,A}$	number density of species X in phase A	$[\text{cm}^{-3}]$
$N_{\text{sites}}$	number of molecules per layers per grain	$10^6$
$n_{\text{grain}}$	number density of grains	$2.2 \times 10^{-12} n_{\text{gas}} [\text{cm}^{-3}]$
$N_{\text{layer}}$	number of ice layers	$n_{\text{ice}}/N_{\text{act}} N_{\text{sites}} n_{\text{grain}}$
$C_{\text{grain}}$	ice mantle dependent prefactor	$\min [1, N_{\text{layer}}^2] / (N_{\text{sites}} n_{\text{grain}}) [\text{cm}^3]$
$\mu$	reduced mass of the reacting species	[g]
$E_{\text{bar}}$	height of the reaction barrier	[erg]
$E_{\text{bind},X}$	binding energy of species X	[erg]
$\nu_X$	vibration frequency of species X	Eq. 2.17[s <sup>-1</sup> ]

$f_{\text{diff}} = 0.5$ , encompasses this measured range.

The chemical models are initialised with molecular abundances. The full list of abundances is given in Appendix 2.B.1). Fully atomic initial conditions are not investigated.

### 2.2.3 CO destruction routes

There are three main pathways to destroy CO (see introduction). These are:

1.  $\text{sCO} + \text{sH} \longrightarrow \text{sHCO}$ , leading to  $\text{sCH}_3\text{OH}$
2.  $\text{sCO} + \text{sOH} \longrightarrow \text{sCO}_2 + \text{sH}$
3.  $\text{CO} + \text{He}^+ \longrightarrow \text{C}^+ + \text{O} + \text{He}$ , leading to  $\text{CH}_4$  and  $\text{C}_2\text{H}_6$

where  $\text{sX}$  denotes that species X is on the grain-surface. The interactions of these reactions with each other and the major competing reactions are shown in Fig. 2.2. For each of these reactions a short analysis on the resulting rates is presented to explain the behaviour of the CO abundance as shown in Sec. 2.3 using the rate coefficients derived in Appendix 2.B.3. Table 2.2 gives an overview of the symbols used, whereas Table 2.3 shows the sensitivity to assumed parameters.

The reaction:



happens on the surface and through further hydrogenation of  $\text{sHCO}$  leads to the formation of  $\text{sCH}_3\text{OH}$ . The initial step in this process is the most important and rate limiting step. This reaction has a barrier,  $E_{\text{bar}} = 2500 \text{ K}$  (Woon 2002), which makes tunnelling of H very important. The total CO destruction rate, assuming that

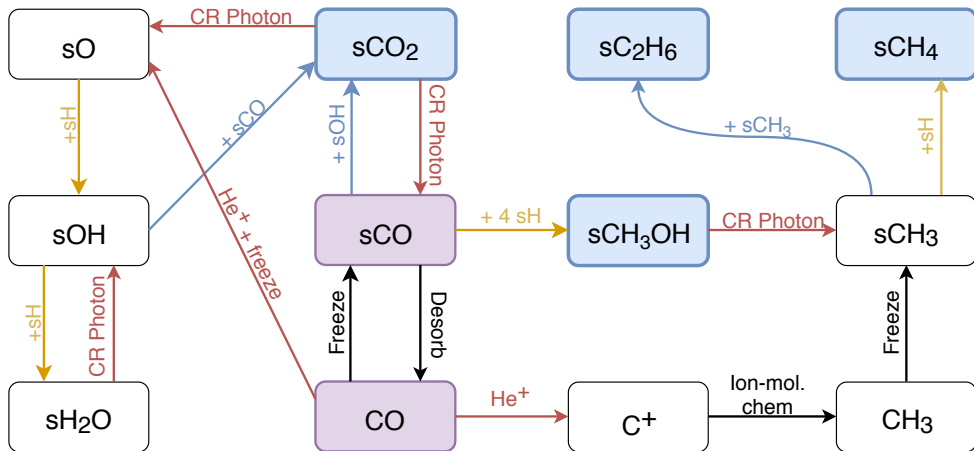


**Figure 2.2:** Chemical reaction network showing the major CO destruction pathways and important competing reactions. Red arrows show reactions that are mediated directly or indirectly by cosmic-ray photons, yellow arrows show hydrogenation reactions and blue arrows show grain-surface reactions. The initial major carbon carrier (CO) is shown in grey-purple. Stable products of CO processing are denoted with blue boxes. sX denotes that species X is on the grain surface.

tunnelling dominates for the reaction barrier, and that the thermal rate dominates for H hopping, can be given by:

$$R_{\text{CO}+\text{H}} = \frac{n_{\text{CO,ice}}n_{\text{H,ice}}}{n_{\text{CO,total}}} C_{\text{grain}} \exp\left[-\frac{2a_{\text{tunnel}}}{\hbar}\sqrt{2\mu E_{\text{bar}}}\right] \times \left(\nu_{\text{H}} \exp\left[-\frac{f_{\text{diff}}E_{\text{bind,H}}}{kT}\right] + \nu_{\text{CO}} \exp\left[-\frac{f_{\text{diff}}E_{\text{bind,CO}}}{kT}\right]\right). \quad (2.2)$$

As noted above, the tunnelling barrier,  $a_{\text{tunnel}}$  is the most important parameter for determining the rate. Changing  $a_{\text{tunnel}} = 0.5 \text{ \AA}$  to  $a_{\text{tunnel}} = 1.5 \text{ \AA}$  decreases the destruction rate through hydrogenation by eight orders of magnitude. This reaction is also suppressed in regions of high temperature where  $n_{\text{CO,ice}}/n_{\text{CO,total}}$  is low.

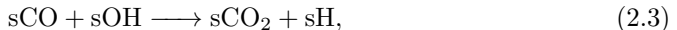
The amount of H in the ice is set by the balance of freeze-out of H and the reaction speed of H with species in the ice. Desorption of H is negligible compared with the reaction of H with radicals on the grain in most of the physical parameter space explored. As such there is no strong decrease in the rate near the H desorption temperature. This also means that the competition of other iceborn radicals for reactions with H strongly influences the rates.

At the lowest temperatures the rates are also slightly suppressed as the hopping rate is slowed. The rate is maximal around the traditional CO iceline temperature of around 20 K as  $n_{\text{CO,ice}}/n_{\text{CO,total}}$  is still high, while thermal hopping is efficient. This is especially so for low values of  $f_{\text{diff}}$ , increasing the hopping and thus the reaction rate. This reaction does not strongly depend on density since the absolute flux of H arriving on grains is nearly constant as function of total gas density and the rest of the rate only depends on the fraction of CO that is frozen out, not the total amount.

The second reaction is the formation of  $\text{CO}_2$  through the grain-surface reaction

**Table 2.3:** Chemical trends with variations in parameters

Parameter		sCO + sOH	sCO + sH
$\uparrow n$	$\downarrow x_{\text{H}}$	$\uparrow$	$\downarrow$
$\uparrow a_{\text{tunnel}}$	$\downarrow P_{\text{reac}}(\text{sCO}, \text{sH})$	–	$\downarrow$
$\uparrow a_{\text{tunnel}}$	$\downarrow P_{\text{reac}}(\text{sOH}, \text{sH}_2)$	$\uparrow$	–
$\uparrow f_{\text{diff}}$	$\downarrow \text{CO mobility}$	$\downarrow$	–



which has a slight barrier of 400 K (Arasa et al. 2013). It competes with the reaction  $\text{sCO} + \text{sOH} \longrightarrow \text{sHOCO}$ . We assume that most of the HOCO formed in this way will be converted into  $\text{CO}_2$  as seen in the experiments (Watanabe et al. 2007; Oba et al. 2010; Ioppolo et al. 2013) and that is also required to explain  $\text{CO}_2$  ice observations. As such we suppress the explicit HOCO formation channel in our model.

The reaction rate for reaction 2.3 is given by:

$$R_{\text{CO}+\text{OH}} = \frac{n_{\text{CO,ice}}n_{\text{OH,ice}}}{n_{\text{CO,total}}} C_{\text{grain}} \exp\left[-\frac{E_{\text{bar}}}{kT}\right] \times \left( \nu_{\text{OH}} \exp\left[-\frac{f_{\text{diff}}E_{\text{bind,OH}}}{kT}\right] + \nu_{\text{CO}} \exp\left[-\frac{f_{\text{diff}}E_{\text{bind,CO}}}{kT}\right] \right). \quad (2.4)$$

As OH has a high binding energy of 2980 K (He & Vidali 2014), sublimation of OH can be neglected. CO sublimation is still important even though the rate is again not dependent on the total CO abundance. Due to the strong temperature dependence of the reaction barrier and the CO hopping rate, this rate is maximal at temperatures just above the CO desorption temperature. Finally the reaction rate depends on the OH abundance. OH in these circumstances is generally created by the cosmic-ray induced photodissociation of  $\text{H}_2\text{O}$ , which means that  $\text{CO}_2$  formation is fastest when there is a large body of  $\text{H}_2\text{O}$  ice<sup>4</sup>. At late times  $\text{H}_2\text{O}$  can also become depleted, with  $\text{CO}_2$  being the major oxygen reservoir, lowering the supply of OH at late times. This lowers the  $\text{CO}_2$  production rate, and the destruction of  $\text{CO}_2$  can increase the CO abundance.

CO has competition with several other radicals for the reaction with OH. The most important of these is the competition with H. At low densities the  $x_{\text{H}}/x_{\text{CO}}$  is high, so OH will mostly react with H to reform  $\text{H}_2\text{O}$ . Similarly when H mobility is increased, by assuming very narrow tunnelling barriers,  $\text{sCO}_2$  formation will slow down. At high density  $x_{\text{H}}/x_{\text{CO}}$  is low, and thus the competition for OH is won by CO.

The last reaction is the only gas-phase route



This reaction is limited by the ionisation rate of He and the subsequent competition for collisions of  $\text{He}^+$  with abundant gas-phase species. As such the CO destruction rate can be expressed as:

$$R_{\text{CO}+\text{He}^+} = 0.65\zeta_{\text{H}_2} \frac{x_{\text{He}}}{x_{\text{CO}}} \frac{k_{\text{ion,CO}}x_{\text{CO}}}{\sum_{\text{X}} k_{\text{ion,XX}}x_{\text{X}}} \quad (2.6)$$

<sup>4</sup>Specifically  $\text{H}_2\text{O}$  in the upper layers of the ice, but by construction our ice mantles are perfectly mixed



**Table 2.4:** Rate coefficients for collisions with  $\text{He}^+$ 

Reaction partner	Rate coeff. ( $\text{cm}^{-3} \text{s}^{-1}$ )	Gas abundance
$\text{H}_2$	$1.14 \times 10^{-14}$	0.5
$\text{N}_2$	$1.6 \times 10^{-9}$	$< 2 \times 10^{-5}$
CO	$1.6 \times 10^{-9}$	$< 10^{-4}$
grains	$2.06 \times 10^{-4}$	$2.2 \times 10^{-12}$

where  $k_{\text{ion},X}$  are the ion-neutral reaction rate coefficients for collisions between  $\text{He}^+$  and the molecule and  $x_X$  is the abundance of species X. The abundances and rate coefficients for important alternative reaction partners of  $\text{He}^+$  between 20 and 40 K are tabulated in Table 2.4, where we have summed the rate coefficients of reactions with multiple outcomes. At high abundances of CO and/or  $\text{N}_2$  the rate scales as:

$$R_{\text{CO+He}^+} \propto \frac{1}{x_{\text{CO}} + x_{\text{N}_2}}, \quad (2.7)$$

which increases with lower abundances. If the sum of the gaseous abundances of CO and  $\text{N}_2$  is  $\ll 3 \times 10^{-7}$  the rate becomes

$$R_{\text{CO+He}^+} = 0.65 \zeta_{\text{H}_2} x_{\text{He}} \frac{k_{\text{ion,CO}}}{k_{\text{ion,H}_2} x_{\text{H}_2} + k_{\text{ion,grains}} x_{\text{grains}}} \quad (2.8)$$

which is independent of the CO abundance.

There are some assumptions in the model that will influence the rates of the chemical pathways discussed here. We do not expect the chemistry to be critically dependent on these assumptions but they might influence the chemical timescales and the relative importance of different chemical pathways. A few important assumptions and their effects on the chemistry are discussed in Appendix. 2.B.4.

## 2.3 Results

We have performed a parameter space study of the chemistry of CO under shielded conditions in protoplanetary disks. In this section we first present the results for the physical parameters studied, namely chemical evolution time, density, temperature and cosmic-ray ionisation rate. Fig. 2.3 focuses on the effects of time and cosmic-ray ionisation rate, while Fig. 2.4 focuses on the effects of temperature and density. Together these figures show that the evolution of the CO abundance depends strongly on the physical conditions assumed in the chemical model, especially the temperature, in addition to the cosmic-ray ionisation rate identified earlier. Finally, the effects of the assumed chemical parameters on four positions in physical parameter space are studied.

### 2.3.1 Physical parameter space

#### Importance of the cosmic-ray ionisation rate

Consistent with previous studies, the cosmic-ray ionisation rate is found to be the driving force behind most of the changes in the CO abundance. A higher cosmic-ray

ionisation rate allows the chemistry to evolve faster, but in a similar way. As such the cosmic-ray ionisation rate and chemical evolution time are mostly degenerate. Fig. 2.3 presents an overview of the dependence of the total CO abundance (gas plus ice) on evolution time and  $\zeta_{\text{H}_2}$ . CO can be efficiently destroyed in 1–3 Myr for  $\zeta_{\text{H}_2} > 5 \times 10^{-18} \text{ s}^{-1}$  and temperatures lower than 25 K.

For models at 15 K and low densities of  $10^6 \text{ cm}^{-3}$ , the CO abundance behavior does not show the degeneracy between  $\zeta_{\text{H}_2}$  and time. This is caused by the formation of NO in the ice. The NO abundance depends non-linearly on the cosmic-ray ionisation rate. A high abundance of NO in the ice lowers the abundance of available atomic H on the ice as it efficiently catalyses the formation of  $\text{H}_2$  on the ice. This effect has also been seen in Penteado et al. (2017) using the same network but under different conditions. A similar catalytic effect for the formation of  $\text{H}_2$  was first noted in the work by Tielens & Hagen (1982).

At high density and temperature ( $35 \text{ K}, 10^{10} \text{ cm}^{-3}$ ), a sequence of CO destruction and then reformation is visible in the CO abundance. The first cycle of this was also seen and discussed in Eistrup et al. (2016) and can be attributed to the lower formation rate of OH due to a decrease in the  $\text{H}_2\text{O}$  abundance on Myr timescales. Some models, especially those with a cosmic-ray ionisation rate of  $10^{-16} \text{ s}^{-1}$  can have five or more of these CO- $\text{CO}_2$  abundance inversions, while the  $\text{H}_2\text{O}$  abundance continues to decrease. For the rest of the results in this section a cosmic-ray ionisation rate of  $10^{-17} \text{ s}^{-1}$  is taken, thought to be typical for dense molecular clouds (e.g., Dalgarno 2006).

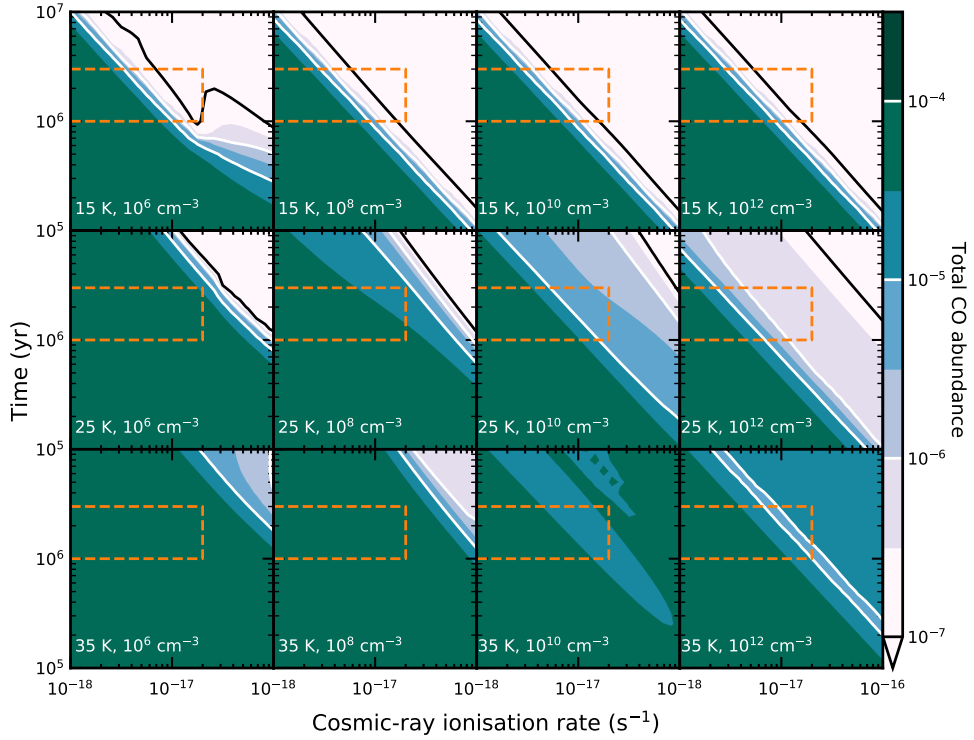
### Importance of temperature

Fig. 2.4 presents the total CO abundance over the entire density-temperature grid at four time steps during the evolution of the chemistry. These figures demonstrate clearly that CO is efficiently destroyed only at low temperatures,  $< 20 \text{ K}$ . This temperature range is only weakly dependent on the density: CO destruction is efficient below 16 K at the lowest densities, while it is efficient up to 19 K at the highest densities. This range is strongly correlated with the desorption of CO from the ice. At high density ( $> 10^{10} \text{ cm}^{-3}$ ), there is a second, local minimum in CO abundance between 24 and 27 K seen at 1 Myr. In this range, the grain-surface formation of  $\text{CO}_2$  from CO and OH is efficient. At these temperatures CO is primarily in the gas-phase but a small fraction is on the grain-surface where it is highly mobile. OH is created during the destruction of  $\text{H}_2\text{O}$  on the ice. This reaction is most efficient under high-density conditions as atomic H competes with CO for the OH radical on the grain. At low densities, the relative abundance of H is higher in the models, thus greatly suppressing the formation rate of  $\text{CO}_2$  from  $\text{CO} + \text{OH}$  on the grain.

At late times,  $> 5 \text{ Myr}$ , there is a strong additional CO destruction at densities  $< 10^7 \text{ cm}^{-3}$  and at temperatures between 20 and 25 K. At this point the  $\text{C}^+$  formed from the  $\text{CO} + \text{He}^+$  reaction can efficiently be converted into  $\text{CH}_4$ , which freezes out on the grains.

### Representative models

Four points in the physical parameter space have been chosen for further examination. They are chosen such that they span the range of parameters that can lead to low total CO abundances within 10 Myr and such that they sample different CO destruction routes. These points are given in Table 2.5 and are marked in Fig. 2.4. Figure 2.5



**Figure 2.3:** Total CO abundance (gas and ice) as function of time and cosmic-ray ionisation rate for the fiducial chemical model. Each subfigure has a different combination of temperature and density as denoted in the bottom left. Time and cosmic-ray ionisation rate are degenerate in most of the parameter space. The orange box denotes the combinations of  $\zeta_{\text{H}_2}$  and time most appropriate for protoplanetary disks.

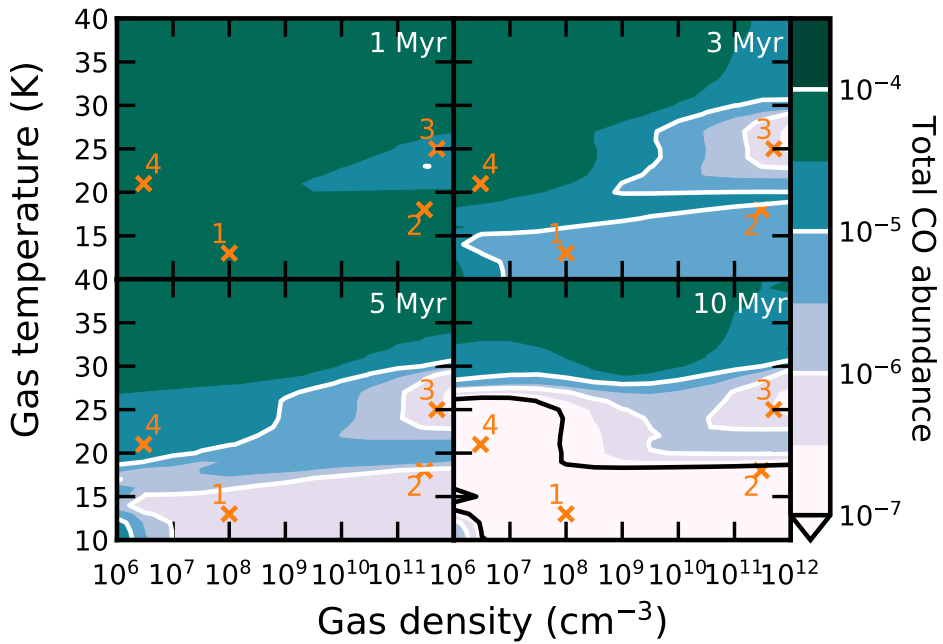


**Figure 2.4:** Time evolution of CO abundance as function of gas temperature and density. Chemical evolution time is denoted in the upper right corner of each panel and  $\zeta = 10^{-17} \text{ s}^{-1}$  for all of these models. The orange numbers show the locations of the physical conditions taken in Sec. 2.3.2. Results at 2 Myr are similar to those at 3 Myr.

presents the total abundance (gas and ice) of CO and its stable reaction products as a function of time for the four physical conditions that have been chosen.

Models #1 (13 K,  $10^8 \text{ cm}^{-3}$ ) and #2 (18 K,  $3 \times 10^{11} \text{ cm}^{-3}$ ) show very similar behaviours, even though they have very different densities. This is due to the combination of the active destruction pathway, CO hydrogenation, and the H<sub>2</sub> formation prescription, which forces a constant atomic hydrogen concentration, leading to a constant CO destruction rate as a function of density. In both models, 90 % of the CO has been converted into CH<sub>3</sub>OH in 1 Myr. Before this time the H<sub>2</sub>CO abundance is constant, balanced between the formation due to CO hydrogenation, and destruction due to hydrogenation. As the CO abundance drops, and thus the formation rate of H<sub>2</sub>CO falls, so does its abundance. After slightly more than 1 Myr, methanol has reached a peak abundance close to  $10^{-4}$ . This marks the end of hydrogenation driven chemical evolution as most molecules on the ice cannot be hydrogenated further. After this, cosmic-ray induced dissociation dominates the abundance evolution, slowly destroying CH<sub>3</sub>OH, forming CH<sub>4</sub> and H<sub>2</sub>O, and destroying CO<sub>2</sub> forming CO and O, both of which quickly hydrogenate to CH<sub>3</sub>OH and H<sub>2</sub>O. A small amount of CH<sub>4</sub> is further converted into C<sub>2</sub>H<sub>6</sub>.

The abundance traces for model #3 (25 K,  $5 \times 10^{11} \text{ cm}^{-3}$ ) show two different destruction pathways for CO at a temperature where most of the CO is in the gas-phase. The presence of H<sub>2</sub>CO at early times points at the effective grain-surface hydrogenation of CO, but the lower abundance relative to Models #1 and #2 indicates that the hydrogenation route is slower due to the lower abundance of CO on the grain-surface. The rise in CO<sub>2</sub> abundance indicates that a significant portion of the CO reacts with OH on the grain-surface to form CO<sub>2</sub>. At 1 Myr nearly 99% of the initial CO has been destroyed. Most of the CO has been incorporated into CO<sub>2</sub> with a significant amount of carbon locked into CH<sub>3</sub>OH and CH<sub>4</sub>, which have equal abundances from  $10^5$  years onward. CH<sub>4</sub> is again mostly formed from the destruction of CH<sub>3</sub>OH by cosmic-ray induced photons. The CH<sub>3</sub>OH abundance does not steeply drop after 1 Myr, in contrast with models #1 and #2. This is due to the destruction of CO<sub>2</sub> by cosmic-ray induced photons. This destruction creates a source of CO that can be hydrogenated to form more CH<sub>3</sub>OH to compensate for the destruction of CH<sub>3</sub>OH by the same mechanism. At these late times, C<sub>2</sub>H<sub>6</sub> acts as a carbon sink, slowly locking up carbon that is created in the form of the CH<sub>3</sub> radical from the dissociation of CH<sub>4</sub> and CH<sub>3</sub>OH.

The abundance traces for model #4 (21 K,  $3 \times 10^6 \text{ cm}^{-3}$ ) are an outlier in this comparison. Most of the CO is in the gas-phase at this temperature and density. H<sub>2</sub>CO is only present at an abundance of  $10^{-10}$  and there is no strong methanol formation in the first Myr. It takes at least 2 Myr to destroy 50% of the CO and 5 Myr to destroy 90% of the CO. For the conditions shown here, most of the CO is destroyed in the gas-phase by dissociative electron transfer with He<sup>+</sup>. This leads to the formation of hydrocarbons in the gas-phase, primarily CH<sub>3</sub> and C<sub>2</sub>H<sub>2</sub>, which freeze-out and are hydrogenated on the grain to form CH<sub>4</sub> and C<sub>2</sub>H<sub>6</sub> (as also seen by Aikawa et al. 1999). The large number of CH<sub>x</sub> (x = 1,2,3) fragments at late times allow for the formation of CH<sub>3</sub>OH on the grain-surface, due to the reaction of CH<sub>2</sub> or CH<sub>3</sub> with OH on the grain-surface.

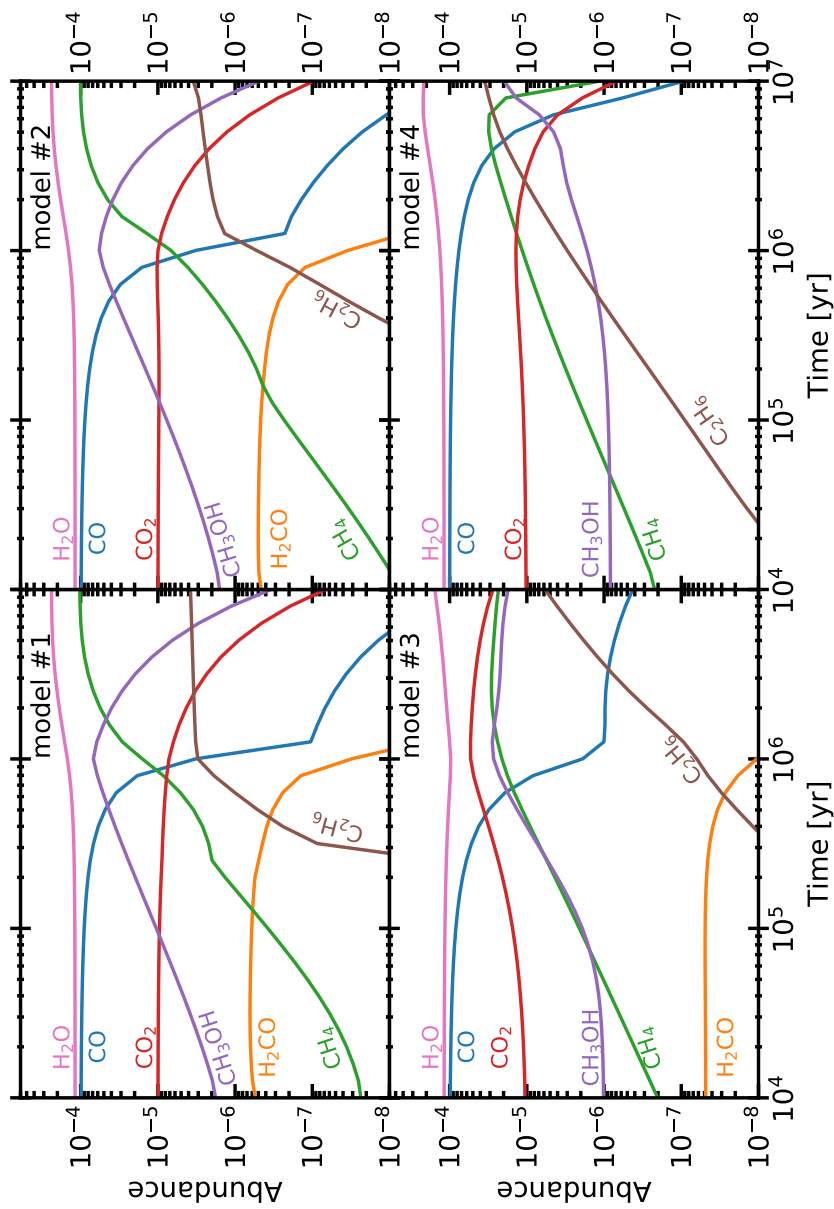


**Figure 2.5:** Abundance traces of CO and its destruction products for the four points denoted in Fig. 2.4 with conditions as tabulated in Table 2.5. Plotted abundances are the sum of the gas and ice abundance for each species.

**Table 2.5:** Physical parameters for the chemical parameters test.

Model #	$n_{\text{gas}}$ ( $\text{cm}^{-3}$ )	$T_{\text{gas}}$ (K)	$\zeta_{\text{H}_2}$ ( $\text{s}^{-1}$ )
1	$1 \times 10^8$	13	$10^{-17}$
2	$3 \times 10^{11}$	18	$10^{-17}$
3	$5 \times 10^{11}$	25	$10^{-17}$
4	$3 \times 10^6$	21	$10^{-17}$

### 2.3.2 Chemical parameter space

For the four different cases listed in Table 2.5, a set of models with varying  $a_{\text{tunnel}}$  and  $f_{\text{diff}}$  have been computed.  $a_{\text{tunnel}}$  primarily changes the reaction probability for grain-surface reactions involving atomic or molecular hydrogen that have a barrier, such as  $\text{sCO} + \text{sH}$  and  $\text{sOH} + \text{sH}_2$ . The value of  $f_{\text{diff}}$  changes the speed at which species can move over the grain-surface. Models #1 and #2 are both in the region of parameter space where CO is frozen out and thus sample pure grain-surface chemistry at low temperature and density, and at a slightly higher temperature and high density respectively. Model #3 is near the local minimum in gaseous CO abundance seen in Fig 2.4. Model #4 is located in a region of parameter space where most changes are still ongoing at later times. Together these four cases should sample the different dominant CO destruction pathways.

The first row of Fig. 2.6 shows the total CO abundance as function of chemical parameters for different times for point #1 in our physical parameter space with CO mostly in the ice. There is a strong dependence on the tunnelling barrier width ( $a_{\text{tunnel}}$ ). This is because the CO destruction in this temperature regime is dominated by the formation of  $\text{sHCO}$ . The  $\text{sCO} + \text{sH}$  reaction has a barrier which strongly limits this reaction, H tunnelling through this barrier thus increases the rate of CO destruction. The primary CO evolution happens in the first 2 Myr and at this point the CO abundance distribution strongly resembles that of the 3 Myr plot.

There are only very weak dependencies on the diffusion-to-binding energy ratio ( $f_{\text{diff}} = E_{\text{diff}}/E_{\text{bind}}$ ) for these very low temperatures. This points at a CO destruction process that is entirely restricted by the tunnelling efficiency of H. If the  $\text{sCO} + \text{sH}$  reaction is quenched by a large barrier, CO destruction is so slow that, due to the destruction of  $\text{CO}_2$  by cosmic-ray induced photons, the CO abundance is actually increased from the initial value. This happens at barrier widths larger than  $2 \text{ \AA}$ . At the lowest  $f_{\text{diff}}$  CO is turned into  $\text{CO}_2$  through  $\text{sCO} + \text{sOH}$  at early times. At later times, the  $\text{CO}_2$  is destroyed, again by cosmic-ray induced photons and more CO is formed, leading to a slower CO abundance decrease at late times.

The second row of Fig. 2.6 shows the total CO abundance as a function of chemical parameters for different times for point #2. Since CO is frozen out for both case #1 ( $T = 13 \text{ K}$ ) and #2 ( $T = 18 \text{ K}$ ), there are strong similarities between the first and second row of models in Fig. 2.6. The only significant difference can be seen at  $a_{\text{tunnel}} > 1.5$  and  $f_{\text{diff}} < 0.2$ . With these chemical parameters and these high densities ( $3 \times 10^{11} \text{ cm}^{-3}$ ),  $\text{sCO} + \text{sOH}$  can be an effective destruction pathway.

The third row of Fig. 2.6 shows the total CO abundance for point #3 in our physical parameter space at  $T = 25 \text{ K}$  and  $n = 5 \times 10^{11} \text{ cm}^{-3}$ . The large and irregular variation in CO abundance in this figure points at a number of competing processes. The two main processes destroying CO at this temperature and density are again  $\text{sCO} + \text{sH}$  and

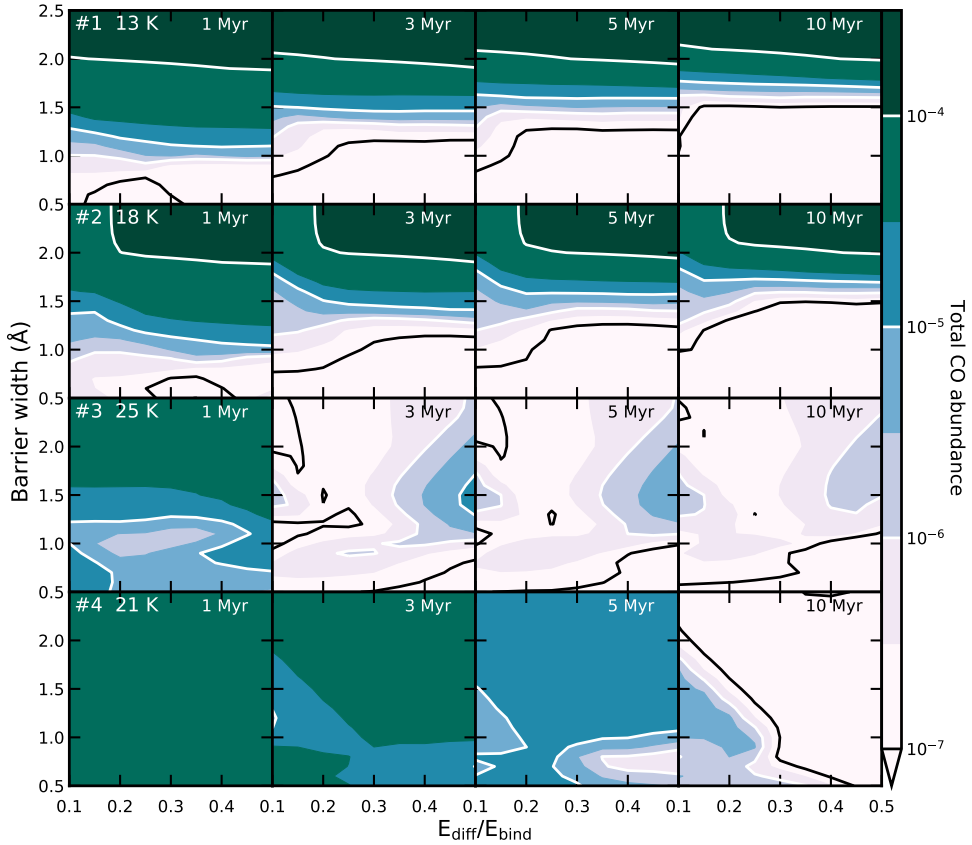


**Figure 2.6:** Time evolution of total CO abundance (ice and gas) as function of the assumed tunnelling barrier width ( $a_{\text{tunnel}}$ ) and diffusion-to-binding energy ratio ( $f_{\text{diff}}$ ). All these models have  $\zeta_{\text{H}_2} = 10^{-17} \text{ s}^{-1}$ . The first row of models uses  $T_{\text{gas}} = 13 \text{ K}$ ,  $n_{\text{gas}} = 10^8 \text{ cm}^{-3}$ . The second row of models uses  $T_{\text{gas}} = 18 \text{ K}$  and  $n_{\text{gas}} = 3 \times 10^{11} \text{ cm}^{-3}$ . The third row of models uses  $T_{\text{gas}} = 25 \text{ K}$  and  $n_{\text{gas}} = 5 \times 10^{11} \text{ cm}^{-3}$ . The fourth row of models uses  $T_{\text{gas}} = 21 \text{ K}$  and  $n_{\text{gas}} = 3 \times 10^6 \text{ cm}^{-3}$ . Results at 2 Myr are similar to those at 3 Myr. Significant reduction of the total CO abundance in less than 3 Myr is only possible if sCO + sH is efficient, which is at low barrier widths or if sOH preferably reacts with sCO, which is enhanced at low values of  $f_{\text{diff}}$ . The fiducial values are  $a_{\text{tunnel}} = 1$  and  $f_{\text{diff}} = 0.3$ .



sCO + sOH. These grain-surface reactions dominate the CO destruction even though CO is primarily in the gas-phase. The fraction of time that CO spends on the grain is long enough to allow the aforementioned reactions to be efficient. At the smallest barrier widths ( $< 1 \text{ \AA}$ ) the conversion of CO into CH<sub>3</sub>OH through hydrogenation dominates the CO abundance evolution, but this pathway quickly gets inefficient if the tunnelling barrier is made wider. At the largest barrier widths the formation of CO<sub>2</sub> dominates. This reaction is quenched at the lowest barrier widths as OH can quickly react with H<sub>2</sub> on the grain to form H<sub>2</sub>O, since its barrier is also lowered.

Although CO is destroyed significantly in this model from 3 Myr onward, there is a clear region in parameter space where the CO destruction is slower. This region at high  $f_{\text{diff}}$  and intermediate  $a_{\text{tunnel}}$  has up to two orders of magnitude higher CO abundance compared with the rest of parameter space. The high  $f_{\text{diff}}$  significantly slows down all reactions that are unaffected by tunnelling. In this region of parameter space, CO mobility is significantly lower than H mobility due to the latter being able to tunnel. This suppresses the sCO + sOH route. On the other hand the barrier is still too wide to allow efficient hydrogenation of CO. With both main destruction routes suppressed in this region, it takes longer to reach a significant amount of CO destruction. Further increasing  $a_{\text{tunnel}}$  from this point slows down the tunnelling of H and thus the formation rate of H<sub>2</sub>O. This leads into a larger OH abundance on the ice, and thus a larger CO<sub>2</sub> formation rate.

The fourth row of Fig. 2.6 shows the total CO abundance at different times for point #4 at a low density of  $3 \times 10^6 \text{ cm}^{-3}$  and  $T = 21 \text{ K}$ . At early times there is no strong destruction of CO, after 3 Myr there is only a very small region where the abundance has dropped by an order of magnitude. CO<sub>2</sub> is formed in this region of parameter space. At 5 Myr, there is a region at low barrier width, around  $0.7 \text{ \AA}$  and  $f_{\text{diff}} > 0.3$ , where the hydrogenation of CO has led to a large decrease in the CO abundance. At 7 Myr this process has caused a decrease of CO abundance of at least two orders of magnitude in this region. At the same time the CO abundance over almost all of the parameter space has dropped by an order of magnitude. This is the effect of the gas-phase route starting with dissociative electron transfer of CO to He<sup>+</sup>:  $\text{CO} + \text{He}^+ \longrightarrow \text{C}^+ + \text{O} + \text{He}$ . In the last 3 Myr of chemical evolution, this reaction pathway removes 99.9 % of the CO in a large part of the parameter space. Only regions that had a significant build up of CO<sub>2</sub> at early times, or where N<sub>2</sub> can be efficiently reformed, show CO abundances  $> 10^{-6}$ , because CO is reformed from CO<sub>2</sub> and because N<sub>2</sub> competes with CO for reactions with He<sup>+</sup> respectively.

In summary, the conclusions of the fiducial models with  $f_{\text{diff}} = 0.3$  and  $a_{\text{tunnel}} = 1$  are robust, except when the tunnelling barrier for the sCO + SH  $\rightarrow$  HCO reaction is much larger than this value. Several independent laboratory experiments show that the CO hydrogenation proceeds fast, even at temperatures as low as 10–12 K (Hiraoka et al. 2002; Watanabe & Kouchi 2002; Fuchs et al. 2009) so a high barrier is unlikely. Reaction probabilities from the Harmonic Quantum Transition State calculations by Andersson et al. (2011) are consistent with  $a_{\text{tunnel}} \approx 0.9$  in our calculations.

## 2.4 Discussion

Our results show that it is possible to chemically process CO under conditions ( $T < 30 \text{ K}$ ,  $n = 10^6 - 10^{12} \text{ cm}^{-3}$ ) that are representative of a large mass fraction of a protoplanetary disk on a few Myr timescale. As such, chemical processing of CO,

specifically the formation of  $\text{CH}_3\text{OH}$  and  $\text{CO}_2$  and on longer timescales hydrocarbons, has a significant effect on the observed CO abundance.

Our results agree with Reboussin et al. (2015), Eistrup et al. (2016) and Schwarz et al. (2018) that a significant cosmic-ray ionisation rate,  $> 5 \times 10^{-18} \text{ s}^{-1}$  in our study, is needed to convert CO.

In contrast with Furuya & Aikawa (2014) and Yu et al. (2016), we do not find that destruction of CO through reactions with  $\text{He}^+$  is a main pathway for a cosmic-ray ionisation rate of  $10^{-17} \text{ s}^{-1}$ . This is mostly because this destruction timescale is  $> 5$  Myr, for these levels of ionisation. However, Furuya & Aikawa (2014) assume a higher cosmic-ray ionisation rate ( $5 \times 10^{-17} \text{ s}^{-1}$ ) whereas Yu et al. (2016) have X-rays that add to the total ionisation rate of the gas. This lowers their CO destruction time-scale significantly (Fig. 2.3).

### 2.4.1 When, where and how is CO destroyed within 3 Myr

There are two main reaction mechanisms that can destroy CO in 3 Myr under cold disk midplane conditions, assuming a cosmic-ray rate of  $10^{-17} \text{ s}^{-1}$ : hydrogenation of CO to  $\text{CH}_3\text{OH}$  and the formation of  $\text{CO}_2$ . Hydrogenation of CO forming  $\text{CH}_3\text{OH}$  reduces CO by an order of magnitude within 1 Myr in the cold regions of the disk where CO is completely frozen out ( $< 20 \text{ K}$ ). By 2 Myr, the CO abundance has dropped by 3 orders of magnitude (Fig. 2.5, top two panels; Fig. 2.7, left column, top two panels). The first step of this pathway  $\text{sCO} + \text{sH}$  has a barrier and thus the time-scale of this reaction is strongly dependent on the assumed hydrogen tunnelling efficiency ( $a_{\text{tunnel}}$ ), with shorter timescales at lower assumed  $a_{\text{tunnel}}$  (Fig. 2.6).

Contrary to Schwarz et al. (2018) we find that  $\text{CH}_3\text{OH}$  formation is only dominant when CO is frozen-out,  $< 20 \text{ K}$ . This is probably due to the more complete grain-surface chemistry in our work, allowing other species to react with atomic H and removing it from the grain-surface before CO can react with it at higher temperatures. This leads us to conclude that  $\text{CO}_2$  formation is always the dominant CO destruction mechanism in the warm molecular layer in the first 5 Myr instead of CO hydrogenation, showing that a larger grain-surface network needs to be considered.

The second pathway,  $\text{CO} + \text{OH} \rightarrow \text{CO}_2$  on the ice, is efficient at slightly higher temperatures, between the CO iceline temperature and up to 30 K at the highest densities (Fig. 2.4). This pathway is slower than the hydrogenation of CO, but still leads to  $\sim 2$  orders decrease in the CO abundance within 3 Myr. The rate of conversion of CO into  $\text{CO}_2$  depends strongly on the assumed chemical parameters in the first Myr. By 3 Myr most of these initial differences have been washed out. Only a very slow assumed diffusion rate ( $f_{\text{bind}} > 0.35$ ) leads to a CO abundance above  $10^{-6}$  after 3 Myr (Fig. 2.6).

Production of hydrocarbons follows the formation of  $\text{CH}_3\text{OH}$  in the first Myr. When the CO abundance has been lowered by 1 to 2 orders of magnitude, production of  $\text{CH}_3\text{OH}$  stops, while the formation of  $\text{CH}_4$  continues. At  $\sim 3$  Myr  $\text{CH}_4$  becomes more abundant than  $\text{CH}_3\text{OH}$ . At even longer timescales,  $\text{CH}_4$  gets turned into  $\text{C}_2\text{H}_6$ . Formation of hydrocarbons starting from  $\text{CO} + \text{He}^+$  in the gas phase is only effective at densities  $< 10^7 \text{ cm}^{-3}$  between the CO and  $\text{CH}_4$  icelines. Even in this region, the timescale is  $> 3$  Myr.

The timescales for these processes scale inversely with the cosmic-ray or X-ray ionisation rate. As such, in regions with lower ionisation rates CO destruction can be

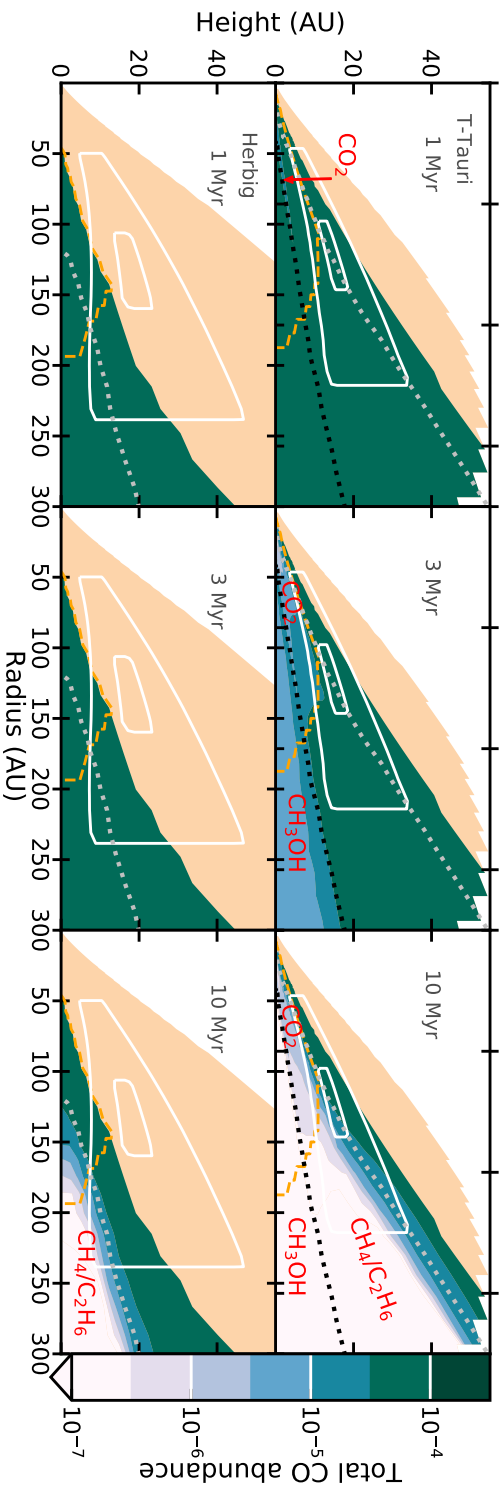


**Figure 2.7:** Total CO abundance (gas and ice) from the chemical models, at 1, 3 and 10 Myr, mapped onto the temperature and density structure of a T-Tauri (*top*) and Herbig (*bottom*) disk model (see Fig. 2.8 and Appendix 2.A). A cosmic-ray ionisation rate of  $10^{-17} \text{ s}^{-1}$  is assumed throughout the disk. The orange hatched area shows the disk region that has a temperature above 40 K and is thus not included in our chemical models. See Fig. 2.8 for the CO abundance in that region using a simple CO chemistry. The white contours shows the area within which 25% and 75% of the C<sup>18</sup>O flux is emitted. The black and grey dotted lines show the 20 K and 30 K contours respectively. The Herbig disk is always warmer than 20 K. The molecules in red denote the dominant carbon carrier in the regions CO is depleted. The orange dashed line encompasses the region that is completely shielded from UV radiation (see Sec. 2.2.1).

slower than described here. The reverse is also true, so if locally produced energetic particles play a significant role, the CO destruction timescales become shorter.

In conclusion, for a nominal cosmic-ray ionisation rate of  $10^{-17} \text{ s}^{-1}$ , CO can be significantly destroyed (orders of magnitude) in the first few Myr of disk evolution under cold conditions. This conclusion is robust against variations in chemical parameters, except if the barrier width for the CO + H tunneling becomes too large. Under warm conditions, CO is at most mildly depleted (<factor of a few).

## 2.4.2 Implications for observations

Mapping the results from the chemical models summarized above onto the physical structure seen in Fig. 2.1 results in Fig. 2.7. It is clear that CO can be destroyed over a region of the disk that contains a significant amount of mass. For the T-Tauri disk a portion of this CO destruction will be in a region of the disk where CO is not traceable by observations, as the CO is frozen out. However, there is also a significant region up to 30 K within and above the CO snow surface where CO is depleted and where the emission from the less abundant  $^{18}\text{O}$  and  $^{17}\text{O}$  isotopologues originates (Miotello et al. 2014). Thus, the processes studied here can explain, at least in part, the observations of low CO abundances within the ice-line in TW Hya (Zhang et al. 2017).

If CO destruction would also be effective in disk regions that are irradiated by moderate amounts ( $< 1 G_0$ ) of (interstellar) UV radiation, then a region responsible for  $> 25\%$  of the emission can be depleted in CO by  $\sim 1$  order of magnitude by 3 Myr, as seen in Fig. 2.7. The other  $\sim 75\%$  is also likely affected due to mixing of CO poor gas from below the iceline into the emitting region (see Sec. 2.4.4). This would result in a drop of the  $\text{C}^{18}\text{O}$  isotopologue flux between 25% and orders of magnitude depending on the vertical mixing efficiency. Rarer isotopologues, whose flux comes from lower, colder layers, would be more severely affected. The T-Tauri model shown in Figs. 2.1 and 2.7 assumes a total source luminosity of around  $0.3 L_\odot$  representative of the bulk of T-Tauri stars in low mass star-forming regions (Alcalá et al. 2017). For disks around stars with a lower luminosity or with higher ages, the effect of CO destruction would be even larger.

The warm upper layers exposed to modest UV have also been modelled by Schwarz et al. (2018). They find that the CO abundance is generally high in these intermediate layers, with significant CO destruction only taking place for high X-ray or cosmic ray ionisation rates. This is consistent with our Fig. 2.7 and Fig. 2.8.

For Herbig sources, only a small region of the disk falls within the range of parameters studied here and an even smaller region is at temperatures under 30 K, while also being shielded (Fig. 2.1). Because Herbig disks host more luminous stars than their T-Tauri counterparts, they also tend to be warmer. This means that a smaller mass fraction of the disk has temperatures between 10 and 30 K, where CO can be efficiently destroyed. As such our chemical models predict that Herbig disks have a CO abundance that is close to canonical, consistent with observations by Kama et al. (2016).

Young disks around T Tauri stars are expected to be warmer due to the accretional heating (Harsono et al. 2015). They are also younger than the time needed to significantly convert CO to other species with grain surface reactions. As such young disks should close to canonical CO abundances, as seems to be observed for at least some disks (van 't Hoff et al. 2018).

### 2.4.3 Observing chemical destruction of CO

In our models, CO is mostly processed into species that are frozen-out in most of the disk, complicating detection of these products with sub-mm lines. Several of the prominent carbon reservoirs, like CO<sub>2</sub>, CH<sub>4</sub> and C<sub>2</sub>H<sub>6</sub>, are symmetric molecules without a dipole moment, so they do not have detectable sub-mm lines. Even CH<sub>3</sub>OH, which does have strong microwave transitions, is difficult to detect since the processes that get methanol ice off the grains mostly destroy the molecule (e.g., Bertin et al. 2016; Walsh et al. 2016). Thus, observing the molecules in the solid state would be the best proof of this chemical processing. Another way to indirectly observe the effects chemical processing of CO would be to compare to cometary abundances. This will be discussed in Sec. 2.4.4.

Ice does not emit strong mid-infrared bands. However, for some highly inclined disks, the outer disk ice content can be probed with infrared absorption against the strong mid-infrared continuum of the inner disk with the line of sight passing through the intermediate height disk layers (Pontoppidan et al. 2005). The processes discussed here will leave a chemical imprint on the ice absorption spectra. The destruction pathways of CO preferentially create CO<sub>2</sub>, CH<sub>3</sub>OH, CH<sub>4</sub> and H<sub>2</sub>O. CO<sub>2</sub> reaches a peak abundance of  $\sim 7 \times 10^{-5}$ , seven times higher than the initial conditions, which would be detectable. A large CO<sub>2</sub> ice reservoir would therefore immediately point at a conversion of CO to CO<sub>2</sub>, either in the disk or *en route* to the disk (Drozdovskaya et al. 2016). The formation of CH<sub>4</sub> and CH<sub>3</sub>OH happens mostly in the coldest regions of the disk (< 20 K) as such observations of large fractions (> 20% with respect to H<sub>2</sub>O) of CH<sub>4</sub> and CH<sub>3</sub>OH in the ice would point at a disk chemistry origin of CO destruction. If large amounts of CH<sub>4</sub> or CH<sub>3</sub>OH are found in infrared absorption spectra, this would also imply that vertical mixing plays a role in the chemical processing, as this is needed to move the CH<sub>4</sub> and/or CH<sub>3</sub>OH ice hosting grains away from the cold midplane up to the layers that can be probed with infrared observations. For H<sub>2</sub>O the increase is generally smaller than a factor of two, so that H<sub>2</sub>O ice is not a good tracer of CO destruction.

If the gas and dust in the midplane is not static, but moves towards the star due to the accretion flow or radial drift of dust grains, then it is expected that the products of CO destruction are thermally desorbed in the inner disk (see Booth et al. 2017; Bosman et al. 2018a). This would cause an observable increase in abundance. Current infrared observations of gaseous CO<sub>2</sub> emission do not show a signal consistent with an CO<sub>2</sub> enriched inner disk, but the optical thickness of the 15  $\mu$ m CO<sub>2</sub> lines in the surface layers might hinder the observation of CO<sub>2</sub> near the disk midplane (Salyk et al. 2011b; Pontoppidan & Blevins 2014; Walsh et al. 2015; Bosman et al. 2017, 2018a). Gibb & Horne (2013) have observed gaseous CH<sub>4</sub> in absorption in the near-infrared in GV Tau N. Their probed CH<sub>4</sub> is rotationally hot (750 K) and is thus likely situated within the inner 1 AU of the disk. They rule out a large column of CH<sub>4</sub> at lower temperatures (100 K). However, this disk is still embedded so it is possibly too young to have converted CO into CH<sub>4</sub> (Carney et al. 2016). Gaseous CH<sub>4</sub> and CH<sub>3</sub>OH have not been detected with *Spitzer*-IRS in disks, but should be detectable with *JWST*-MIRI. If lines from these molecules are brighter than expected for inner disk chemistry, it could point at a scenario in which CO is converted to CH<sub>4</sub> and CH<sub>3</sub>OH in the cold (< 20 K) outer-midplane regions of the disk, and that the reaction products are brought into the inner disk via accretion or radial drift.

### 2.4.4 Interactions with disk dynamics

The chemical timescales needed for an order of magnitude decrease of the CO dependence are close to 1 Myr. This timescale is significantly longer than the turbulent mixing timescales, even in the outer disk. As such it is not inconceivable that either vertical mixing or gas accretion influences the abundance of CO. For both the sCO + sH and the sCO + sOH route, the rate scales with the abundance of CO in the ice: the higher the abundance, the faster the rate, although the dependence can be sub-linear. This means that, if vertical mixing replenishes the disk mid-plane CO reservoir, the destruction of CO can happen at a higher rate for a longer time. This converts CO to other species not only in the regions where the processes described in this paper are effective, but also in the regions around it. For mixing to have a significant effect at 100 AU, a turbulent  $\alpha$  of  $10^{-4}$  or higher is needed (see, e.g. Ciesla 2010; Semenov & Wiebe 2011; Bosman et al. 2018a).

The freeze-out of CO on grains that are large enough to have settled below the CO snow surface can also lower the abundance of CO in the disk atmosphere. This process is thought to happen for H<sub>2</sub>O to explain the low observed abundances of H<sub>2</sub>O in the outer disk (Hogerheijde et al. 2011; Krijt & Ciesla 2016; Du et al. 2017). Using a toy model Kama et al. (2016) showed that the CO abundance in the disk atmosphere can be lowered by 1-2 orders of magnitude in the disk lifetime. This process can work in concert with the chemical destruction of CO to lower the CO abundance in the outer disk. If large grains are locking up a significant fraction of the CO near the midplane outside of the CO iceline then this CO would come off the grains near the CO iceline, leading to an strong increase in the CO abundance. Zhang et al. (2017) show however, that for TW Hya, this is not the case: CO also has a low abundance of  $\sim 3 \times 10^{-6}$  within the CO iceline. Further observations will have to show if this is the case for all disks with a low CO abundance, or if TW Hya is the exception and this low CO abundance is caused by its exceptional age of  $\sim 8$  Myr (Donaldson et al. 2016).

If the destruction of CO within the CO snowline is a general feature of protoplanetary disks, then a mechanism to stop any CO locked up in grains from being released in the gas phase will need to be considered. This is hard to do without actually halting radial drift completely, for the same reasons that it is hard to stop CO<sub>2</sub> from desorbing off the grain at its respective snowline (Bosman et al. 2018a).

The fact that comets in the solar system do contain significant amounts of CO (up to 30% with respect to H<sub>2</sub>O) (Mumma & Charnley 2011; Le Roy et al. 2015) suggests that these comets were formed in a cold CO rich environment, possibly before the bulk of the CO was converted into other molecules. In other disks, such CO-rich grains must then have been trapped outside the CO iceline to prevent significant CO sublimating in the inner regions.

## 2.5 Conclusions

We performed a kinetic chemical modelling study of the destruction of CO under UV shielded, cold ( $< 40$  K) and dense ( $10^6$ – $10^{12}$  cm<sup>-3</sup>) conditions. Both grain-surface and gas-phase routes to destroy CO are considered and their efficiencies and timescales evaluated using a gas-grain chemical network. Furthermore we studied the effects of the assumed ice diffusion speed (through the diffusion-to-binding energy ratio,  $f_{\text{diff}}$ ) and the assumed H and H<sub>2</sub> tunnelling efficiency (through the tunnelling barrier width,

$a_{\text{tunnel}}$ ) on the evolution of the CO abundance both in the gas-phase and on the grain-surface. Our findings can be summarised as follows:

- CO destruction is linearly dependent on the assumed  $\text{H}_2$  ionisation rate by energetic particles (cosmic-rays, X-rays) over a large region of the considered physical parameter space. Only high enough cosmic-ray ionisation rates,  $> 5 \times 10^{-18} \text{ s}^{-1}$  can destroy CO on a  $< 3$  Myr timescale (Sec. 2.3.1, Fig. 2.3).
- The chemical processing of CO is most efficient at low temperatures. A relation between disk temperature and measured CO abundance is expected. The coldest disks would have the lowest CO abundances; in contrast, flaring disks around luminous Herbig stars should close to canonical CO abundances.
- At low temperatures, hydrogenation of CO is efficient when CO is fully frozen-out, leading to a reduction of the total CO abundance by  $\sim 3$  orders assuming  $\zeta_{\text{H}_2} = 10^{-17} \text{ s}^{-1}$ . This route is only weakly dependent on the temperature and density, as long as CO is fully frozen-out (Sec. 2.3.1, Fig. 2.4).
- At temperatures of 20–30 K, just above the desorption temperature of CO, formation of  $\text{CO}_2$  from the reaction of CO with OH on the ice is efficient. Timescales are longer than for the hydrogenation of CO, but the CO abundance can still be reduced by two orders of magnitude in 2–3 Myr for  $\zeta_{\text{H}_2} = 10^{-17} \text{ s}^{-1}$ . The formation of  $\text{CO}_2$  is more efficient at higher densities (Sec. 2.3.1, Fig. 2.4).
- Gas-phase destruction of CO by  $\text{He}^+$ , eventually leading to the formation  $\text{CH}_4$  and  $\text{H}_2\text{O}$ , only operates on timescales  $> 5$  Myr for  $\zeta_{\text{H}_2} = 10^{-17} \text{ s}^{-1}$ . Furthermore, this pathway is only effective at low densities ( $< 10^7 \text{ cm}^{-3}$ ) and in a small range of temperatures (20 – 25 K). As such, this pathway is not important in the context of protoplanetary disk midplanes (Sec. 2.3.1, Fig. 2.4).
- The assumed tunnelling barrier width ( $a_{\text{tunnel}}$ ) strongly influences the speed of CO hydrogenation with efficient tunnelling leading to fast hydrogenation of CO. The CO destruction due to  $\text{CO}_2$  formation is only weakly dependent on the assumed chemical parameters. Only when  $f_{\text{diff}}$  is increased above 0.35 can this reaction be slowed down (Sec. 2.3.2, Fig. 2.1).
- $\text{CO}_2$ ,  $\text{CH}_3\text{OH}$  and to a lesser extent  $\text{CH}_4$  are all abundantly formed in the regions where CO is destroyed. Observations of anomalously high abundances of  $\text{CH}_4$ ,  $\text{CH}_3\text{OH}$  or  $\text{CO}_2$  either in infrared absorption spectroscopy towards edge-on systems, or in infrared emission from the inner disk, can help in distinguishing the chemical pathway responsible for CO destruction.
- Vertical mixing can bring gas from the warmer, CO richer layers to the lower colder layers, where CO can be converted into  $\text{CH}_3\text{OH}$  or  $\text{CO}_2$ . This would allow for the chemical processes to also lower the CO abundance in the higher, warmer layers of the disk.

In conclusion, chemical reprocessing of CO can have a significant impact on the measured disk masses if sufficient ionising radiation is present in the cold ( $< 30$  K) regions of the disk. Further modelling of individual disks will have to show to which degree chemical processes are important and where other physical processes will need to be invoked.

## Appendix

### 2.A Dali protoplanetary disk models

For Fig. 2.1 two DALI models (Bruderer et al. 2012; Bruderer 2013) have been run to generate maps of the temperature and radiation field for the disks given the gas and dust density structures and stellar spectra as inputs. The input parameters can be found in Table 2.6. In the following the modelling procedure is shortly reiterated.

Radially the gas and dust are distributed using a tapered powerlaw,

$$\Sigma_{\text{gas}} = \Sigma_c \left( \frac{R}{R_c} \right)^{-\gamma} \exp \left[ - \left( \frac{R}{R_c} \right)^{2-\gamma} \right], \quad (2.9)$$

$$\Sigma_{\text{dust}} = \frac{\Sigma_c}{g/d} \left( \frac{R}{R_c} \right)^{-\gamma} \exp \left[ - \left( \frac{R}{R_c} \right)^{2-\gamma} \right]. \quad (2.10)$$

Vertically the gas and dust are distributed according to a Gaussian, the dust is divided into a "large" grain and a "small" grain population (see, Table 2.6, the large grain population contains a fraction  $f_{\text{large}}$  of the mass.

$$\rho_{\text{gas}}(R, \Theta) = \frac{\Sigma_{\text{gas}}(R)}{\sqrt{2\pi} R h_{\text{gas}}(R)} \exp \left[ - \frac{1}{2} \left( \frac{\pi/2 - \Theta}{h(R)} \right)^2 \right], \quad (2.11)$$

$$\rho_{\text{dust, small}}(R, \Theta) = \frac{(1 - f_{\text{large}}) \Sigma_{\text{dust}}(R)}{\sqrt{2\pi} R h_{\text{gas}}(R)} \exp \left[ - \frac{1}{2} \left( \frac{\pi/2 - \Theta}{h_{\text{gas}}(R)} \right)^2 \right], \quad (2.12)$$

$$\rho_{\text{dust, large}}(R, \Theta) = \frac{f_{\text{large}} \Sigma_{\text{gas}}(R)}{\sqrt{2\pi} R h_{\text{large}}(R)} \exp \left[ - \frac{1}{2} \left( \frac{\pi/2 - \Theta}{h_{\text{large}}(R)} \right)^2 \right], \quad (2.13)$$

where  $h_{\text{gas}}(R) = h_c(R/R_c)^\psi$  and  $h_{\text{large}}(R) = \chi h_{\text{gas}}(R)$ . The smaller scale height for the larger grains mimics a degree of settling. The dust temperature and the radiation field are calculated using the continuum ray-tracing module of DALI. Fig. 2.8 shows the density, dust temperature, radiation field and fractional abundance of CO for the DALI models. The CO abundance map does not include the effects of the grain surface chemistry discussed in this paper.

### 2.B Chemical model

The abundance evolution is computed by a chemical solver based on its counterpart in the DALI code (Bruderer et al. 2012; Bruderer 2013). To solve the set of differential equations, CVODE from the SUNDIALS suite is used (Hindmarsh et al. 2005). CVODE was chosen over LIMEX, the which normally used in DALI, as CVODE is faster and more stable on the very stiff grain-surface chemistry models as well as being thread safe, enabling the calculation of multiple chemical models in parallel with OpenMP<sup>5</sup>.

<sup>5</sup><http://www.openmp.org/>



**Table 2.6:** Adopted model parameters for T-Tauri and Herbig disks.

Parameter		T-Tauri	Herbig
Star			
Mass	$M_{\star} [M_{\odot}]$	0.2	2.5
Luminosity	$L_{\star} [L_{\odot}]$	0.3	20
Effective temperature	$T_{\text{eff}} [\text{K}]$	3500	10000
Accretion luminosity	$L_{\text{accr}} [L_{\odot}]$	0.04	0
Accretion temperature	$T_{\text{accr}} [\text{K}]$	10000	–
Disk			
Disk Mass ( $g/d = 100$ )	$M_{\text{disk}} [M_{\odot}]$	0.01	0.024
Surface density index	$\gamma$	1.0	1.0
Characteristic radius	$R_c [\text{AU}]$	35	75
Inner radius	$R_{\text{in}} [\text{AU}]$	0.07	0.221
Scale height index	$\psi$	0.3	0.3
Scale height angle	$h_c [\text{rad}]$	0.1	0.1
Large grain height scaling	$\chi$	0.2	0.2
Dust properties <sup>a</sup>			
Large grain fraction	$f_{\text{large}}$	0.90	0.90
Size small	$a[\mu\text{m}]$	0.005 – 1	0.005 – 1
Size large	$a[\mu\text{m}]$	0.005 – 1000	0.005 – 1000
Size distribution		$dn/da \propto a^{-3.5}$	
Composition		ISM	
Total gas-to-dust ratio	$g/d$	100	

**Notes.** <sup>(a)</sup> Dust composition is taken from Draine & Lee (1984) and Weingartner & Draine (2001).

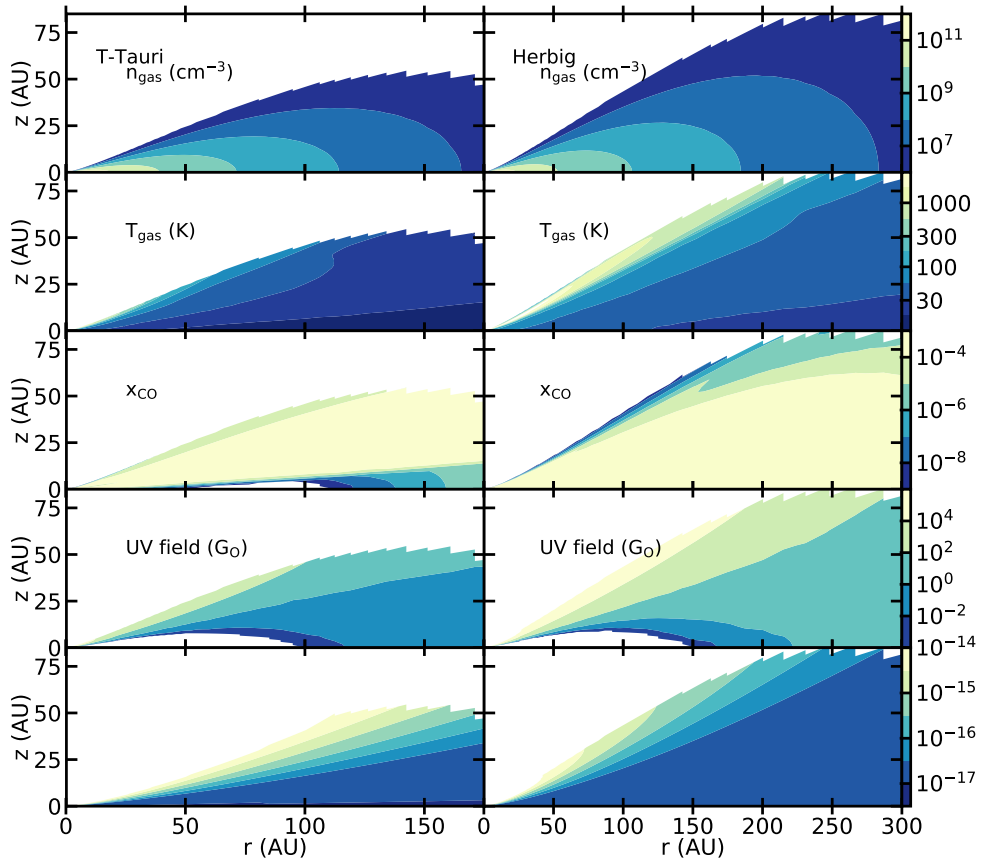


**Figure 2.8:** Gas number density, gas temperature, gas-phase CO fractional abundance and UV radiation field for the T-Tauri and Herbig models. A full gas-grain model was not considered for the CO abundance. Freeze-out, desorption, gas-phase reactions and photo dissociation are included in the chemical computation. CO abundance after 1 Myr of chemical evolution is shown.

**Table 2.7:** Initial gas-phase abundances for the chemical network

molecule	abundance	molecule	abundance
H <sub>2</sub>	0.5	He	9.75(-2)
NH <sub>3</sub>	1.45(-6)	H <sub>2</sub> O	1.18(-4)
CO	1(-4)	N <sub>2</sub>	2(-5)
Si	4(-10)	CH <sub>3</sub> OH	1(-6)
H <sub>2</sub> S	1.91(-8)	CO <sub>2</sub>	1(-5)
Fe	4.27(-7)	grains	2.2(-12)

**Table 2.8:** Binding energies for all the species in the chemical network.

molec.	$E_{\text{bind}}$ (K)	molec.	$E_{\text{bind}}$ (K)	molec.	$E_{\text{bind}}$ (K)	molec.	$E_{\text{bind}}$ (K)
H	600	H <sub>2</sub>	430	He	100	C	800
CH	873	CH <sub>2</sub>	945	N	800	CH <sub>3</sub>	1018
NH	1577	CH <sub>4</sub>	1090	NH <sub>2</sub>	2354	O	800
NH <sub>3</sub>	3130	OH	2850	H <sub>2</sub> O	5770	C <sub>2</sub>	1600
C <sub>2</sub> H	2137	C <sub>2</sub> H <sub>2</sub>	2587	CN	1600	C <sub>2</sub> H <sub>3</sub>	3037
HCN	3610	HNC	2050	C <sub>2</sub> H <sub>4</sub>	3487	CO	855
H <sub>2</sub> CN	2400	N <sub>2</sub>	790	Si	2700	C <sub>2</sub> H <sub>5</sub>	3937
CH <sub>2</sub> NH	3428	HCO	1600	SiH	3150	C <sub>2</sub> H <sub>6</sub>	2300
H <sub>2</sub> CO	2050	NO	1600	SiH <sub>2</sub>	3600	CH <sub>2</sub> OH	4330
CH <sub>3</sub> O	2655	HNO	2050	SiH <sub>3</sub>	4050	CH <sub>3</sub> OH	4930
O <sub>2</sub>	1000	S	1100	SiH <sub>4</sub>	4500	HS	1500
O <sub>2</sub> H	3650	H <sub>2</sub> O <sub>2</sub>	5700	H <sub>2</sub> S	2743	C <sub>3</sub>	2400
C <sub>3</sub> H	2937	C <sub>2</sub> N	2400	C <sub>3</sub> H <sub>2</sub>	3387	H <sub>2</sub> CCC	2110
CH <sub>2</sub> CCH	3837	HCCN	3780	C <sub>2</sub> O	1950	CH <sub>2</sub> CCH <sub>2</sub>	4287
CH <sub>2</sub> CN	4230	CH <sub>3</sub> CCH	4287	SiC	3500	CH <sub>3</sub> CN	4680
HC <sub>2</sub> O	2400	HCSi	1050	CH <sub>2</sub> CO	2200	CH <sub>3</sub> CHCH <sub>2</sub>	5187
CNO	2400	NH <sub>2</sub> CN	1200	OCN	2400	SiCH <sub>2</sub>	1100
SiN	3500	CH <sub>3</sub> CO	2320	HCNO	2850	HNCO	2850
HNSi	1100	HOCN	2850	HONC	2850	SiCH <sub>3</sub>	1150
CH <sub>3</sub> CHO	3800	CO <sub>2</sub>	2990	CS	1900	N <sub>2</sub> O	2400
SiO	3500	COOH	5120	HCS	2350	C <sub>2</sub> H <sub>5</sub> OH	5200
CH <sub>3</sub> OCH <sub>3</sub>	3300	H <sub>2</sub> CS	2700	H <sub>2</sub> SiO	1200	HCOOH	5000
NO <sub>2</sub>	2400	NS	1900	C <sub>4</sub>	3200	SO	2600
C <sub>4</sub> H	3737	C <sub>3</sub> N	3200	C <sub>4</sub> H <sub>2</sub>	4187	C <sub>4</sub> H <sub>3</sub>	4637
HC <sub>3</sub> N	4580	HNC <sub>3</sub>	4580	C <sub>3</sub> O	2750	CH <sub>2</sub> CHCCH	5087
NCCN	1300	SiC <sub>2</sub>	1300	CH <sub>2</sub> CHCN	5480	SiC <sub>2</sub> H	1350
C <sub>2</sub> H <sub>4</sub> CN	5930	C <sub>4</sub> H <sub>6</sub>	5987	SiC <sub>2</sub> H <sub>2</sub>	1400	SiNC	1350
C <sub>2</sub> H <sub>5</sub> CN	6380	C <sub>2</sub> S	5320	Fe	4200	CH <sub>3</sub> COCH <sub>3</sub>	3300
CH <sub>2</sub> OHCO	6230	COOCH <sub>3</sub>	3650	C <sub>5</sub>	4000	CH <sub>2</sub> OHCHO	6680
CH <sub>3</sub> COOH	6300	HCOOCH <sub>3</sub>	4000	OCS	2888	SiO <sub>2</sub>	4300
SiS	3800	C <sub>5</sub> H	4537	C <sub>4</sub> N	4000	C <sub>5</sub> H <sub>2</sub>	4987
CH <sub>3</sub> C <sub>4</sub> H	5887	S <sub>2</sub>	2200	SO <sub>2</sub>	5330	SiC <sub>3</sub>	1600
CH <sub>3</sub> C <sub>3</sub> N	6480	HS <sub>2</sub>	2650	SiC <sub>3</sub> H	1650	H <sub>2</sub> S <sub>2</sub>	3100
C <sub>3</sub> S	3500	C <sub>6</sub>	4800	C <sub>6</sub> H	5337	C <sub>5</sub> N	4800
C <sub>6</sub> H <sub>2</sub>	5787	HC <sub>5</sub> N	6180	SiC <sub>4</sub>	1900	C <sub>6</sub> H <sub>6</sub>	7587
C <sub>4</sub> S	4300	C <sub>7</sub>	5600	C <sub>7</sub> H	6137	C <sub>7</sub> H <sub>2</sub>	6587
CH <sub>3</sub> C <sub>6</sub> H	7487	CH <sub>3</sub> C <sub>5</sub> N	7880	C <sub>8</sub>	6400	C <sub>8</sub> H	6937
C <sub>7</sub> N	6400	C <sub>8</sub> H <sub>2</sub>	7387	HC <sub>7</sub> N	7780	C <sub>9</sub>	7200
C <sub>9</sub> H	7737	C <sub>9</sub> H <sub>2</sub>	8187	CH <sub>3</sub> C <sub>7</sub> N	9480	C <sub>9</sub>	8000
C <sub>10</sub> H	8537	C <sub>10</sub> H <sub>2</sub>	8987	C <sub>9</sub> N	8000	HC <sub>9</sub> N	9380
C <sub>11</sub>	8800						

## 2.B.1 Initial abundances

Table 2.7 shows the input volatile abundances used in our chemical model. These abundances are depleted in Si and S but not in Fe with respect to solar. Fe will be frozen-out and will not play an active part in the chemistry.

Table 2.8 enumerates all the binding energies used in the model. The list is sorted (left to right, top to bottom) according to molecular mass. Binding energies come from the recommended values from Penteado et al. (2017) For NH, NH<sub>2</sub>, CH, CH<sub>2</sub> and CH<sub>3</sub>, the binding energy was increased compared with the values from Penteado et al. (2017). NH and NH<sub>2</sub> were calculated using the method of Garrod & Herbst (2006), while for CH, CH<sub>2</sub> and CH<sub>3</sub> the binding energy are calculated by linearly scaling between the values for C and CH<sub>4</sub> to the number of hydrogen atoms.

## 2.B.2 H<sub>2</sub> formation rate

The formation of H<sub>2</sub> is implemented following Cazaux & Tielens (2004), who give the H<sub>2</sub> formation rate as (in H<sub>2</sub> molecules per unit volume per unit time):

$$R_{\text{H}_2} = \frac{1}{2} n_{\text{H}} v_{\text{H}} N_{\text{grain}} \pi a_{\text{grain}}^2 \epsilon_{\text{H}_2} S_{\text{H}}(T), \quad (2.14)$$

where  $n_{\text{H}}$  is the number density of gaseous H,  $v_{\text{H}}$  is the thermal velocity of atomic hydrogen,  $N_{\text{grain}}$  is the absolute number density of grains,  $a_{\text{grain}}$  is the grain radius.  $S_{\text{H}}(T)$  is the sticking efficiency (Cuppen et al. 2010), given by,

$$S_{\text{H}}(T) = \frac{1}{1.0 + 0.04 \sqrt{T_{\text{gas}} + T_{\text{dust}}} + 2 \times 10^{-3} T_{\text{gas}} + 8 \times 10^{-6} T_{\text{gas}}^2}. \quad (2.15)$$

Furthermore,  $\epsilon_{\text{H}_2}$  is the H<sub>2</sub> recombination efficiency given by:

$$\begin{aligned} \epsilon_{\text{H}_2} = & \left( 1 + \frac{1}{4} \left( 1 + \sqrt{\frac{E_{\text{H}_C} - E_S}{E_{\text{H}_P} - E_S}} \right)^2 \exp \left[ -\frac{E_S}{kT_{\text{dust}}} \right] \right)^{-1} \\ & \times \left[ 1 + \frac{v_{\text{H}_C}}{2F} \exp \left( -\frac{1.5E_{\text{H}_C}}{kT_{\text{dust}}} \right) \left( 1 + \sqrt{\frac{E_{\text{H}_C} - E_S}{E_{\text{H}_P} - E_S}} \right)^2 \right]^{-1}, \end{aligned} \quad (2.16)$$

where  $E_{\text{H}_P} = 600$  K,  $E_{\text{H}_C} = 10000$  K and  $E_S = 200$  K are the energies of a physisorbed H (H<sub>P</sub>), chemisorbed H (H<sub>C</sub>) and the energy of the saddle point between the previous two, respectively.  $F = 10^{-10}$  monolayers s<sup>-1</sup> is the accretion flux of H on the ice for the H<sub>2</sub> formation.

## 2.B.3 Calculation of grain-surface rates

To calculate the reaction rate coefficients of grain-surface reactions, the mobility of the molecules over the grain-surface needs to be known. This requires knowledge of the vibrational frequency of a molecule in its potential well on the grain-surface (assuming a harmonic oscillator. This is the frequency at which the molecule will attempt displacements:

$$\nu_{\text{X}} = \sqrt{\frac{N_{\text{sites}} E_{\text{X, bind}}}{2\pi^3 a_{\text{grain}}^2 m_{\text{X}}}}, \quad (2.17)$$

where  $N_{\text{sites}}$  is the number of adsorption sites per grain,  $E_{\text{X, bind}}$  is the binding energy of the molecule to the grain,  $a_{\text{grain}} = 10^{-5}$  cm is the grain radius and  $m_{\text{X}}$  is the mass of the molecule. The hopping rate is the vibrational frequency multiplied by the hopping probability, which in the thermal case is:

$$R_{\text{hop, X}} = \nu_{\text{X}} \exp \left( -\frac{f_{\text{diff}} E_{\text{bind, X}}}{kT} \right), \quad (2.18)$$

where  $k$  is the Boltzmann constant and  $T$  is the dust-grain temperature. For atomic and molecular hydrogen, tunnelling is also allowed:

$$R_{\text{hop, tunnel, X}} = \nu_{\text{X}} \exp \left[ -\frac{2a_{\text{tunnel}}}{\hbar} \sqrt{2\mu f_{\text{diff}} E_{\text{bind, X}}} \right]. \quad (2.19)$$

For atomic and molecular hydrogen, the fastest of these two rates is used which will almost always be the thermal rate. Only for models with a high  $f_{\text{diff}}$ , low  $a_{\text{tunnel}}$  and low temperature is tunnelling faster than thermal hopping.

The rate coefficient for a grain-surface reaction between species X and Y forming product(s) Z on the grain-surface is given by:

$$\begin{aligned} k(X + Y, Z) &= \min \left[ 1, \left( \frac{N_{\text{act}}^2 N_{\text{sites}}^2 n_{\text{grain}}}{n_{\text{ice}}^2} \right) \right] P_{\text{react}}(X + Y, Z) \left( \frac{R_{\text{hop}, X}}{N_{\text{sites}}} + \frac{R_{\text{hop}, Y}}{N_{\text{sites}}} \right) \\ &= C_{\text{grain}} P_{\text{react}}(X + Y, Z) (R_{\text{hop}, X} + R_{\text{hop}, Y}) \end{aligned} \quad (2.20)$$

where  $N_{\text{act}} = 2$  is the number of chemically active layers,  $N_{\text{sites}} = 10^6$  is the number of molecules per ice monolayer,  $n_{\text{grain}} = 2.2 \times 10^{-12} n_{\text{gas}}$  is the number density of grains with respect to  $\text{H}_2$  and  $n_{\text{ice}}$  is the total number density of species on the grain.  $P_{\text{react}}(X + Y, Z)$  is the reaction probability for the reaction. This includes the branching ratios if multiple products are possible as well as a correction for reactions that have a barrier.

The reaction probability is given by:

$$P_{\text{react}}(X + Y, Z) = b_r(X + Y, Z) \exp \left( -\frac{E_{\text{bar}}(X + Y, Z)}{kT} \right), \quad (2.21)$$

where  $b_r(X + Y, Z)$  is the branching ratio,  $E_{\text{bar}}(X + Y, Z)$  is the energy barrier for the reaction. If either H or  $\text{H}_2$  is participating in the reaction, tunnelling is included:

$$P_{\text{react, tun}}(X + Y, Z) = b_r(X + Y, Z) \exp \left( -\frac{2a_{\text{tunnel}}}{\hbar} \sqrt{2\mu E_{\text{bar}}(X + Y, Z)} \right). \quad (2.22)$$

The largest of the tunnelling and thermal crossing probability is taken for the actual rate calculation, for most reactions tunnelling dominates in contrast with hopping, where thermal crossing dominates.

## 2.B.4 Implications of modelling assumptions

### Variations in the $\text{H}_2$ formation rate

The formation speed of  $\text{H}_2$  from atomic hydrogen is very important in our models as, together with the destruction rate of  $\text{H}_2$ , it sets the abundance of atomic hydrogen in the gas. For the formation rate, the prescription of Cazaux & Tielens (2004) is used. The formalism forces the atomic H gaseous abundance to  $\sim 1 \text{ cm}^{-3}$  for  $\zeta_{\text{H}_2} = 10^{-17} \text{ s}^{-1}$  irrespective of total gas density. A higher or lower atomic hydrogen abundance would strongly affect both the sCO + sH route, which would increase in effectiveness with higher atomic hydrogen abundances, and the sCO + sOH route, which would decrease in effectiveness with higher atomic hydrogen abundances.

### Initial conditions

The initial conditions for the chemistry are shown in Table. 2.7. The focus was on testing the CO destruction, hence we start with CO as the major volatile carbon reservoir, with trace amounts of  $\text{CO}_2$  (10% of CO) and  $\text{CH}_3\text{OH}$  (1% of CO). At the

densities considered here, there is no strong chemical alteration before freeze-out and desorption are balanced. Furthermore, a small portion of N is in  $\text{NH}_3$ , with the rest of the nitrogen in  $\text{N}_2$ .

The initial conditions can have a significant impact on the evolution of the CO abundances. The amount of  $\text{H}_2\text{O}$  ice on the grains determines the formation rate of OH on the grain, which in turn impacts the transformation of CO to  $\text{CO}_2$ . If the chemical evolution is started with a larger portion of carbon in hydrocarbons than assumed in this work, with the excess oxygen put into  $\text{H}_2\text{O}$ , then a shorter CO destruction time-scale will be found in the regions where  $\text{CO}_2$  formation is effective.

The time-scale of the  $\text{CO} + \text{He}^+$  route is especially sensitive to the initial abundances. Starting with a significant fraction of the CO already incorporated into  $\text{CO}_2$ , such as predicted by Drozdovskaya et al. (2016) and as observed in ices in collapsing envelopes (Pontoppidan et al. 2008b), can shorten chemical timescales significantly. Chemical timescales can be further shortened by the removal of  $\text{N}_2$  from the gas-phase, such as by starting the chemical model with  $\text{NH}_3$  as the dominant nitrogen carrier.

The time-scale of the  $\text{sCO} + \text{sH}$  route is not very sensitive to the initial abundances, as long as they are molecular. The maximal amount of CO removal is a function of the amount of  $\text{CO}_2$  in the ice initially, but as hydrogenation of CO is at least two orders of magnitude faster than the dissociation of  $\text{CO}_2$  due to cosmic-rays, this means that even when  $\text{CO}_2$  is the dominant carbon reservoir, the CO abundance can still be reduced below  $10^{-6}$  by  $\text{sCO} + \text{sH}$  even with the CO replenishment.

### Chemically active surface

All our models assume that only the molecules in the top two layers of our ices are participating in chemical reactions. The composition of these layers is assumed to be the same of that of the bulk ice. If the number of layers that can participate in chemical reactions is doubled, then the timescales for all grain-surface reactions decrease by a factor of four (see Equation 2.20). However, most of our grain-surface reactions are not limited by the speed of the grain-surface reactions, but by the availability of H-atoms and OH-radicals in the ice. The availability of H-atoms is set by the arrival rate of H-atoms on the grains, and this linearly depends on the total grain-surface but not on the number of chemically active layers. The availability of the OH radical is primarily set by the destruction rate of  $\text{H}_2\text{O}$  which is independent of the ice thickness. As such the effect of changing the number of active layers is mostly in setting the exact location of the icelines as a larger number of active layers results in a faster sublimation rate at equal temperatures. Varying the number of active layers between one and eight changes the ice-line temperature by less than 1.5 K. This effect is similar to the effect of an one order of magnitude change in the total density.

The total amount of grain-surface, and thus the assumed size of the grains does have some effect on the timescales of CO destruction. The atomic hydrogen arrival rate on the grain scales with the total available surface, which decreases if the grain size is increased and the gas-to-dust mass ratio is held fixed. However, the  $\text{H}_2$  formation rate as calculated by Cazaux & Tielens (2004) also depends on the total surface area, thus if the total surface area is decreased, that means that the abundance of atomic hydrogen should increase, cancelling the effect of the grain size on the hydrogenation reaction of CO. The production of  $\text{CO}_2$  actually increases with increasing grain size (and thus decreasing surface area). As the total grain-surface area decreases, a smaller

amount of the cosmic-ray induced UV photons are absorbed by the dust grains, as such the dissociation rate for  $\text{H}_2\text{O}$  should be slightly higher, creating more OH radicals and thus increasing the rate of  $\text{CO}_2$  production.

### Mixed ice model

The code assumes a perfectly mixed ice, that is to say that all species are assumed to be present in the upper chemically active layers at the relative abundances that they are included in the bulk of the ice. Observations of dark clouds indicate that in that stage ice mantles are not perfectly mixed, but have a layered structure (Tielens et al. 1991; Boogert et al. 2015) with a CO-rich layer on top of the  $\text{H}_2\text{O}$ -rich layers. It is expected that ice mantles in protoplanetary disks are also layered. The perfect mixing assumption can have some profound effects on the chemistry of CO. A layered ice below the CO freeze-out temperature would have a higher fraction of CO in the surface layers than currently assumed. This would initially speed-up the formation of  $\text{CH}_3\text{OH}$ , however, as the CO in the top layers is converted into  $\text{CH}_3\text{OH}$ , the rate of CO destruction would go down. At that point the CO destruction rate would be dependent on the CO exchange rate of the bulk ice and the surface layers which is expected to be slower than the surface diffusion speed. Just above the CO freeze-out temperature the top layers of the ice would be made-up of mostly  $\text{CH}_3\text{OH}$ ,  $\text{CO}_2$  and  $\text{CH}_4$ . Since the top layers have very little  $\text{H}_2\text{O}$ , this would lead to very low abundances of OH radicals in the surface layers and might thus quench the  $\text{sCO} + \text{sOH}$  route to form  $\text{CO}_2$ .

Mixing of an ice through bulk diffusion is a slow process. However, in the high density midplanes another process can mix ices: grain-grain collisions. In large parts of the disk, the grain size distribution is in coagulation-fragmentation equilibrium. Especially the destructive collisions leading to cratering and fragmentation should be able to mix up the layered structure.

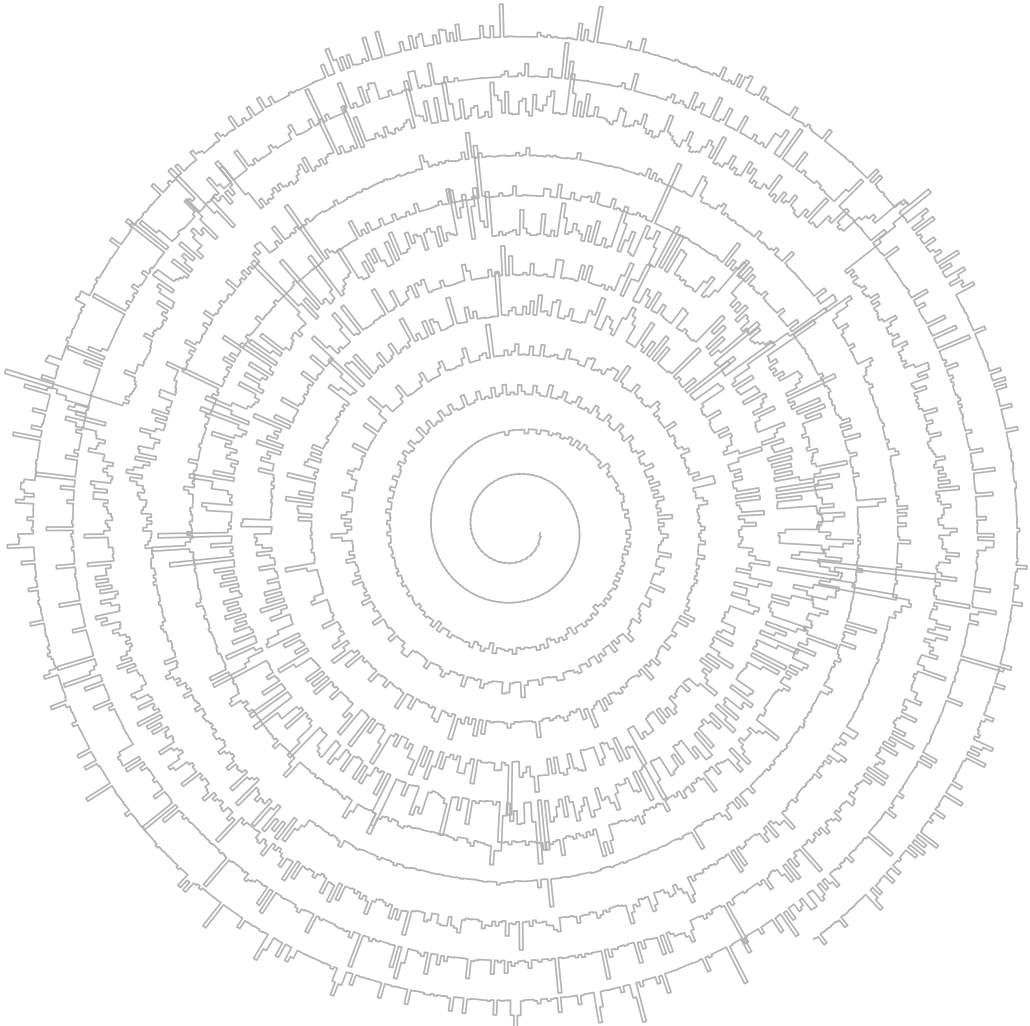
Multi-phase models that include layering explicitly have been developed (e.g. Taquet et al. 2012; Furuya et al. 2016). Drozdovskaya et al. (2016) compared the results from their two-phase (gas and ice) chemical model to the three-phase (gas, surface ice and bulk ice) chemical model from Furuya et al. (2015). They conclude that the two-phase model and the three-phase model that includes swapping between bulk and surface ice produces comparable amounts of  $\text{CO}_2$  in the ice, but that if swapping is excluded,  $\text{CO}_2$  production is efficiently quenched. More detailed models of disk midplanes that included layering should be done in the future to better quantify the effects of assuming a fully mixed ice on the results presented here.

### CO binding energy

The binding energy of CO depends strongly on the surface on which it is frozen (Collings et al. 2003; Acharyya et al. 2007). Here the binding energy of CO on a pure CO ice surface is used, which is applicable to the cold ( $< 20$  K) regions, where CO is primarily in the ice. In warmer regions however, CO will mostly be bound to  $\text{CO}_2$ ,  $\text{CH}_3\text{OH}$  and  $\text{H}_2\text{O}$ , slightly increasing the binding energy of CO (Collings et al. 2003; Noble et al. 2012; Acharyya et al. 2007). The higher binding energy, and thus slower CO diffusion, moves upwards and broadens the temperature range over which the reaction to form  $\text{CO}_2$  (Equation 2.3) is efficient.

# 3

## CO<sub>2</sub> INFRARED EMISSION AS A DIAGNOSTIC OF PLANET-FORMING REGIONS OF DISKS



A. D. Bosman, S. Bruderer and E. F. van Dishoeck, 2017, A&A 601, 36



## Abstract

**Context:** The infrared ro-vibrational emission lines from organic molecules in the inner regions of protoplanetary disks are unique probes of the physical and chemical structure of planet-forming regions and the processes that shape them. These observed lines are mostly interpreted with local thermal equilibrium (LTE) slab models at a single temperature.

**Aims:** We aim to study the non-LTE excitation effects of carbon dioxide ( $\text{CO}_2$ ) in a full disk model to evaluate: (i) what the emitting regions of the different  $\text{CO}_2$  ro-vibrational bands are; (ii) how the  $\text{CO}_2$  abundance can be best traced using  $\text{CO}_2$  ro-vibrational lines using future JWST data and; (iii) what the excitation and abundances tell us about the inner disk physics and chemistry.  $\text{CO}_2$  is a major ice component and its abundance can potentially test models with migrating icy pebbles across the iceline.

**Methods:** A full non-LTE  $\text{CO}_2$  excitation model has been built starting from experimental and theoretical molecular data. The characteristics of the model are tested using non-LTE slab models. Subsequently the  $\text{CO}_2$  line formation was modelled using a two-dimensional disk model representative of T-Tauri disks where  $\text{CO}_2$  is detected in the mid-infrared by the *Spitzer Space Telescope*.

**Results:** The  $\text{CO}_2$  gas that emits in the  $15\ \mu\text{m}$  and  $4.5\ \mu\text{m}$  regions of the spectrum is not in LTE and arises in the upper layers of disks, pumped by infrared radiation. The  $v_2\ 15\ \mu\text{m}$  feature is dominated by optically thick emission for most of the models that fit the observations and increases linearly with source luminosity. Its narrowness compared with that of other molecules stems from a combination of the low rotational excitation temperature ( $\sim 250\ \text{K}$ ) and the inherently narrower feature for  $\text{CO}_2$ . The inferred  $\text{CO}_2$  abundances derived for observed disks range from  $3 \times 10^{-9}$  to  $1 \times 10^{-7}$  with respect to total gas density for typical gas/dust ratios of 1000, similar to earlier LTE disk estimates. Line-to-continuum ratios are low, in the order of a few percent, stressing the need for high signal-to-noise ( $S/N > 300$ ) observations for individual line detections.

**Conclusions:** The inferred  $\text{CO}_2$  abundances are much lower than those found in interstellar ices ( $\sim 10^{-5}$ ), indicating a reset of the chemistry by high temperature reactions in the inner disk. JWST-MIRI with its higher spectral resolving power will allow a much more accurate retrieval of abundances from individual  $P$ - and  $R$ -branch lines, together with the  $^{13}\text{CO}_2$   $Q$ -branch at  $15\ \mu\text{m}$ . The  $^{13}\text{CO}_2$   $Q$ -branch is particularly sensitive to possible enhancements of  $\text{CO}_2$  due to sublimation of migrating icy pebbles at the iceline(s). Prospects for *JWST-NIRSpec* are discussed as well.

### 3.1 Introduction

Most observed exo-planets orbit close to their parent star (for a review see: Udry & Santos 2007; Winn & Fabrycky 2015). The atmospheres of these close-in planets show a large diversity in molecular composition (Madhusudhan et al. 2014). This diversity in molecular composition must be set during planet formation and thus be representative of the natal protoplanetary disk. Understanding the chemistry of the inner, planet-forming regions of circumstellar disks around young stars will thus give us another important piece of the puzzle of planet formation. Prime molecules for such studies are  $\text{H}_2\text{O}$ ,  $\text{CO}$ ,  $\text{CO}_2$  and  $\text{CH}_4$  which are the major oxygen- and carbon-bearing species that set the overall C/O ratio (Öberg et al. 2011).

The chemistry in the inner disk, that is, its inner few AU, differs from that in the outer disk. It lies within the  $\text{H}_2\text{O}$  and  $\text{CO}_2$  icelines so all icy planetesimals are sublimated. The large range of temperatures (100–1500 K) and densities ( $10^{10} - 10^{16} \text{ cm}^{-3}$ ) then makes for a diverse chemistry across the inner disk region (see e.g. Willacy et al. 1998; Markwick et al. 2002; Agúndez et al. 2008; Henning & Semenov 2013; Walsh et al. 2015). The driving cause for this diversity is high temperature chemistry: some molecules such as  $\text{H}_2\text{O}$  and  $\text{HCN}$  have reaction barriers in their formation pathways that make it difficult to produce the molecule in high abundances at temperatures below a few hundred Kelvin. As soon as the temperature is high enough to overcome these barriers, formation is fast and these molecules become major reservoirs of oxygen and nitrogen. An interesting example is formed by the main oxygen bearing molecules,  $\text{H}_2\text{O}$  and  $\text{CO}_2$ : the gas phase formation of both these molecules includes the OH radical. At temperatures below  $\sim 200$  K the formation of  $\text{CO}_2$  is faster, leading to high gas phase abundances, up to  $\sim 10^{-6}$  with respect to (w.r.t.) total gas density, in regions where  $\text{CO}_2$  is not frozen out. When the temperature is high enough,  $\text{H}_2\text{O}$  formation will push most of the gas phase oxygen into  $\text{H}_2\text{O}$  and the  $\text{CO}_2$  abundance drops to  $\sim 10^{-8}$  (Agúndez et al. 2008; Walsh et al. 2014, 2015). Such chemical transitions can have strong implications for the atmospheric content of gas giants formed in these regions if most of their atmosphere is accreted from the surrounding gas.

A major question is to what extent the inner disk abundances indeed reflect high temperature chemistry or whether continuously migrating and sublimating icy planetesimals and pebbles at the icelines replenish the disk atmospheres (Stevenson & Lunine 1988; Ciesla & Cuzzi 2006). Interstellar ices are known to be rich in  $\text{CO}_2$ , with typical abundances of 25% w.r.t.  $\text{H}_2\text{O}$  ice, or about  $10^{-5}$  w.r.t. total gas density (de Graauw et al. 1996; Gibb et al. 2004; Bergin et al. 2005; Pontoppidan et al. 2008b; Boogert et al. 2015). Cometary ices show similarly high  $\text{CO}_2/\text{H}_2\text{O}$  abundance ratios (Mumma & Charnley 2011; Le Roy et al. 2015). Of all molecules with high ice abundances,  $\text{CO}_2$  shows the largest contrast between interstellar ice and high temperature chemistry abundances, and could therefore be a good diagnostic of its chemistry. Pontoppidan & Blevins (2014) argue based on *Spitzer Space Telescope* data that  $\text{CO}_2$  is not inherited from the interstellar medium but is reset by chemistry in the inner disk. However, that analysis used a local thermodynamic equilibrium (LTE)  $\text{CO}_2$  excitation model coupled with a disk model and did not investigate the potential of future instruments, which could be more sensitive to a contribution from sublimating planetesimals. Here we re-consider the retrieval of  $\text{CO}_2$  abundances in the inner regions of protoplanetary disks using a full non-LTE excitation and radiative transfer disk

model, with a forward look to the new opportunities offered by the *James Webb Space Telescope* (JWST).

The detection of infrared vibrational bands seen from CO<sub>2</sub>, C<sub>2</sub>H<sub>2</sub> and HCN, together with high energy rotational lines of OH and H<sub>2</sub>O, was one of the major discoveries of the *Spitzer* Space Telescope (e.g. Lahuis et al. 2006; Carr & Najita 2008; Salyk et al. 2008, 2011b; Pascucci et al. 2009; Pontoppidan et al. 2010; Carr & Najita 2011; Najita et al. 2011; Pascucci et al. 2013). These data cover wavelengths in the 10–35  $\mu\text{m}$  range at low spectral resolving power of  $\lambda/\Delta\lambda=600$ . Complementary ground-based infrared spectroscopy of molecules such as CO, OH, H<sub>2</sub>O, CH<sub>4</sub>, C<sub>2</sub>H<sub>2</sub> and HCN also exists at shorter wavelengths in the 3–5  $\mu\text{m}$  range (e.g. Najita et al. 2003; Gibb et al. 2007; Salyk et al. 2008, 2011a; Fedele et al. 2011; Mandell et al. 2012; Gibb & Horne 2013; Brown et al. 2013). The high spectral resolving power of  $R = 25000 - 10^5$  for instruments like Keck/NIRSPEC and VLT/CRIFRES have resolved the line profiles and have revealed interesting kinematical phenomena, such as disk winds in the inner disk regions (Pontoppidan et al. 2008b, 2011a; Bast et al. 2011; Brown et al. 2013). Further advances are expected with VLT/CRIFRES+ as well as through modelling of current data with more detailed physical models.

Protoplanetary disks have a complex physical structure (see Armitage 2011, for a review) and putting all physics, from magnetically induced turbulence to full radiative transfer, into a single model is not feasible. This means that simplifications must be made. During the *Spitzer* era, the models used to explain the observations were usually LTE excitation slab models at a single temperature. With 2D physical models such as RADLITE (Pontoppidan et al. 2009) and with full 2D physical-chemical models such as Dust and Lines (DALI, Bruderer et al. 2012; Bruderer 2013) or Protoplanetary Disk Model (ProDiMo, Woitke et al. 2009) it is now possible to fully take into account the large range of temperatures and densities as well as the non-local excitation effects. For example, it has been shown that it is important to include radiative pumping introduced by hot (500 – 1500 K) thermal dust emission of regions just behind the inner rim. This has been done for H<sub>2</sub>O by Meijerink et al. (2009) who concluded that to explain the mid-infrared water lines observed with *Spitzer*, water is located in the inner  $\sim 1$  AU in a region where the local gas-to-dust ratio is 1–2 orders of magnitude higher than the interstellar medium (ISM) value. Antonellini et al. (2015, 2016) performed a protoplanetary disk parameter study to see how disk parameters affect the H<sub>2</sub>O emission. Mandell et al. (2012) compared an LTE disk model analysis using RADLITE with slab models and concluded that, while inferred abundance ratios were similar with factors of a few, there could be orders of magnitude differences in absolute abundances depending on the assumed emitting area in slab models (see also discussion in Salyk et al. 2011b). Thi et al. (2013) concluded that the CO infrared emission from disks around Herbig stars was rotationally cool and vibrationally hot due to a combination of infrared and ultraviolet (UV) pumping fields (see also Brown et al. 2013). Bruderer et al. (2015) modelled the non-LTE excitation and emission of HCN concluding that the emitting area for mid-infrared lines can be ten times larger in disks than the assumed emitting area in slab models due to infrared pumping. Our study of CO<sub>2</sub> is along similar lines as that for HCN.

As CO<sub>2</sub> cannot be observed through rotational transitions in the far-infrared and submillimeter, because of the lack of a permanent dipole moment, it must be observed through its vibrational transitions at near- and mid-infrared wavelengths. The CO<sub>2</sub> in our own atmosphere makes it impossible to detect these CO<sub>2</sub> lines from astronomical

sources from the ground, and even at altitudes of 13 km with SOFIA. This means that CO<sub>2</sub> has to be observed from space. CO<sub>2</sub> has been observed by *Spitzer* in protoplanetary disks through its  $v_2$   $Q$ -branch at 15  $\mu\text{m}$  where many individual  $Q$ -band lines combine into a single broad  $Q$ -branch feature at low spectral resolution (Lahuis et al. 2006; Carr & Najita 2008). These gaseous CO<sub>2</sub> lines have first been detected in high mass protostars and shocks with the *Infrared Space Observatory* (ISO, e.g. van Dishoeck et al. 1996; Boonman et al. 2003a,b). CO<sub>2</sub> also has a strong band around 4.3  $\mu\text{m}$  due to the  $v_3$  asymmetric stretch mode. This mode has high Einstein  $A$  coefficients and thus should thus be easily observable, but has not been seen from CO<sub>2</sub> gas towards protoplanetary disks or protostars, in contrast with the corresponding feature in CO<sub>2</sub> ice (van Dishoeck et al. 1996).

The CO<sub>2</sub>  $v_2$   $Q$ -branch profile is slightly narrower than that of C<sub>2</sub>H<sub>2</sub> and HCN observed at similar wavelengths. These results suggest that CO<sub>2</sub> is absent (or strongly under-represented) in the inner, hottest regions of the disk. Full disk LTE modelling of RNO 90 by Pontoppidan & Blevins (2014) using RADLITE showed that the observations of this disk favour a low CO<sub>2</sub> abundance ( $10^{-4}$  w.r.t. H<sub>2</sub>O,  $\approx 10^{-8}$  w.r.t. total gas density). The slab models by Salyk et al. (2011b) indicate smaller differences between the CO<sub>2</sub> and H<sub>2</sub>O abundances, although CO<sub>2</sub> is still found to be 2 to 3 orders of magnitude lower in abundance.

To properly analyse CO<sub>2</sub> emission from disks, a full non-LTE excitation model of the CO<sub>2</sub> ro-vibrational levels must be made, using molecular data from experiments and detailed quantum calculations. This model can then be used to perform a simple slab model study to see under which conditions non-LTE effects may be important. These same slab model tests are also used to check the influences of the assumptions made in setting up the ro-vibrational excitation model. Such CO<sub>2</sub> models have been developed in the past for evolved asymptotic giant branch stars (Cami et al. 2000; González-Alfonso & Cernicharo 1999, e.g.) and shocks (e.g. Boonman et al. 2003b), but not applied to disks.

Our CO<sub>2</sub> excitation model is coupled with a full protoplanetary disk model computed with DALI to investigate the importance of non-LTE excitation, infrared pumping and dust opacity on the emission spectra. In addition, the effects of varying some key disk parameters such as source luminosity and gas/dust ratios on line fluxes and line-to-continuum ratios are investigated. Finally, *Spitzer* data for a set of T-Tauri disks are analysed to derive the CO<sub>2</sub> abundance structure using parametrized abundances.

*JWST* will allow a big leap forward in our observing capabilities at near- and mid-infrared wavelengths, where the inner planet-forming regions of disks emit most of their lines. The spectrometers on board *JWST*, NIRSPEC and MIRI (Rieke et al. 2015) with their higher spectral resolving power ( $R \approx 3000$ ) compared to *Spitzer* ( $R = 600$ ) will not only separate many blended lines (Pontoppidan et al. 2010) but also boost line-to-continuum ratios allowing detection of individual  $P$ ,  $Q$  and  $R$ -branch lines thus giving new information on the physics and chemistry of the inner disk. Here we simulate the emission spectra of CO<sub>2</sub> and its <sup>13</sup>CO<sub>2</sub> isotopologue from a protoplanetary disk at *JWST* resolution. We investigate which subset of these lines is the most useful for abundance determinations at different disk heights and point out the importance of detecting the <sup>13</sup>CO<sub>2</sub> feature. We also investigate which features could signify high CO<sub>2</sub> abundances around the CO<sub>2</sub> iceline due to sublimating planetesimals.

## 3.2 Modelling CO<sub>2</sub> emission

### 3.2.1 Vibrational states

The structure of a molecular emission spectrum depends on the vibrational level energies and transitions between these levels that can be mediated by photons. Figure 3.1 shows the vibrational energy level diagram for CO<sub>2</sub> from the HITRAN database (Rothman et al. 2013). Lines denote the transitions that are dipole allowed. Colours denote the part of the spectrum where features will show up. This colour coding is repeated in Fig. 3.2 where a model CO<sub>2</sub> spectrum is presented.

CO<sub>2</sub> is a linear molecule with a  $^1\Sigma_g^+$  ground state. It has a symmetric,  $v_1$ , and an asymmetric,  $v_3$ , stretching mode (both of the  $\Sigma$  type) and a doubly degenerate bending mode,  $v_2$  ( $\Pi$  type) with an angular momentum,  $l$ . A vibrational state is denoted by these quantum numbers as:  $v_1v_2^lv_3$ . The vibrational constant of the symmetric stretch mode is very close to twice that of the bending mode. Due to this resonance, states with the same value for  $2v_1 + v_2$  and the same angular momentum mix. This mixing leads to multiple vibrational levels that have different energies in a process known as Fermi splitting. The Fermi split levels have the same notation as the unmixed state with the highest symmetric stretch quantum number,  $v_1$  and numbered in order of decreasing energy.<sup>1</sup> This leads to the vibrational state notation of:  $v_1v_2^lv_3(n)$  where  $n$  is the numbering of the levels. This full designation is used in Fig. 3.1. For the rest of the paper we will drop the  $(n)$  for the levels where there is only one variant.

The number of vibrational states in the HITRAN database is much larger than the set of states used here. Not all of the vibrational states are needed to model CO<sub>2</sub> in a protoplanetary disk because some the higher energy levels can hardly be excited, either collisionally or with radiation, so they should not have an impact on the emitted line radiation. We adopt the same levels as used for AGB stars in González-Alfonso & Cernicharo (1999) and add to this set the 03<sup>3</sup>0 vibrational level.

### 3.2.2 Rotational ladders

The rotational ladder of the ground state is given in Fig. 3.1. All states up to  $J=80$  in each vibrational state are included; this rotational level corresponds to an energy of approximately 3700 K ( $2550\text{ cm}^{-1}$ ) above the vibrational state energy. The rotational structure of CO<sub>2</sub> is more complex than that of a linear diatomic like CO. This is due to the fully symmetric wavefunction of CO<sub>2</sub> in the ground electronic state. This means that all states of CO<sub>2</sub> need to be fully symmetric to satisfy Bose-Einstein statistics. As a result, not all rotational quantum numbers  $J$  exist in all of the vibrational states: some vibrational states miss all odd or all even  $J$  levels. There are also additional selections on the Wang parity of the states ( $e, f$ ). For the ground vibrational state this means that only the rotational states with even  $J$  numbers are present and that the parity of these states is  $e$ .

The rotational structure is summarized in Table 3.1. The states with  $v_2 = v_3 = 0$  all have the same rotational structure as the ground vibrational state. The 01<sup>1</sup>0(1) state has both even and odd  $J$  levels starting at  $J = 1$ . The even  $J$  levels have  $f$  parity, while the odd  $J$  levels have  $e$  parity. In general for levels with  $v_2 \neq 0$  and

---

<sup>1</sup>For example: Fermi splitting of the theoretical 02<sup>0</sup>0 and 10<sup>0</sup>0 levels leads to two levels denoted as 10<sup>0</sup>0(1) and 10<sup>0</sup>0(2) where the former has the higher energy.

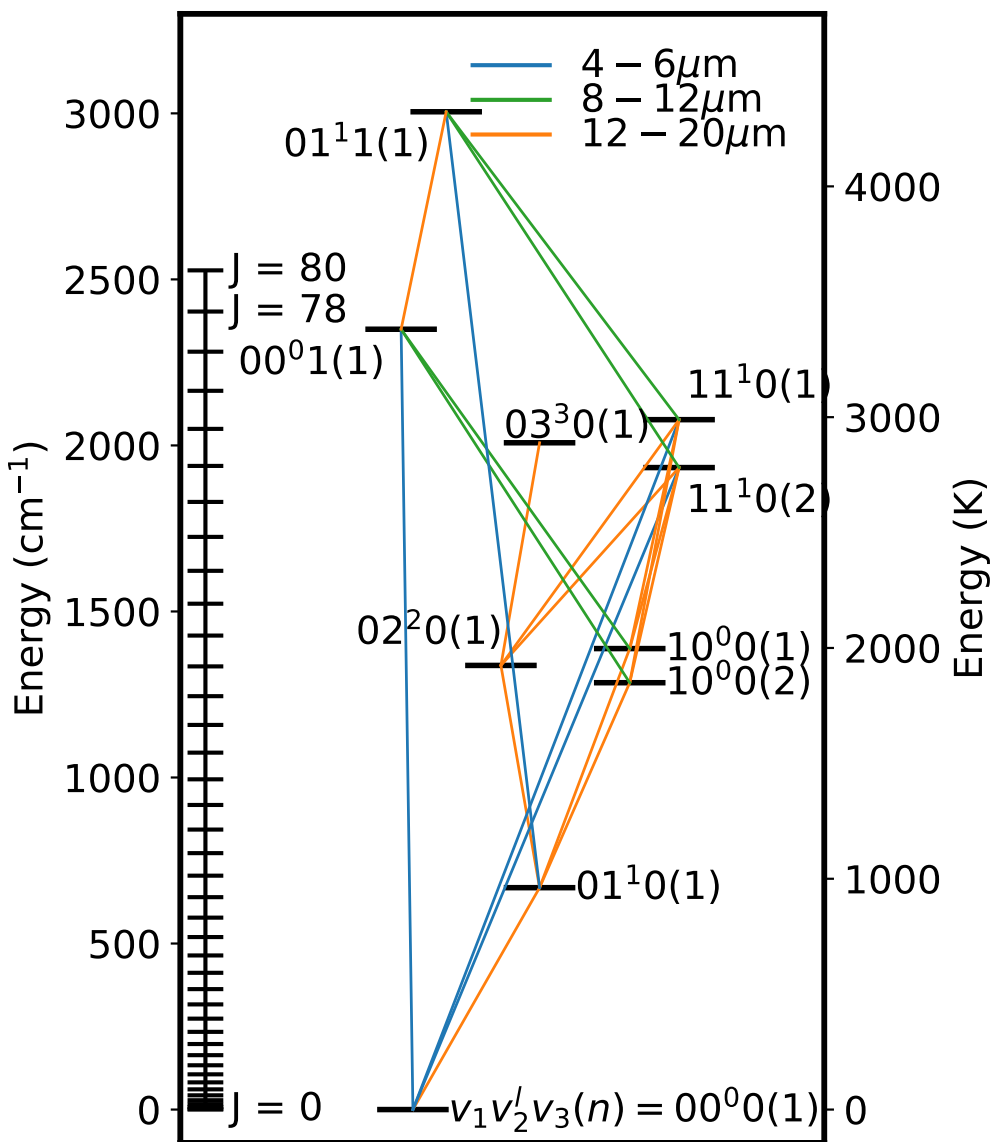


**Figure 3.1:** Vibrational energy levels of the CO<sub>2</sub> molecule (right) together with the rotational ladder of the ground state (left). We note that for the ground state the rotational ladder increases with  $\Delta J = 2$ . Lines connecting the vibrational levels denote the strongest absorption and emission pathways. The colour indicates the wavelength range of the transition: blue, 4–6 μm, green, 8–12 μm and red, 12–20 μm (spectrum in Fig. 3.2). More information on the rotational ladders is given in Sec. 3.2.2.

**Table 3.1:** Rotational structure of the vibrational levels included in the model.

Vibrational level	lowest $J$	$J$ levels and parity
00 <sup>0</sup> 0(1)	0	even $J$ , $e$
01 <sup>1</sup> 0(1)	1	even $J$ , $f$ ; odd $J$ , $e$
02 <sup>2</sup> 0(1)	2	even $J$ , $e$ ; odd $J$ , $f$
10 <sup>0</sup> 0(1, 2)	0	even $J$ , $e$
03 <sup>3</sup> 0(1)	3	even $J$ , $f$ ; odd $J$ , $e$
11 <sup>1</sup> 0(1, 2)	1	even $J$ , $f$ ; odd $J$ , $e$
00 <sup>0</sup> 1(1)	1	odd $J$ , $e$
01 <sup>1</sup> 1(1)	1	even $J$ , $e$ ; odd $J$ , $f$

$v_3 = 0$ , the rotational ladder starts at  $J = v_2$  with an even parity, with the parity alternating in the rotational ladder with increasing  $J$ . For  $v_3 \neq 0$  and  $v_2 = 0$ , only odd  $J$  levels exist if  $v_3$  is odd, whereas only even  $J$  levels exist if  $v_3$  is even. All levels have an  $e$  parity. For  $v_2 \neq 0$  and  $v_3 \neq 0$ , the rotational ladder is the same as for the  $v_2 \neq 0$  and  $v_3 = 0$  case if  $v_3$  is even, whereas the parities relative to this case are switched if  $v_3$  is odd.

### 3.2.3 Transitions between states

To properly model the emission of infrared lines from protoplanetary disks non-LTE effects must be taken into account. The population of each level was determined by the balance of the transition rates, both radiative and collisional. The radiative transition rates were set by the Einstein coefficients and the ambient radiation field. Einstein coefficients for CO<sub>2</sub> have been well studied, both in the laboratory and in detailed quantum chemical calculations (see e.g. Rothman et al. 2009; Jacquinet-Husson et al. 2011; Rothman et al. 2013; Tashkun et al. 2015, and references therein). These are collected in several databases for CO<sub>2</sub> energy levels and Einstein coefficients such as the Carbon Dioxide Spectroscopic Database (CSDS) (Tashkun et al. 2015) and as part of large molecular databases such as HITRAN (Rothman et al. 2013) and GEISA (Jacquinet-Husson et al. 2011). Here the <sup>12</sup>CO<sub>2</sub> and <sup>13</sup>CO<sub>2</sub> data from the HITRAN database were used. It should be noted that the differences between the three databases are small for the lines considered here, within a few % in line intensity and less than 1% for the line positions.

The HITRAN database gives the energies of the ro-vibrational levels above the ground state and the Einstein  $A$  coefficients of transitions between them. Only transitions above a certain intensity at 296 K are included in the databases. The weakest lines included in the line list are 13 orders of magnitude weaker than the strongest lines. With expected temperatures in the inner regions of disks ranging from 100–1000 K, no important lines should be missed due to this intensity cut. In the final, narrowed down set of states all transitions that are dipole allowed have been accounted for.

Collisional rate coefficients between vibrational states are collected from literature sources. The measured rate of the relaxation of the 01<sup>1</sup>0 to the 00<sup>0</sup>0 state by collisions with H<sub>2</sub> from Allen et al. (1980) is used. Vibrational relaxation of the 00<sup>0</sup>1 state due to collisions with H<sub>2</sub> is taken from Nevdakh et al. (2003). For the transitions between the Fermi split levels the rate by Jacobs et al. (1975) for collisions between CO<sub>2</sub> with CO<sub>2</sub> is used with a scaling for the decreased mean molecular mass. Although data used

here supersede those in Taylor & Bitterman (1969), that paper does give a sense for the uncertainties of the experiments. The different experiments in Taylor & Bitterman (1969) usually agree within a factor of two, and the numbers used here from Allen et al. (1980) and Nevdakh et al. (2003) fall within the spread for their respective transitions. It is thus expected that the accuracy of the individual collisional rate coefficients is better than a factor of two.

No information is available from the literature for pure rotational transitions induced by collisions of CO<sub>2</sub> with other molecules. We therefore adopt the CO rotational collisional rate coefficients from the LAMDA database (Schöier et al. 2005; Yang et al. 2010; Neufeld 2012). Due to the lack of dipole moment, the critical density for rotational transitions of CO<sub>2</sub> is expected to be very low ( $n_{\text{crit}} < 10^4$ ) cm<sup>-3</sup> and thus the exact collisional rate coefficients are not important for the higher density environments considered here. A method similar to Faure & Josselin (2008); Thi et al. (2013); Bruderer et al. (2015) is used to create the full state-to-state collisional rate coefficient matrix. The method is described in Appendix 3.A.

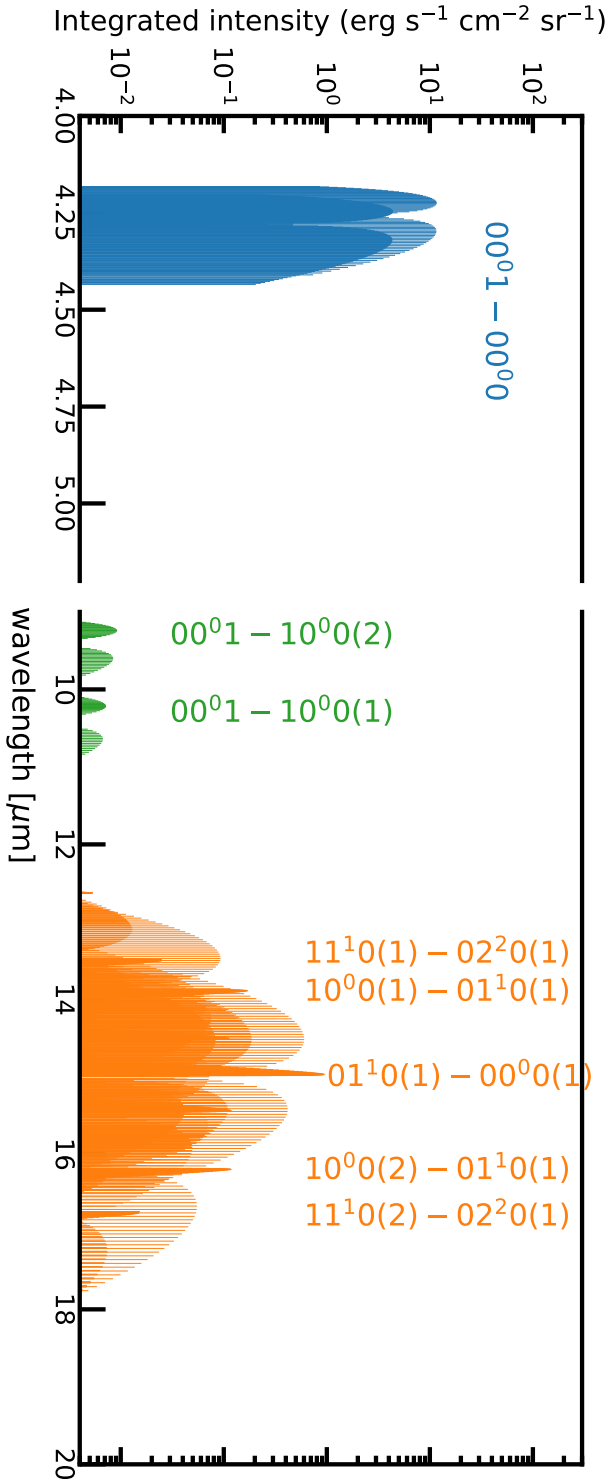
### 3.2.4 CO<sub>2</sub> spectra

Figure 3.2 presents a slab model spectrum of CO<sub>2</sub> computed using the RADEX programme (van der Tak et al. 2007). A density of 10<sup>16</sup> cm<sup>-3</sup> was used to ensure close to LTE populations of all levels. A column density of 10<sup>16</sup> cm<sup>-2</sup> was adopted, close to the observed value derived by Salyk et al. (2011b), with a temperature of 750 K and linewidth of 1 km s<sup>-1</sup>. The transitions are labelled at the approximate location of their *Q*-branch. The spectrum shows that, due to the Fermi splitting of the bending and stretching modes, the 15 μm feature is very broad stretching from slightly shorter than 12 μm to slightly longer than 20 μm for the absorption in the Earth atmosphere. For astronomical sources, the lines between 14 and 16 μm are more realistic targets.

Two main emission features are seen in the spectrum. The strong feature around 4.3 μm is caused by the radiative decay of the 00<sup>0</sup>1 vibration level to the vibrational ground state. As a Σ – Σ transition this feature does not have a *Q*-branch, but the *R* and *P* branches are the brightest features in the spectrum in LTE at 750 K. The second strong feature is at 15 μm. This emission is caused by the radiative decay of the 01<sup>1</sup>0 vibrational state into the ground state. It also contains small contribution by the 02<sup>2</sup>0 → 01<sup>1</sup>0 and 03<sup>3</sup>0 → 02<sup>2</sup>0 transitions. This feature does have a *Q*-branch that has been observed both in absorption (Lahuis et al. 2006) and emission (Carr & Najita 2008; Pontoppidan et al. 2010). The CO<sub>2</sub> *Q*-branch is found to be narrow compared to the other *Q*-branches of HCN and C<sub>2</sub>H<sub>2</sub> measured in the same sources.

The narrowness is partly due to the fact that the CO<sub>2</sub> *Q*-branch is intrinsically narrower than the same feature for HCN. This is connected with the change in the rotational constant between the ground and excited vibrational states. A comparison between *Q*-branch profiles for CO<sub>2</sub> and HCN for two optically thin LTE models is presented in Fig. 3.3. The lighter HCN has a full width half maximum (FWHM) that is about 50% larger than that of CO<sub>2</sub>. The difference in the observed width of the feature is generally larger (Salyk et al. 2011b): the HCN feature is typically twice as wide as the CO<sub>2</sub> feature. Thus the inferred temperature from the CO<sub>2</sub> *Q*-branch from the observations is low compared to the temperature inferred from the HCN feature. The difference is amplified by the intrinsically narrower CO<sub>2</sub> *Q*-branch, making it more striking.





**Figure 3.2:** CO<sub>2</sub> slab model spectrum calculated with RADEX (van der Tak et al. 2007), each line in the spectrum is plotted separately. Slab model parameters are: density,  $10^{16} \text{cm}^{-3}$ ; column density of CO<sub>2</sub>,  $10^{16} \text{cm}^{-2}$ ; kinetic temperature, 750K and linewidth,  $1 \text{km s}^{-1}$ . For these densities, the level populations are close to local thermal equilibrium (LTE). Spectrum and label colour correspond to the colours in Fig. 3.1

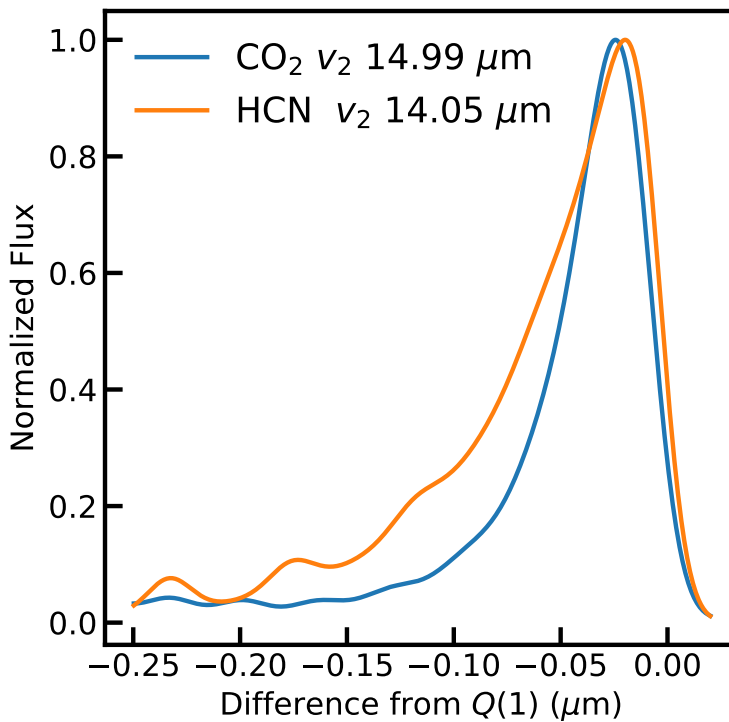


**Figure 3.3:**  $v_2$  Q-branch profile of CO<sub>2</sub> and HCN at a temperature of 400 K. Flux is plotted as function of the offset from the lowest energy line (wavelength given in the legend). The lines are convolved to a resolving power  $R=600$  appropriate for *Spitzer* data. The full width half maximum (FWHM) for CO<sub>2</sub> and HCN are 0.4 and 0.6  $\mu\text{m}$  respectively.

### 3.2.5 Dependence on kinetic temperature, density and radiation field

The excitation of, and the line emission from, a molecule depend strongly on the environment of the molecule, especially the kinetic temperature, radiation field and collisional partner density. In Fig. 3.4 slab model spectra of CO<sub>2</sub> for different physical parameters are compared. The dependence on the radiation field is modelled by including a blackbody field of 750 K diluted with a factor  $W$ :  $\langle J_\nu \rangle = WB_\nu(T_{\text{rad}})$  with  $T_{\text{rad}} = 750$  K. When testing the effects of the kinetic temperature and density, no incident radiation field is included ( $W = 0$ ).

Figure 3.4 shows that at a constant density of  $10^{12}$  cm<sup>-3</sup> the 4.3  $\mu\text{m}$  band is orders of magnitude weaker than the 15  $\mu\text{m}$  band. The 15  $\mu\text{m}$  band increases in strength and also in width, with increasing temperature as higher  $J$  levels of the CO<sub>2</sub>  $v_2$  vibrational mode can be collisionally excited. Especially the spectrum at 1000 K shows additional Q branches from transitions originating from the higher energy  $10^0(1)$  and  $10^0(2)$  vibrational levels at 14 and 16  $\mu\text{m}$ .

In the absence of a pumping radiation field, collisions are needed to populate the higher energy levels. With enough collisions, the excitation temperature becomes equal to the kinetic temperature. The density at which the excitation temperature of a level reaches the kinetic temperature depends on the critical density:  $n_c = A_{ul}/K_{ul}$  for a two-level system, where  $A_{ul}$  is the Einstein  $A$  coefficient from level  $u$  to level  $l$  and  $K_{ul}$  is the collisional rate coefficient between these levels. For densities below the critical density the radiative decay is much faster than the collisional excitation and de-excitation. This means that the line intensity scales as  $n/n_c$ . Above the critical density collisional excitation and de-excitation are fast: the intensity is then no longer dependent on the density. The critical density of the 15  $\mu\text{m}$  band is close to  $10^{12}$  cm<sup>-3</sup>, so there is little change in this band when increasing the density above this value. However, when decreasing the density below the critical value this results in a strong reduction of the band strength. The critical density of the 4.3  $\mu\text{m}$  feature is close to  $10^{15}$  cm<sup>-3</sup> so below this the lines are orders of magnitude weaker than would be expected from LTE.

Adding a radiation field has a significant impact on both the 4.3 and 15  $\mu\text{m}$  features. The radiation of a black body of 750 K peaks around 3.8  $\mu\text{m}$  so the 4.3  $\mu\text{m}$ /15  $\mu\text{m}$  flux ratio in these cases is larger than the flux ratio without radiation field for densities below the critical density of the 4.3  $\mu\text{m}$  lines. Another difference between the collisionally excited and radiatively excited states is that in the latter case vibrational levels that cannot be directly excited from the ground state by photons, such as the  $10^0(1)$  and  $10^0(2)$  levels, are barely populated at all.

## 3.3 CO<sub>2</sub> emission from a protoplanetary disk

To properly probe the chemistry in the inner disk from infrared line emission one needs to go beyond slab models with their inherent degeneracies. A protoplanetary disk model such as that used here includes more realistic geometries and contains a broad range of physical conditions constrained by observational data. Information can be gained on the location and extent of the emitting CO<sub>2</sub> region as well as the nature of the excitation process. By comparing with observational data, molecular abundances can be inferred as function of location. A critical aspect of the models is the infrared

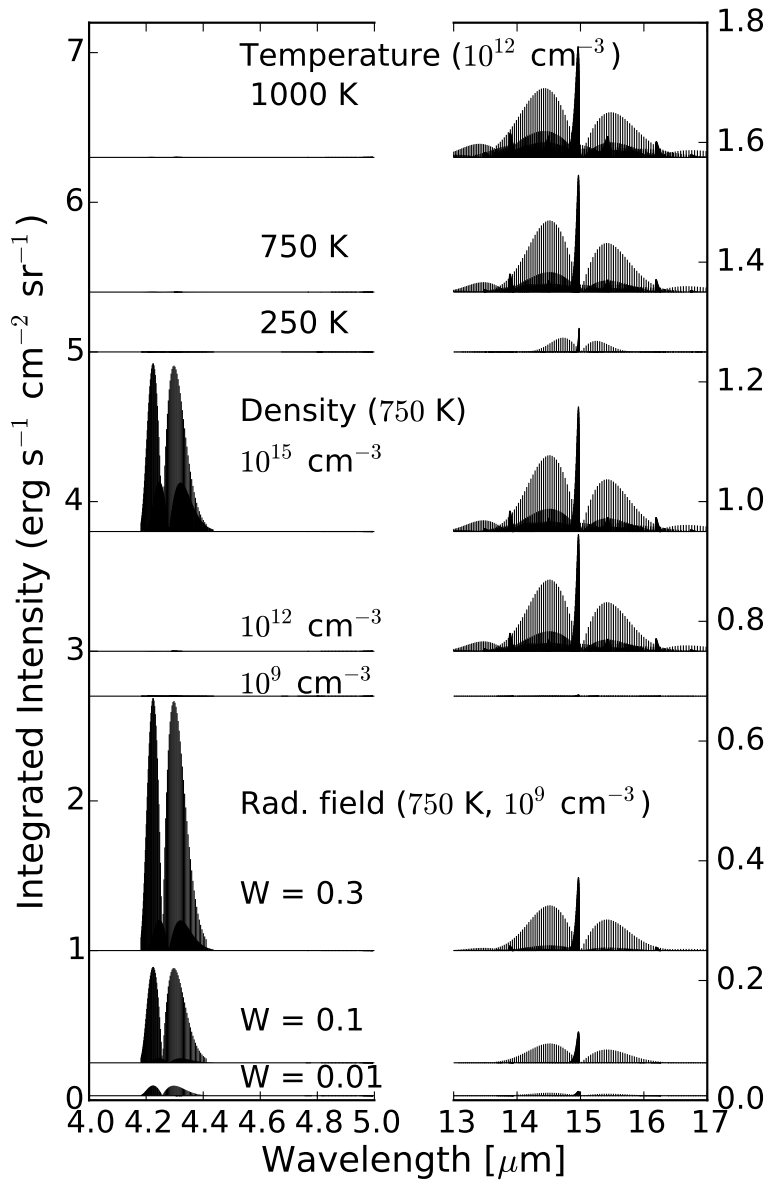


**Figure 3.4:** CO<sub>2</sub> slab model spectra for multiple kinetic temperatures, densities and radiation fields. For all the cases the CO<sub>2</sub> column density is kept at  $10^{16} \text{ cm}^{-2}$  and the intrinsic linewidth is set to  $1 \text{ km s}^{-1}$ . The spectra are offset for clarity. All spectra are calculated with RADEX (van der Tak et al. 2007).

continuum radiation field, which has to be calculated accurately throughout the disk. This means that detailed wavelength dependent dust opacities need to be included and dust temperatures have to be calculated on a very fine grid, since the pumping radiation can originate in a different part of the disk than the lines, for example, the near-infrared for close to the inner rim. The dust is also important in absorbing some of the line flux, effectively hiding parts of the disk from our view.

In this section, the CO<sub>2</sub> spectra are modelled using the DALI (Dust and Lines) code (Bruderer et al. 2012; Bruderer 2013). The focus is on emission from the 15 μm lines that have been observed with *Spitzer* and will be observable with *JWST*-MIRI. Trends in the shape of the  $v_2$  Q-branch and the ratios of lines in the P- and R-branches are investigated and predictions are presented. First the model and its parameters are introduced and the results of one particular model are used as illustration. Finally the effects of various parameters on the resulting line fluxes are shown, in particular source luminosity and gas/dust ratio. As in Bruderer et al. (2015), the model is based on the source AS 205 (N) but should be representative of a typical T-Tauri disk.

### 3.3.1 Model setup

Details of the full DALI model and benchmark tests are reported in Bruderer et al. (2012) and Bruderer (2013). Here we use the same parts of DALI as in Bruderer et al. (2015). The model starts with the input of a dust and gas surface density structure. The gas and dust structures are parametrized with a surface density profile

$$\Sigma(R) = \Sigma_c \left( \frac{R}{R_c} \right)^{-\gamma} \exp \left[ - \left( \frac{R}{R_c} \right)^{2-\gamma} \right] \quad (3.1)$$

and vertical distribution

$$\rho(R, \Theta) = \frac{\Sigma(R)}{\sqrt{2\pi}Rh(R)} \exp \left[ - \frac{1}{2} \left( \frac{\pi/2 - \Theta}{h(R)} \right)^2 \right], \quad (3.2)$$

with the scale height angle  $h(R) = h_c(R/R_c)^\psi$ . The values of the parameters for the AS 205 (N) disk are taken from Andrews et al. (2009) who fitted both the SED and submillimeter images simultaneously. As the inferred structure of the disk is strongly dependent on the dust opacities and size distribution, the same values from Andrews et al. (2009) are used. They are summarized in Table 3.2 and the gas density structure is shown in Fig. 3.5, panel *a*. The central star is a T-Tauri star with excess UV due to accretion. All the accretion luminosity is assumed to be released at the stellar surface as a 10<sup>4</sup> K blackbody. The density and temperature profile are typical for a strongly flared disk as used here. The temperature, radiation field and CO<sub>2</sub> excitation structure can be found in the appendix, Fig. 3.17.

In setting up the model special care was taken at the inner rim, where optical and UV photons are absorbed by the dust over a very short physical path. To properly get the temperature structure of the disk directly after the inner rim, high resolution in the radial direction is needed. Varying the radial width of the first cells showed that the temperature structure only converges when the cell width of the first handful of cells is smaller than the mean free path of the UV photons.

The model dust structure is irradiated by the star and the interstellar radiation field. A Monte-Carlo radiative transfer module calculates the dust temperature and

the local radiation field at all positions throughout the disk. The gas temperature is then assumed to be equal to the dust temperature. This is not true for the upper and outer parts of the disk. For the regions where  $\text{CO}_2$  is abundant in our models the difference between dust temperature and gas temperature computed by self-consistently calculating the chemistry and cooling is less than 5%. The excitation module calculates the  $\text{CO}_2$  level populations, using a 1+1D escape probability that includes the continuum radiation due to the dust (Appendix A.2 in Bruderer 2013). Finally the synthetic spectra are derived using the ray tracing module, which solves the radiative transfer equation along rays through the disk. The ray tracing module as presented in Bruderer et al. (2012) is used as well as a newly developed ray-tracing module that is presented in Appendix 3.B which is orders of magnitude faster, but a few percent less accurate. In the ray-tracing module a thermal broadening and turbulent broadening with FWHM  $\sim 0.2 \text{ km s}^{-1}$  is used, which means that thermal broadening dominates above  $\sim 40 \text{ K}$ . The gas is in Keplerian rotation around the star. This approach is similar to Meijerink et al. (2009) and Thi et al. (2013) for  $\text{H}_2\text{O}$  and  $\text{CO}$  respectively. However Thi et al. (2013) used a chemical network to determine the abundances, whereas here only parametric abundance structures are used to avoid the added complexity and uncertainties of the chemical network.

The adopted  $\text{CO}_2$  abundance is either a constant abundance or a jump abundance profile. The abundance throughout the paper is defined as the fractional abundance w.r.t  $n_{\text{H}} = n(\text{H}) + 2n(\text{H}_2)$ . The inner region is defined by  $T > 200 \text{ K}$  and  $A_V > 2 \text{ mag}$ , which is approximately the region where the transformation of  $\text{OH}$  into  $\text{H}_2\text{O}$  is faster than the reaction of  $\text{OH}$  with  $\text{CO}$  to form  $\text{CO}_2$ . The outer region is the region of the disk with  $T < 200 \text{ K}$  or  $A_V < 2 \text{ mag}$ , where the  $\text{CO}_2$  abundance is expected to peak. No  $\text{CO}_2$  is assumed to be present in regions with  $A_V < 0.5 \text{ mag}$  as photodissociation is expected to be very efficient in this region. The physical extent of these regions is shown in panel *b* of Fig. 3.5.

As shown by Meijerink et al. (2009) and Bruderer et al. (2015), the gas-to-dust ("G/D") ratio is very important for the resulting line fluxes as the dust photosphere can hide a large portion of the potentially emitting  $\text{CO}_2$ . Here the gas-to-dust ratio is changed in two ways, by increasing the amount of gas, or by decreasing the amount of dust. When the gas mass is increased and thus the dust mass kept at the standard value of  $2.9 \times 10^{-4} M_{\odot}$ , this is denoted by  $g/d_{\text{gas}}$ . If the dust mass is decreased and the gas mass kept at  $0.029 M_{\odot}$  this is denoted by  $g/d_{\text{dust}}$ .

### 3.3.2 Model results

Panel *c* of Fig. 3.5 presents the contribution function for one of the  $15 \mu\text{m}$  lines, the  $v_2 1 \rightarrow 0 Q(6)$  line. The contribution function shows the relative, azimuthally integrated contribution to the total integrated line flux. Contours show the areas in which 25% and 75% of the emission is located. Panel *c* also includes the  $\tau = 1$  surface for the continuum due to the dust, the  $\tau = 1$  surface for the  $v_2 1 \rightarrow 0 Q(6)$  line and surface where the density is equal to the critical density. The area of the disk contributing significantly to the emission is large, an annulus from approximately 0.7 to 30 AU. The dust temperature in the  $\text{CO}_2$  emitting region is between 100 and 500 K and the  $\text{CO}_2$  excitation temperature ranges from 100–300 K (see Fig. 3.17). The density is lower than the critical density at any point in the emitting area.

Panel *d* of Fig. 3.5 shows the contribution for the  $v_3 1 \rightarrow 0 R(7)$  line with the

**Table 3.2:** Adopted standard model parameters for the AS 205 (N) star plus disk.

Parameter		Value
Star		
Mass	$M_{\star} [M_{\odot}]$	1.0
Luminosity	$L_{\star} [L_{\odot}]$	4.0
Effective temperature	$T_{\text{eff}} [\text{K}]$	4250
Accretion luminosity	$L_{\text{accr}} [L_{\odot}]$	3.3
Accretion temperature	$T_{\text{accr}} [\text{K}]$	10000
Disk		
Disk Mass ( $g/d = 100$ )	$M_{\text{disk}} [M_{\odot}]$	0.029
Surface density index	$\gamma$	0.9
Characteristic radius	$R_c [\text{AU}]$	46
Inner radius	$R_{\text{in}} [\text{AU}]$	0.19
Scale height index	$\psi$	0.11
Scale height angle	$h_c [\text{rad}]$	0.18
Dust properties <sup>a</sup>		
Size	$a [\mu\text{m}]$	0.005 – 1000
Size distribution		$dn/da \propto a^{-3.5}$
Composition		ISM
Gas-to-dust ratio		100
Distance	$d [\text{pc}]$	125
Inclination	$i [^{\circ}]$	20

**Notes.** <sup>(a)</sup> Dust properties are the same as those used in Andrews et al. (2009) and Bruderer et al. (2015). Dust composition is taken from Draine & Lee (1984) and Weingartner & Draine (2001).

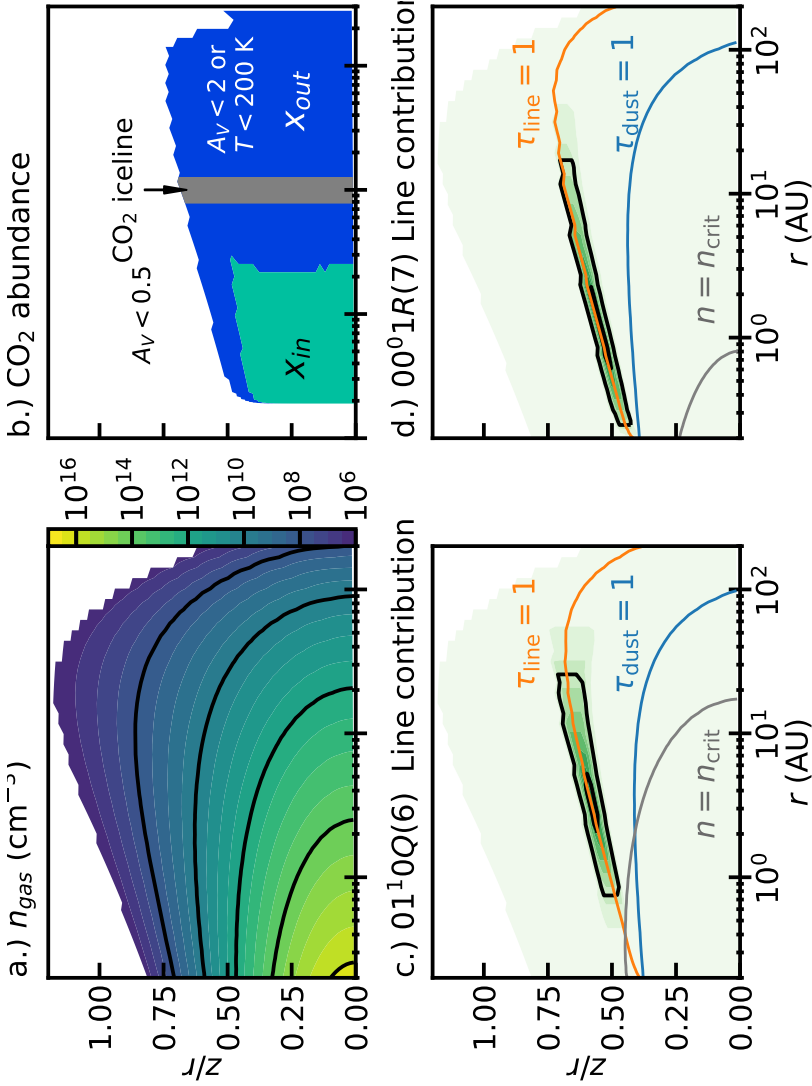


**Figure 3.5:** Overview of one of the DALI models showing the disk structure, abundance structure and emitting regions for the Q(6) 01<sup>1</sup><sub>0</sub> and R(7) 00<sup>0</sup><sub>1</sub> lines. The model shown has a gas-to-dust ratio,  $g/d_{\text{gas}} = 1000$  and a constant  $\text{CO}_2$  abundance of  $10^{-7}$  with respect to H. The panels show: (a) gas density structure; (b) abundance structure used models:  $x_{\text{in}}$  and  $x_{\text{out}}$  are the  $\text{CO}_2$  abundances in the inner and outer region respectively, the grey region is part of the outer region and denotes the region around the  $\text{CO}_2$  iceline where planetesimals are assumed to vaporize. The abundance in this region is varied in the models in Sec. 3.4.2; (c) line contribution function of the Q(6) 01<sup>1</sup><sub>0</sub> line at 15  $\mu\text{m}$ , the contours show the areas in which 25% and 75% of the total flux is emitted; (d) contribution function for the R(7) 00<sup>0</sup><sub>1</sub> line at 4.3  $\mu\text{m}$ . Panels c and d have the  $\tau = 1$  surface of dust (blue) and line (red) and the  $n = n_{\text{crit}}$  surface (black) overplotted for the relevant line.



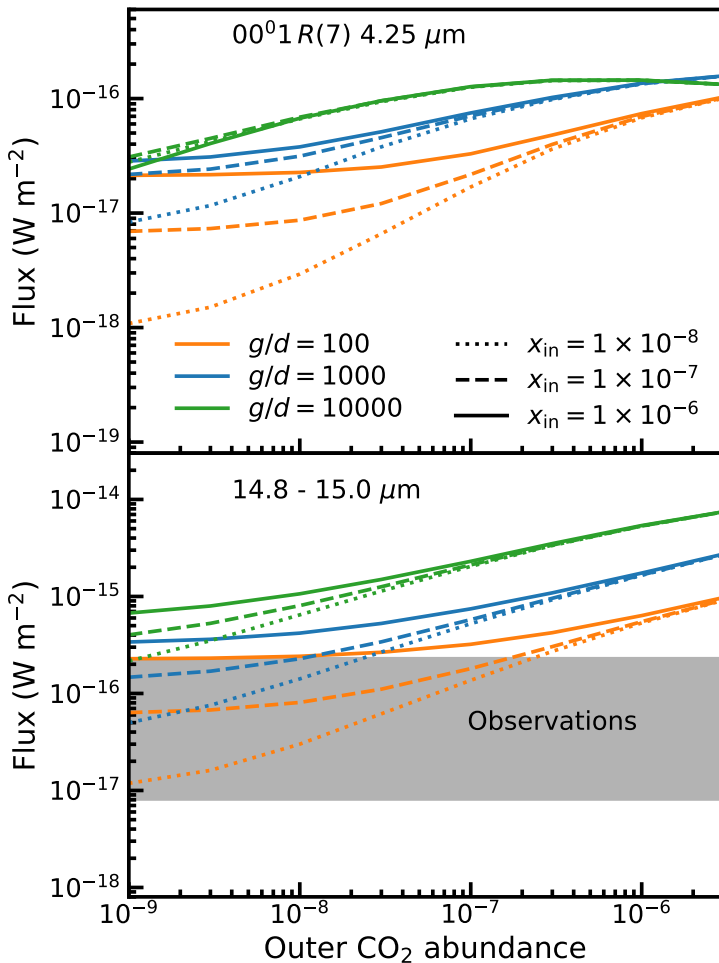


**Figure 3.6:** Line fluxes as functions of outer CO<sub>2</sub> abundances for models with constant dust mass ( $g/d_{gas}$ ) and varying gas/dust ratios. The upper panel shows the flux of the  $R(7)$  line from the fundamental asymmetric stretch band at 4.3 μm. The lower panel shows the flux contained in the 15 μm  $Q$ -branch feature. The grey region denotes the full range in CO<sub>2</sub> fluxes from the disks that are reported in Salyk et al. (2011b), scaled to the distance of AS 205 (N). The 15 μm feature contains the flux from multiple  $Q$ -branches with  $\Delta v_2 = 1$ . The CO<sub>2</sub> flux depends primarily on the outer CO<sub>2</sub> abundance and the total  $g/d$  ratio and does not strongly depend on the inner CO<sub>2</sub> abundances. Only for very low outer CO<sub>2</sub> abundances is the effect of the inner abundance on the line fluxes visible. The fluxes for models with  $g/d_{dust}$  are given in Fig. 3.18.

same lines and contours as panel *c*. The critical density for this line is very high,  $\sim 10^{15} \text{ cm}^{-3}$ . This means that except for the inner 1 AU near the mid-plane, the level population of the  $v_3$  level is dominated by the interaction of the molecule with the surrounding radiation field. The emitting area of the  $v_3 1 \rightarrow 0 R(7)$  line is smaller compared to that of the line at  $15 \mu\text{m}$ . The emitting area stretches from close to the sublimation radius up to  $\sim 10 \text{ AU}$ . The excitation temperatures for this line are also higher, ranging from 300–1000 K in the emitting region (see Fig. 3.17).

In Fig. 3.6 the total flux for the  $00^0_1 - 00^0_0 R(7)$  line at  $4.25 \mu\text{m}$  and the  $15 \mu\text{m}$  feature integrated from  $14.8$  to  $15.0 \mu\text{m}$  are presented as functions of  $x_{\text{out}}$ , for different gas-to-dust ratios and different  $x_{\text{in}}$ . The  $15 \mu\text{m}$  flux shows an increase in flux for increasing total  $\text{CO}_2$  abundance and gas-to-dust ratio and so does the line flux of the  $4.25 \mu\text{m}$  line for most of the parameter space. The total flux never scales linearly with abundance, due to different opacity effects. The dust is optically thick at infrared wavelengths up to  $100 \text{ AU}$ , so there will always be a reservoir of gas that will be hidden by the dust. The lines themselves are strong (have large Einstein  $A$  coefficients) and the natural line width is relatively small ( $0.2 \text{ km s}^{-1}$  FWHM). As a result the line centres of transitions with low  $J$  values quickly become optically thick. Therefore, if the abundance, and thus the column, in the upper layers of the disk is high, the line no longer probes the inner regions. This can be seen in Fig. 3.6 as the fluxes for models with different  $x_{\text{in}}$  converge with increasing  $x_{\text{out}}$ . Convergence happens at lower  $x_{\text{out}}$  for higher gas-to-dust ratios. The inner region is quickly invisible through the  $4.25 \mu\text{m}$  line with increasing gas-to-dust ratios: for a gas-to-dust ratio of 10000, there is a less than 50% difference in fluxes between the models with different inner abundances, even for the lowest outer abundances. This is not seen so strongly in the  $15 \mu\text{m}$  feature as it also includes high  $J$  lines which are stronger in the hotter inner regions and are not as optically thick as the low  $J$  lines. There is no significant dependence of the flux on the inner abundance of  $\text{CO}_2$  if the outer abundance is  $> 3 \times 10^{-7}$  and the gas to dust ratio is higher than 1000. In these models the  $15 \mu\text{m}$  feature traces part of the inner 1 AU but only the upper layers.

Different ways of modelling the gas-to-dust ratio has little effect on the resulting fluxes. Fig. 3.6 shows the fluxes for a constant dust mass and increasing gas mass for increasing the gas-to-dust ratio, whereas Fig. 3.18 in Appendix 3.D shows the fluxes for decreasing dust mass for a constant gas mass. The differences in fluxes are very small for models with the same gas/dust ratio times  $\text{CO}_2$  abundance, irrespective of the total gas mass: fluxes agree within 10% for most of the models. This reflects the fact that the underlying emitting columns of  $\text{CO}_2$  are similar above the dust  $\tau = 1$  surface. Only the temperature of the emitting gas changes: higher temperatures for gas that is emitting higher up in a high gas mass disk and lower temperatures for gas that is emitting deeper into the disk in a low dust mass disk.

The grey band in Fig. 3.6 and Fig. 3.18 shows the range of fluxes observed for protoplanetary disks scaled to a common distance of  $125 \text{ pc}$  (Salyk et al. 2011b). This figure immediately shows that low  $\text{CO}_2$  abundances,  $x_{\text{out}} < 3 \times 10^{-7}$ , are needed to be consistent with the observations. Some disks have lower fluxes than given by the lowest abundance model, which can be due to other parameters. A more complete comparison between model and observations is made in Sec. 3.4.1.

In Appendix 3.E a comparison is made between the fluxes of models with  $\text{CO}_2$  in LTE and models for which the excitation of  $\text{CO}_2$  is calculated from the rate coefficients and the Einstein  $A$  coefficients. The line fluxes differ by a factor of about three between

the models, similar to the differences found by Bruderer et al. (2015) (their Fig. 6) for the case of HCN.

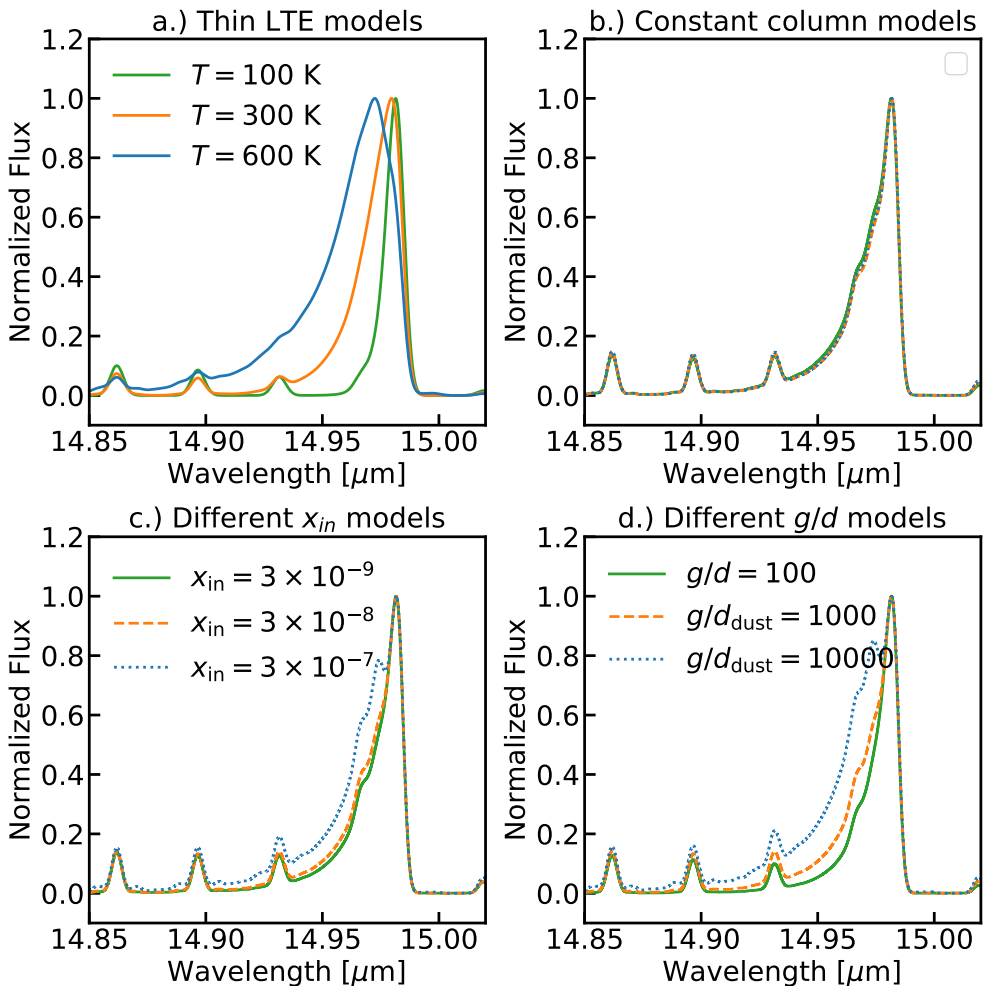
### The $v_2$ band emission profile

Figure 3.7 shows the  $v_2$   $Q$ -branch profile at 15  $\mu\text{m}$  for a variety of models. All lines have been convolved to the resolving power of *JWST*-MIRI at that wavelength ( $R = 2200$ , Rieke et al. 2015; Wells et al. 2015) with three bins per resolution element. Panel *a* shows the results from a simple LTE slab model at different temperatures whereas panels *b* and *c* presents the same feature from the DALI models. Panel *b* contains models with different gas-to-dust ratios and abundances (assuming  $x_{\text{in}} = x_{\text{out}}$ ) scaled so  $g/d \times x_{\text{CO}_2}$  is constant. It shows that gas-to-dust ratio and abundance are degenerate. It is expected that these models show similar spectra, as the total amount of CO<sub>2</sub> above the dust photosphere is equal for all models. The lack of any significant difference shows that collisional excitation of the vibrationally excited state is insignificant compared to radiative pumping. Panel *c* of Fig. 3.7 shows the effect of different inner abundances on the profile. For the highest inner abundance shown,  $1 \times 10^{-6}$ , an increase in the shorter wavelength flux can be seen, but the differences are far smaller than the differences between the LTE models. Panel *d* shows models with similar abundances, but with increasing  $g/d_{\text{dust}}$ . The flux in the 15  $\mu\text{m}$  feature increases with  $g/d_{\text{dust}}$  for these models as can be seen in Fig. 3.18. This is partly due to the widening of the feature as can be seen in Panel *d* which is caused by the removal of dust. Due to the lower dust photosphere it is now possible for a larger part of the inner region to contribute to this emission. The inner region is hotter and thus emits more towards high  $J$  lines causing the  $Q$ -branch to widen.

Fitting of LTE models to DALI model spectra in Fig. 7b-d results in inferred temperatures of 300–600 K. Only the models with a strong tail (blue lines in 7b and 7d) need temperatures of 600 K for a good fit, the other models are well represented with  $\sim 300$  K. For comparison, the actual temperature in the emitting layers is 150–350 K (Fig. 3.17), illustrating that the optically thin model overestimates the inferred temperatures. The proper inclusion of optical depth effects for the lower- $J$  lines lowers the inferred temperatures. This means that care has to be taken when interpreting a temperature from the CO<sub>2</sub> profile. A wide feature can be due to high optical depths or high rotational temperature of the gas.

A broader look at the CO<sub>2</sub> spectrum is thus needed. The left panel of Fig. 3.8 shows the  $P$ ,  $Q$  and  $R$ -branches of the vibrational bending mode transition at  $R = 2200$ , for models with different inner CO<sub>2</sub> abundances and the same outer abundance of  $10^{-7}$ . The shape for the  $R$ - and  $P$ -branches is flatter for low to mid- $J$  and slightly more extended at high  $J$  in the spectrum from the model with an inner CO<sub>2</sub> abundance of  $10^{-6}$  than the other spectra. The peaks at 14.4  $\mu\text{m}$  and 15.6  $\mu\text{m}$  are due to the  $Q$ -branches from the transitions between  $11^10(1) \rightarrow 10^01(1)$  and  $11^10(2) \rightarrow 10^01(2)$  respectively. These are overlapping with lines from the bending fundamental P and R branches. For the constant and low inner CO<sub>2</sub> abundances,  $10^{-7}$  and  $10^{-8}$  respectively  $R$ - and  $P$ -branch shapes are similar, with models differing only in absolute flux. Decreasing the inner CO<sub>2</sub> abundance from  $10^{-8}$  to lower values has no effect of the line strengths.

The right panel of Fig. 3.8 shows Boltzmann plots of the spectra on the left. The number of molecules in the upper state inferred from the flux is given as a function of the upper state energy. The number of molecules in the upper state is given by:  $\mathcal{N}_u =$



**Figure 3.7:** *Q*-branch profiles of different models shown at *JWST*-MIRI resolving power. All fluxes are normalized to the maximum of the feature. Panel a. shows LTE point models with a temperature of 200K (cyan), 400 K (red) and 800 K (blue). Panel b. shows DALI disk models with a constant abundance profile for which the product of abundance times gas-to-dust ratio is constant. All these models have very similar total fluxes. The models shown are  $g/d_{\text{gas}} = 100$ ,  $x_{\text{CO}_2} = 3 \times 10^{-7}$  in red;  $g/d_{\text{gas}} = 1000$ ,  $x_{\text{CO}_2} = 3 \times 10^{-8}$  in blue and  $g/d_{\text{gas}} = 10000$ ,  $x_{\text{CO}_2} = 3 \times 10^{-9}$  in cyan. The spectra are virtually indistinguishable. Panel c. shows DALI disk models with a jump abundance profile, a  $g/d_{\text{dust}} = 1000$ , an outer  $\text{CO}_2$  abundance of  $3 \times 10^{-8}$  and an inner abundance of  $3 \times 10^{-7}$  (red),  $3 \times 10^{-8}$  (blue),  $3 \times 10^{-9}$  (cyan). The model with the highest inner abundance shows a profile that is slightly broader than those of the other two. Panel d. shows DALI disk models with the same, constant abundance of  $x_{\text{CO}_2} = 3 \times 10^{-8}$ , but with different  $g/d_{\text{dust}}$  ratios. Removing dust from the upper layers of the disk preferentially boosts the high  $J$  lines in the tail of the feature as emission from the dense and hot inner regions of the disk is less occulted by dust.

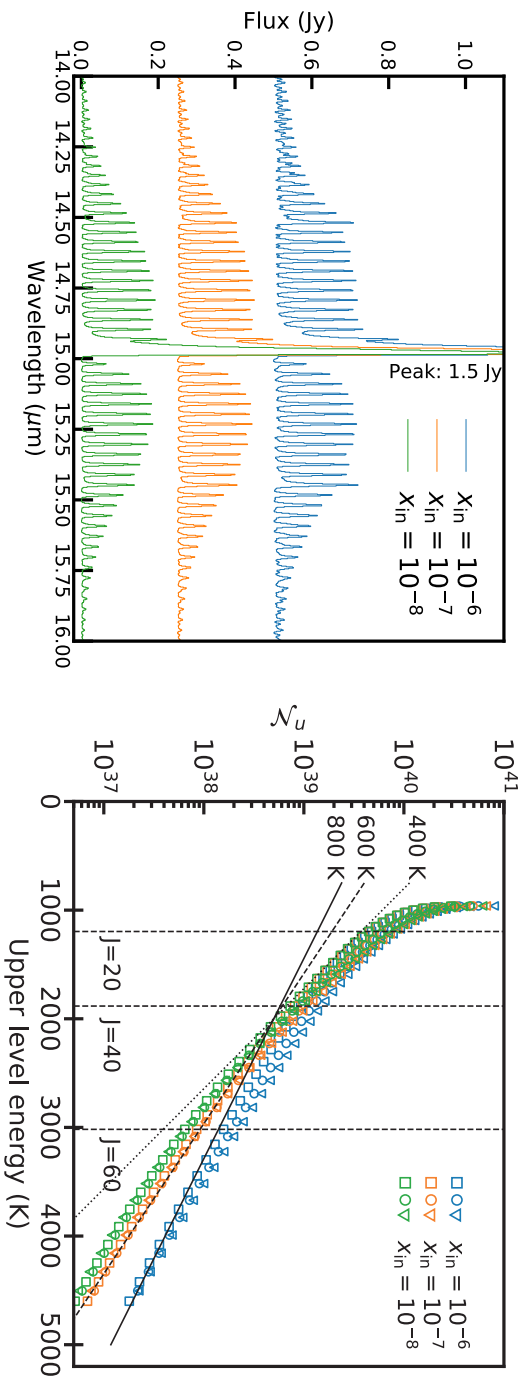


**Figure 3.8:** Left: Full disk spectra at *JWST*-MIRI resolving power ( $R=2200$ ) for three disk models with different inner CO<sub>2</sub> abundances. The outer CO<sub>2</sub> abundance is  $10^{-7}$  with  $g/d_{gas} = 1000$ . The models with an inner abundance of  $10^{-8}$  and  $10^{-7}$  are hard to distinguish, with very similar  $P$  and  $R$ -branch shapes. The spectrum of the model with high inner abundances of  $10^{-6}$  are flatter in the region from 14.6 to 14.9  $\mu\text{m}$  and the wings are also more extended leading to higher high to mid  $J$  line ratios. Right: Number of molecules in the upper state as function of the upper level energy inferred from the spectra on the left (Boltzmann plot). Inverse triangles denote the number of molecules inferred from  $P$ -branch lines, squares from  $Q$ -branch lines and circles from  $R$ -branch lines. Vertical dashed lines show the upper level energies of the  $J = 20, 40, 60, v_2 = 1$  levels. the black dotted, dashed and solid lines show the expected slope for a rotational excitation temperature of 400, 600 and 800 K respectively. The near vertical asymptote near upper level energies of 1000 K (the  $v_2 = 1$  rotational ground state energy) is due to the regions with large optical depths that dominate the emission from these levels. From around  $J = 20$  the curve flattens somewhat and between  $J = 20$  and  $J = 40$  the curve is well approximated by the theoretical curve for emission from a 400 K gas. At higher  $J$  levels, the model with the highest inner abundance starts to deviate from the other two models as inner and deeper region become more important for the total line emission. Above  $J = 60$  the models in with an inner abundance of  $10^{-8}$  and  $10^{-7}$  are well approximate with a 600 K gas, while the higher inner abundance model is better approximated with a 800 K gas.

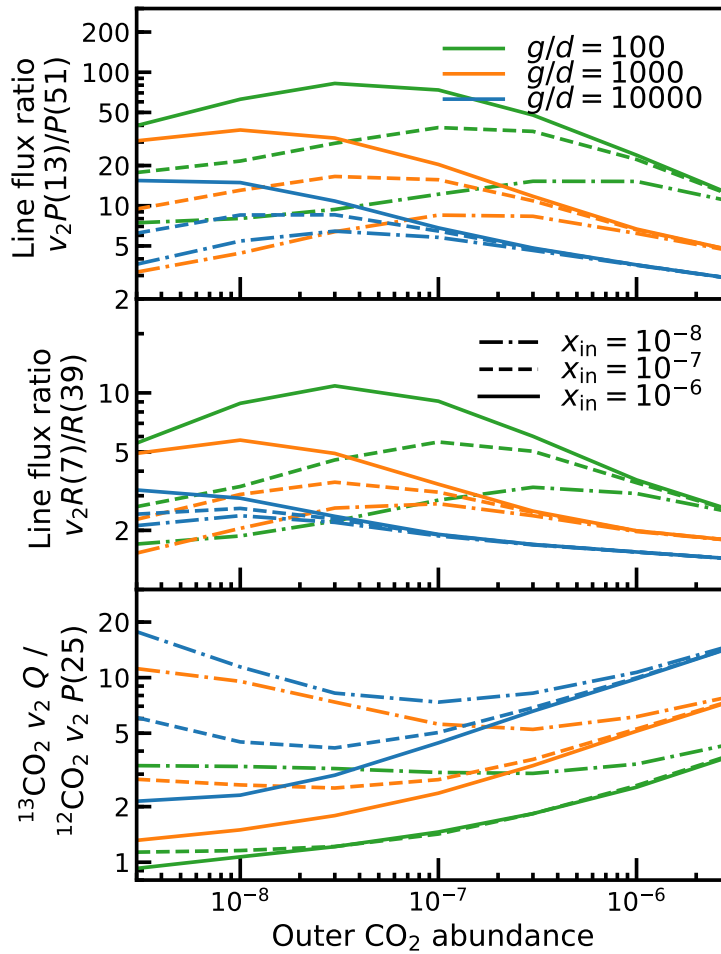


**Figure 3.9:** Line ratios as functions of outer abundance, inner abundance and gas to dust ratio ( $g/d_{gas}$ ). One line ratio in the P branch ( $P(15):P(51)$ ) (top panel), one line ratio in the R branch ( $R(7):R(39)$ ) (middle panel) of the  $01^1_0 \rightarrow 00^0_0$   $15 \mu\text{m}$  transition are shown together with the line ratio between the  $^{13}\text{CO}_2$  Q-branch and the neighbouring  $^{12}\text{CO}_2$  P(25) line. See the main text for more details.

$4\pi d^2 F / (A_{ul} h \nu_{ul} g_u)$ , with  $d$  the distance to the object,  $F$  the integrated line flux,  $g_u$  the statistical weight of the upper level and  $A_{ul}$  and  $\nu_{ul}$  the Einstein  $A$  coefficient and the frequency of the transition. From slope of  $\log(\mathcal{N}_u)$  vs  $E_{\text{up}}$  a rotational temperature can be determined. The expected slopes for 400, 600 and 800 K are given in the figure. It can be seen that the models do not show strong differences below  $J = 20$ , where emission is dominated by optically thick lines. Towards higher  $J$ , the model with  $x_{\text{in}} = 10^{-6}$  starts to differ more and more from the other two models. The models with  $x_{\text{in}} = 10^{-7}$  and  $x_{\text{in}} = 10^{-8}$  stay within a factor of two of each other up to  $J = 80$  where the molecule model ends.

Models with similar absolute abundances of CO<sub>2</sub> (constant  $g/d \times x_{\text{CO}_2}$ ) but different  $g/d_{\text{gas}}$  ratios are nearly identical: the width of the  $Q$ -branch and the shapes of the  $P$ - and  $R$ -branches are set by the gas temperature structure. This temperature structure is the same for models with different  $g/d_{\text{gas}}$  ratios as it is set by the dust structure. The temperature is, however, a function of  $g/d_{\text{dust}}$ , but those temperature differences are not large enough for measurable effects. From this it also follows that the exact collisional rate coefficients are not important: The density is low enough that the radiation field can set the excitation of the vibrational levels. At the same time the density is still high enough to be higher than the critical density for the rotational transitions, setting the rotational excitation temperature equal to the gas kinetic temperature.

The branch shapes are a function of  $g/d_{\text{dust}}$  at constant absolute abundance. Apart from the total flux which is slightly higher at higher  $g/d_{\text{dust}}$  (Fig. 3.18), the spectra are also broader (Panel d. Fig. 3.7). This is because the hotter inner regions are less occulted by dust for higher  $g/d_{\text{dust}}$  ratios. This hotter gas has more emission coming from high  $J$  lines, boosting the tail of the  $Q$ -branch.

To quantify the effects of different abundance profiles, line ratios can also be informative. The lines are chosen so they are free from water emission (see Appendix 3.F). The top two panels of Fig. 3.9 shows the line ratios for lines in the 01<sup>1</sup>0(1) → 00<sup>0</sup>0(1) 15 μm band:  $R(37) : R(7)$  and  $P(15) : P(51)$ . The  $R(7)$  and  $P(15)$  lines come from levels with energies close to the lowest energy level in the vibrational state (energy difference is less than 140 K). These levels are thus easily populated and the lines coming from these levels are quickly optically thick. The  $R(37)$  and  $P(51)$  lines come from levels with rotational energies at least 750 K above the ground vibrational energy. These lines need high kinetic temperatures to show up strongly and need higher columns of CO<sub>2</sub> at prevailing temperatures to become optically thick. From observation of Fig. 3.9 a few things become clear. First, for very high outer abundances, it is very difficult to distinguish between different inner abundances based on the presented line ratio. Second, models with high outer abundances are nearly degenerate with models that have a low outer abundance and a high inner abundance. A measure of the optical depth will solve this. In the more intermediate regimes the line ratios presented here or a Boltzmann plot will supplement the information needed to distinguish between a cold, optically thick CO<sub>2</sub> reservoir and a hot, more optically thin CO<sub>2</sub> reservoir that would be degenerate in just  $Q$ -branch fitting.

### <sup>13</sup>CO<sub>2</sub> $v_2$ band

An easier method to break these degeneracies is to use the <sup>13</sup>CO<sub>2</sub> isotopologue. <sup>13</sup>CO<sub>2</sub> is approximately 68 times less abundant compared to <sup>12</sup>CO<sub>2</sub>, using a standard local interstellar medium value (Wilson & Rood 1994; Milam et al. 2005). This means that

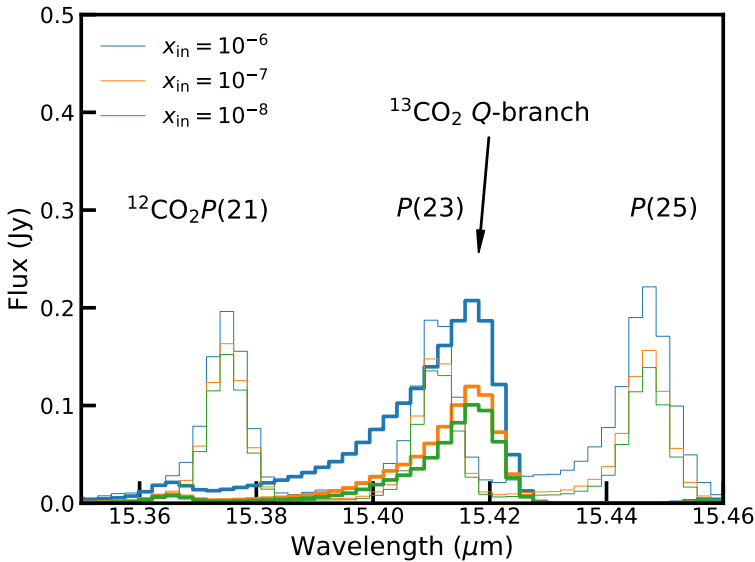


**Figure 3.10:** Zoom in of the spectra in Fig. 3.8 with added spectra of  $^{13}\text{CO}_2$  emission (thick lines). The  $^{13}\text{CO}_2$  Q-branch is more sensitive to higher inner abundances.

the isotopologue is much less likely to be optically thick and thus  $^{13}\text{CO}_2$ : $^{12}\text{CO}_2$  line ratios can be used as a measure of the optical depth, adding the needed information to lift the degeneracies. The bottom panel of Fig. 3.9 shows the ratio between the flux in the  $^{13}\text{CO}_2$   $v_2$  Q-branch and the  $^{12}\text{CO}_2$   $v_2$  P(25) line.

As the Q-branch for  $^{13}\text{CO}_2$  is less optically thick, it is also more sensitive to the abundance structure. The Q-branch, situated at  $15.42 \mu\text{m}$ , partially overlaps with the P(23) line of the more abundant isotopologue so both isotopologues need to be modelled to properly account for the contribution of these lines. Figure 3.10 shows the same models as in Fig. 3.8 but now with the  $^{13}\text{CO}_2$  emission in thick lines. The  $^{13}\text{CO}_2$  Q-branch is predicted to be approximately as strong as the nearby  $^{12}\text{CO}_2$  lines for the highest inner abundances. The total flux in the  $^{13}\text{CO}_2$  Q-branch shows a stronger dependence on the inner  $\text{CO}_2$  abundance than the  $^{12}\text{CO}_2$  Q-branch. A hot reservoir of  $\text{CO}_2$  strongly shows up as an extended tail of the  $^{13}\text{CO}_2$  Q-branch between  $15.38$  and  $15.40 \mu\text{m}$ .

### Emission from the $v_3$ band

The  $v_3$  band around  $4.25 \mu\text{m}$  is a strong emission band in the disk models, containing a larger total flux than the  $v_2$  band. Even so, the  $4.3 \mu\text{m}$  band of gaseous  $\text{CO}_2$  has not been seen in observations of *ISO* with the Short Wave Spectrometer (SWS) towards high mass protostars in contrast with the  $15 \mu\text{m}$  band that has been seen towards these sources in absorption (van Dishoeck et al. 1996; Boonman et al. 2003a). This may be largely due to the strong solid  $\text{CO}_2$   $4.2 \mu\text{m}$  ice feature obscuring the gas-phase lines for the case of protostars, but for disks this should not be a limitation. Fig. 3.11



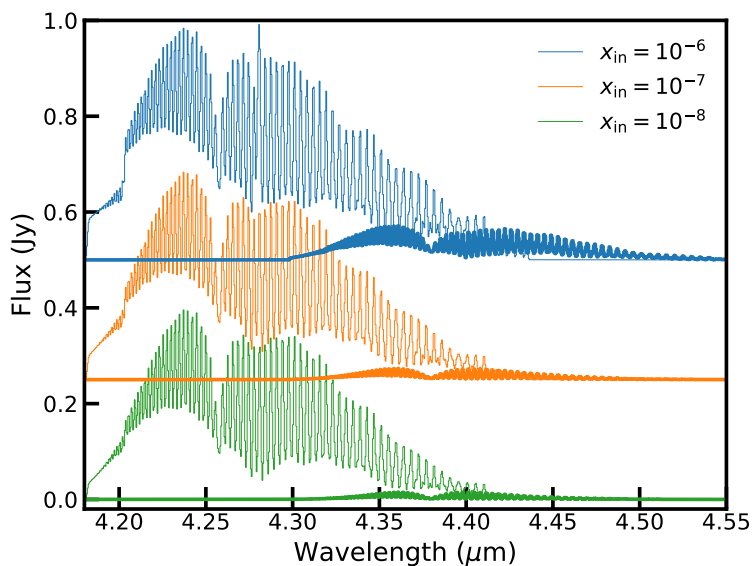


**Figure 3.11:** Full disk 4.3  $\mu\text{m}$  spectra at  $R=3000$  for three disk models with different inner CO<sub>2</sub> abundances. The outer  $^{12}\text{CO}_2$  abundance is  $10^{-7}$  with  $g/d_{gas} = 1000$ . Thin lines show the emission from  $^{12}\text{CO}_2$ , thick lines the emission from  $^{13}\text{CO}_2$ . For both isotopes individual line peaks can be seen but the lines blend together in the wings forming a single band. Spectra are shifted vertically for display purposes.

shows the spectrum of gaseous CO<sub>2</sub> in the  $v_3$  band around 4.3  $\mu\text{m}$  at *JWST*-NIRSpec resolving power. The resolving power of NIRSpec is taken to be  $R = 3000$ , which is not enough to fully separate the lines from each other. The CO<sub>2</sub> emission thus shows up as an extended band.

The band shapes in Fig. 3.11 are very similar. The largest difference is the strength of the 4.2  $\mu\text{m}$  discontinuity, which is probably an artefact of the model as only a finite number of  $J$  levels are taken into account. The total flux over the whole feature does depend on the inner abundance, but the difference is of the order of  $\sim 10\%$  for 2 orders of magnitude change of the inner abundance.

Figure 3.11 also shows the <sup>13</sup>CO<sub>2</sub> spectrum. The lines from <sup>13</sup>CO<sub>2</sub> are mostly blended with much stronger lines from <sup>12</sup>CO<sub>2</sub>. At the longer wavelength limit, <sup>13</sup>CO<sub>2</sub> lines are stronger than those of <sup>12</sup>CO<sub>2</sub> but there the 6  $\mu\text{m}$  water band and 4.7  $\mu\text{m}$  CO band start to complicate the detection of <sup>13</sup>CO<sub>2</sub> in the 4–5  $\mu\text{m}$  region.

Average abundances of CO<sub>2</sub> can be derived from observations of the 4.3  $\mu\text{m}$  band. While inferring the abundance structure will be easier from the 15  $\mu\text{m}$  band there are some observational advantages of using the 4.3  $\mu\text{m}$  band. NIRSpec has multi-object capabilities and will thus be able to get large samples of disks in a single exposure, especially for more distant clusters where there are many sources in a single FOV. NIRSpec has the additional advantages that it does not suffer from detector fringing and that it is more sensitive (NIRSpec pocket guide<sup>2</sup>, Rieke et al. 2015; Wells et al. 2015). As both the 4.3  $\mu\text{m}$  and 15  $\mu\text{m}$  bands are pumped by infrared radiation, the flux ratios between these two will mostly contain information about the ratio of the continuum radiation field between the wavelengths of these bands.

### 3.3.3 Line-to-continuum ratio

The line-to-continuum ratio is potentially an even better diagnostic of the gas/dust ratio than line ratios (Meijerink et al. 2009). In Fig. 3.12 we present spectra with the continuum added to it. The spectra have been shifted, as the continua for these models overlap. The models for which the spectra are derived all have a CO<sub>2</sub> abundance of  $10^{-8}$  but differ in the gas-to-dust ratio. The gas-to-dust ratio, determines the column of CO<sub>2</sub> that can contribute to the line. A large part of the CO<sub>2</sub> reservoir near the mid-plane cannot contribute due to the large continuum optical depth of the dust. It is thus not surprising that the line-to-continuum ratio is strongly dependant on the gas-to-dust ratio. The precise method for setting the gas-to-dust ratio (by increasing the amount of gas, or decreasing the amount of dust) does not really matter for the line-to-continuum ratio. It does matter for the absolute scaling of the continuum, which decreases if the amount of dust is decreased.

Meijerink et al. (2009) could constrain the gas-to-dust ratio from the data since there is an upper limit to the H<sub>2</sub>O abundance from the atomic O abundance. Here it is not possible to make a similar statement as CO<sub>2</sub> is not expected to be a major reservoir of either the oxygen or the carbon in the disk. On the contrary, from Fig. 3.6 it can be seen that with a gas-to-dust ratio of 100 an abundance of  $10^{-7}$  is high enough to explain the brightest of the observed line fluxes. The line-to-continuum ratios from the *Spitzer*-IRS spectra of 5–10% are also matched by the same models (see Fig. 3.13). External information such as can be obtained from H<sub>2</sub>O is needed to

---

<sup>2</sup><https://jwst.stsci.edu/>

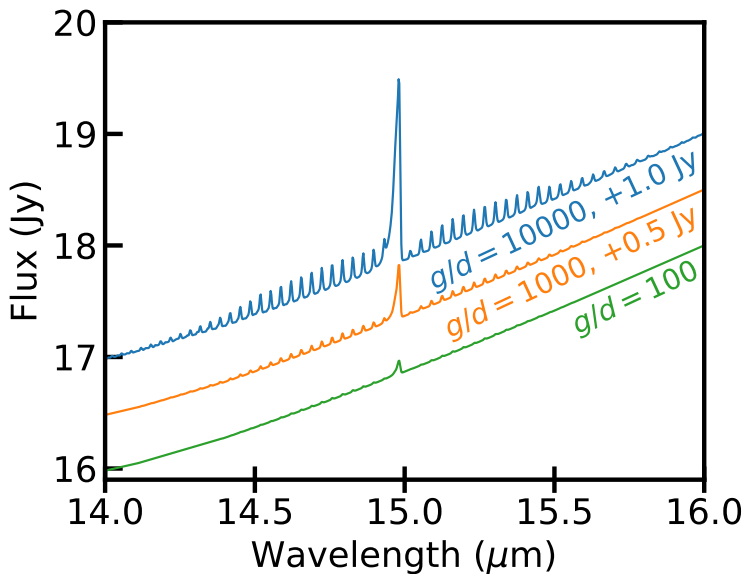


**Figure 3.12:** Full disk spectra with added continuum for models with different gas-to-dust ratios. All spectra have been convolved to a spectral resolving power of  $R = 2200$ . All models have the same CO<sub>2</sub> abundance of  $10^{-8}$ . The spectra have been shifted by the amount shown.

lift the degeneracy between high gas-to-dust ratio and high abundance: if one of the two is fixed, the other can be determined from the flux or line-to-continuum ratio.

The line-to-continuum ratio is very important for planning observations, however, as it sets the limit on how precisely the continuum needs to be measured to be able to make a robust line detection. Fig. 3.13 shows the line-to-continuum ratios for models with a constant abundance. These figures show that high signal-to-noise ( $S/N$ ) on the continuum is needed to be able to get robust line detections. The <sup>12</sup>CO<sub>2</sub> Q-branch should be easily accessible for most protoplanetary disks. To be able to probe individual P- and R-branch lines of the <sup>12</sup>CO<sub>2</sub> 15 μm feature as well as the <sup>13</sup>CO<sub>2</sub> Q-branch, deeper observations (reaching  $S/N$  of at least 300, up to 1000) will be needed to probe down to disks with CO<sub>2</sub> abundances of  $10^{-8}$  and gas-to-dust ratios of 1000.

### 3.3.4 CO<sub>2</sub> from the ground

As noted earlier, there is a large part of the CO<sub>2</sub> spectrum that cannot be seen from the ground because of atmospheric CO<sub>2</sub>. There are a few lines, however, that could be targeted from the ground using high spectral resolution. The high  $J$  lines ( $J > 70$ ) of the  $v_1 = 1 - 0$  transition in the R branch around 4.18 μm are visible with a resolving power of  $R = 30000$  or higher. At this resolution the CO<sub>2</sub> atmospheric lines are resolved and at  $J > 70$  they are narrow enough to leave 20 – 50% transmission

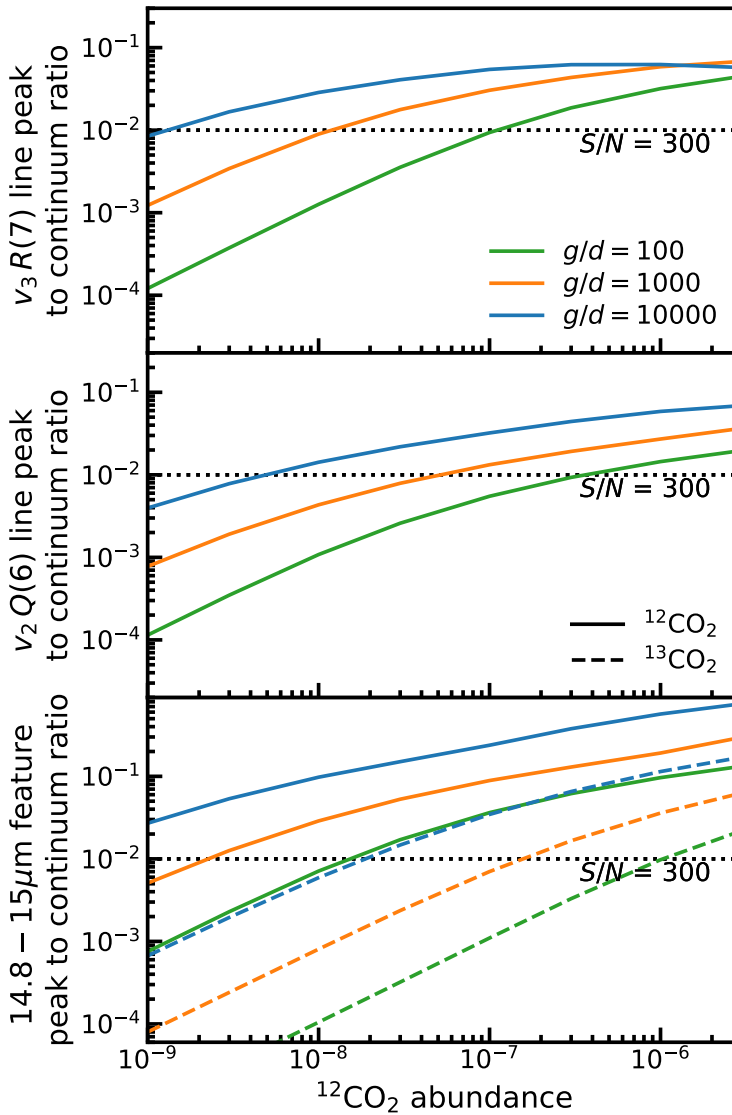


**Figure 3.13:** Line-to-continuum for  $^{12}\text{CO}_2$  as function of abundance for different gas-to-dust ratios in solid lines. In the bottom plot the line-to-continuum for  $^{13}\text{CO}_2$   $Q$ -branch is shown in dashed lines. A dotted black line shows a line-to-continuum of 0.01, lines with this line-to-continuum ratio can be observed if the signal-to-noise ( $S/N$ ) on the continuum is more than 300. With a  $S/N$  on the continuum of 300, observations of the  $Q$ -branch should be able to probe down to  $10^{-9}$  in abundance for a gas-to-dust ratio of 1000. With similar gas-to-dust ratio and  $S/N$ , individual lines the  $15\ \mu\text{m}$  band will only be observable in disk with  $\text{CO}_2$  abundances higher than  $3 \times 10^{-8}$ .

windows between them (ESO skycalc<sup>3</sup>). The lines are expected to have a peak line-to-continuum ratio of 1:100. So a  $S/N$  of 10 on the line peak translates to a  $S/N$  of 1000 on the continuum. The FWHM of the atmospheric lines is about  $30 \text{ km s}^{-1}$ . So half of the emission line profile should be observable when the relative velocity shift between observer and source is more than  $15 \text{ km s}^{-1}$ . Since the Earth's orbit allows for velocity shifts up to  $30 \text{ km s}^{-1}$  in both directions, observing the full line profile is possible in two observations at different times of year for sources close to the orbital plane of the earth. The exposure time needed to get a  $S/N$  of 1000 on the continuum at  $4.18 \mu\text{m}$ , which is  $6.7 \text{ Jy}$  in our AS 205 (N) model, with a 40% sky transmission on the lines, is about ten hours for VLT-CRIRES<sup>4</sup>. The high  $J$   $P$ -branch lines of CO<sub>2</sub> are close to atmospheric lines from N<sub>2</sub>O, O<sub>3</sub> and H<sub>2</sub>O resulting in a very opaque atmosphere at these wavelengths (Noll et al. 2012; Jones et al. 2013).

The other lines that can be seen from the ground are between  $9$  and  $12 \mu\text{m}$  (in the N band). These originate from the  $01^1_1$  and  $00^0_1$  levels. The line to continuum ratios vary from 1:40 to 1:3000 for the brighter lines in the  $00^0_1 \rightarrow 10^0_0(1)$  band with the most likely models having line to continuum ratios between 1:200 and 1:2000. For a continuum of  $\sim 11 \text{ Jy}$  a  $S/N$  of 2000 for  $R = 10^5$  could potentially be achieved in about three to ten minutes of integration with the European Extremely Large Telescope (E-ELT). At the location of the CO<sub>2</sub> atmospheric absorption lines in this part of the spectrum the sky transmittance is  $\sim 50\%$  and the atmospheric lines have a FWHM of  $\sim 50 \text{ km s}^{-1}$ .

### 3.3.5 CO<sub>2</sub> model uncertainties

The fluxes derived from the DALI models depend on the details of the CO<sub>2</sub> excitation processes included in the model. The collisional rate coefficients are particularly uncertain, since the measured set is incomplete. There are multiple ways to extrapolate what is measured to what is needed to complete the model. Modelling slabs of CO<sub>2</sub> using different extrapolations such as: absolute scaling of the rotational collision rate coefficients, including temperature dependence of the vibrational collisional rate coefficients and different implementations of the collision rate coefficients between the vibrational levels with  $2v_1 + v_2 = \text{constant}$ , show that fluxes can change by up to 50% for specific combinations of radiation fields and densities. The highest differences are seen in the  $4\text{--}5 \mu\text{m}$  band, usually at low densities. The flux in the  $15 \mu\text{m}$  band usually stays within 10% of the flux of the model used here. These uncertainties are small compared to other uncertainties in disk modelling such as the chemistry or parameters of the disk hosting protostar. The main reason that the fluxes are relatively insensitive to the details of the collisional rate coefficients is due to the importance of radiative pumping in parallel with collisions.

The assumption  $T_{\text{dust}} = T_{\text{gas}}$  is not entirely correct, since the gas temperature can be up to 5% higher than the dust temperature in the CO<sub>2</sub> emitting regions. This affects our line fluxes. For the  $4.3 \mu\text{m}$  fluxes the induced difference in flux is always smaller than 10%. For the  $15 \mu\text{m}$  fluxes difference are generally smaller than 10%, whereas some of the higher  $J$  lines are up to 25% brighter.

A very simplified abundance structure was taken. It is likely that protoplanetary

<sup>3</sup><http://www.eso.org/observing/etc/bin/gen/form?INS.MODE=swspectr+INS.NAME=SKYCALC>

<sup>4</sup>Exposure times have been calculated with the ESO exposure time calculator <https://www.eso.org/observing/etc/> for CRIRES (version 5.0.1)

disks will not have the abundance structure adopted here. Full chemical models indeed show much more complex chemical structures (see e.g. Walsh et al. 2015). The analysis carried out in this work here should still be appropriate for more complex abundance structures, and future work will couple such chemistry models directly with the excitation and radiative transfer.

The stellar parameters for the central star and the exact parameters of the protoplanetary disk also influence the resulting CO<sub>2</sub> spectrum. The central star influences the line emission through its UV radiation that can both dissociate molecules and heat the gas. Since for our models no chemistry is included, only the heating of the dust by stellar radiation is important for our models. The CO<sub>2</sub> flux in the emission band around 15  $\mu\text{m}$  scales almost linearly with the bolometric luminosity of the central object (see Fig. 3.14).

## 3.4 Discussion

### 3.4.1 Observed 15 $\mu\text{m}$ profiles and inferred abundances

The  $v_2$  15  $\mu\text{m}$  feature of CO<sub>2</sub> has been observed in many sources with *Spitzer-IRS* (Pontoppidan et al. 2010; Salyk et al. 2011b). The SH (Short-High) mode barely resolves the 15  $\mu\text{m}$   $Q$ -branch, but that is enough to compare with the models. We used the spectra that have been reduced with the Caltech High-res IRS pipeline (CHIP) (Pontoppidan et al. 2010; Pontoppidan 2016). The sources selected out of the repository have a strong emission feature of CO<sub>2</sub> but no distinguishable H<sub>2</sub>O emission in the 10–20  $\mu\text{m}$  range. The sources and some stellar parameters are listed in Table 3.3. The observed spectra are continuum subtracted (Appendix 3.G) and the observed profiles are compared with model profiles by eye (Fig. 3.15).

Two sets of comparisons are made. For the first set, the model fluxes are only corrected for the distance to the objects. For the other set, the model fluxes are scaled for the distance but also scaled for the luminosity of the central source, using  $L_{\text{CO}_2} \propto L_*$ . This relation is found by running a set of models with a range of luminosities, presented in Fig. 3.14. Aside from the luminosity of the star, all other parameters have been kept the same including the shape of the stellar spectrum. The effective temperature of the star mostly affects the fraction of short wavelength UV photons which can photodissociate molecules, but since no detailed chemistry is included, the use of a different stellar temperature would not change our results. Other tests (not shown here) have indeed shown that the shape of the spectrum does not really matter for the CO<sub>2</sub> line fluxes in this parametric model. All models have a gas-to-dust ratio of 1000 and a constant CO<sub>2</sub> abundance of  $10^{-8}$ .

Both the total flux in the range between 14.7 and 15.0  $\mu\text{m}$  and that of a single line in this region (the 01<sup>1</sup>0  $Q(6)$  line) have an almost linear relation with luminosity of the central star. For the 00<sup>0</sup>1  $R(7)$  line around 4.3  $\mu\text{m}$  the dependence on the central luminosity is slightly more complex. Below a stellar luminosity of  $1 L_\odot$  the dependence is stronger than linear, but above that the dependence becomes weaker than linear. Overall, it is reasonable to correct the 15  $\mu\text{m}$  fluxes from our model for source stellar luminosities using the linear relationship. This is because the amount of infrared continuum radiation that the disk produces scales linearly with the amount of energy that is put into the disk by the stellar radiation. It is the infrared continuum radiation that sets the molecular emission due to radiative pumping, the dominant

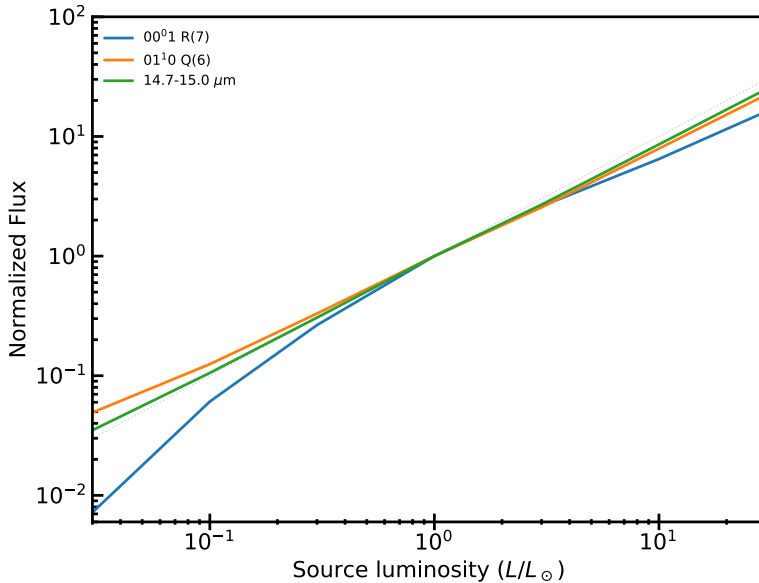


**Figure 3.14:** CO<sub>2</sub> flux versus stellar luminosity for three different features in the spectrum. All fluxes have been normalized to the flux of the 1  $L_{\odot}$  model. Both the flux in the 14.7 to 15  $\mu\text{m}$  region, which corresponds to the  $v_2$  Q-branch, and the flux from the 01<sup>1</sup>0 Q(6) line have a nearly linear dependence on the stellar luminosity. The dependence of the 00<sup>0</sup>1 R(7) line at 4.3  $\mu\text{m}$  on source luminosity is more complex.

vibrational excitation mechanism for CO<sub>2</sub>.

The model spectra are overplotted on the continuum subtracted observations in Fig. 3.15. The flux in these models has been scaled with the distance of the source and the luminosity of the central star. A gas-to-dust ratio of 1000 is adopted as inferred from H<sub>2</sub>O observations (Meijerink et al. 2009).

An overview of the inferred abundances is given in Table 3.4. For the DALI models the emitting CO<sub>2</sub> column and the number of emitting CO<sub>2</sub> molecules have been tabulated in Table 3.4. The column is defined as the column of CO<sub>2</sub> above the  $\tau_{\text{dust}} = 1$  line at the radial location of the peak of the contribution function (Fig. 3.5d). The number of molecules is taken over the region that is responsible for half the total emission as given by the contribution function. The number of molecules shown is thus the minimum amount of CO<sub>2</sub> needed to explain the majority of the flux and a sets lower limit for the amount of CO<sub>2</sub> needed to explain all of the emission. The inferred abundances range from  $10^{-9} - 10^{-7}$ . They agree with that inferred by Pontoppidan & Blevins (2014) using an LTE disk model appropriate for the RNO 90 disk, demonstrating that non-LTE excitation effects are minor (see also Appendix 3.E).

For GW Lup and SZ 50 the emitting CO<sub>2</sub> columns found by Salyk et al. (2011b) are within a factor of two from those inferred here, whereas for DN Tau and IM Lup our inferred columns are consistent with the upper limits from the slab models (tabulated in Table 3.4). However, the inferred column for HD101412 differs greatly. For all disks the number of molecules in our models is at least an order of magnitude higher than the number of molecules inferred from the LTE models. The emitting area used by

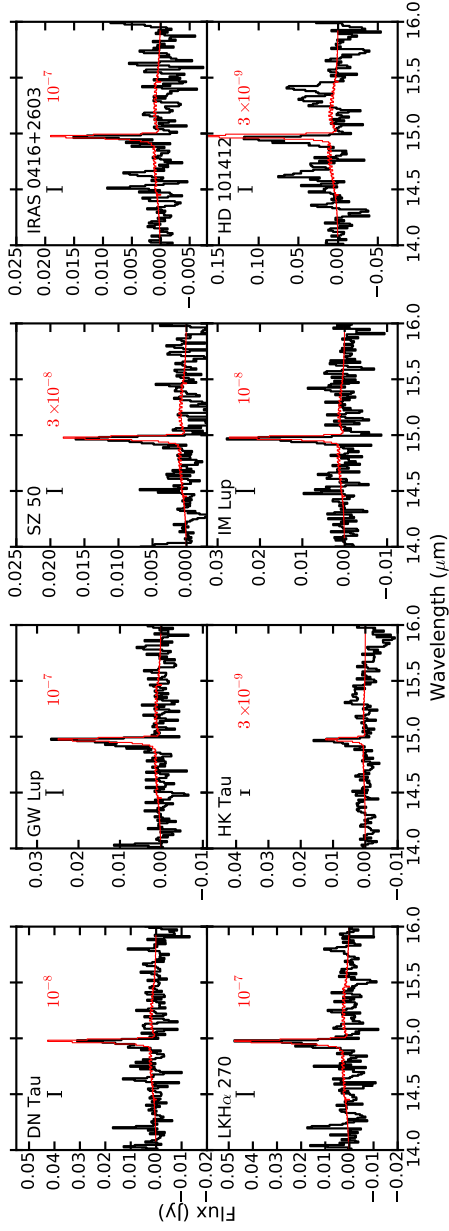


**Figure 3.15:** Continuum subtracted spectra (black) with DALI  $\text{CO}_2$  emission models (red) for the eight selected sources. The abundance used in the DALI model is given in each frame, taken to be constant over the whole disk. The line fluxes have been corrected for the distances to the sources. The errorbar in the top left corner of each panel shows the median errorbar on the data.



**Table 3.3:** Stellar parameters.

Object	Source luminosity ( $L_{\odot}$ )	Spectral type	Stellar mass ( $M_{\odot}$ )	Distance (pc)	Ref.
DN Tau	1.62	M0	0.62	140	[1]
GW Lup/Sz 71	0.3	M1.5	0.42	150	[1]
SZ50	0.57	M4	0.27	178	[3]
IRAS 04216+2603	0.2	M0	0.57	140	[1], [4]
LkH $\alpha$ 270	1.4	K2	?	235	[5]
HK Tau	1.12	M0.5	0.56	140	[1]
IM Lup/Sz 82	3.53	M0	0.56	190	[1]
HD101412	25	A0	2.3	160	[6]

**Notes.** [1]Rigliaco et al. (2015), [2] Alcalá et al. (2014), [3] Manara et al. (2016a), [4] Andrews et al. (2013), [5] Winston et al. (2010), [6] van der Plas et al. (2008)

Salyk et al. (2011b) in fitting the CO<sub>2</sub> feature was fixed and generally taken to be slightly larger than the inner 1 AU. This is very small compared to the emitting area found in this work which extends up to 30 AU. It is thus unsurprising that the total number of CO<sub>2</sub> molecules inferred is lower for the LTE slab models from Salyk et al. (2011b). The high number of molecules needed for the emission in our models is also related to the difference in excitation: the vibrational excitation temperature of the gas in the non-LTE models is lower (100–300 K) than the temperature fitted for the LTE models ( $\sim 650$  K). Thus in the non-LTE models a larger number of molecules is needed to get the same total flux. The narrow CO<sub>2</sub> profile is due to low rotational temperatures as emission from large radii  $> 2$ –10 AU dominates the strongest lines. The visual contrast is enhanced by the fact that the CO<sub>2</sub> feature is also intrinsically narrower at similar temperatures than that of HCN (Fig. 3.3). For HD 101412 the model feature is notably narrower than the observed feature signifying either a higher CO<sub>2</sub> rotational temperature, or a more optically thick emitting region.

There are of course caveats in the comparisons done here. The standard model uses a T-Tauri star that is luminous (total luminosity of  $7.3 L_{\odot}$ ) and that disk is known to have very strong H<sub>2</sub>O emission. The sample of comparison protostars consists of 7 T-Tauri stars that have luminosities a factor of 2 – 35 lower than assumed in our model and a Herbig Ae star that is more than three times as luminous. A simple correction for source luminosity is only an approximation. All of these sources have little to no emission lines of H<sub>2</sub>O in the mid-infrared. This may be an indication of different disk structures, and the disk model used in this work may not be representative of these water-rich disks. Indeed, Banzatti & Pontoppidan (2015) found that the emitting radius of the CO ro-vibrational lines scales inversely with the vibrational temperature inferred from the CO emission. This relation is consistent with inside-out gap opening. Comparing the CO ro-vibrational data with H<sub>2</sub>O infrared emission data from VLT-CRIRES and Spitzer-IRS Banzatti et al. (2016) found that there is a correlation between the radius of the CO ro-vibrational emission and the strength of the water emission lines: The larger the radius of the CO emission, the weaker the H<sub>2</sub>O emission. This suggests that the H<sub>2</sub>O-poor sources may also have inner gaps, where both CO and H<sub>2</sub>O are depleted. There are only two H<sub>2</sub>O-poor sources in our sample that overlap with Banzatti et al. (2016).

However, if our analysis is applied to sources that do have water emission, the range of best-fit CO<sub>2</sub> abundances is found to be similar. Figure G.2 shows CO<sub>2</sub> model spectra compared to observations for a set of the strongest water emitting sources. The conclusion that the abundance of CO<sub>2</sub> in protoplanetary disks is around 10<sup>-8</sup> is, therefore, robust.

The inferred CO<sub>2</sub> abundances are low, much lower than the expected ISM value of 10<sup>-5</sup> if all of the CO<sub>2</sub> would result from sublimated ices. This demonstrates that the abundances have been reset by high temperature chemistry, as also concluded by Pontoppidan & Blevins (2014).

The inferred low abundances agree well with chemical models by Walsh et al. (2015). However, the column found for chemical models by Agúndez et al. (2008),  $\sim 6 \times 10^{16} \text{ cm}^{-2}$ , is more than an order of magnitude higher. Agúndez et al. (2008) used a different lower vertical bound for their column integration and only considered the inner 3 AU. Either of these assumptions may explain the difference in the CO<sub>2</sub> column.

### 3.4.2 Tracing the CO<sub>2</sub> iceline

One of the new big paradigms in (giant) planet formation is pebble accretion. Pebbles, in models defined as dust particles with a Stokes number around one, are badly coupled to the gas, but generally not massive enough to ignore the interaction with the gas. This means that these particles settle to the mid-plane and radially drift inward on short time scales. This pebble flux allows in theory a planetesimal to accrete all the pebbles that form at radii larger than its current location (Ormel & Klahr 2010; Lambrechts & Johansen 2012; Levison et al. 2015).

This flux of pebbles also has consequences for the chemical composition of the disk. These pebbles should at some point encounter an iceline, if they are not stopped before. At the iceline they should release the corresponding volatiles. The same holds for any drifting planetesimals (Ciesla & Cuzzi 2006). As the ice composition is very different from the gas composition, this can in principle strongly change the gas content in a narrow region around the ice line. For this effect to become observable in mid-infrared lines, the sublimated ices should also be mixed vertically to higher regions in the disk.

From chemical models the total gas-phase abundance of CO<sub>2</sub> around the CO<sub>2</sub> iceline is thought to be relatively low, (10<sup>-8</sup>, Walsh et al. 2015) similar to the value found in this work. The CO<sub>2</sub> ice content in the outer disk can be orders of magnitude higher. Both chemical models and measurements of comets show that the CO<sub>2</sub> content in ices can be more than 20% of the total ice content (Le Roy et al. 2015; Eistrup et al. 2016), with CO<sub>2</sub> ice even becoming more abundant than H<sub>2</sub>O ice in some models of outer disk chemistry (Drozdovskaya et al. 2016). This translates into an abundance up to a few  $\times 10^{-5}$ . Here, we investigate whether the evaporation of these CO<sub>2</sub> ices around the iceline would be observable.

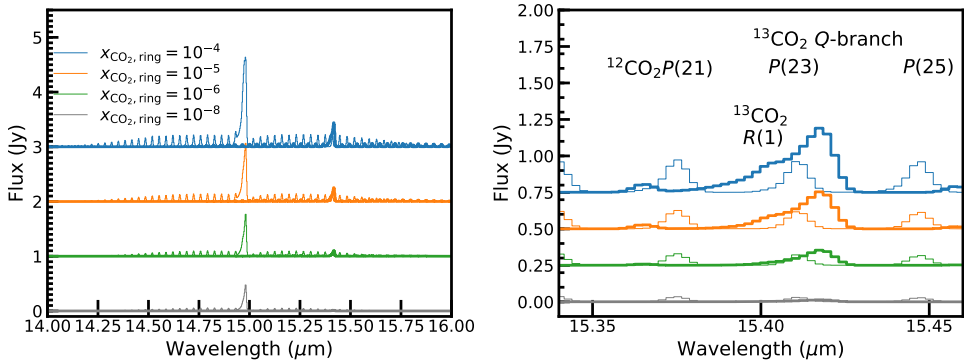
To model the effect of pebbles moving over the iceline, a model with a constant CO<sub>2</sub> abundance of  $1 \times 10^{-8}$  and a gas-to-dust ratio of 1000 is taken. In addition, the abundance of CO<sub>2</sub> is enhanced in an annulus where the midplane temperature is between 70 K and 100 K (grey region in Fig. 3.5b), corresponding to the sublimation temperature of pure CO<sub>2</sub> ice (Harsono et al. 2015). This results in a radial area between 8 and 15 AU in our case. The abundance is taken to be enhanced over the total vertical extent of the CO<sub>2</sub> in the model, as in the case of strong vertical mixing.

Table 3.4: Inferred CO<sub>2</sub> abundances from Spitzer data

Object	Inferred abundance (w.r.t H)			Salyk et al. (2011b)		LTE slab results		DALI Non-LTE results	
	$d$	corr.	$d$ and $L_*$	Column (cm <sup>-2</sup> )	$N_{\text{tot,CO}_2}$ (mol.)	Column (cm <sup>-2</sup> )	$N_{\text{tot,CO}_2}$ (mol.) <sup>a</sup>	Column (cm <sup>-2</sup> )	$N_{\text{tot,CO}_2}$ (mol.) <sup>a</sup>
DN Tau	1(-9)		1(-8)	< 5.0(14)	< 3.8(41)	2(14)	2(44)	2(14)	2(44)
GW Lup	1(-9)		1(-7)	1.5(15)	1.1(42)	2(15)	8(44)	2(15)	8(44)
SZ50	1(-9)		3(-8)	1.0(15)	7.6(41)	7(14)	5(44)	7(14)	5(44)
IRAS 04216+2603	< 1(-9)		1(-7)	-	-	2(15)	8(44)	2(15)	8(44)
LkH $\alpha$ 270	0.3-1(-8)		1(-7)	3.9(15)	4.1(42)	2(15)	8(44)	2(15)	8(44)
HK Tau	< 1(-9)		3(-9)	-	-	5(13)	1(44)	5(13)	1(44)
IM Lup	1-3(-9)		1(-8)	< 7.9(14)	< 6.9(41)	2(14)	2(44)	2(14)	2(44)
HD 101412	1(-8)		1-3(-9)	1.0(16)	1.94(43)	2-5(13)	0.7-1(44)	2-5(13)	0.7-1(44)

Notes.  $a(b) = a \times 10^b$

<sup>(a)</sup> Minimal number of CO<sub>2</sub> molecules responsible for half of the emission



**Figure 3.16:**  $^{12}\text{CO}_2$  (thin lines) and  $^{13}\text{CO}_2$  spectra (thick lines) of models with an enhanced  $\text{CO}_2$  abundance around the  $\text{CO}_2$  iceline. The models have a constant abundance of  $\text{CO}_2$  of  $10^{-8}$  throughout most of the disk. The grey lines denote the model without any local enhancements in the  $\text{CO}_2$  abundance in an annulus around the  $\text{CO}_2$  iceline. The cyan, red and blue lines show the models with an enhanced abundance of  $10^{-6}$ ,  $10^{-5}$  and  $10^{-4}$ , respectively. The  $^{12}\text{CO}_2$  flux is enhanced by a factor of 2 to 4 over the complete range of the spectra. The  $^{13}\text{CO}_2$   $Q$ -branch however becomes more than an order of magnitude stronger, and the peak flux of the feature becomes higher than the peak flux of the neighbouring  $^{12}\text{CO}_2$  lines for the highest abundances. The spectra with enhanced  $\text{CO}_2$  abundances are shifted vertically for clarity.

The spectra from three models with enhanced abundances of  $x_{\text{CO}_2, \text{ring}} = 10^{-6}$ ,  $10^{-5}$  and  $10^{-4}$  in this ring can be seen in Fig. 3.16 together with the spectrum for the constant  $x_{\text{CO}_2} = 10^{-8}$  model. We note that  $\text{CO}_2$  ice is unlikely to be pure, and that some of it will likely also come off at the  $\text{H}_2\text{O}$  iceline, but such a multi-step sublimation model is not considered here.

The spectra in Fig. 3.16 show both  $^{12}\text{CO}_2$  and  $^{13}\text{CO}_2$  for the model with a constant abundance, an enhanced abundance of  $1 \times 10^{-6}$ ,  $1 \times 10^{-5}$ , and  $1 \times 10^{-4}$  around the  $\text{CO}_2$  iceline. The enhanced  $\text{CO}_2$  increases the  $^{12}\text{CO}_2$  flux up to a factor of 3. The optically thin  $^{13}\text{CO}_2$  feature is however increased by a lot more, with the peak flux in the  $^{13}\text{CO}_2$   $Q$ -branch reaching fluxes that are more than two times higher than peak fluxes of the nearby  $^{12}\text{CO}_2$   $P$ -branch lines.

Enhanced abundances in the outer regions can be distinguished from an enhanced abundance in the inner regions by looking at the tail of the  $^{13}\text{CO}_2$   $Q$ -branch. An over-abundant inner region will show a significant flux (10–50% of the peak) from the  $^{13}\text{CO}_2$   $Q$ -branch in the entire region between the locations of the  $^{12}\text{CO}_2$   $P(21)$  and  $P(23)$  lines and will show a smoothly declining profile with decreasing wavelength. If the abundance enhancement is in the outer regions, where the gas temperature and thus the rotational temperature is lower, the flux between the  $^{12}\text{CO}_2$   $P(21)$  and  $P(23)$  lines will be lower for the low enhancements (0–20% of the peak flux), for the higher enhancements the  $R(1)$  line shows up in the short wavelength side of the profile. Other  $R$  and  $P$  branch lines from  $^{13}\text{CO}_2$  can also show up in the spectrum if the abundance can reach up to  $10^{-4}$  in the ring around the  $\text{CO}_2$  iceline.

### 3.4.3 Comparison of CO<sub>2</sub> with other inner disk molecules

With the models presented in this paper, four molecules with rovibrational transitions coming from the inner disk have been studied by non-LTE disk models: H<sub>2</sub>O (Antonellini et al. 2015, 2016; Meijerink et al. 2009), CO (Thi et al. 2013), HCN (Bruderer et al. 2015) and CO<sub>2</sub> (this work). Of these CO is special, as it can be excited by UV radiation and fluoresces to excited vibrational states that in turn emit infrared radiation. For the other molecules absorption of a UV photon mostly leads to dissociation of the molecule (Heays et al. 2017). H<sub>2</sub>O, HCN and CO all have an permanent dipole moment and can thus also emit strongly in the sub-millimeter. This means that these molecules will have lower rotational temperatures than CO<sub>2</sub> in low density gas but they are actually observed to have broader profiles in the mid-infrared. Thus, our models reinforce the conclusion from the observed profiles that CO<sub>2</sub> comes from relatively cold gas (200-300 K) (See panel *c* of Fig. 3.5 and panel *d* of Fig. 3.17).

For the disk around AS 205 (N), the emission of both HCN and CO<sub>2</sub> has now been analysed under non-LTE conditions in DALI. As such it is possible to infer the HCN to CO<sub>2</sub> abundance ratio in the disk. The representative, constant abundance model for the CO<sub>2</sub> emission from AS 205 N has an abundance of  $3 \times 10^{-8}$  with a gas-to-dust ratio of 1000 but the inner abundance can easily vary by an order of magnitude or more while still being in agreement with observations. The models from Bruderer et al. (2015) that best reproduce the data have outer HCN abundances between  $10^{-10}$  and  $10^{-9}$  for gas-to-dust ratios of 1000. This translates into CO<sub>2</sub>/HCN abundance ratios of 30–300 in the region from 2 to 30 AU. The higher abundance of CO<sub>2</sub> in the outer regions of the disk explains the colder inferred rotational temperature of CO<sub>2</sub> compared to HCN.

## 3.5 Conclusion

Results of DALI models are presented, modelling the full continuum radiative transfer, non-LTE excitation of CO<sub>2</sub> in a typical protoplanetary disk model, with as the main goal: to find a way to measure the CO<sub>2</sub> abundance in the emitting region of disks with future instruments like JWST and test different assumptions on its origin. Spectra of CO<sub>2</sub> and <sup>13</sup>CO<sub>2</sub> in the 4–4.5 μm and 14–16 μm regions were modelled for disks with different parametrized abundance structures, gas masses and dust masses. The main conclusions of this study are:

- The critical density of the CO<sub>2</sub> 00<sup>0</sup>1 state, responsible for emission around 4.3 μm, is very high,  $> 10^{15} \text{ cm}^{-3}$ . As a result, in the absence of a pumping radiation field, there is no emission from the 00<sup>0</sup>1 state at low densities. If there is a pumping infrared radiation field, or if the density is high enough, the emission around 4.3 μm will be brighter than that around 15 μm.
- The infrared continuum radiation excites CO<sub>2</sub> up to large radii (10s of AU). The region probed by the CO<sub>2</sub> emission can therefore be an order of magnitude larger (in radius) than typically assumed in LTE slab models. Temperatures inferred from optically thin LTE models can also be larger than the actual temperature of the emitting gas. Differences between LTE and non-LTE full disk model flux are typically a within factor of three.

- Current observations of the  $15\ \mu\text{m}$   $Q$ -branch fluxes are consistent with models with constant abundances between  $10^{-9}$  and  $10^{-7}$  for a gas-to-dust ratio of 1000. Observations of lines corresponding to levels with high rotational quantum numbers or the  $^{13}\text{CO}_2$   $Q$ -branch will have to be used to properly infer abundances. In particular, the  $^{13}\text{CO}_2$   $Q$ -branch can be a good indicator of abundance structure from inner to outer disk.
- The gas-to-dust ratio and fractional abundance are largely degenerate. The column of  $\text{CO}_2$  above the dust infrared photosphere sets the emission. Models with similar columns have very similar spectra irrespective of total dust and gas mass, due to the excitation mechanism of  $\text{CO}_2$ . If the gas-to-dust ratio is constrained from other observations such as  $\text{H}_2\text{O}$  the fractional abundance can be determined from the spectra.
- The abundance of  $\text{CO}_2$  in protoplanetary disks inferred from modelling,  $10^{-9}$ – $10^{-7}$ , is at least two orders of magnitude lower than the  $\text{CO}_2$  abundance in ISM ices. This implies that disk chemical abundances are not directly inherited from the ISM and that significant chemical processing happens between the giant molecular cloud stage and the protoplanetary disk stage.
- The  $^{13}\text{CO}_2$   $v_2$   $Q$ -branch at  $15.42\ \mu\text{m}$  will be able to identify an overabundance of  $\text{CO}_2$  in the upper layers of the inner disk, such as could be produced by sublimating pebbles and planetesimals around the iceline(s).

Our work shows that the new instruments on JWST will be able to give a wealth of information on the  $\text{CO}_2$  abundance structure, provided that high  $S/N$  ( $> 300$  on the continuum) spectra are obtained.

## Appendix

### 3.A Collisional rate coefficients

The collisional rate coefficients are calculated in a way very similar to Bruderer et al. (2015), that is by combining vibrational coefficients with rotational rate coefficients to get the state-to-state ro-vibrational rate coefficients. Only collisions with  $\text{H}_2$  are considered, which is the dominant gas species in the regions where  $\text{CO}_2$  is expected to be abundant. The vibrational coefficients were taken from the laser physics and atmospheric physics papers. An overview of the final vibrational rate coefficients used are shown in Table 3.5. The temperature dependence of the rates is suppressed for the de-excitation collisional rate coefficients and the rate for 300 K are used throughout. The vibrational rate coefficients are not expected to vary much over the range of temperatures considered here. The de-excitation rate coefficient of the bending mode by  $\text{H}_2$  ( $01^10 \rightarrow 00^00$  transition) from Allen et al. (1980) is  $5 \times 10^{-12}\ \text{cm}^{-3}\text{s}^{-1}$ , an order of magnitude faster than the He (Taylor & Bitterman 1969; Allen et al. 1980). This is probably due to vibrational-rotational energy exchange in collisions with rotationally excited  $\text{H}_2$  (Allen et al. 1980). For levels higher up in the vibrational ladder we extrapolate the rates as in Procaccia & Levine (1975) and Chandra & Sharma (2001).

**Table 3.5:** Vibrational rate coefficients as measured/extrapolated.

Initial state	Final state	Rate coef. [ $\text{cm}^3\text{s}^{-1}$ ]
01 <sup>1</sup> 0	00 <sup>0</sup> 0	5(-12)
10 <sup>0</sup> 0(2)	00 <sup>0</sup> 0	3.3(-12)
10 <sup>0</sup> 0(2)	01 <sup>1</sup> 0	1(-11)
02 <sup>2</sup> 0	00 <sup>0</sup> 0	3.3(-12)
02 <sup>2</sup> 0	01 <sup>1</sup> 0	1(-11)
02 <sup>2</sup> 0	10 <sup>0</sup> 0(2)	5.8(-12)
10 <sup>0</sup> 0(1)	00 <sup>0</sup> 0	3.3(-12)
10 <sup>0</sup> 0(1)	01 <sup>1</sup> 0	1(-11)
10 <sup>0</sup> 0(1)	10 <sup>0</sup> 0(2),02 <sup>2</sup> 0	5.8(-12)
11 <sup>1</sup> 0(2)	00 <sup>0</sup> 0(1)	3(-12)
11 <sup>1</sup> 0(2)	01 <sup>1</sup> 0(1)	9(-12)
11 <sup>1</sup> 0(2)	10 <sup>0</sup> 0(1, 2),02 <sup>2</sup> 0	1.5(-11)
03 <sup>3</sup> 0	00 <sup>0</sup> 0	3(-12)
03 <sup>3</sup> 0	01 <sup>1</sup> 0	9(-12)
03 <sup>3</sup> 0	10 <sup>0</sup> 0(1, 2),02 <sup>2</sup> 0	1.5(-11)
03 <sup>3</sup> 0	11 <sup>1</sup> 0(2)	5.8(-12)
11 <sup>1</sup> 0(1)	00 <sup>0</sup> 0	3(-12)
11 <sup>1</sup> 0(1)	01 <sup>1</sup> 0	9(-12)
11 <sup>1</sup> 0(1)	10 <sup>0</sup> 0(1, 2),02 <sup>2</sup> 0	1.5(-11)
11 <sup>1</sup> 0(1)	11 <sup>1</sup> 0(2),03 <sup>3</sup> 0	5.8(-12)
00 <sup>0</sup> 1	11 <sup>1</sup> 0(1, 2),03 <sup>3</sup> 0	4.5(-14)
01 <sup>1</sup> 1	11 <sup>1</sup> 0(1, 2),03 <sup>3</sup> 0	4.5(-14)
01 <sup>1</sup> 1	00 <sup>0</sup> 1	5(-12)

**Notes.**  $a(b) = a \times 10^b$

Combining Eqs. 6 and 8 from the later paper we get, for  $v > w$ , the relation

$$k(v_2 = v \rightarrow v_2 = w) = v \frac{2w + 1}{2v + 1} k(v_2 = 1 \rightarrow v_2 = 0). \quad (3.3)$$

The rate coefficient measured by Nevdakh et al. (2003) is actually the total quenching rate of the 00<sup>0</sup>1 level. Here we assume that the relaxation of the 00<sup>0</sup>1 level goes to the three closest lower energy levels (03<sup>3</sup>0, 11<sup>1</sup>0(1), 11<sup>1</sup>0(2)) in equal measure. For the all the rates between the levels of the Fermi degenerate states and the corresponding bending mode with higher angular momentum the CO<sub>2</sub>–CO<sub>2</sub> rate measured by Jacobs et al. (1975) was used scaled to the reduced mass of the H<sub>2</sub>–CO<sub>2</sub> system. The states with constant  $2v_1 + v_2$  are considered equal to the pure bending mode with respect to the collisional rate coefficients to other levels.

No information exists on the rotational rate coefficients of CO<sub>2</sub> with H<sub>2</sub>. We have decided to use the CO rate coefficients from Yang et al. (2010) instead. Since CO<sub>2</sub> does not have a dipole moment, the exact rate coefficients are not expected to be important since the critical densities for the levels in the rotational ladders are very low,  $< 10^4 \text{ cm}^{-3}$ .

The method suggested by Faure & Josselin (2008) was employed to calculate the

state-to-state de-excitation rate coefficients for initial levels  $v, J$  to all levels  $v', J'$  with a smaller ro-vibrational energy. This is assuming a decoupling of rotational and vibrational levels, so we can write

$$k(v, J \rightarrow v', J'; T) = k(v \rightarrow v') \times P_{(J, J')}(T), \quad (3.4)$$

where

$$P_{(J, J')}(T) = \frac{k(0, J \rightarrow 0, J'; T) \sum_J g_J \exp(-E_{v, J}/kT)}{\sum_J g_J \exp(-E_{v, J}/kT) \sum_{J'} k(0, J \rightarrow 0, J'; T)}, \quad (3.5)$$

with the statistical weights  $g_i$  of the levels. All the excitation rates are calculated using the detailed balance.

### 3.B Fast line ray tracer

For the calculation of the CO<sub>2</sub> lines a new ray tracer was used. The conventional ray tracer used in DALI (Bruderer et al. 2012) can take up to ten minutes to calculate the flux from one line. The CO<sub>2</sub> molecule model used here includes more than 3600 lines. Not all of these lines are directly important but to get the complete spectrum of both the 4.3  $\mu\text{m}$  and the 15  $\mu\text{m}$  bands, a few hundred lines need to be ray traced for each model.

To enable the calculation of a large number of lines a module has been implemented into DALI that can calculate a line flux in a few seconds versus a few minutes for the conventional ray tracer. The module uses the fact that, along a line of sight, the velocity shear due to the finite height of the disk is approximately linear (Horne & Marsh 1986, Eqs. 9 and 10). Using this, the spectrum for an annulus in the disk can be approximated. At the radius of the annulus in question, the spectra are calculated for different velocities shears. These spectra are calculated by vertically integrating the equation of radiative transfer through the disk and correcting for the projected area for non face-on viewing angles. Then the total spectrum of the annulus is calculated by iterating over the azimuthal direction. For each angle the velocity shear is calculated and the spectrum is interpolated from the pre-calculated spectra. A simple sum over the spectra in all annuli is now sufficient to calculate the total spectrum.

This approximation is a powerful tool for calculating the total flux in a line especially for low inclinations. For the models presented in this paper the fluxes differ by about 4% for the 15  $\mu\text{m}$  lines and 1.5% for the 4.3  $\mu\text{m}$  lines. This is small compared to the other uncertainties in the models.

The approximation breaks down at high inclinations and should be used with care for any inclination larger than 45°. The total line shape is also close to the line shape from the traditional ray tracer, but with the high S/N from ALMA, using the traditional ray tracer is still advised for doing direct comparisons. This is also the case for images for which the errors will be larger than for the integrated flux or line shape as some of the errors made in making the image will cancel out (in first order) when integrating over the annulus.

### 3.C Model temperature and radiation structure

Figure 3.17 shows the model temperature, radiation field and excitation temperature structure corresponding to the model shown in Fig. 3.5. Panel *a* shows the dust



temperature structure, panels *b* and *c* show the excitation temperature of the  $v_2 1 \rightarrow 0$   $Q(6)$  line and  $v_3 1 \rightarrow 0$   $R(7)$  lines. For the excitation temperature only the upper and lower state of the line are used. This is thus a vibrational excitation temperature and can be different from the ground state rotational excitation temperature (that follows the dust temperature) and the rotational excitation temperature within a vibrationally excited state. Where the density is higher than the critical density the excitation temperature is equal to the dust temperature. In the disk atmosphere the  $Q(6)$  is mostly subthermally excited, while the  $R(7)$  line is superthermally excited. For both lines there is a maximum in the vertical excitation temperature distribution at the point where the gas becomes optically thick to its own radiation. Panel *d* shows the dust temperature of the region from which most of the  $\text{CO}_2$   $15 \mu\text{m}$  emission originates as function of radius. Most of the emitting gas is at temperatures between 150 and 350 K. Panel *e* and *f* show the strength of the radiation field at  $15 \mu\text{m}$  and  $4.3 \mu\text{m}$  is shown as a factor of the radiation field of a 750 K blackbody. This shows where there is a sufficient photon density to radiatively pump  $\text{CO}_2$ .

### 3.D Model fluxes $g/d_{\text{dust}}$

As mentioned in the main text, two different way of changing the gas-to-dust ratio were considered, increasing the gas mass and decreasing the dust mass w.r.t. the gas-to-dust ratio 100 case. Fig. 3.18 is the counterpart to Fig. 3.6 showing the modelled fluxes for different inner  $\text{CO}_2$  abundances, outer  $\text{CO}_2$  abundances and different gas-to-dust ratios. In this case the gas-to-dust ratio is varied by keeping the gas mass of the disk constant and decreasing the amount of dust in the disk.

There are only very slight differences between Fig. 3.18 and Fig. 3.6, and all observations made for the figure in the main text are true for this figure as well.

### 3.E LTE vs non-LTE

The effects of the LTE assumption on the line fluxes in a full disk model on the  $v_3, 1 \rightarrow 0, R(7)$  line and the  $15 \mu\text{m}$  feature are shown in Fig. 3.19. Only the models with constant abundance ( $x_{\text{out}} = x_{\text{in}}$ ) are shown for clarity but the differences between LTE and non-LTE for these models are representative for the complete set of models. For the  $15 \mu\text{m}$  flux the differences between the LTE and non-LTE models is small, of the order of 30%. The radial extent of the emission is, however, different: the region emitting 75% of the  $15 \mu\text{m}$  flux extends twice as far in the non-LTE models (extent of the  $15 \mu\text{m}$  non-LTE emission is seen in Fig. 3.5, panel f). This a clear sign of the importance of infrared pumping that is included in the non-LTE models. The difference between the fluxes in the  $4.25 \mu\text{m}$  line are greater, up to an order of magnitude. The difference are strongest in the models that have a low total  $\text{CO}_2$  content (so low abundance and low gas-to-dust ratio). This is mostly due to the larger radial extent of the emitting region extending up to 20 times further out in the non-LTE models compared to the corresponding LTE model (Extent of the  $4.3 \mu\text{m}$  non-LTE emission is seen in Fig. 3.5, panel i). This is in line with the higher Einstein  $A$  coefficient and upper level energy (and thus higher critical density) of the  $v_3, 1 \rightarrow 0, R(7)$  line, giving rise to a large importance of infrared pumping relative to

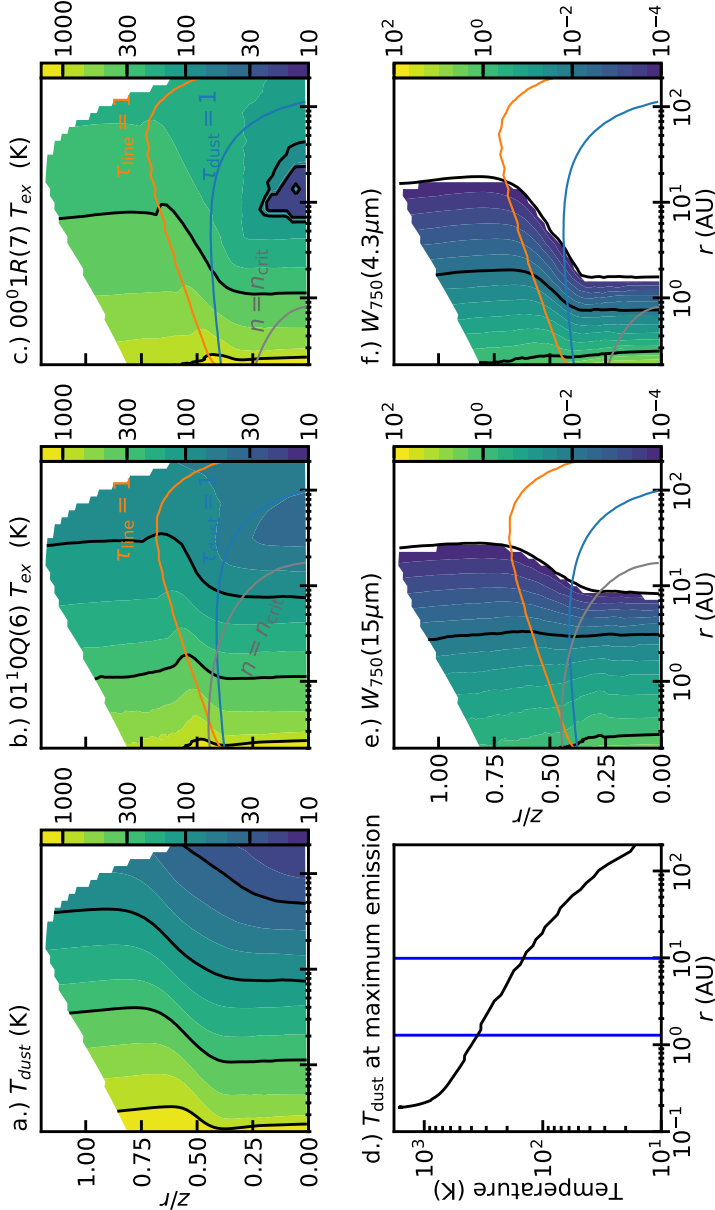


**Figure 3.17:** Dust temperature, excitation temperature and radiation field for a model with  $g/d_{gas} = 1000$ , and a constant abundance of  $10^{-7}$ . The red line in panels *b, c, e* and *f* shows the  $CO_2$  line  $\tau = 1$  surface, the blue line shows the  $\tau = 1$  line for the dust. Panel *d* shows the dust temperature at the height from which most of the emission of the  $15 \mu m$   $Q(6)$  line originates as function of radius. The vertical blue lines enclose the radii that account for 50% of the emission.

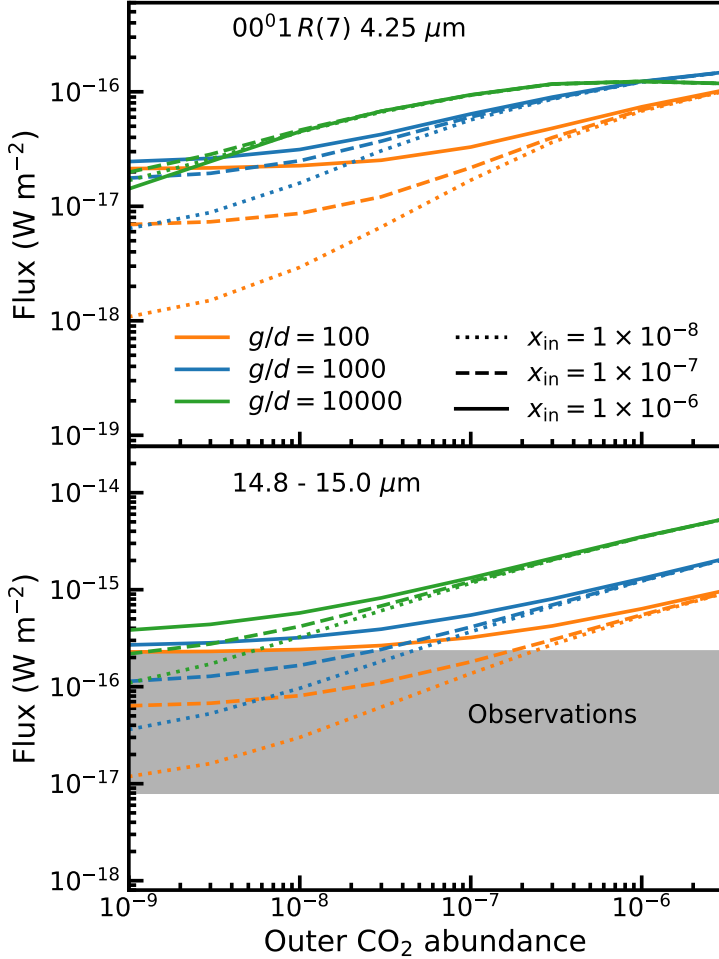


**Figure 3.18:** Line fluxes for models with constant gas mass ( $g/d_{dust}$ ). The upper panel shows the flux of the R(7) line from the fundamental asymmetric stretch band at 4.3  $\mu\text{m}$ . The lower panel shows the flux contained in the 15  $\mu\text{m}$  feature. The grey region denotes the range in line fluxes as observed by Salyk et al. (2011b) scale to the distance of AS 205 N. This feature contains the flux from multiple  $Q$ -branches with  $\Delta v_2 = 1$ . The CO<sub>2</sub> flux depends primarily on the outer CO<sub>2</sub> abundance and the total  $g/d$  ratio and does not strongly depend on the inner CO<sub>2</sub> abundances. Only for the very low CO<sub>2</sub> absolute abundances in the outer regions is the effect of the inner abundance on the line fluxes visible.

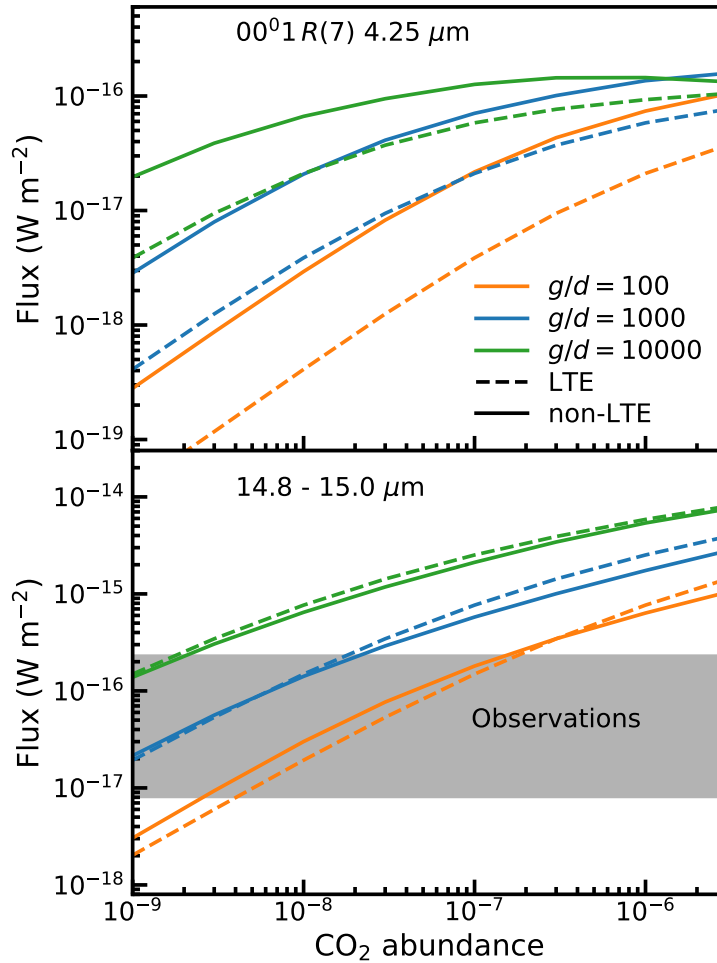


**Figure 3.19:** Flux comparison between LTE and non-LTE models. The upper panels show the flux of the R(7) line from the fundamental asymmetric stretch band. The lower panels show the flux contained in the 15 μm feature. The grey region shows the range of observed flux by Salyk et al. (2011b). The abundance in these models is constant over the whole disk. For the 15 μm feature the flux differences are small of the order of 30%. The differences are more pronounced in the 4.25 μm flux where the differences can get as large as a factor of 4.

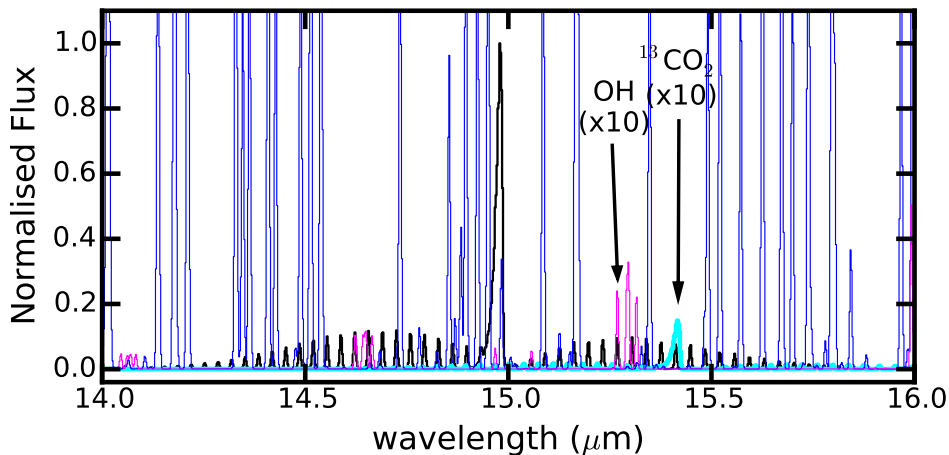


**Figure 3.20:** Slab model spectrum comparing CO<sub>2</sub> emission (black) and <sup>13</sup>CO<sub>2</sub> emission (cyan) with the H<sub>2</sub>O emission (blue) and OH emission (magenta) at a resolving power of 2200. Slab models uses the parameters fitted by Salyk et al. (2011b) for AS 205 (N) (See. Table 3.6). The large number of strong water lines strongly contaminates the CO<sub>2</sub> spectrum. All spectra are normalized to the peak of the CO<sub>2</sub> emission. A lot of single water lines are up to four times as strong as the peak of the CO<sub>2</sub> 15 μm feature. The <sup>13</sup>CO<sub>2</sub> and OH fluxes have been multiplied by a factor of 10 for clarity.

collisional excitation. Fig. 3.19 uses  $g/d_{\text{dust}} = 1000$ , but the plot for  $g/d_{\text{gas}} = 1000$  is very similar.

### 3.F Line blending by H<sub>2</sub>O and OH

One of the major challenges in interpreting IR-spectra of molecules in T-Tauri disks are the ubiquitous water lines. H<sub>2</sub>O has a large dipole moment and thus has strong transitions. As H<sub>2</sub>O chemically favours hot regions (Agúndez et al. 2008; Walsh et al. 2015) there are a lot of rotational lines in the mid infra-red. Fig. 3.20 shows the H<sub>2</sub>O rotational lines near the CO<sub>2</sub> 15 μm feature. The spectra are simulated with a LTE slab model using the same parameters as fitted by Salyk et al. (2011b) for AS 205 (N) as reproduced in Table 3.6. It should be noted that AS 205 (N) is a very water rich disk (in its spectra) explaining the large number of strong lines. Fortunately, there are still some regions in the CO<sub>2</sub> spectrum that are not blended with H<sub>2</sub>O or OH lines and thus can be used for tracing the CO<sub>2</sub> abundance structure independent of a H<sub>2</sub>O emission model. The situation improves at higher resolving power as can be seen in Fig. 3.21. The resolving power of 28000 has been chosen to match with the resolving power of the *SPICA* HRS mode. At this point the line widths are dominated by the assumed Keplerian linewidth of 20 km s<sup>-1</sup>. At this resolution the individual *Q*-branch lines are separable and a lot of the line blends that happen at a resolving power of 2200 are no longer an issue.

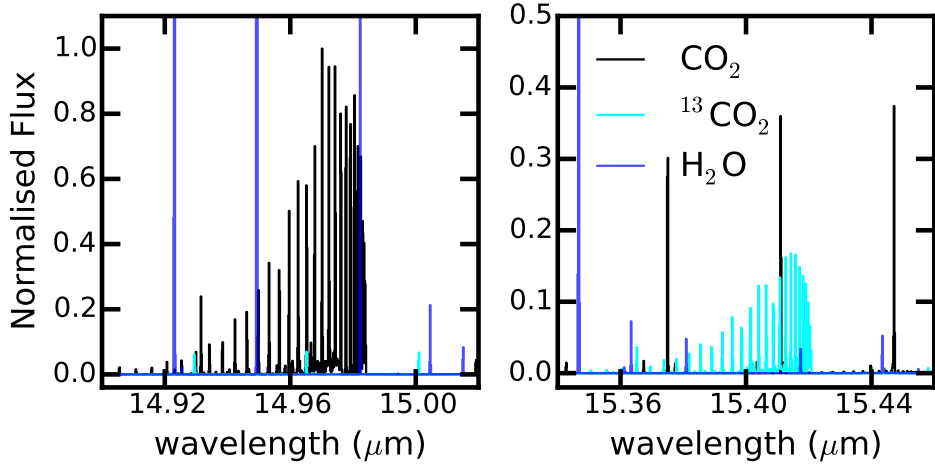


**Figure 3.21:** Slab model spectrum comparing CO<sub>2</sub> emission (black) and <sup>13</sup>CO<sub>2</sub> emission (cyan) with the H<sub>2</sub>O emission (blue) at a resolving power of 28000. The left panel shows a zoom of the 15 μm region, right panel shows a zoom in of the region where the <sup>13</sup>CO<sub>2</sub> *v*<sub>2</sub> *Q*-branch resides. Slab models uses the parameters fitted by Salyk et al. (2011b) for AS 205 (N) (See. Table 3.6). Due to the high resolving power individual *Q*-branch lines can be observed and blends are less likely to happen. A Keplerian linewidth of 20 km s<sup>-1</sup> has been assumed. The <sup>13</sup>CO<sub>2</sub> fluxes have been multiplied by a factor of 10 for clarity.

**Table 3.6:** Parameters for the slab models

Molecule	column (cm <sup>-2</sup> )	Temperature (K)
CO <sub>2</sub>	$4 \times 10^{15}$	300
H <sub>2</sub> O	$4 \times 10^{20}$	300
OH	$6 \times 10^{16}$	700

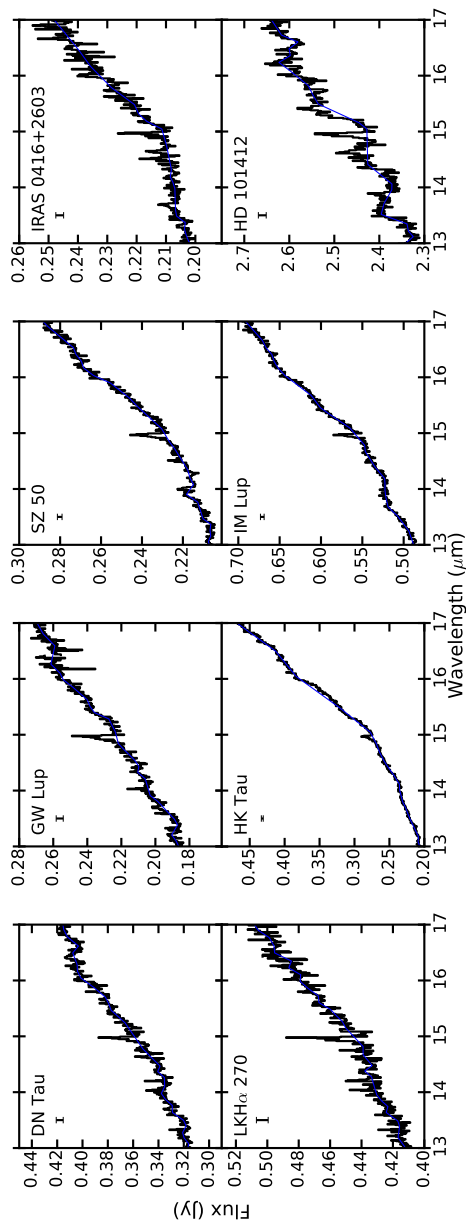
**Table 3.7:** Stellar parameters

Object	Source luminosity ( $L_{\odot}$ )	Distance (pc)	References
AS 205 N	7.3	125	Andrews et al. (2009)
DR Tau	1.0	140	Rigliaco et al. (2015)
DoAr24E	11	125	Rigliaco et al. (2015)
RNO 90	2.7	125	Rigliaco et al. (2015)

### 3.G *Spitzer*-IRS spectra

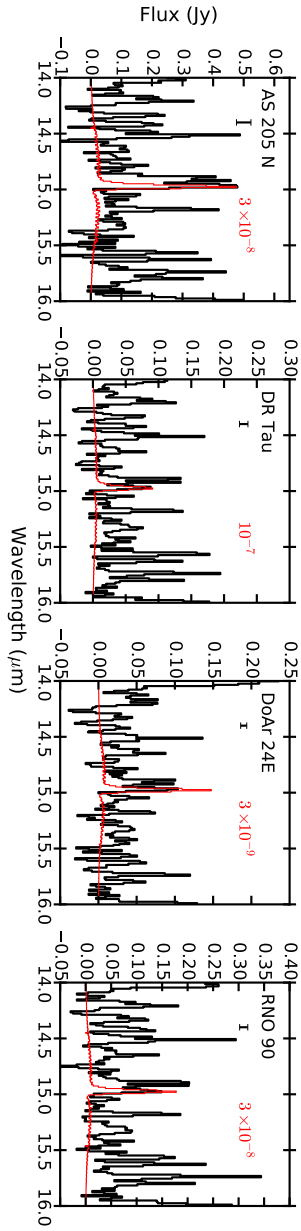
Fig. 3.22 shows the spectra as observed by *Spitzer*-IRS reduced with the CHIP software (Pontoppidan et al. 2010; Pontoppidan 2016). Continua that have been fitted to these spectra are also indicated on the figure. The objects have been chosen because their spectra are relatively free of H<sub>2</sub>O emission. Even without H<sub>2</sub>O lines, it is still tricky to determine a good baseline for the continuum as there are a lot of spectral slope changes, even in the narrow wavelength range considered here. This is especially true for HD 101412 where the full spectrum shows a hint of what looks like *R*- and *P*-branches. If these are features due to line emission, it becomes arbitrary where one puts the actual continuum, thus these features are counted here as part of the continuum. Whether these feature are real or not will not matter a lot for the abundance determination as the CO<sub>2</sub> *Q*-branch is separated from the strong *R*- and *P*-branch lines.

Figure 3.23 shows a comparison between observed spectra of disk with strong H<sub>2</sub>O emission and CO<sub>2</sub> model spectra. The spectra are corrected for source luminosity and distance as explained in Sec. 3.4.1. Assumed distances and luminosities are given in Table. 3.7.



**Figure 3.22:** Observations from *Spitzer-IRS* over 13–17  $\mu\text{m}$  (black) with continuum as fitted (blue) for the eight selected sources. Typical rms noise on the continuum is shown under the object name. DN Tau, GW Lup and LKH $\alpha$  270 had a spike in the observed flux at 16.48  $\mu\text{m}$  due to artefacts at the edge of the observing order. This single data point has been removed from these three spectra.

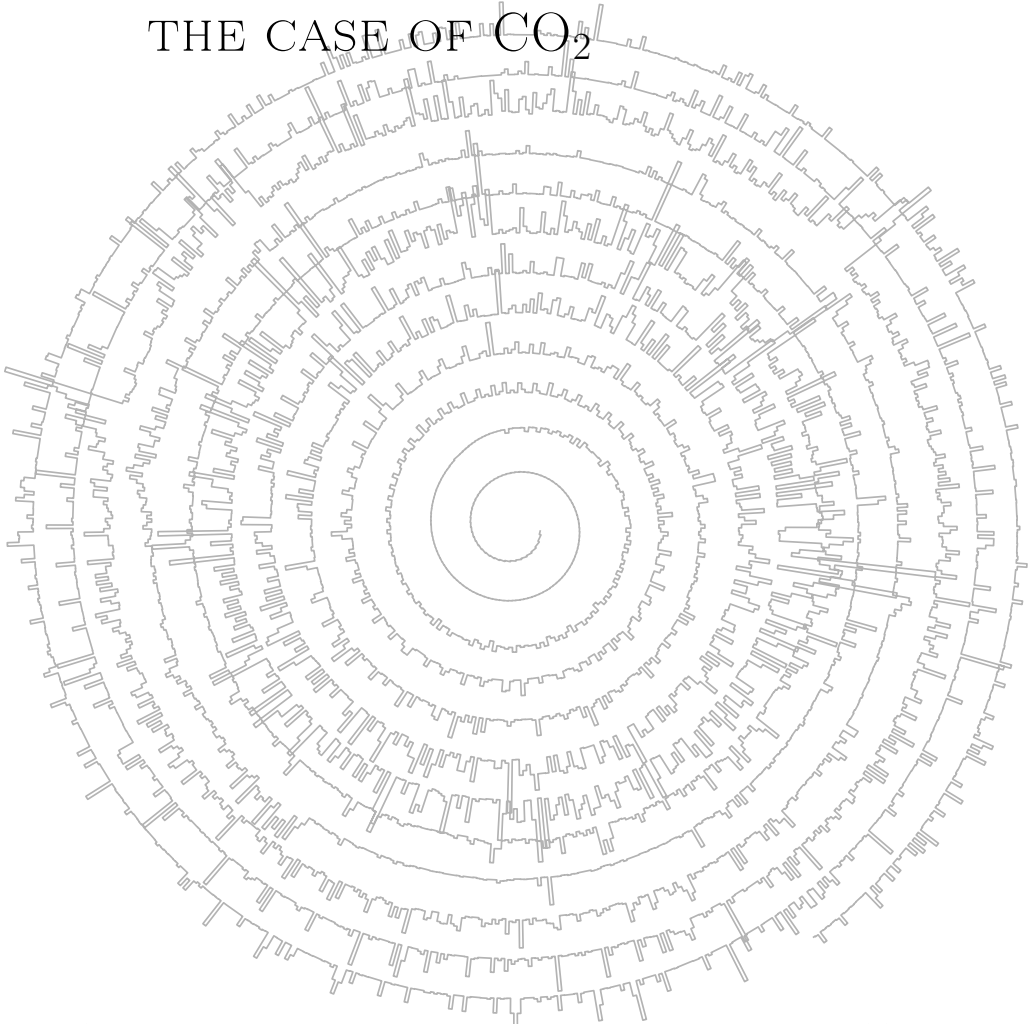




**Figure 3.23:** Comparison of continuum subtracted *Spitzer* observations with luminosity and distance corrected model spectra for CO<sub>2</sub>. Object name and median rms noise in the spectra are given in the upper left corner of each panel. All of the sources here have strong H<sub>2</sub>O emission.

# 4

## EFFICIENCY OF RADIAL TRANSPORT OF ICES IN PROTOPLANETARY DISKS PROBED WITH INFRARED OBSERVATIONS: THE CASE OF CO<sub>2</sub>



A. D. Bosman, A. G. G. M. Tielens and E. F. van Dishoeck, 2018, A&A 611, 80

## Abstract

**Context:** Radial transport of icy solid material from the cold outer disk to the warm inner disk is thought to be important for planet formation. However, the efficiency at which this happens is currently unconstrained. Efficient radial transport of icy dust grains could significantly alter the composition of the gas in the inner disk, enhancing the gas-phase abundances of the major ice constituents such as H<sub>2</sub>O and CO<sub>2</sub>.

**Aims:** Our aim is to model the gaseous CO<sub>2</sub> abundance in the inner disk and use this to probe the efficiency of icy dust transport in a viscous disk. From the model predictions, infrared CO<sub>2</sub> spectra are simulated and features that could be tracers of icy CO<sub>2</sub>, and thus dust, radial transport efficiency are investigated.

**Methods:** We have developed a 1D viscous disk model that includes gas accretion and gas diffusion as well as a description for grain growth and grain transport. Sublimation and freeze-out of CO<sub>2</sub> and H<sub>2</sub>O has been included as well as a parametrisation of the CO<sub>2</sub> chemistry. The thermo-chemical code DALI was used to model the mid-infrared spectrum of CO<sub>2</sub>, as can be observed with *JWST*-MIRI.

**Results:** CO<sub>2</sub> ice sublimating at the iceline increases the gaseous CO<sub>2</sub> abundance to levels equal to the CO<sub>2</sub> ice abundance of  $\sim 10^{-5}$ , which is three orders of magnitude more than the gaseous CO<sub>2</sub> abundances of  $\sim 10^{-8}$  observed by *Spitzer*. Grain growth and radial drift increase the rate at which CO<sub>2</sub> is transported over the iceline and thus the gaseous CO<sub>2</sub> abundance, further exacerbating the problem. In the case without radial drift, a CO<sub>2</sub> destruction rate of at least  $10^{-11} \text{ s}^{-1}$  or a destruction timescale of at most 1000 yr is needed to reconcile model prediction with observations. This rate is at least two orders of magnitude higher than the fastest destruction rate included in chemical databases. A range of potential physical mechanisms to explain the low observed CO<sub>2</sub> abundances are discussed.

**Conclusions:** We conclude that transport processes in disks can have profound effects on the abundances of species in the inner disk such as CO<sub>2</sub>. The discrepancy between our model and observations either suggests frequent shocks in the inner 10 AU that destroy CO<sub>2</sub>, or that the abundant midplane CO<sub>2</sub> is hidden from our view by an optically thick column of low abundance CO<sub>2</sub> due to strong UV and/or X-rays in the surface layers. Modelling and observations of other molecules, such as CH<sub>4</sub> or NH<sub>3</sub>, can give further handles on the rate of mass transport.

## 4.1 Introduction

To date, a few thousand planetary systems have been found<sup>1</sup>. Most of them have system architectures that are very different from our own solar system (Madhusudhan et al. 2014) and explaining the large variety of systems is a challenge for current planet formation theories (see, e.g. Morbidelli & Raymond 2016, and references therein). Thus, the birth environment of planets – protoplanetary disks – are an active area of study. A young stellar system inherits small dust grains from the interstellar medium. In regions with high densities and low turbulence, the grains start to coagulate. In the midplane of protoplanetary disks, where densities are higher than  $10^8 \text{ cm}^{-3}$ , grain growth can really take off. Grain growth and the interactions of these grown particles with the gaseous disk are of special interest to planet formation (see, e.g. Weiden- schilling 1977; Lambrechts & Johansen 2012; Testi et al. 2014). The growth of dust grains to comets and planets is far from straightforward, however.

Pebbles, that is, particles that are large enough to slightly decouple from the gas, have been invoked to assist the formation of planets in different ways (Johansen & Lambrechts 2017). They are not supported by the pressure gradient from the gas, but they are subject to gas drag. As a result pebbles drift on a time-scale that is an order of magnitude faster than the gas depletion time-scale. This flow of pebbles, if intercepted or stopped, can help with planet formation. The accretion of pebbles onto forming giant planetary cores should help these cores grow beyond their classical isolation mass (Ormel & Klahr 2010; Lambrechts & Johansen 2012) while the interactions of gas and pebbles near the inner edge of the disk can help with the formation of ultra compact planetary systems as found by the *Kepler* satellite (Tan et al. 2016; Ormel et al. 2017). Efficient creation and redistribution of pebbles would lead to quick depletion of the solid content of disks increasing their gas-to-dust ratios by one to two orders of magnitude in 1 Myr (e.g. Ciesla & Cuzzi 2006; Brauer et al. 2008; Birnstiel et al. 2010).

Observations of disks do not show evidence of strong dust depletion. The three disks that have far-infrared measurements of the HD molecule to constrain the gas content show gas-to-dust ratios smaller than 200 (Bergin et al. 2013; McClure et al. 2016; Trapman et al. 2017), including the 10 Myr old disk TW Hya (Debes et al. 2013). Gas-to-dust ratios found from gas mass estimates using CO line fluxes are inconsistent with strong dust depletion as well (e.g. Ansdell et al. 2016; Miotello et al. 2017). Manara et al. (2016b) also argue from the observed relation between accretion rates and dust masses, that the gas-to-dust ratio in the 2–3 Myr old Lupus region should be close to 100.

It is thus of paramount importance that a way is found to quantify the inwards mass flux of solid material due to radial drift from observations. This is especially important for the inner ( $< 10 \text{ AU}$ ) regions of protoplanetary disks. Here we propose to look for a signature of efficient radial drift in protoplanetary disks through molecules that are a major component of icy planetesimals.

Radial drift is expected to transport large amounts of ice over the iceline, depositing a certain species in the gas phase just inside and ice just outside the iceline (Stevenson & Lunine 1988; Piso et al. 2015; Öberg & Bergin 2016). This has been modelled in detail for the water iceline by Ciesla & Cuzzi (2006) and Schoonenberg & Ormel (2017), for the CO iceline by Stammer et al. (2017) and in general for the H<sub>2</sub>O, CO

---

<sup>1</sup>[exoplanets.org](http://exoplanets.org) as of 28 Nov 2017

and CO<sub>2</sub> icelines by Booth et al. (2017). In all cases the gaseous abundance of a molecule in the ice is enhanced inside of the iceline as long as there is an influx of drifting particles. The absolute value and width of the enhancement depend on the mass influx of ice and the strength of viscous mixing. Such an enhancement may be seen directly with observations of molecular lines. Out of the three most abundant ice species (CO, H<sub>2</sub>O and CO<sub>2</sub>), CO<sub>2</sub> is the most promising candidate for a study of this nature. Both CO and H<sub>2</sub>O are expected to be highly abundant in the inner disk based on chemical models (see, e.g. Aikawa & Herbst 1999; Markwick et al. 2002; Walsh et al. 2015; Eistrup et al. 2016). As such any effect of radial transport of icy material will be difficult to observe. CO<sub>2</sub> is expected to be abundant in outer disk ices (with abundances around 10<sup>-5</sup> if inherited from the cloud or produced in situ in the disk, Pontoppidan et al. 2008b; Boogert et al. 2015; Le Roy et al. 2015; Drozdovskaya et al. 2016), but it is far less abundant in the gas in the inner regions of the disk (with abundances around 10<sup>-8</sup>, Pontoppidan et al. 2010; Bosman et al. 2017). This gives a leverage of three orders of magnitude to see effects from drifting icy pebbles.

Models by Cyr et al. (1998); Ali-Dib et al. (2014), for example, predict depletion of volatiles in the inner disk. In these models, all volatiles are locked up outside of the iceline in stationary solids. In Ali-Dib et al. (2014) this effect is strengthened by the assumption that the gas and the small dust in the disk midplane are moving radially outwards such as proposed by Takeuchi & Lin (2002). Together this leads to very low inner disk H<sub>2</sub>O abundances in their models. CO<sub>2</sub> is not included in these models, but the process for H<sub>2</sub>O would also work for CO<sub>2</sub>, but slightly slower, as the CO<sub>2</sub> iceline is slightly further out. However, these models do not include the diffusion of small grains through the disk, which could resupply the inner disk with volatiles at a higher rate than that caused by the radial drift of large grains.

Bosman et al. (2017) showed that an enhancement of CO<sub>2</sub> near the iceline would be observable in the <sup>13</sup>CO<sub>2</sub> mid infrared spectrum, if that material were mixed up to the upper layer. Here we continue on this line of research by constraining the maximal mass transport rate across the iceline and by investigating the shape and amplitude of a possible CO<sub>2</sub> abundance enhancement near the iceline due to this mass transport.

To constrain the mass transport we have build a model along the same lines as Ciesla & Cuzzi (2006) and Booth et al. (2017) except that we do not include planet formation processes. As in Booth et al. (2017) we use the dust evolution prescription from Birnstiel et al. (2012). The focus is on the chemistry within the CO<sub>2</sub> iceline to make predictions on the CO<sub>2</sub> content of the inner disk. In contrast with Schoonenberg & Ormel (2017) a global disk model is used to maintain consistency between the transported mass and observed outer disk masses. Chemical studies of the gas in the inner disk have been presented by, for example Agúndez et al. (2008), Eistrup et al. (2016), Walsh et al. (2015) but transport processes are not included in these studies. Cridland et al. (2017) use an evolving disk, including grain growth and transport, coupled with a full chemical model in their planet formation models. However, they do not include transport of ice and gas species due to the various physical evolution processes.

§4.2 presents the details of our physical model, whereas §4.3 discusses various mid-plane chemical processes involving CO<sub>2</sub> and our method for simulating infrared spectra. §4.4 presents the model results for a range of model assumptions and parameters. One common outcome of all of these models is that the CO<sub>2</sub> abundance in the inner disk is very high, orders of magnitude more than observed, making it difficult to quan-

tify mass transport. §4.5 discusses possible ways to mitigate this discrepancy and the implications for the physical and chemical structure of disks, suggesting JWST-MIRI observations of  $^{13}\text{CO}_2$  that can test them.

## 4.2 Physical model

### 4.2.1 Gas dynamics

To investigate the effect of drifting pebbles on inner disk gas-phase abundances we build a 1-D dynamic model. This model starts with an  $\alpha$ -disk model (Shakura & Sunyaev 1973). The evolution of the surface density of gas  $\Sigma_{\text{gas}}(t, r)$  can be described as:

$$\frac{\partial \Sigma_{\text{gas}}}{\partial t} = \frac{3}{r} \frac{\partial}{\partial r} \left[ r^{1/2} \frac{\partial}{\partial r} \left( \frac{\alpha c_s^2}{\Omega} \Sigma_{\text{gas}} r^{1/2} \right) \right], \quad (4.1)$$

where  $r$  is the distance to the star,  $t$  is time,  $\alpha$  is the dimensionless Sakura-Sunyaev parameter,  $\Omega$  is the local Keplerian frequency and  $c_s = \sqrt{k_b T / (\mu)}$  is the local sound speed, with  $k_b$  the Boltzmann constant,  $T$  the local temperature and  $\mu$  the mean molecular mass which is taken to be 2.6 amu.  $\alpha c_s^2 / \Omega$  is also equal to  $\nu_{\text{turb}}$ , the (turbulent) gas viscosity. The viscosity, or the resistance of the gas to shear, is responsible for the exchange of angular momentum. The origin of the viscosity is generally assumed to be turbulence stirred up by the Magneto-Rotational Instability (MRI) (Turner et al. 2014) although Eq. (4.1) is in principle agnostic to the origin of the viscosity as long as the correct  $\alpha$  value is included. For the rest of the paper, we assume that the viscosity originates from turbulence and that the process responsible for the viscous evolution is also the dominant process in mixing constituents of the disk radially.

The evolution of the surface density of a trace quantity has two main components. First, all gaseous constituents are moving with the flow of the gas. This advection is governed by:

$$\frac{\partial \Sigma_{x,\text{gas}}}{\partial t} = \frac{1}{r} \frac{\partial}{\partial r} \left( F_{\text{gas}} r \frac{\Sigma_{x,\text{gas}}}{\Sigma_{\text{gas}}} \right), \quad (4.2)$$

where  $F_{\text{gas}}$  is the total radial flux, which is related to the radial velocity of the gas due to viscous accretion,  $u_{\text{gas}}$ , and is given by:

$$F_{\text{gas}} = \Sigma_{\text{gas}} u_{\text{gas}} = \frac{3}{\sqrt{r}} \frac{\partial}{\partial r} \nu \Sigma_{\text{gas}} \sqrt{r}. \quad (4.3)$$

Second, the gas is also mixed by the turbulence, smoothing out variations in abundance. This diffusion can be written as (Clarke & Pringle 1988; Desch et al. 2017)

$$\frac{\partial \Sigma_{x,\text{gas}}}{\partial t} = \frac{1}{r} \frac{\partial}{\partial r} \left( r D_x \Sigma_{\text{gas}} \frac{\partial}{\partial r} \left( \frac{\Sigma_{x,\text{gas}}}{\Sigma_{\text{gas}}} \right) \right), \quad (4.4)$$

where  $D_x$  is the gas mass diffusion coefficient. The diffusivity is related to the viscosity by:

$$\text{Sc} = \frac{\nu_{\text{gas}}}{D_x}, \quad (4.5)$$

with Sc the Schmidt number. For turbulent diffusion in a viscous disk it is expected to be of order unity. As such,  $\text{Sc} = 1$  is assumed for all gaseous components.

Advection and diffusion are both effective in changing the abundance of a trace species if an abundance gradient exists. Diffusion is most effective in the presence of strong abundance gradients and strong changes in the abundance gradient, such as near the iceline. At the icelines the diffusion of a trace species will generally dominate over the advection due to gas flow.

## 4.2.2 Dust growth and dynamics

The dynamics of dust grains are strongly dependent on the grain size. A grain with a large surface area relative to its mass is well coupled to the gas and will not act significantly different from a molecule in the gas. Solid bodies with a very small surface area relative to its mass, for example, planetesimals, will not be influenced by the gas pressure or turbulence, their motions are then completely governed by gravitational interactions. Dust particles with sizes between these extremes will be influenced by the presence of the gas in various ways. To quantify these regimes it is useful to consider a quantity known as the Stokes number: The Stokes number is, assuming Epstein drag and spherical particles in a vertically hydrostatic disk, given by (Weidenschilling 1977; Birnstiel et al. 2010):

$$\text{St} = \frac{a_{\text{grain}} \rho_s \pi}{\Sigma_{\text{gas}}} \frac{\pi}{2}. \quad (4.6)$$

Particles with a very small Stokes number ( $\ll 1$ ) are very well coupled to the gas and the gas pressure gradients and particles with very large Stokes number ( $\gg 1$ ) are decoupled from the gas.

The coupling between gas and dust determines both the diffusivity of the dust, that is, how well the dust mixed due to turbulent motions of the disk as well as advection of the dust due to bulk flows of the gas. Youdin & Lithwick (2007) derived that the diffusivity  $D_{\text{dust}}$  of a particle with a certain Stokes number can be related to the gas diffusivity by:

$$D_{\text{dust}} = \frac{D_{\text{gas}}}{1 + \text{St}^2}. \quad (4.7)$$

Similarly the advection speed of dust due to gas advection can be given by:

$$u_{\text{dust,adv}} = \frac{u_{\text{gas}}}{1 + \text{St}^2}. \quad (4.8)$$

When particles are not completely coupled to the gas they are also no longer completely supported by the gas pressure gradient. The gas pressure gradient, from high temperature, high density material close to the star, to low temperature, low density material far away from the star provides an outwards force, such that the velocity with which the gas has a stable orbit around the star is lower than the Keplerian velocity. Particles that start to decouple from the gas thus also need to speed up relative to the gas to stay in a circular orbit. This induces a velocity difference between the gas and the dust particles. The velocity difference between the gas velocity and a Keplerian orbital velocity is given by:

$$\Delta u = \Omega r - \sqrt{\Omega^2 r^2 - \frac{r}{\rho_{\text{gas}}} \frac{\partial P}{\partial r}}, \quad (4.9)$$

with  $P$  the pressure of the gas. We note that in the case of a positive pressure gradient, the gas will be moving faster than the Keplerian velocity

As a result of this velocity difference the particles are subjected to a drag force, which, in the case of a negative pressure gradient, removes angular momentum from the particles. The loss of angular momentum results in an inwards spiral of the dust particles. This process is known as radial drift. The maximal drift velocity can be given as (Weidenschilling 1977):

$$u_{\text{drift}} = \frac{2\Delta u}{\text{St} + \text{St}^{-1}}. \quad (4.10)$$

The drift velocity will thus be maximal for particles with a Stokes number of unity. Drift velocities of  $\sim 1\%$  of the orbital velocity are typical for particles with a Stokes number of unity.

The dynamics of dust are thus intrinsically linked to the size, or rather size distribution of the dust particles. The dust size distribution is set by the competition of coagulation and fragmentation<sup>2</sup>. When two particles collide in the gas they can either coagulate, that is, the particles stick together and continue on as a single larger particle, or they can fragment, the particles break apart into many smaller particles. The outcome of the collision depends on the relative velocity of the particles and their composition. At low velocities particles are expected to stick, while at high velocities collisions lead to fragmentation. The velocity that sets the boundary between the two outcomes is called the fragmentation velocity. For pure silicate aggregates the fragmentation velocities are low ( $1 \text{ m s}^{-1}$ ) while aggregates with a coating of water ice can remain intact in collisions with relative velocities up to a order of magnitude higher (Blum & Wurm 2008; Gundlach & Blum 2015).

Dust size distributions resulting from the coagulation and fragmentation processes can generally not be computed analytically. Calculations have been done for both static and dynamic disks (Brauer et al. 2008; Birnstiel et al. 2010; Krijt & Ciesla 2016). These models are very numerically intensive and do not lend themselves to the inclusion of additional physics and chemistry nor to large parameter studies. As such we will use the simplified dust evolution prescription from Birnstiel et al. (2012). This prescription has been benchmarked against models with a more complete grain growth and dust dynamics prescription from Brauer et al. (2008). The prescription only tracks the ends of the dust size distribution, the smallest grains of set size and the largest grains at a location in the disk of a variable size. As this prescription is a key part of the model we will reiterate some of the key arguments, equations and assumption of this prescription here, for a more complete explanation, see Birnstiel et al. (2012).

The prescription assumes that the dust size distribution can be in one of three stages at any point in the disk. Either the largest particles are still growing, the largest particle size is limited by radial drift, or the largest particle size is limited by fragmentation. In the first and second case, the size distribution is strongly biased towards larger sizes. In the final case the size distribution is a bit flatter (see, Brauer et al. 2008). The size distribution in all cases is parametrised by a minimal grain size, the monomer size, a maximal grain size, which depends on the local conditions, and the fraction of mass in the large grains.

---

<sup>2</sup>Cratering and bouncing are neglected for simplicity



From physical considerations one can write a maximal expected size of the particles due to different processes. Growth by coagulation is limited by the amount of collisions and thus by the amount of time that has passed. The largest grain expected in a size distribution at a given time is given by:

$$a_{\text{grow}}(t) = a_{\text{mono}} \exp \left[ \frac{t - t_0}{\tau_{\text{grow}}} \right], \quad (4.11)$$

where  $a_{\text{mono}}$  is the monomer size,  $t_0$  is the starting time,  $t$  is the current time and  $\tau_{\text{grow}}$  is the local growth time scale, given by:

$$\tau_{\text{grow}} = \frac{\Sigma_{\text{gas}}}{\Sigma_{\text{dust}} \Omega}. \quad (4.12)$$

Radial drift moves the particles inwards: the larger the particles, the faster the drift. There is thus a size at which particles are removed faster due to radial drift than they are replenished by grain growth, limiting the maximal size of particles. This maximal size is given by:

$$a_{\text{drift}} = f_d \frac{8 \Sigma_{\text{dust}} \pi r^2 \Omega^2}{\rho_s c_s^2} \gamma^{-1}, \quad (4.13)$$

with  $f_d$  a numerical factor,  $\rho_s$  is the density of the grains and  $\gamma$  is the absolute power law slope of the gas pressure:

$$\gamma = \left| \frac{d \ln P_{\text{gas}}}{d \ln r} \right|. \quad (4.14)$$

As mentioned before, particles that collide with high velocities are expected to fragment. For this model we consider two sources of relative velocities. One source of fragmentation is differential velocities due to turbulence (see, Ormel & Cuzzi 2007, for a more complete explanation). This limiting size is given by:

$$a_{\text{frag}} = f_f \frac{2}{3\pi} \frac{\Sigma_{\text{gas}}}{\rho_s \alpha} \frac{u_f^2}{c_s^2}, \quad (4.15)$$

where  $f_f$  is a numerical fine tuning parameter and  $u_f$  is the fragmentation velocity. The other source of fragmentation considered is different velocities due to different radial drift speeds. The limiting size for this process is given by:

$$a_{\text{df}} = \frac{u_f r \Omega}{c_s^2 (1 - N)} \frac{4 \Sigma_{\text{gas}}}{\rho_s} \gamma^{-1}, \quad (4.16)$$

$N$  is the average Stokes number fraction between two colliding grains, here we use  $N = 0.5$ .

The size distribution at a location in the disk spans from the monomer size ( $a_{\text{mono}}$ ) to the smallest of the four limiting sizes above. In the model the grains size distribution is split into ‘small’ and ‘large’ grains. The mass fraction of the large grains depends on the process limiting the size: if the grain size is limited by fragmentation ( $\min(a_{\text{frag}}, a_{\text{df}}) < a_{\text{drift}}$ ), the fraction of mass in large grains ( $f_{m, \text{frag}}$ ) is assumed to be 75%. If the grain size is limited by radial drift ( $a_{\text{drift}} < \min(a_{\text{frag}}, a_{\text{df}})$ ), the fraction of mass in large grains ( $f_{m, \text{drift}}$ ) is assumed to be 97%. These fractions were determined by Birnstiel et al. (2012) by matching the simplified model to more complete grain-growth models.

Using these considerations the advection-diffusion equation for the dynamics of the dust can be rewritten:

$$\begin{aligned} \frac{\partial \Sigma_{\text{dust}}}{\partial t} = & \frac{1}{r} \frac{\partial}{\partial r} \left[ (u_{\text{dust},s} r (1 - f_m) \Sigma_{\text{dust}} + u_{\text{dust},l} r f_m \Sigma_{\text{dust}}) \right. \\ & \left. + r \Sigma_{\text{gas}} \left( D_{\text{dust},s} \frac{\partial}{\partial r} \left( \frac{(1 - f_m) \Sigma_{\text{dust}}}{\Sigma_{\text{gas}}} \right) + D_{\text{dust},l} \frac{\partial}{\partial r} \left( \frac{f_m \Sigma_{\text{dust}}}{\Sigma_{\text{gas}}} \right) \right) \right], \end{aligned} \quad (4.17)$$

where  $D_{\text{dust},x} = D_{\text{gas}} / (1 + \text{St}_x^2)$ ,  $u_{\text{dust},x} = u_{\text{gas}} / (1 + \text{St}_x^2) + u_{\text{drift},x}$  where  $u_{\text{drift}}$  is the velocity due to radial drift (Eq. 4.10). Here it is assumed that the large grains never get a Stokes number larger than unity, which holds for the models presented here.

The final part of the dynamics concerns the ice on the dust. The ice moves with the dust, so both the large scale movements as well as the mixing diffusion of dust must be taken into account. For the model we assume that the ice is distributed over the grains according to the mass of the grains. This means that if large grains have a mass fraction  $f_m$ , then the large grains will have the same mass fraction of  $f_m$  of the available ice. This is a reasonable assumption, as long as the grain size distribution is in fragmentation equilibrium and the largest grains are transported on a timescale longer than the local growth timescale. The algorithm used here forces the latter condition to be true everywhere in the disk, while the former condition is generally true for the CO<sub>2</sub> and H<sub>2</sub>O icelines (Brauer et al. 2008), but not for the CO iceline (Stammler et al. 2017). With this assumption the advection-diffusion equation for the ice can be written as:

$$\frac{\partial \Sigma_{\text{ice},x}}{\partial t} = \frac{1}{r} \frac{\partial}{\partial r} r \left( F_{\text{dust}} \frac{\Sigma_{\text{ice},x}}{\Sigma_{\text{dust}}} + \Sigma_{\text{dust}} (D_{\text{dust},s} (1 - f_m) + D_{\text{dust},l} f_m) \frac{\partial}{\partial r} \frac{\Sigma_{\text{ice},x}}{\Sigma_{\text{dust}}} \right). \quad (4.18)$$

Here  $F_{\text{dust}}$  is the radial flux of dust, this is given by:

$$\begin{aligned} F_{\text{dust}} = & \Sigma_{\text{dust}} (u_{\text{dust},s} (1 - f_m) + u_{\text{dust},l} f_m) \\ & + \Sigma_{\text{dust}} \left( D_{\text{dust},s} \frac{\partial}{\partial r} \left( \frac{(1 - f_m) \Sigma_{\text{dust}}}{\Sigma_{\text{gas}}} \right) + D_{\text{dust},l} \frac{\partial}{\partial r} \left( \frac{f_m \Sigma_{\text{dust}}}{\Sigma_{\text{gas}}} \right) \right). \end{aligned} \quad (4.19)$$

### 4.2.3 Model parameters

For our study, we pick a disk structure that should be representative of a young disk around a one solar mass star. The initial surface density structure is given by:

$$\Sigma_{\text{gas}}(r) = \Sigma_{1\text{AU}} \left( \frac{r}{1\text{AU}} \right)^{-p} \exp \left[ \left( -\frac{r}{r_{\text{taper}}} \right)^{2-p} \right] \quad (4.20)$$

where  $p$  controls the steepness of the surface density profile,  $r_{\text{taper}}$  the extent of the disk and  $\Sigma_{1\text{AU}}$  sets the normalisation of the surface density profile. For our models we use  $p = 1$  and  $r_{\text{taper}} = 40$  AU. The temperature profile is given by a simple power law:

$$T(r) = T_{1\text{AU}} \left( \frac{r}{1\text{AU}} \right)^{-q}. \quad (4.21)$$

The disk is assumed to be viscous with a constant  $\alpha$ , as such there is a constraint on the power law slopes  $p$  and  $q$ , if we want the gas surface density to be a self similar solution to Eq. 4.1, it is required to have  $p + q = 3/2$  (Hartmann et al. 1998).

To calculate the volume densities, a vertical Gaussian distribution of gas with a scale height  $H_p(r) = h_p r$ , with  $h_p = 0.05$ , is used.

The disk is populated with particles of  $0.1\mu\text{m}$  at the start of the model, this is also the size of the small dust in the model. The gas-to-dust ratio is taken to be 100 over the entire disk. The density of the grains is assumed to be  $2.5\text{ g cm}^{-3}$  and grains are assumed to be solid spheres.

The molecules are initially distributed through simple step functions. These step functions have a characteristic radius ‘iceline’ which differentiates between the inner disk and the outer disk. Within this radius the gas phase abundance of the molecule is initialised, outside of this radius the solid phase abundance is initialised. Water is distributed equally through the disk with an abundance of  $1.2 \times 10^{-4}$ , whereas  $\text{CO}_2$  is initially depleted in the inner disk with an abundance of  $10^{-8}$  (Pontoppidan et al. 2011a; Bosman et al. 2017) and has a high abundance in the outer disk of  $4 \times 10^{-5}$ . This ice abundance of  $\text{CO}_2$  is motivated by the ISM ice abundance (Pontoppidan et al. 2008b; Boogert et al. 2015), cometary abundances (Le Roy et al. 2015) and chemical models of disk formation (Drozdovskaya et al. 2016).

A summary of the initial conditions, fixed and variable parameters is given in Table 4.1.

#### 4.2.4 Boundary conditions

Due to finite computational capabilities, the calculation domain of the model needs to be limited. The assumptions made for the edges can have significant influences on the model results. For the inner edge, it is assumed that gas leaves the disk with an accretion rate as assumed from a self similar solution ( $p + q = 3/2$ ) according to the viscosity and surface density at the inner edge. The accretion rate is given by:

$$\dot{M} = 3\pi\Sigma_{\text{gas}}\nu_{\text{gas}}. \quad (4.22)$$

All gas constituents advect with the gas over the inner boundary or, in the case of large grains, drift over the boundary. Diffusion over the inner boundary is not possible. For the outer boundary, the assumption is made that the surface density of gas outside the domain is zero. Again viscous evolution or an advection process can remove grains and other gas constituents from the computational domain.

### 4.3 Chemical processes

#### 4.3.1 Freeze-out and sublimation

Freeze-out and sublimation determine the fraction of a molecule that is in the gas phase and the fraction that is locked up on the grains. Freeze-out of a molecule, or a molecule’s accretion onto a grain is given by the collision rate of a molecule with the grain surface times the sticking fraction,  $f_s$ , which is assumed to be unity:

$$R_{\text{acc},x} = f_s\sigma_{\text{dust}}n_{\text{grain}}v_{\text{therm},x}, \quad (4.23)$$

**Table 4.1:** Initial conditions, fixed parameters and variables

Description	symbol	value
Initial conditions and fixed parameters		
Disk physical structure		
Central stellar mass	$M_\star$	1 $M_\odot$
Surface density at 1 AU	$\Sigma_{1\text{AU}}$	15000 $\text{kg m}^{-2}$
Temperature at 1 AU	$T_{1\text{AU}}$	300 K
Exponential taper radius	$r_{\text{taper}}$	40 AU
$\Sigma$ density power law slope	$p$	1
$T$ power law slope	$q$	0.5
Total initial disk mass	$M_{\text{gas},0}$	0.02 $M_\odot$
Disk FWHM angle	$h_{\text{FWHM}}$	0.05 rad
Dust properties		
Gas-to-dust ratio	g/d	100
Monomer size	$a_{\text{small}}$	0.1 $\mu\text{m}$
Grain density	$\rho_s$	2.5 $\text{g cm}^{-3}$
Drift lim. large grain frac.	$f_{m, \text{drift}}$	0.97
Frag. lim. large grain frac.	$f_{m, \text{frag}}$	0.75
Num. factor fragmentation size	$f_f$	0.37
Num. factor drift size	$f_d$	0.55
Chemical parameters		
Sticking fraction	$f_s$	1.0
Cosmic ray ionisation rate	$\zeta_{\text{H}_2}$	$10^{-17} \text{ s}^{-1}$
Number of active ice layers	$N_{\text{act}}$	2
Step radius water	$r_{\text{step}, \text{H}_2\text{O}}$	3 AU
Inner disk $\text{H}_2\text{O}$ abundance	$x_{\text{in}, \text{H}_2\text{O}}$	$1.2 \times 10^{-4}$
Outer disk $\text{H}_2\text{O}$ abundance	$x_{\text{out}, \text{H}_2\text{O}}$	$1.2 \times 10^{-4}$
$\text{H}_2\text{O}$ binding energy	$E_{\text{bind}, \text{H}_2\text{O}}$	5600 K
$\text{H}_2\text{O}$ desorption prefactor	$p_{\text{H}_2\text{O}}$	$10^{30} \text{ cm}^{-2} \text{ s}^{-1}$
$\text{H}_2\text{O}$ CR destruction efficiency	$k_{\text{H}_2\text{O}}/\zeta_{\text{H}_2}$	1800
Step radius $\text{CO}_2$	$r_{\text{step}, \text{CO}_2}$	10 AU
Inner disk $\text{CO}_2$ abundance	$x_{\text{in}, \text{CO}_2}$	$1 \times 10^{-8}$
Outer disk $\text{CO}_2$ abundance	$x_{\text{out}, \text{CO}_2}$	$4 \times 10^{-5}$
$\text{CO}_2$ binding energy	$E_{\text{bind}, \text{CO}_2}$	2900 K
$\text{CO}_2$ desorption prefactor	$p_{\text{CO}_2}$	$9.3 \times 10^{26} \text{ cm}^{-2} \text{ s}^{-1}$
Variables		
Viscosity parameter	$\alpha$	
Fragmentation velocity	$u_f$	
$\text{CO}_2$ destruction rate	$R_{\text{destr}, \text{CO}_2}$	

where  $\sigma_{\text{dust}}$  is the average dust surface area,  $n_{\text{grain}}$  is the number density of grains and the thermal velocity  $v_{\text{therm},x} = \sqrt{8kT/\pi m_x}$ , with  $k$  the Boltzmann constant,  $T$  the temperature and  $m_x$  the mass of the molecule. Molecules that are frozen-out on the grain can sublimate or desorb. For a grain covered with many monolayers of ice, the rate per unit volume for this process is given by:

$$f_{\text{des},x} = R_{\text{des},x} n_{\text{x,ice}} = p_x \sigma_{\text{dust}} n_{\text{grain}} N_{\text{act}} \exp \left[ -\frac{E_{\text{bind}}}{kT} \right], \quad (4.24)$$

where  $p_x$  is the zeroth-order ‘prefactor’ encoding the frequency of desorption attempts per unit surface area,  $\sigma_{\text{dust}}$  is the surface area per grain,  $n_{\text{grain}}$  is the number density of grains.  $N_{\text{act}}$  is the number of active layers, that is, the number of layers that can participate in the sublimation,  $N_{\text{act}} = 2$  is used,  $T$  is the dust temperature, which we take equal to the gas temperature. For mixed ices this rate can be modified by a covering fraction  $\chi_x = n_{\text{ice},x}/\sum_x n_{\text{ice},x}$ , however, this is neglected here. We note that  $f_{\text{des},x}$  in its current form is independent of the amount of molecules frozen out on the dust grains. Using these rates we get the following differential equation:

$$\frac{\partial n_{\text{x,gas}}}{\partial t} = -R_{\text{acc},x} n_{\text{x,gas}} + f_{\text{des},x}, \quad (4.25)$$

which has an analytical solution:

$$n_{\text{x,gas}}(t) = \min \left[ n_{\text{x,tot}}, \left( n_{\text{x,gas}}(t_0) - \frac{f_{\text{des},x}}{R_{\text{acc},x}} \right) \exp(-R_{\text{acc},x}(t-t_0)) + \frac{f_{\text{des},x}}{R_{\text{acc},x}} \right]. \quad (4.26)$$

where  $n_{\text{x,tot}}$  is the total number density of a molecule (gas and ice). The number density of ice is given by:

$$n_{\text{x,ice}}(t) = n_{\text{x,tot}} - n_{\text{x,gas}}(t). \quad (4.27)$$

The ice line temperature, defined as the temperature for which  $n_{\text{x,gas}} = n_{\text{x,dust}}$ , that is, when freeze-out and sublimation balance, depends on the total number density of the molecule considered. At lower total molecule number densities, the iceline will be at lower temperatures.

For  $\text{CO}_2$  we use a binding energy of 2900 K, representative for  $\text{CO}_2$  mixed with water (Sandford & Allamandola 1990; Collings et al. 2004). More recent measurements have suggested that the binding energy is lower, around 2300 K (Noble et al. 2012). Using the lower binding energy moves the  $\text{CO}_2$  iceline further out from 90 to 80 K or from 6 to 8 AU in our standard model. The prefactor,  $p_{x,\text{CO}_2}$ , of  $9.3 \times 10^{26} \text{ cm}^{-2} \text{ s}^{-1}$  from (Noble et al. 2012) is used. The change in iceline location has a minimal effect on the evolution of the abundance profiles. The mixing time-scale becomes longer at larger radii which would increase mixing times. For  $\text{H}_2\text{O}$  a binding energy of 5600 K and prefactor,  $p_{x,\text{H}_2\text{O}}$ , of  $10^{30} \text{ cm}^{-2} \text{ s}^{-1}$  (Fraser et al. 2001).

### 4.3.2 Midplane formation and destruction processes

Radial drift and radial diffusion and advection will quickly move part of the outer disk  $\text{CO}_2$  ice reservoir into the inner disk, enhancing the inner disk abundances. To get a good measure of the amount of  $\text{CO}_2$  in the inner disk it is necessary to also take

into account the processes that form and destroy  $\text{CO}_2$  in gas and ice. The density is highest near the mid-plane, as such this is where formation and destruction process are expected to be most relevant for the bulk of the  $\text{CO}_2$ . However, in the less dense upper layers, there are UV-photons that can dissociate and ionise molecules, possibly influencing the overall abundance of  $\text{CO}_2$ .

### Gas-phase formation of $\text{CO}_2$

The formation of  $\text{CO}_2$  in the inner disk mainly goes through the warm gas-phase route. Here  $\text{CO}_2$  forms through the reaction  $\text{CO} + \text{OH} \longrightarrow \text{CO}_2 + \text{H}$ . The reaction has a slight activation barrier of 176 K (Smith et al. 2004). The parent molecule CO is very stable and is expected to be present at high abundances in the inner disk ( $10^{-4}$ ) (Walsh et al. 2015). The OH radical is expected to be less abundant, and it is the fate of this radical that determines the total production rate of  $\text{CO}_2$ . OH is formed either directly from  $\text{H}_2\text{O}$  photodissociation (Heays et al. 2017), or by hydrogenation of atomic oxygen,  $\text{O} + \text{H}_2 \longrightarrow \text{OH} + \text{H}$ , in a reaction that has an activation barrier of 3150 K (Baulch et al. 1992). The atomic oxygen itself also has to be liberated from, in this case, either CO,  $\text{CO}_2$  or  $\text{H}_2\text{O}$  by X-rays or UV-photons. The production rate of  $\text{CO}_2$  is thus severely limited if there is no strong radiation field present to release oxygen from one of the major carriers.

The  $\text{CO}_2$  formation reaction,  $\text{CO} + \text{OH} \longrightarrow \text{CO}_2 + \text{H}$ , has competition from the  $\text{H}_2\text{O}$  formation reaction,  $\text{OH} + \text{H}_2 \longrightarrow \text{H}_2\text{O} + \text{H}$ . The hydrogenation of OH has a higher activation energy, 1740 K, than the formation of  $\text{CO}_2$ , but since  $\text{H}_2$  is orders of magnitude more abundant than CO, the formation of water will dominate over the formation of  $\text{CO}_2$  at high temperatures. The rate for  $\text{CO}_2$  formation is given by (Smith et al. 2004):

$$f_{\text{form},\text{CO}_2} = 2.81 \times 10^{-13} n_{\text{CO}} n_{\text{OH}} \exp\left(-\frac{176\text{K}}{T}\right). \quad (4.28)$$

The formation rate for  $\text{H}_2\text{O}$  formation is given by (Baulch et al. 1992):

$$f_{\text{form},\text{H}_2\text{O}} = 2.05 \times 10^{-12} n_{\text{H}_2} n_{\text{OH}} \left(\frac{T}{300\text{K}}\right)^{1.52} \exp\left(-\frac{1740\text{K}}{T}\right). \quad (4.29)$$

This means that the expected  $x_{\text{CO}_2}/x_{\text{H}_2\text{O}}$  fraction from formation is:

$$\frac{f_{\text{form},\text{CO}_2}}{f_{\text{form},\text{H}_2\text{O}}} = 0.14 x_{\text{CO}} \left(\frac{T}{300\text{K}}\right)^{-1.52} \exp\left(\frac{1564\text{K}}{T}\right) \quad (4.30)$$

This function is plotted in Fig. 4.1 which shows that the formation of  $\text{CO}_2$  is faster below temperatures of 150 K, whereas above this temperature formation of water is faster. Above a temperature of 300 K water formation is a thousand times faster than  $\text{CO}_2$  formation. The implication is that gaseous  $\text{CO}_2$  formation is only effective in a narrow temperature range, 50–150 K, and then only if OH is present as well, requiring UV photons or X-rays to liberate O and OH from CO or  $\text{H}_2\text{O}$ .

### Destruction of $\text{CO}_2$ : Cosmic rays

Cosmic rays, 10–100 MeV protons and ions, have enough energy to penetrate deeply into the disk. Cosmic-rays can ionise  $\text{H}_2$  in regions where UV photons and X-rays

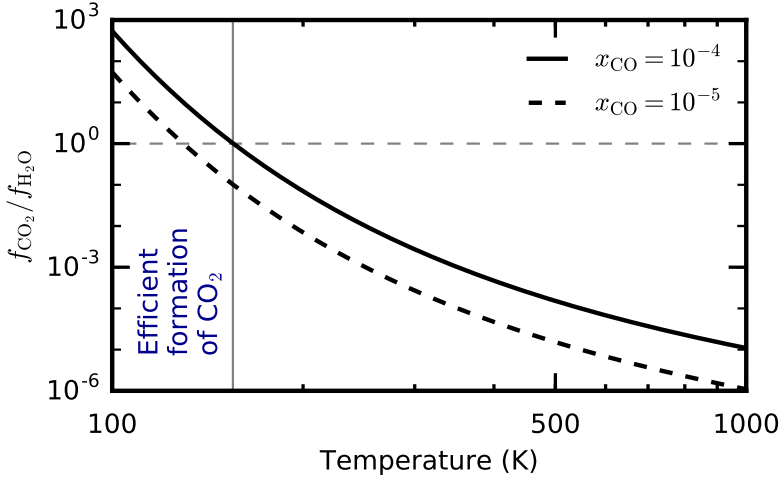


**Figure 4.1:** Ratio of the  $\text{CO}_2$  to  $\text{H}_2\text{O}$  formation rate from a reaction of OH with CO and  $\text{H}_2$  respectively. Hydrogenation of OH to  $\text{H}_2\text{O}$  dominates above 150 K. Formation times of  $\text{CO}_2$  and  $\text{H}_2\text{O}$  from OH are faster than the inner disk mixing time for all temperatures considered here.

cannot penetrate. The primary ionisation as well as the collisions of the resulting energetic electron with further  $\text{H}_2$  creates electronically excited  $\text{H}_2$  as well as excited H atoms. These excited atoms and molecules radiatively decay, resulting in the emission of UV-photons (Prasad & Tarafdar 1983). These locally generated UV-photons can dissociate and ionise molecules. Here only the dissociation rate of  $\text{CO}_2$  is taken into account as ionisation of  $\text{CO}_2$  by this process is negligible. Following Heays et al. (2017) the destruction rate of species  $X$  is written as:

$$k_X = \frac{\zeta_{\text{H}_2} x_{\text{H}_2}}{x_X} \int P(\lambda) p_X(\lambda) d\lambda, \quad (4.31)$$

where  $\zeta_{\text{H}_2}$  is the direct cosmic ray ionisation rate of  $\text{H}_2$ ,  $x_X$  is the abundance of species  $X$  w.r.t.  $\text{H}_2$ ,  $P(\lambda)$  is the photon emission probability per unit spectral density for which we use the spectrum from Gredel et al. (1987).  $p_X(\lambda)$  is the absorption probability of species  $X$  for a photon of wavelength  $\lambda$ . This probability is given by:

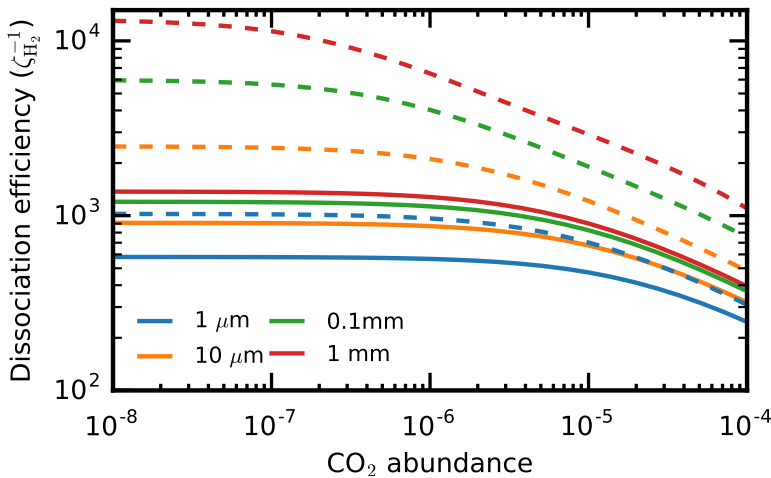
$$p_X(\lambda) = \frac{x_X \sigma_X^{\text{destr}}(\lambda)}{x_{\text{dust}} \sigma_{\text{dust}}^{\text{abs}}(\lambda) + \sum_j x_j \sigma_j^{\text{abs}}(\lambda)}, \quad (4.32)$$

where  $\sigma_X^{\text{destr}}(\lambda)$  is the wavelength dependent destruction or absorption cross section of species  $X$  and  $x_{\text{dust}} \sigma_{\text{dust}}^{\text{abs}}$  is the dust cross section per hydrogen molecule. For the calculation of the cosmic-ray dissociation rate of  $\text{CO}_2$  we assume that the destruction cross section in the UV is equal to the absorption cross section for  $\text{CO}_2$ , that is, every absorption of a photon with a wavelength shorter than 227 nm leads to the destruction of a  $\text{CO}_2$  molecule. For the calculations the cross sections from Heays et al. (2017) are used<sup>3</sup>. These cross sections can also be used to compute destruction rates for  $\text{CO}_2$  by stellar UV radiation in the surface layers of the disk.

<sup>3</sup>UV cross-sections can be found here: <http://home.strw.leidenuniv.nl/~ewine/photo/>

**Table 4.2:** Gas-phase abundances assumed for the cosmic ray induced dissociation rate calculations

Molecule	Abundance inside H <sub>2</sub> O iceline	Abundance outside H <sub>2</sub> O iceline
H <sub>2</sub>	1	1
H	10 <sup>-12</sup>	10 <sup>-10</sup>
CO	10 <sup>-5</sup>	10 <sup>-5</sup>
N <sub>2</sub>	10 <sup>-5</sup>	10 <sup>-5</sup>
CO <sub>2</sub>	10 <sup>-8...-4</sup>	10 <sup>-8...-4</sup>
H <sub>2</sub> O	10 <sup>-4</sup>	10 <sup>-8</sup>

**Figure 4.2:** Dissociation rate of CO<sub>2</sub> due to cosmic ray induced photons, for different dust size distributions. Solid lines are for condition inside of the H<sub>2</sub>O iceline, dashed lines for conditions outside of the H<sub>2</sub>O iceline. The efficiency multiplied by  $\zeta_{\text{H}_2}$  gives the CO<sub>2</sub> dissociation rate.

The dust absorption is an important factor in these calculations and can be the dominant contribution to the total absorption in parts of the spectrum. The dust absorption greatly depends on the dust opacities assumed. A standard ISM dust composition was taken following Weingartner & Draine (2001), the mass extinction coefficients are calculated using Mie theory with the MIEX code (Wolf & Voshchinnikov 2004) and optical constants by Draine (2003) for graphite and Weingartner & Draine (2001) for silicates. Grain sizes are distributed assuming an MRN distribution starting at 5 nm, with varying maximum size are used. The resulting mass opacities and cross sections are shown in Fig. 4.14.

Cosmic ray induced destruction rates for CO<sub>2</sub> are calculated for each dust size distribution for a range of CO<sub>2</sub> abundances between 10<sup>-8</sup> and 10<sup>-4</sup>. The o-p ratio of H<sub>2</sub>, important for the H<sub>2</sub> emission spectrum, is assumed to be 3:1, representative for high temperature gas. The abundances of the other shielding species used in the calculation are shown in Table. 4.2. The destruction rate for CO<sub>2</sub> is plotted in Fig. 4.2.

The CO<sub>2</sub> destruction is faster for grown grains and low abundances of CO<sub>2</sub>. At



abundances above  $10^{-7}$ , the strongest transitions start to saturate, lowering the destruction rate with increasing abundance. Even though the dust opacity changes by more than an order of magnitude, the dissociation rates stay within a factor of 3 for all  $\text{CO}_2$  abundances. This is due to the inclusion of  $\text{H}_2\text{O}$  into our calculations.  $\text{H}_2\text{O}$  has large absorption cross sections in the same wavelength regimes as  $\text{CO}_2$ . When  $\text{H}_2\text{O}$  is depleted, such as would be expected between the  $\text{H}_2\text{O}$  and  $\text{CO}_2$  icelines,  $\text{CO}_2$  destruction rates increase, especially for the largest grains. Even in this optimal case, the destruction rate for  $\text{CO}_2$  is limited to  $2 \times 10^{-13} \text{ s}^{-1}$  for typical  $\zeta_{\text{H}_2}$  of  $10^{-17} \text{ s}^{-1}$ .

Aside from generating a UV field, cosmic-rays also create ions, the most important of these being  $\text{He}^+$ . Due to the large ionisation potential of He, electron transfer reactions with  $\text{He}^+$  generally lead to dissociation of the newly created ion. For example,  $\text{CO}_2 + \text{He}^+$  preferably leads to the creation of  $\text{O} + \text{CO}^+$ . Destruction of  $\text{CO}_2$  due to  $\text{He}^+$  is limited by the creation of  $\text{He}^+$  and the competition between  $\text{CO}_2$  and other reaction partners of  $\text{He}^+$ . The total reaction rate coefficient of  $\text{CO}_2$  with  $\text{He}^+$  is  $k_{\text{ion,CO}_2} = 1.14 \times 10^{-9} \text{ cm}^3 \text{ s}^{-1}$  (Adams & Smith 1976). The three main competitors for reactions with  $\text{He}^+$  are  $\text{H}_2\text{O}$ ,  $\text{CO}$  and  $\text{N}_2$ , with reaction rate coefficients of  $k_{\text{ion,H}_2\text{O}} = 5.0 \times 10^{-10}$ ,  $k_{\text{ion,CO}} = 1.6 \times 10^{-9}$  and  $k_{\text{ion,N}_2} = 1.6 \times 10^{-9} \text{ cm}^3 \text{ s}^{-1}$  respectively (Mauclaire et al. 1978; Anicich et al. 1977; Adams & Smith 1976). Assuming a cosmic  $\text{He}^+$  ionisation rate of  $0.65\zeta_{\text{H}_2}$  (Umebayashi & Nakano 2009), the destruction rate for  $\text{CO}_2$  due to  $\text{He}^+$  reaction can be written as,

$$R_{\text{destr,He}^+} = 0.65\zeta_{\text{H}_2} \frac{x_{\text{He}} k_{\text{ion,CO}_2} x_{\text{CO}_2}}{x_{\text{CO}_2} \sum_X k_{\text{ion,X}} x_X}, \quad (4.33)$$

where the sum is over all reactive collision partners of  $\text{He}^+$  of which  $\text{CO}$ ,  $\text{N}_2$  and  $\text{H}_2\text{O}$  are most important. For typical abundances of He of 0.1 and  $\text{N}_2$ ,  $\text{CO}$  and  $\text{H}_2\text{O}$  of  $10^{-4}$ ,  $R_{\text{destr,He}^+}$  is below  $650\zeta_{\text{H}_2}$  for all  $\text{CO}_2$  abundances. Thus cosmic-ray induced photodissociation will always be more effective than destruction due to  $\text{He}^+$ .

Altogether the destruction time-scale for midplane  $\text{CO}_2$  by cosmic ray induced processes is long,  $\sim 3 \text{ Myr}$  for a  $\zeta_{\text{H}_2} = 10^{-17} \text{ s}^{-1}$ . The latter value is likely an upper limit for the inner disk given the possibility of attenuation and exclusion of cosmic rays (Umebayashi & Nakano 1981; Cleaves et al. 2015).

### Destruction of $\text{CO}_2$ : Gas-phase reactions

In warm gas it is possible to destroy  $\text{CO}_2$  by endothermic reactions with H or  $\text{H}_2$  (Talbi & Herbst 2002). The reaction



has an activation barrier of 13 300 K and a pre-exponential factor of  $2.5 \times 10^{-10} \text{ cm}^3 \text{ s}^{-1}$  for temperatures between 300 and 2500 K (Tsang & Hampson 1986) while the reaction



has an activation barrier of 56 900 K and has a pre-exponential factor of  $3.3 \times 10^{-10} \text{ cm}^3 \text{ s}^{-1}$  at 1000 K. This means that for gas at 300 K, an  $\text{H}_2$  density of  $10^{12} \text{ cm}^{-3}$ , and a corresponding H density of  $1 \text{ cm}^{-3}$ , the rate for destruction by atomic hydrogen is  $1.4 \times 10^{-29} \text{ s}^{-1}$ , while the destruction rate by molecular hydrogen is  $1.4 \times 10^{-80} \text{ s}^{-1}$ . Both are far too low to be significant in the inner disk. However, if the atomic H abundance

is higher, destruction of CO<sub>2</sub> by H can become efficient at high temperatures. As such the destruction of CO<sub>2</sub> becomes very dependent on the formation speed of H<sub>2</sub> at high densities and temperatures. The CO<sub>2</sub> abundance as a function of temperature for a gas-phase model is shown in Fig. 4.15. Temperatures of >700 K are needed to lower the CO<sub>2</sub> abundance below 10<sup>-7</sup>, even with a high atomic H abundance.

### 4.3.3 Simulating spectra

To compare the model abundances with observations, infrared spectra are simulated with the thermochemical code DALI (Bruderer et al. 2012; Bruderer 2013). DALI is used to calculate a radial temperature profile, from dust and gas surface density profiles and stellar parameters. The viscous evolution model is initialised using the same surface density distribution as the DALI model. The temperature slope  $q$  is taken so that the surface density slope  $p$  is consistent with a self-similar solution  $q = 1.5 - p = 0.9$ . The temperature at 1 AU is taken from the midplane temperatures as calculated by the DALI continuum ray-tracing module. No explicit chemistry is included in this version of DALI, but the abundances are parametrised using the output of the dynamical model. The viscous model run with  $\alpha = 10^{-3}$ ,  $u_f = 3 \text{ m s}^{-1}$  and a CO<sub>2</sub> destruction rate varying between 10<sup>-13</sup> and 10<sup>-9</sup> s<sup>-1</sup>. The results from Sect. 4.4.4 show that these parameters represent the bulk of the model results.

After simulating 1 Myr of evolution, the gas-phase CO<sub>2</sub> abundance profile is extracted as function of temperature and interpolated onto the DALI midplane temperatures. The abundance is taken to be vertically constant up to the point where  $A_V = 1$ . In some variations an abundance floor of 10<sup>-9</sup> or 10<sup>-8</sup> is used for cells with  $A_V > 1$  to simulate local CO<sub>2</sub> production. Using the resulting abundance structure, the non-LTE excitation of CO<sub>2</sub> is calculated using the rate coefficients from Bosman et al. (2017). Finally the DALI line ray-tracing module calculates the line fluxes for CO<sub>2</sub> and its <sup>13</sup>C isotope.

For calculating the spectra, the same disk model is used as in Bruderer et al. (2015) and Bosman et al. (2017). The model is based on the disk AS 205 N. The parameters for the DALI models can be found in Table 4.3. For more specifics on the modelling of the spectra and adopted parameters, see Bruderer et al. (2015) and Bosman et al. (2017). To simulate the high gas-to-dust ratios that are inferred from water observations (Meijerink et al. 2009), the overall gas-to-dust ratio is set at 1000 throughout the disk. The artificially high gas-to-dust ratio does not affect any of the modelling, except for the line formation, which is only sensitive to the upper optically thin layers of the disk. High gas-to-dust ratios effectively mimic settled dust near the midplane containing ~90% of the dust mass.

## 4.4 Results

### 4.4.1 Pure viscous evolution

To start, a dynamical model without grain growth and without any chemistry (except for freeze-out and desorption) is investigated. Fig. 4.3 shows the time evolution for a model with  $\alpha = 10^{-3}$ . As expected, the total gas and dust surface densities barely change over 10<sup>6</sup> yr. The gas and dust evolve viscously, some mass is accreted onto the

**Table 4.3:** Adopted standard model parameters for the DALI modelling.

Parameter		Value
Star		
Mass	$M_{\star} [M_{\odot}]$	1.0
Luminosity	$L_{\star} [L_{\odot}]$	4.0
Effective temperature	$T_{\text{eff}} [\text{K}]$	4250
Accretion luminosity	$L_{\text{accr}} [L_{\odot}]$	3.3
Accretion temperature	$T_{\text{accr}} [\text{K}]$	10000
Disk		
Dustdisk mass	$M_{\text{dust}} [M_{\odot}]$	$2.9 \times 10^{-4}$
Surface density index	$p$	0.9
Characteristic radius	$R_c [\text{AU}]$	46
Inner radius	$R_{\text{in}} [\text{AU}]$	0.19
Scale height index <sup>b</sup>	$\psi$	0.11
Scale height angle <sup>b</sup>	$h_c [\text{rad}]$	0.18
DALI dust properties <sup>a</sup>		
Size	$a [\mu\text{m}]$	0.005 – 1000
Size distribution		$dn/da \propto a^{-3.5}$
Composition		ISM
Gas-to-dust ratio		1000
Distance	$d [\text{pc}]$	125
Inclination	$i [^{\circ}]$	20
<sup>12</sup> CO <sub>2</sub> : <sup>13</sup> CO <sub>2</sub> ratio		69

**Notes.** <sup>(a)</sup> Dust properties are the same as those used in Andrews et al. (2009) and Bruderer et al. (2015). Dust composition and optical constants are taken from Draine & Lee (1984) and Weingartner & Draine (2001). <sup>(b)</sup> Only used in the DALI model, not in the viscous disk model. The viscous disk model assumes a geometrically flat disk.

star while the outer disk spreads a little bit. There are no changes in gas-to-dust ratio in the disk.

The water abundance in the right panel of Fig. 4.3 shows no evolution at all. This is to be expected because the only radial evolution is due to the gas viscosity, which affects gas and dust equally. Diffusion of the icy dust grains is equally quick as the diffusion of the water vapour. This means that all the water vapour that diffuses outwards is compensated by icy dust grains diffusing inwards.

The abundance of CO<sub>2</sub> in the middle panel of Fig. 4.3 does show evolution. Initially there is only a little bit of CO<sub>2</sub> gas in the inner disk, but a large amount of ice in the outer disk. The abundance gradient together with the viscous accretion makes the icy CO<sub>2</sub> move inwards, filling up the inner disk with CO<sub>2</sub> gas. This continues for about  $1 \times 10^6$  yr until the gaseous abundance of CO<sub>2</sub> is equal to the abundance of icy CO<sub>2</sub>. This time-scale directly scales with the assumed  $\alpha$  parameter. For  $\alpha = 10^{-4}$  it takes more than 3 Myr to get a flat abundance profile in the inner disk.

#### 4.4.2 Viscous evolution and grain growth

For the models including grain growth, we tested a range of fragmentation velocities from 1 to 30 m s<sup>-1</sup>. For some of these models, especially those with low fragmentation velocities and high  $\alpha$ , the results are indistinguishable from the case without grain growth. Figs. 4.4 and 4.5 show two models where the effect of grain growth and resulting drift can be seen.

Fig. 4.4 shows the surface density and abundance evolution for a model with a fragmentation velocity of 3 m s<sup>-1</sup> as appropriate for pure silicate grains. The surface density of the dust shows a small evolution due to radial drift. Instead of decreasing, the surface density of dust in the inner 4 AU slightly increases in the first 300'000 yr due to the supply of dust particles from outside this radius.

The abundance profiles in Fig. 4.4 show distinct effects of radial drift. Both the gaseous H<sub>2</sub>O and CO<sub>2</sub> abundances are high at all times due to the influx of drifting icy grains. There is also a decrease in the abundance of ices at large radii. This is because the grains carrying the ices have moved inwards, increasing the gas-to-ice ratios.

The models are not in steady state after 1 Myr. If these models are evolved further, at first the abundances of H<sub>2</sub>O and CO<sub>2</sub> will increase further. At some point in time the influx of dust will slow down, because a significant part of the dust in the outer disk will have drifted across the snowline. At this point the inner disk abundances of H<sub>2</sub>O and CO<sub>2</sub> start to decrease as these molecules are lost due to accretion onto the star but no longer replenished by dust from the outer disk. For the model shown in Fig. 4.4 the average gas-to-dust ratio in the disk would be around 500 after 3 Myr.

For higher  $\alpha$  the effects of radial drift are limited as the high rate of mixing smooths out concentration gradients created by radial drift. At the same time the maximum grain size is limited due to larger velocity collisions at higher turbulence. As such, for  $\alpha = 0.01$  a fragmentation velocity higher than 10 m s<sup>-1</sup> is needed to see significant effects of radial drift and grain growth.

For lower  $\alpha$  the effects of grain growth get more pronounced, 90% of the dust mass is accreted onto the star in 2.5 Myr for a fragmentation velocity of 1 m s<sup>-1</sup>. In this time a lot of molecular material is released into the inner disk and peak abundances of  $10^{-3}$  and  $10^{-2}$  are reached for CO<sub>2</sub> and H<sub>2</sub>O, respectively, after 1 Myr of evolution. Due to the low turbulence in the gas, the volatiles released are not well mixed, neither

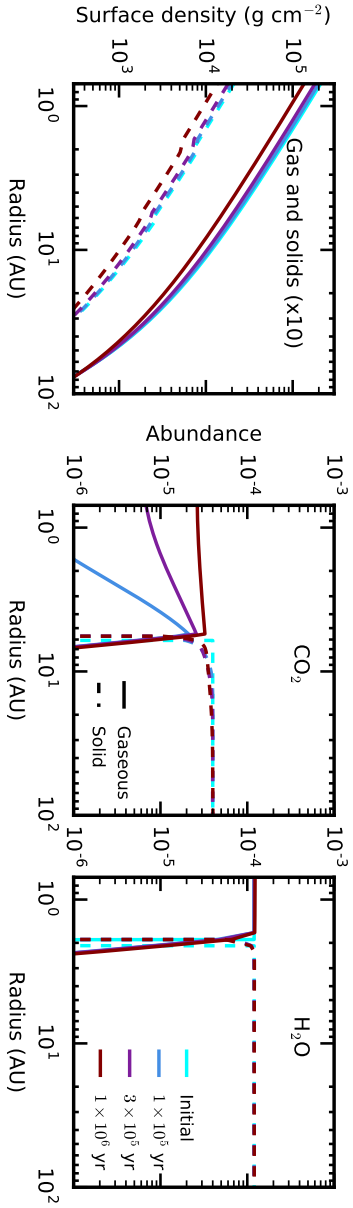


**Figure 4.3:** Time evolution series for a model without grain growth. This model assumes an  $\alpha$  of  $10^{-3}$ . *Left:* Surface density of the gas (solid lines) and solids (dashed lines), the solid surface density is the sum of the dust and ice surface densities, it has been multiplied by a factor of 10 for visualization. *Middle:* Abundance of  $\text{CO}_2$ . *Right:* Abundance of  $\text{H}_2\text{O}$ .

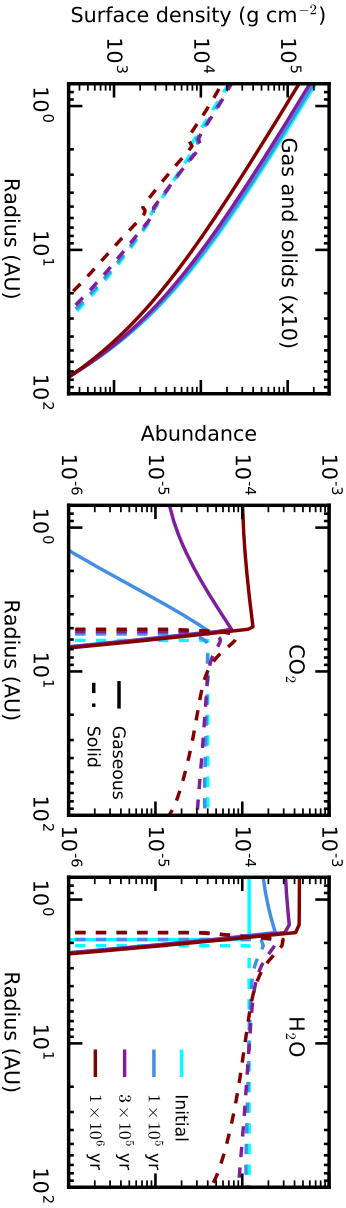


**Figure 4.4:** Time evolution series for a model with grain growth. This model assumes an  $\alpha$  of  $10^{-3}$ . The fragmentation velocity for this model is  $3 \text{ m s}^{-1}$ . Panels as in Fig. 4.3.

inwards nor outwards, so there is no strong enhancement of the ice surface density just outside of the iceline. An overview of the different model evolutions can be found in App. 4.C.

Increasing the fragmentation velocity allows grains in the model to grow to larger sizes, leading again to larger amounts of radial drift. Fig 4.5 shows the evolution of the same model as shown in Fig. 4.4, but with a fragmentation velocity of  $30 \text{ m s}^{-1}$ , representative for grains coated in water ice. The solid surface density distribution clearly shows the effects of grain growth. At all radii, mass is moved inwards at a high rate. When the silicate surface density has dropped by an order of magnitude, a local enhancement in the surface density of the total solids is seen at the icelines. This enhancement is about a factor of 2 for both icelines.

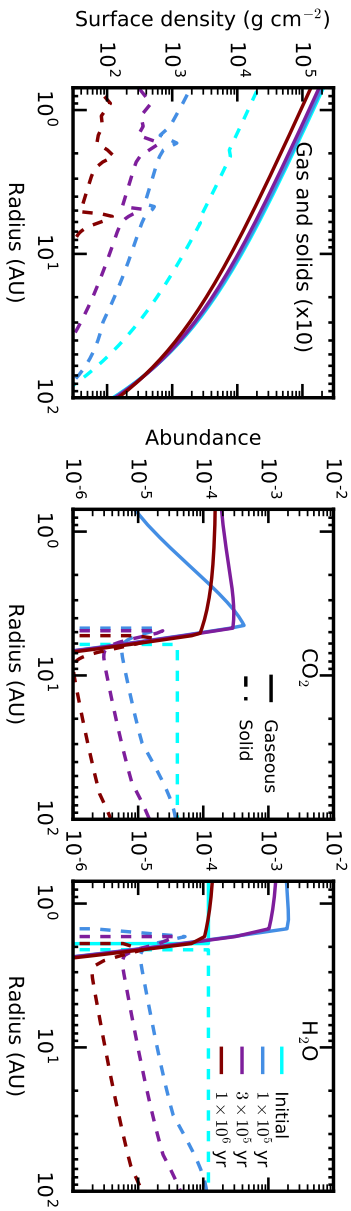
The gas-phase abundances of  $\text{CO}_2$  and  $\text{H}_2\text{O}$  both show a large increase in the first  $3 \times 10^5 \text{ yr}$  due to the large influx of icy pebbles. At later times, the abundances are decreased again as the volatiles are accreted onto the star. After  $3 \times 10^6 \text{ yr}$  the  $\text{H}_2\text{O}$  and  $\text{CO}_2$  abundances are lower than  $10^{-5}$ .

### 4.4.3 Viscous evolution and $\text{CO}_2$ destruction

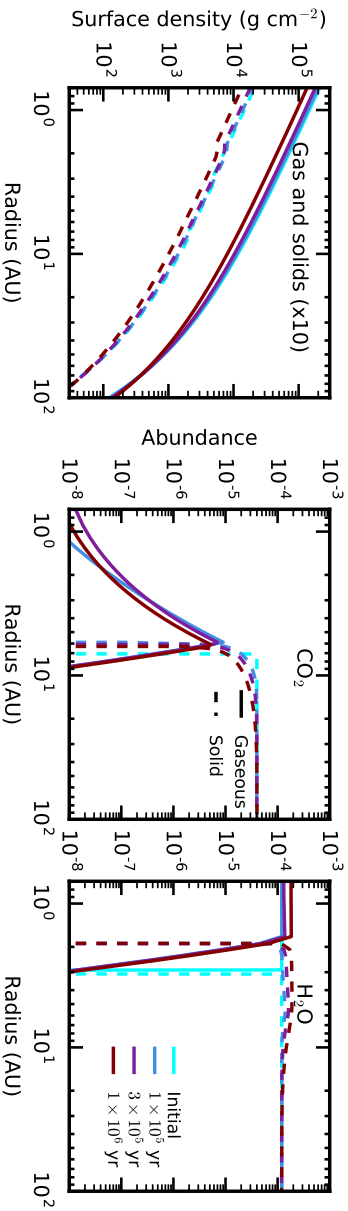
The models shown in Fig. 4.3–4.5 without any chemical processing predict  $\text{CO}_2$  abundances that are very high in the inner regions,  $10^{-5}$ – $10^{-4}$ , orders of magnitude higher than the value of  $\sim 10^{-8}$  inferred from observations (Pontoppidan & Blevins 2014; Bosman et al. 2017). There are multiple explanations for this disparity, both physical and chemical, which are discussed in §5. Here we investigate how large any missing chemical destruction route for gaseous  $\text{CO}_2$  would need to be. As discussed in Sect. 4.3 and App. 4.B.1, midplane  $\text{CO}_2$  can only be destroyed by cosmic-ray induced processes in the current networks. However, both cosmic ray induced photodissociation and  $\text{He}^+$  production are an order of magnitude slower than the viscous mixing time. We therefore introduce additional destruction of gaseous  $\text{CO}_2$  with a rate that is a constant over the entire disk. This rate is varied between  $10^{-13}$  and  $10^{-9} \text{ s}^{-1}$  to obtain agreement with observations. For comparison, the cosmic ray induced process generally have a rate of the order of  $10^{-14} \text{ s}^{-1}$  (see Sect. 4.3.2). The rate is implemented as an effective destruction rate, so there is no route back to  $\text{CO}_2$  after destruction. To get the absolute rate one has to also take into account the reformation efficiency, but that can be strongly dependent on the destruction pathway, of which we are agnostic. These efficiencies are discussed in §5 and App. 4.B.

Fig. 4.6 shows the abundance evolution for a model where only gaseous  $\text{CO}_2$  is destroyed, at a rate of  $10^{-11} \text{ s}^{-1}$ . In this case the innermost parts of the disk are empty of  $\text{CO}_2$ , whereas the abundance of  $\text{CO}_2$  reaches values close to the initial ice abundances around the iceline. Due to the constant destruction of  $\text{CO}_2$  near the iceline, the actual ice abundance of  $\text{CO}_2$  is also lower than the initial value.

The left panel of Fig. 4.7 shows the  $\text{CO}_2$  abundance distribution for models with  $\alpha = 10^{-3}$ . The abundance profiles after 1 Myr of evolution are presented, when a semi-steady state has been reached. The peak abundance and peak width of the  $\text{CO}_2$  gas abundance profile both depend on the assumed destruction rate: a higher rate leads to a lower peak abundance and a narrower peak, while a lower rate leads to the opposite. A rate of  $\sim 10^{-11} \text{ s}^{-1}$  or higher is needed to decrease the average gaseous  $\text{CO}_2$  abundance below the observational limit (see below). Increasing the rate moves the location of the iceline further out, as the total available  $\text{CO}_2$  near the iceline



**Figure 4.5:** Time evolution series for a model with grain growth. The fragmentation velocity for this model is  $30 \text{ m s}^{-1}$  and  $\alpha = 10^{-3}$ . The vertical scales are different from Figs. 4.3 and 4.4. Panels as in Fig. 4.3.



**Figure 4.6:** Time evolution series for a model without grain growth but with a constant destruction rate of gaseous  $\text{CO}_2$  of  $10^{-11} \text{ s}^{-1}$ . This model assumes an  $\alpha$  of  $10^{-3}$ . Panels as in Fig. 4.3, but with different vertical scales.

decreases. The viscosity also influences the width of the abundance profile, higher viscosities lead to a broader abundance peak.

#### 4.4.4 Viscous evolution, grain growth and CO<sub>2</sub> destruction

The next step is to include CO<sub>2</sub> destruction in viscous evolution models with grain growth. Here only models that retain the disk dust mass, that is, models that have an overall gas-to-dust ratio smaller than 1000 after 1 Myr of evolution are considered since there is no observational evidence for very high gas-to-dust ratios. This means that the grains in our models do not reach pebble sizes such as have been inferred from observations (e.g. Pérez et al. 2012; Tazzari et al. 2016). It is unclear how these large grains are retained in the disk as the radial drift timescale for these particles is expected to be shorter than the disk lifetime (e.g. Birnstiel et al. 2010; Krijt et al. 2016b). The requirement of dust retention restricts our models to  $\alpha = 10^{-4}$  and  $u_f = 1 \text{ m s}^{-1}$ ,  $\alpha = 10^{-3}$  and  $u_f = 1, 3 \text{ m s}^{-1}$ , and  $\alpha = 10^{-2}$  and  $u_f = 1, 3, 10 \text{ m s}^{-1}$ .

The abundance profiles for different CO<sub>2</sub> destruction rates are shown in the right panel of Fig. 4.7 for the model with  $\alpha = 10^{-3}$  and  $u_f = 3 \text{ m s}^{-1}$ . The abundance profiles are determined after 1 Myr, when the disk is in a semi-steady state. A destruction rate higher than  $10^{-12} \text{ s}^{-1}$  will create an abundance profile with clear abundance maximum at the iceline, but for this rate  $10^{-12} \text{ s}^{-1}$  the disk surface area averaged CO<sub>2</sub> abundance is still higher than the observed value for both cases. Only for a rate of around  $10^{-10} \text{ s}^{-1}$  do the models predict an abundance profile with a disk surface area averaged CO<sub>2</sub> abundance that is consistent with the high end of the observations. Only the models with destruction rate higher than  $10^{-9} \text{ s}^{-1}$  have a peak in the abundance that is consistent with the maximal inferred abundances from the observations. As shown in Fig. 4.7 the model with a rate of  $10^{-11} \text{ s}^{-1}$  will create a spectrum consistent with the observations, even though the average CO<sub>2</sub> abundance is higher than the observed abundance limit.

For the selected models, the effect of different fragmentation velocities is small, with differences in peak abundances less than a factor of five between similar models, as seen in Fig. 4.7. This is unsurprising as the selection criteria for the models only consider models that have a transport velocity of solids that is less than an order of magnitude faster than the transport velocity of the model without grain growth and radial drift. For models with faster growth it becomes more arbitrary to give a representative abundance profile as semi steady state is not reached at any point in time before the disk is depleted of most of the dust and volatiles in the inner regions. However, for very young disks that may have very efficient radial drift of grains, a high gas-phase CO<sub>2</sub> abundance is expected within the CO<sub>2</sub> iceline unless the destruction rate is  $10^{-11} \text{ s}^{-1}$  or higher.

#### 4.4.5 Model spectra

The spectral modelling focuses on the CO<sub>2</sub> bending mode around centred at  $15 \mu\text{m}$ . This bending mode has a strong *Q*-branch that has been observed by *Spitzer* in protoplanetary disks (Carr & Najita 2008; Pontoppidan et al. 2010). This region also has a weaker feature due to the *Q*-branch of <sup>13</sup>CO<sub>2</sub> at  $15.42 \mu\text{m}$  which can be used, together with the <sup>12</sup>CO<sub>2</sub> *Q*-branch, to infer information on the abundance structure (Bosman et al. 2017).



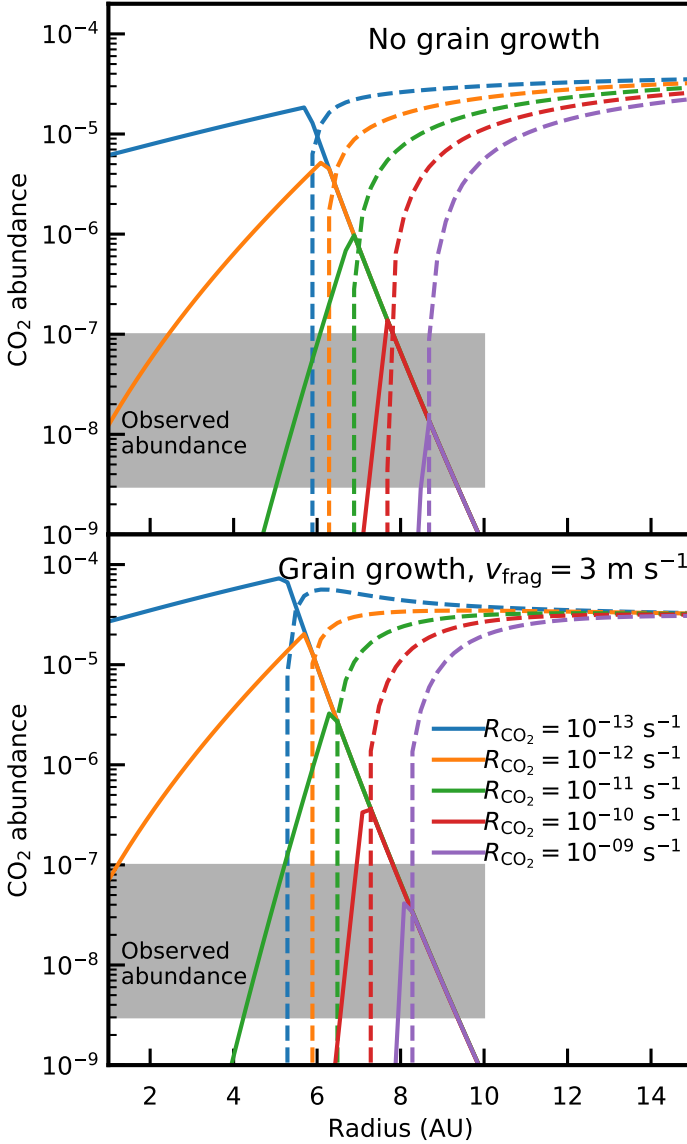


**Figure 4.7:** Abundance of  $\text{CO}_2$  as function of radii for models with different destruction rates of  $\text{CO}_2$ . These model use  $\alpha = 10^{-3}$  and  $u_f = 0 \text{ m s}^{-1}$  (*top*) and  $u_f = 3 \text{ m s}^{-1}$  (*bottom*). Abundance profiles after 1 Myr of evolution are shown. At this point the disk has reached a semi steady state. A destruction rate of at least  $10^{-11} \text{ s}^{-1}$  is needed to keep the averaged  $\text{CO}_2$  abundance below the observational limit. The iceline is further out for models with higher destruction rates as the destruction of gas-phase  $\text{CO}_2$  lowers the total abundance of  $\text{CO}_2$  within 10 AU where  $\text{CO}_2$  can sublimate.

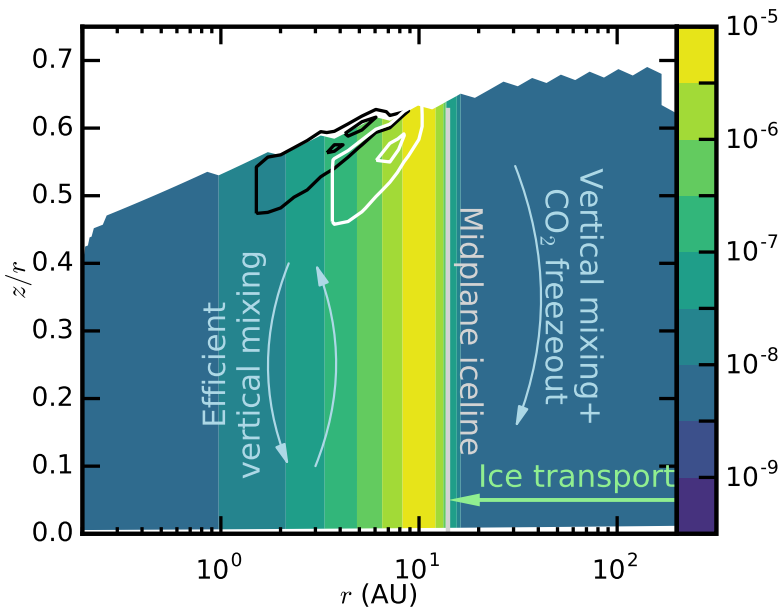


**Figure 4.8:** 2D  $\text{CO}_2$  abundance distribution from the  $R_{\text{destr,CO}_2} = 10^{-11}$  model with an abundance floor of  $10^{-9}$ . Black and white lines show the regions where 25% and 75% of the emission of respectively  $^{12}\text{CO}_2$  and  $^{13}\text{CO}_2$  is emitted from. The  $^{13}\text{CO}_2$  emission is more concentrated around the region with the abundance enhancement.

For the model with  $\alpha = 10^{-3}$  and  $R_{\text{destr,CO}_2} = 10^{-11}$ , the 2D abundance distribution assumed for the ray-tracing is shown in Fig. 4.8. The enhanced  $\text{CO}_2$  abundance around the iceline shows up clearly. The results of the continuum ray-tracing can be found in Fig. 5 of Bosman et al. (2017). The temperature at 1 AU is 320 K. This is higher than the value assumed for the models in the previous sections and is in line with the high luminosity of the modelled source of  $7.7 L_{\odot}$ . The higher temperature moves the  $\text{CO}_2$  iceline slightly further out. The abundance profiles from the viscous model with dust growth and  $\text{CO}_2$  destruction are still very similar to those from the previous section.

Fig. 4.8 also shows the emitting region of the  $\text{CO}_2$   $Q(6)$  line for both isotopologues. This is one of the strongest lines in the  $\text{CO}_2$  spectrum and part of the  $Q$ -branch. As such it is a good representative for the complete  $Q$ -branch. Due to its high abundance, the  $^{12}\text{CO}_2$  lines have a high optical depth over a larger area in the disk. As such a large part of the disk contributes to the emission of the  $^{12}\text{CO}_2$  lines. For  $^{13}\text{CO}_2$  the emission is from a more compact area, close to the peak in  $\text{CO}_2$  abundance.

Fig. 4.9 shows  $\text{CO}_2$  spectra for different destruction rates and abundance floor of  $10^{-8}$ . Line-to-continuum ratios for the individual  $R$  and  $P$  branch lines are all greater than 0.01 and are detectable by *JWST* (Bosman et al. 2017). Note that only even  $J$  levels exist in the vibrational ground state, so  $P$ ,  $Q$  and  $R$  branch lines exist only every other  $J$  for this band. Both the  $^{12}\text{CO}_2$  and the  $^{13}\text{CO}_2$   $Q$ -branch fluxes are influenced by the different destruction rates. For a rate of  $10^{-12} \text{ s}^{-1}$  the  $^{12}\text{CO}_2$   $Q$ -branch is a factor

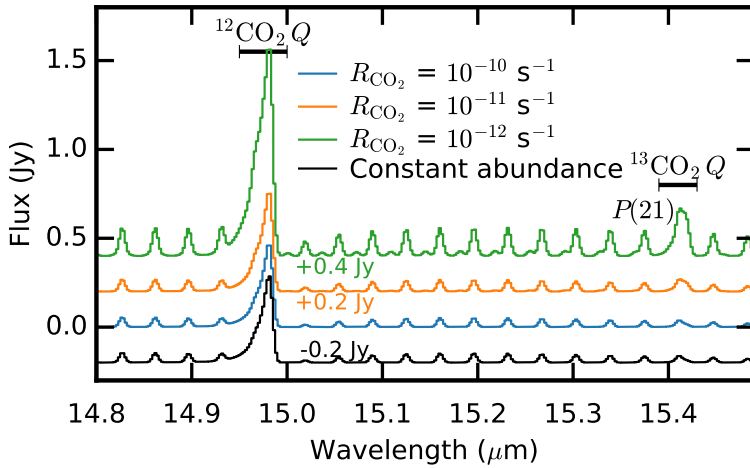


**Figure 4.9:** Spectra  $^{12}\text{CO}_2$  and  $^{13}\text{CO}_2$  for models with different destruction rates at a spectral resolving power  $R = 2200$  appropriate for JWST-MIRI. The abundance floor is taken to be  $10^{-8}$ . The black line shows the model results for a constant abundance as used in Bosman et al. (2017). The regions where the  $Q$ -branch flux is extracted is shown in the black lines. The  $^{13}\text{CO}_2$   $Q$ -branch is blended with the  $^{12}\text{CO}_2$   $P(23)$  line. The neighbouring  $P(21)$  line is indicated. Note that the models with destruction rates of  $10^{-11}$  and  $10^{-10} \text{ s}^{-1}$  are indistinguishable in their  $^{12}\text{CO}_2$  spectra.

of two brighter than for the higher rates, which give fluxes very similar in magnitude for the  $^{12}\text{CO}_2$   $Q$ -branch. For  $^{13}\text{CO}_2$  the model with a destruction rate of  $10^{-12} \text{ s}^{-1}$  is at least a factor of five brighter than the models with higher rates of  $10^{-11} \text{ s}^{-1}$  and  $10^{-10} \text{ s}^{-1}$ . Since the latter two  $^{12}\text{CO}_2$  spectra are indistinguishable observationally, a conservative lower limit to the destruction rate of  $10^{-11} \text{ s}^{-1}$  is chosen. For  $^{13}\text{CO}_2$  however, there is a factor of three difference between the two higher rate models; here the  $^{13}\text{CO}_2$   $Q$ -branch flux is determined by subtracting the contribution from the  $^{12}\text{CO}_2$   $P(23)$ -line assuming it is the same as that of the neighbouring  $P(21)$  line.

The flux ratio of the  $^{13}\text{CO}_2$   $Q$ -branch over the  $^{12}\text{CO}_2$   $Q$ -branch is shown in Fig. 4.10 for a range of  $\text{CO}_2$  destruction rates. Three regimes can be seen. For ratios larger than  $\sim 0.13$  the  $\text{CO}_2$  released from the ice dominates the abundance profile and spectrum, due to the relatively low destruction rate. The high  $\text{CO}_2$  column, due to the high abundance around the iceline sets the small flux ratio. At ratios smaller than 0.03, corresponding to destruction rates larger than  $5 \times 10^{-11} \text{ s}^{-1}$ , the  $\text{CO}_2$  released from the ice at the iceline is destroyed so fast that it can not leave an imprint on the  $Q$ -branch fluxes. In the region in between, both the  $\text{CO}_2$  released at the iceline as well as the upper layer  $\text{CO}_2$  influence the spectra, as such the flux ratio not only depends on the  $\text{CO}_2$  destruction rate, but also on the  $\text{CO}_2$  abundance floor used.

Note that Bosman et al. (2017) show that a high  $^{13}\text{CO}_2$   $Q$ -branch over  $^{12}\text{CO}_2$   $Q$ -branch flux ratio may also be an indication of a high abundance in the inner disk. More generally it can be said that a high flux ratio indicates that the  $\text{CO}_2$  responsible for the emission is highly optically thick. In these cases the width of the  $^{13}\text{CO}_2$   $Q$ -branch can be a measure for the temperature of this emitting gas, which can be related to the radial location of the origin of the emission. An analysis like this will probably only

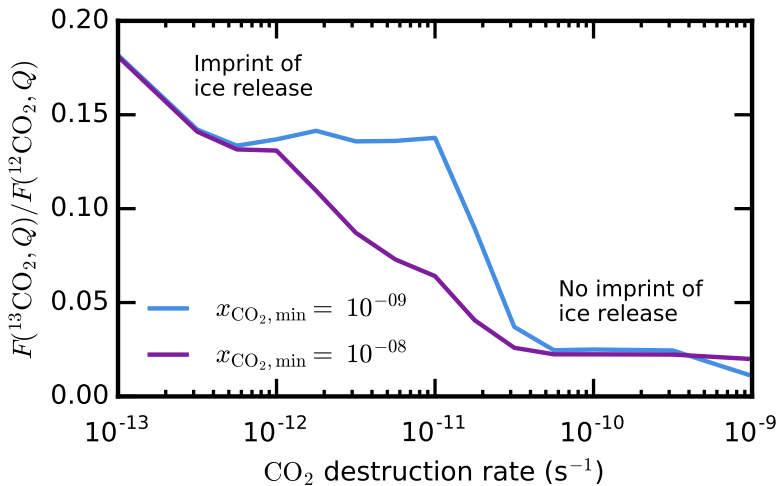


**Figure 4.10:** Flux ratios of the  $^{13}\text{CO}_2$  and  $^{12}\text{CO}_2$   $Q$ -branches, determined by integrating the region shown in Fig. 4.9. The  $^{13}\text{CO}_2$   $Q$ -branch flux is corrected for the emission of the  $P(23)$  line by subtraction of the neighbouring  $P(21)$  line flux.

be possible with disk specific modelling.

The spectral modelling done here is meant as an illustration to what could be possible with *JWST*-MIRI observations and to show what kind of spectral features could hold clues to new insights into disk dynamics. As such the model setup is not entirely self consistent. Foremost, the temperature profiles calculated from the radiative transfer are not exactly the same as the temperature profile used in the viscous disk model. Furthermore, the starting point for our viscous evolution is rather arbitrary.

Another uncertainty is the vertical distribution of the  $\text{CO}_2$  sublimated from the ices. The assumed turbulent viscosity would not only mix material radially, but also vertically, and the  $\text{CO}_2$  that comes off the grain near the midplane should make it up to the upper layers of the disk where the infrared emission is generated.

The vertical dispersion of a species injected into the disk midplane grows with time as  $\sigma_X = \sqrt{D_{\text{gas}} t}$  (Ciesla 2010). A steady state is reached if  $\sigma_X = H$ , the scale height of the disk, at which point a constant abundance is reached. As such we can estimate the time needed for vertical mixing. For a self-similar disk, this time scale becomes:

$$t_{\text{vert, eq}} = 9.1 \left( \frac{0.01}{\alpha} \right) \left( \frac{r}{1\text{AU}} \right)^{0.5+q} \left( \frac{200}{T_{1\text{AU}}} \right)^q \left( \frac{h_{\text{FWHM}}}{0.05} \right) \text{yr}. \quad (4.36)$$

If a similar mixing speed ( $\alpha$ ) is assumed for the radial and vertical processes, then vertical mixing should happen well within the lifetime of the disk for locations near the  $\text{CO}_2$  iceline.

Given these uncertainties, a simple constant abundance up to a certain height has been chosen. However higher up in the disk, photodissociation by stellar radiation and processing by stellar X-rays become important.  $\text{CO}_2$  is removed in our model in the harshest environments ( $A_V < 1$  mag), but  $\text{CO}_2$  photodissociation is still possible in the upper disk regions where  $\text{CO}_2$  is included. The location and thickness of this layer is discussed in Sect. 4.5.2 and 4.5.2

## 4.5 Discussion

Viscous disk models including only freeze-out and desorption of CO<sub>2</sub> predict a higher CO<sub>2</sub> abundance than observed. This conclusion holds even for models without grain growth and radial drift. The discussion is divided into two sections, first the gas and grain surface chemistry is discussed to explore alternative chemical destruction routes. Subsequently physical effects are investigated, some of which also imply chemical effects to happen. Fig 4.11 shows the CO<sub>2</sub> abundance structure in the disk with some of the mechanisms discussed here that could obtain agreement between observations and models.

### 4.5.1 Chemical processes

In the scenario that the CO<sub>2</sub> released at the iceline is destroyed, an effective destruction rate of  $10^{-11} \text{ s}^{-1}$  or higher is required to match the observed and computed abundances. In Sect. 4.3.2 and Sect. 4.3.2 a number of known destruction processes for midplane CO<sub>2</sub> were discussed, but none of these chemical processes is able to account for the destruction rate of  $10^{-11} \text{ s}^{-1}$ .

#### Clues from high-mass protostars?

Our finding that a CO<sub>2</sub> ice desorption model is inconsistent with CO<sub>2</sub> gas-phase observations is not the first to do so. For high mass protostars Boonman et al. (2003a) noted a similar disagreement between simple in-fall and desorption models, which predict CO<sub>2</sub> gas-phase abundances around  $10^{-5}$  whereas observations are more consistent with an abundance of  $\sim 10^{-7}$ , a two orders of magnitude difference. Assuming that the CO<sub>2</sub> ice sublimates and is destroyed within the dynamical time of  $10^4 \text{ yr}$ , a destruction rate of at least  $10^{-11} \text{ s}^{-1}$  is needed for protostars as well, of the same order as the rate needed in disks. If the CO<sub>2</sub> destruction mechanism is similar in both types of sources, then this would most likely be a chemical destruction mechanism with no or a weak dependence on total density since densities in protostellar envelopes are orders of magnitude lower than in the inner disk midplanes and the physical environments are very different. However, as argued below the existence of such a chemical pathway is unlikely, except for destruction by UV photons or X-rays.

#### Alternative gas phase destruction routes

Here we investigate whether a chemical pathway could be missing in the chemical networks. Since ion-molecule reactions initiated by He<sup>+</sup> have already been discarded, the assumption is that this destruction comes from a neutral-neutral reactive collision. The rate for a two-body reaction can be written as:

$$R_{\text{CO}_2, \text{destr}} = f_X k_{2\text{-body}} n_{\text{gas}} x_X \quad (4.37)$$

where  $n_{\text{gas}}$  is the gas number density,  $k_{2\text{-body}}$  is the two-body reaction rate coefficient,  $x_X$  is the abundance of the collision partner and  $f_X$  is the branching ratio to any product that does not cycle back to CO<sub>2</sub>. Near the iceline densities are around  $10^{13} \text{ cm}^{-3}$ , a typical rate coefficient for a barrier-less neutral-neutral reaction is around  $10^{-11} \text{ cm}^3 \text{ s}^{-1}$ . As such the partner abundance needs to be higher than  $10^{-13}$  to destroy CO<sub>2</sub> at a fast enough rate. The only species that have a nearly barrier-less reaction with CO<sub>2</sub>

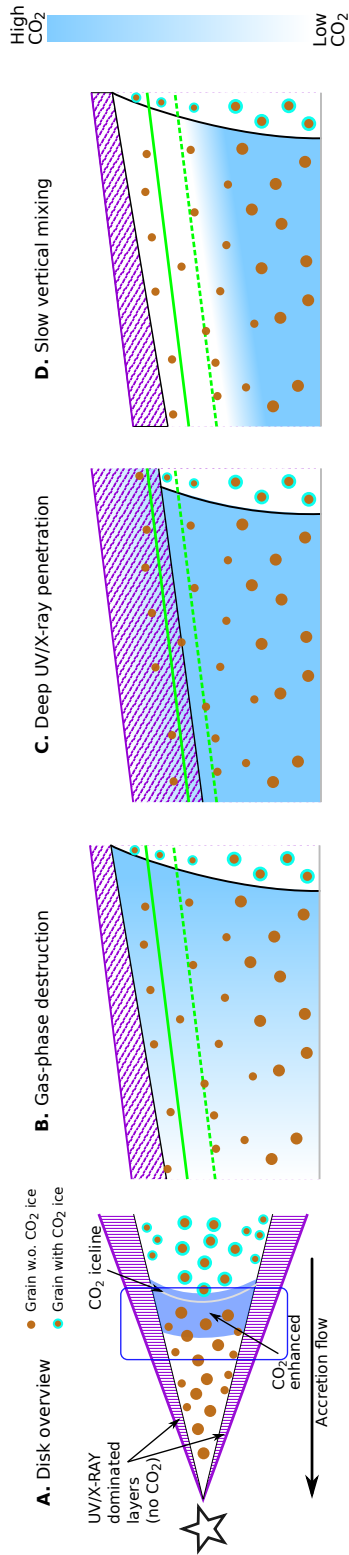


**Figure 4.11:** Schematic representation of the CO<sub>2</sub> abundance near the iceline in the  $r - z$  plane. Panels B, C and D approximately represent the top half of the blue box in panel A. The straight green lines denote the  $\tau = 1$  surface for <sup>12</sup>CO<sub>2</sub> (solid) and <sup>13</sup>CO<sub>2</sub> (dashed). Panels B, C and D show the abundance structure under different mechanisms to explain the difference in CO<sub>2</sub> abundance between the predictions of the viscous model and the IR observations. Panel B represents the case for a constant gas-phase destruction rate due to some as yet unidentified process (Sect. 4.4.4). Panel C shows the abundance structure for deep UV/X-ray penetration (Sect. 4.5.2 and 4.5.2). In more extreme cases, the <sup>13</sup>CO<sub>2</sub>  $\tau = 1$  surface can also be in the UV/X-ray dominated region. Panel D shows the abundance structure for negligible vertical mixing (Sect. 4.5.2). Image not to scale.

in either the UMIST (McElroy et al. 2013) or KIDA (Wakelam et al. 2012) databases are C, CH<sub>2</sub> and Si. Reaction rates for CO<sub>2</sub> with C to form two CO molecules and with CH<sub>2</sub> to form CO + H<sub>2</sub>CO are  $10^{-15}$  cm<sup>3</sup> s<sup>-1</sup> and  $3.9 \times 10^{-14}$  cm<sup>3</sup> s<sup>-1</sup> (Tsang & Hampson 1986), however, both rates are high temperature estimates and extrapolated to low temperatures (Hébrard et al. 2009). The rate for CO<sub>2</sub> + Si  $\longrightarrow$  CO + SiO has been measured at room temperature to be  $1.1 \times 10^{-11}$  cm<sup>3</sup> s<sup>-1</sup> (Husain & Norris 1978), McElroy et al. (2013) assume a small energy barrier of 282 K, in line with the high temperature measurements. Other species in the databases that have an exothermic reaction with CO<sub>2</sub> are CH and N; both of these reactions are thought to have a barrier of 3000 and 1710 K respectively (Mitchell 1984; Avramenko & Krasnen'kov 1967). Other neutral-neutral reactions in the chemical networks are highly endothermic, for example CO<sub>2</sub> + S  $\longrightarrow$  CO + SO is endothermic by  $\sim 20000$  K (Singleton & Cvetanovic 1988), effectively nullifying this reaction in the temperature range we are interested in.

C, CH<sub>2</sub> and Si are, due to their high reactivity, only present in very low quantities in the gas-phase with abundances at the solver accuracy limit of  $10^{-17}$  for C and CH<sub>2</sub>, and  $10^{-16}$  for Si and thus can hardly account for the destruction of a significant amount of CO<sub>2</sub> unless it is possible to quickly reform the initial reactant from the reaction products. The reactions products, CO, H<sub>2</sub>CO and SiO, are again very stable, thus it is unlikely that these molecules quickly react further to form the initial reactants again. This means that the abundance of C, CH<sub>2</sub> and Si will go down with time if more and more CO<sub>2</sub> is added.

### Alternative ice destruction routes

The low CO<sub>2</sub> abundance observed could also be explained if CO<sub>2</sub> is converted to other species while in the ice. Bisschop et al. (2007) report that CO<sub>2</sub> bombarded with H does not lead to HCOOH at detectable levels in their experiments. There are no data available on grain surfaces reactions of CO<sub>2</sub> ice with N, Si or C. If any of these reaction pathways were to destroy CO<sub>2</sub> in the ice, they should be very efficient,  $\sim 99\%$  conversion, but at the same time be able to explain the high CO<sub>2</sub> ice abundances in comets. This quickly limits the temperature range in which these reactions can be efficient to 30–80 K.

In short, due to the high stability of CO<sub>2</sub>, only a handful of highly reactive radicals or atoms can destroy CO<sub>2</sub>, whether in the gas or ice. None of these species is predicted to be abundant enough to quickly destroy the large flux of CO<sub>2</sub> that is brought into the inner disk due to dynamic processes of CO<sub>2</sub>-containing icy grains.

### 4.5.2 Physical processes

The abundance profiles computed in this work all assume that the CO<sub>2</sub> can move freely through the disk, both in radial and vertical directions, while being shielded from UV and X-ray radiation. It is also assumed that all CO<sub>2</sub> ice sublimates at the CO<sub>2</sub> iceline and that CO<sub>2</sub> is highly abundant in the ice, as found in the ISM. Several physical processes could make these assumptions invalid. An important constraint is that due to the difference between the ice abundances (around  $10^{-5}$ ) and the inferred gas abundance ( $< 10^{-7}$ ) any process needs reduce the CO<sub>2</sub> abundance in the infrared emitting layers by at least two orders of magnitude.

### Impact of reduced turbulence

The current models assume a standard viscously spreading and evolving disk with a constant  $\alpha$  value. Magneto-hydrodynamical (MHD) simulations currently favour disks with strongly changing viscosity in radial and vertical directions (e.g. Gammie 1996; Turner et al. 2007; Bai & Stone 2013). In these simulations turbulence is only expected to be high at those locations where the ionisation fraction of the gas is also high, that is, the upper and outer regions of the disk. In the disk mid-plane the viscous  $\alpha$  may be as low as  $10^{-6}$ , especially if non-ideal MHD effects are taken into account. In this regime, radial and vertical mixing due to the turbulence becomes a very slow process, with mixing time-scales close to the disk lifetime. Laminae accretion through the midplane would still enrich the inner disk midplane with  $\text{CO}_2$  but the low vertical mixing would greatly reduce the amount of material that is lifted into the IR-emitting layers of the disk. A mixing time of  $10^6$  years would imply an effective vertical  $\alpha$  of  $10^{-6}$  for a  $\text{CO}_2$  iceline at 10 AU (Eq. 4.36, Ciesla 2010). Note that this still means that  $\text{CO}_2$  is mixed upwards within  $10^5$  years in the inner 1 AU, which would be visible as an added warmer component to the  $\text{CO}_2$  emission. Observations of another species created primarily on grains at high abundance,  $> 10^{-7}$ , such as  $\text{CH}_4$ ,  $\text{NH}_3$  or  $\text{CH}_3\text{OH}$  near their respective icelines can be used to rule out inefficient vertical mixing.

### Trapping of $\text{CO}_2$ in large solids

There are ways to trap a volatile in a less volatile substance and prevent or delay its sublimation to higher temperatures. One possibility is to lock up the  $\text{CO}_2$  inside the water ice. This can be done in the bulk of the amorphous ice, below the surface layers, or by the formation of clathrates in the water ice at the high midplane pressures. Even in the case that  $\text{CO}_2$  is completely trapped in  $\text{H}_2\text{O}$  ice,  $\text{CO}_2$  still comes off the grain together with the  $\text{H}_2\text{O}$  at the  $\text{H}_2\text{O}$  iceline. At this point the  $\text{CO}_2$  is in the gas phase and free to diffuse around in the disk. The strong negative abundance gradient outside the  $\text{H}_2\text{O}$  iceline will transport the  $\text{CO}_2$  outwards until the  $\text{CO}_2$  starts to freeze-out of its own accord at the  $\text{CO}_2$  iceline. This would still result in gas-phase abundances within the  $\text{CO}_2$  iceline close to the original icy  $\text{CO}_2$  abundances of the outer disk.

Spherical grains between  $0.1 \mu\text{m}$  and 1 mm are coated with  $10^2$  to  $10^{10}$  layers of water ice, respectively. In the case of small particles, with only 100 layers of ice, it is hard to imagine that the water traps a significant amount of  $\text{CO}_2$ . For the larger grains with a smaller relative surface area, however, the water ice could readily trap a lot of  $\text{CO}_2$ . In a fully mixed  $\text{H}_2\text{O}$  and  $\text{CO}_2$  ice, the sublimation of  $\text{CO}_2$  from the upper 100 million ice layers will still keep the fraction of sublimated  $\text{CO}_2$  below 1%, however efficient grain fragmentation, such as assumed in our models, will expose  $\text{CO}_2$  rich layers allowing for the sublimation of more  $\text{CO}_2$ . For small grains, clathrates may keep the  $\text{CO}_2$  locked-up in the upper layers to prevent sublimation. However, to trap a single  $\text{CO}_2$  molecule at least six  $\text{H}_2\text{O}$  molecules are needed (Fleyfel & Devlin 1991).

For amorphous ices similar restrictions exist on the  $\text{H}_2\text{O}$  to  $\text{CO}_2$  ratio for trapping  $\text{CO}_2$  in the water ice. For ices with a  $\text{H}_2\text{O}$  to  $\text{CO}_2$  ratio of 5:1,  $\text{CO}_2$  desorption happens at the  $\text{CO}_2$  desorption temperature, only at a ratio of 20:1 is the  $\text{CO}_2$  fully trapped within the  $\text{H}_2\text{O}$  ice (Sandford & Allamandola 1990). Collings et al. (2004) show that the majority of the trapped  $\text{CO}_2$  desorbs at temperatures just below the desorption temperature of  $\text{H}_2\text{O}$ , due to the crystallization of water. Fayolle et al. (2011) note that the fraction of trapped  $\text{CO}_2$  also depends on the thickness of the ice. They are



able to trap 65% of the CO<sub>2</sub> in a 5:1 ice, which means that a significant fraction of the CO<sub>2</sub> still comes of at the CO<sub>2</sub> iceline.

Both of these mechanisms need to have all the CO<sub>2</sub> mixed with water. For interstellar dust grains there is observational evidence that this is not the case: high quality *Spitzer* spectra indicate that CO<sub>2</sub> is mixed in both the CO-rich layers of the ice as well as the H<sub>2</sub>O-rich layers of the ice (Pontoppidan et al. 2008b). Sublimation of CO from these mixed ices would create a CO<sub>2</sub> rich layer around the mixed H<sub>2</sub>O:CO<sub>2</sub> inner layers.

Another option would be to lock the CO<sub>2</sub> in the refractory material. We note however that the CO<sub>2</sub> ice abundance is of the same order as the Mg, Fe and Si abundances (Asplund et al. 2009), as such it is unlikely that CO<sub>2</sub> can be locked up in the refractory material without chemical altering that material, such as conversion into, for example, CaCO<sub>3</sub>.

Measurements from 67P/Churyumov-Gerasimenko indicate that even a kilometre-sized object outgasses CO<sub>2</sub> at 3.5 AU distance (Hässig et al. 2015). For larger objects, CO<sub>2</sub> retention might be possible, but locking up 99% of the CO<sub>2</sub> ice in these bodies seems highly unlikely.

### Trapping icy grains outside of the iceline

It is possible to stop the CO<sub>2</sub> from sublimating if the CO<sub>2</sub> ice never reaches the CO<sub>2</sub> iceline, for example by introducing a dust trap (van der Marel et al. 2013). Stopping the CO<sub>2</sub> ice from crossing the iceline would also mean stopping the small dust from crossing the iceline. This would lead to fast depletion of the dust in the inner disk, creating a transition disk, although some small dust grains can still cross the gap (Pinilla et al. 2016). Indeed, most disks for which CO<sub>2</sub> has been measured have strong near- and mid-infrared continuum emission, indicating that the inner dust disks cannot be strongly depleted. Furthermore, measurements by Kama et al. (2015) show that for Herbig Ae stars, the accreting material coming from a full disk has a refractory material content close to the assumed ISM values even though these disks have no detectable infrared CO<sub>2</sub> emission with *Spitzer* (Pontoppidan et al. 2010).

### Shocks

For high-mass protostars, Charnley & Kaufman (2000) proposed that C-shocks with speeds above 30 km s<sup>-1</sup> passing through the region within the CO<sub>2</sub> iceline could account for the low observed CO<sub>2</sub> abundance. Dense C-shocks can elevate temperatures above 1000 K and create free atoms such as H, N and C, so all of the CO<sub>2</sub> in the shocked layer can then be efficiently converted to H<sub>2</sub>O and CO. At the higher densities in disks, lower velocity shocks can reach the same temperature. For example, Stammer & Dullemond (2014) calculate that a 5 km s<sup>-1</sup> shock would reach temperatures upwards of 1000 K in the post shock gas. If shocks with such speeds occur in disks as well this could be an explanation for the low CO<sub>2</sub> abundance. However, assuming the shock only destroys gas-phase CO<sub>2</sub>, not the ice, shocks must happen at least once every  $3 \times 10^3$  years ( $1/10^{-11}$  s<sup>-1</sup>) and the shock speeds have to be of the order of the Keplerian velocity.

These nebular shocks have been invoked to explain the ubiquitous chondrules found in meteorites. For these chondrules to form, dense gas needs to be flash heated, so that grains can evaporate and quickly reform as the gas cools (Hewins et al. 2005). Desch

& Connolly (2002) proposed that a slow shock ( $\sim 7 \text{ km s}^{-1}$ ) in the dense midplane can heat up the gas to temperature around 2000 K, enough to start sublimation (see also Stammer & Dullemond 2014). In the case of efficient cooling, it takes the gas a few minutes to cool, but this would be enough for the  $\text{CO}_2 + \text{H} \rightarrow \text{CO} + \text{OH}$  reaction to significantly reduce the  $\text{CO}_2$  abundance. Slower shocks, with low cooling rates would also be able to destroy  $\text{CO}_2$  efficiently, as long as temperatures of 750 K are reached (see Fig. 4.15). To effectively destroy  $\text{CO}_2$ , these shocks need to affect the entire inner disk at least once every few thousand years. Each shock could then also induce chondrule formation. There is evidence that chondrules went through multiple creation events, but the frequency of these events is currently not constrained (Ruzicka et al. 2008; Desch et al. 2012).

Further out in the disk, shocks can sputter ices, including  $\text{CO}_2$  ice, from the grains (Charnley & Kaufman 2000). However, sputtering does not necessarily destroy the  $\text{CO}_2$ . Moreover, full destruction of ices by shocks is unlikely since  $\text{CO}_2$  needs to survive in the comet formation regions of the disk.

### UV-dominated layers

The inner disk chemical models by Walsh et al. (2015) show that there is a surface layer in the disk where UV destruction becomes important resulting in abundances of  $10^{-8}$ – $10^{-7}$ . Depending on the time-scale of the chemical processes and the extent of this layer, it may be optically thick in the  $^{12}\text{CO}_2$  infrared lines. This means that low abundances of  $\text{CO}_2$  will be measured in  $^{12}\text{CO}_2$  irrespective of the amount of sublimating  $\text{CO}_2$  ice in the midplane. If this UV-dominated layer is not too thick,  $^{13}\text{CO}_2$  could still have an imprint of the deeper, more abundant  $\text{CO}_2$  that is coming from the iceline. On the other hand, if this layer is thick enough that even  $^{13}\text{CO}_2$  becomes optically thick to its own radiation, then the more abundant  $\text{CO}_2$  sublimating from the iceline would be hidden from our view (see Fig. 4.10 and Fig. 4.13). This would happen at  $\text{CO}_2$  columns larger than  $10^{18} \text{ cm}^{-2}$ .

The (vertical) thickness of the photon dominated layer is very dependent on the UV flux and dust opacity in the upper layers of the disk. For a disk that has only small grains ( $< 1 \mu\text{m}$ ) in the upper atmosphere, the UV opacity is high. In this case the UV dominated layer only contains a short column of gas, and thus  $\text{CO}_2$  (Fig. 4.13). Observations of such a disk would lead to the spectra as presented in Sect. 4.4.5. If it is assumed that grains have grown to mm sizes, even in the upper atmosphere, then the UV can penetrate a lot deeper. This leads to a larger column of UV dominated gas and that could hide the high abundance  $\text{CO}_2$  in the midplane, if the  $\text{CO}_2$  in this layer becomes optically thick to its own IR radiation or if the dust becomes optically thick at IR wavelengths in the UV dominated layer. The first scenario is sketched in panel C of Fig. 4.11. To probe the midplane  $\text{CO}_2$  abundance one would need to observe disks with a lot of small grains in the upper atmosphere, preferably around UV weak sources such that the  $\text{CO}_2$  column in the UV dominated layer is minimised.

### X-ray induced dissociation

T-Tauri stars are known to have strong X-ray emission  $10^{28}$ – $10^{34} \text{ erg s}^{-1}$  (Feigelson et al. 2002). These X-rays can ionise the gas and create a local UV field in the same way as cosmic-rays, destroying molecules in the gas (see, for example, the models by Stauber et al. 2005, for high mass protostars). As X-rays are more quickly attenuated

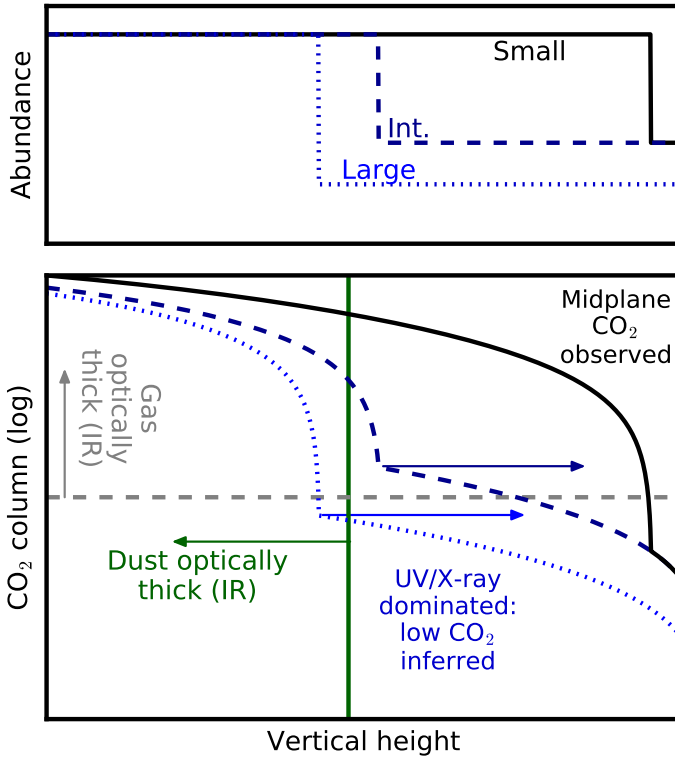


**Figure 4.12:** Schematic of the vertical CO<sub>2</sub> abundance (top panel) and upwards column (bottom panel) as function of disk height. Three different cases are shown in solid black, dashed dark blue and dotted blue lines. The black line shows the case for shallow UV or X-ray penetration, in this case an abundance similar to the midplane CO<sub>2</sub> abundance will be measured. The dashed dark blue line shows a slightly deeper penetration of radiation, in which case a lower CO<sub>2</sub> abundance will be inferred from the observations because the gas is optically thick and hiding the higher abundance deeper into the disk. The dotted blue line shows the case of deep penetration. In this case a low CO<sub>2</sub> abundance will be inferred due to the dust hiding the bulk of the CO<sub>2</sub>. The vertical lines in the upper panel show where the disk becomes optically thick to CO<sub>2</sub> lines, the solid and dashed grey line, show where the gas becomes optically thick for the small and intermediate PDR or XDR respectively, the green dotted line shows where the dust becomes optically thick, which is above where the gas becomes optically thick for the large PDR or XDR.

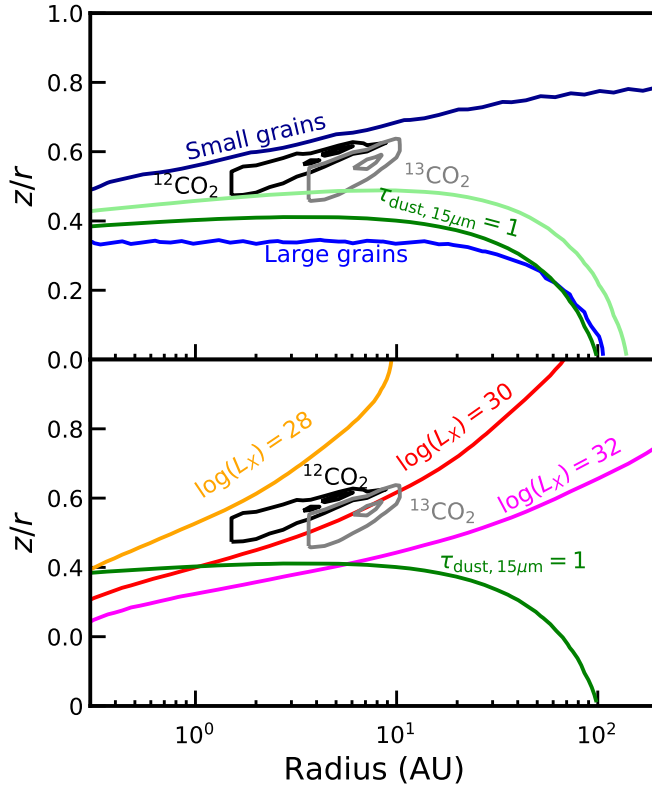


**Figure 4.13:** *Top:* depth into the disk to which UV can destroy  $\text{CO}_2$  at a rate of  $10^{-11} \text{ s}^{-1}$  for a disk with an upper disk gas-to-dust ratio of 1000 and large grains (cyan) and small grains (blue). The black and grey contours show the area from which 25% and 75% of the emission of  $^{12}\text{CO}_2$  and  $^{13}\text{CO}_2$  respectively originates. The green lines show the dust  $\tau = 1$  surface at  $15 \mu\text{m}$  for the large grains (up to 1 mm, dark green) and small grains (up to  $1 \mu\text{m}$ , light green) respectively. The UV photo destruction rate has a stronger dependence on the grain size distribution than this  $\mu\text{m}$  dust photosphere. *Bottom:* depth into the disk to which X-rays can destroy  $\text{CO}_2$  at a rate of  $10^{-11} \text{ s}^{-1}$  for different stellar X-ray luminosities ( $L_X$  in  $\text{erg s}^{-1}$ ). The black and grey contours show the area from which 25% and 75% of the emission of  $^{12}\text{CO}_2$  and  $^{13}\text{CO}_2$  respectively is coming from. The green line shows the dust  $\tau = 1$  surface at  $15 \mu\text{m}$  for the large grains (up to 1 mm).

than the higher energy cosmic-rays, they are not efficient in destroying  $\text{CO}_2$  in the disk midplane, however, X-rays do penetrate further into the disk atmosphere than UV photons. Thus, X-rays can help in decreasing the  $\text{CO}_2$  abundance in the atmosphere of the disk, especially if hard X-ray flare, such are thought to occur in TW Hya are common in other T-Tauri stars as well (Kastner et al. 2002; Cleevés et al. 2015, 2017).

For our specific DALI model, a total X-ray flux of  $10^{30} \text{ erg s}^{-1}$ , emitted as a  $10^7 \text{ K}$  black body, would have a destruction rate of  $10^{-11} \text{ s}^{-1}$  in most of the  $^{12}\text{CO}_2$  emitting region and could thus have an effect on the  $^{12}\text{CO}_2$  fluxes (Fig. 4.13). A total X-ray flux of  $10^{32} \text{ erg s}^{-1}$  would be needed to have the same destruction rate in most of the  $^{13}\text{CO}_2$  emitting region. Thus, a source that has a time-averaged X-ray luminosity  $> 10^{30} \text{ erg s}^{-1}$  could show a low  $\text{CO}_2$  abundance in the atmosphere and have a higher abundance underneath. If the X-ray luminosity of the source is lower than  $10^{32} \text{ erg s}^{-1}$ , this should be reflected in the  $^{13}\text{CO}_2$  measurement. Note however that the X-rays do not reach into the midplane mass reservoir. Since the vertical transport for a fully viscous disk is orders of magnitude faster than the radial transport, the replenishment rate of  $\text{CO}_2$  in the upper layers due to mixing from the midplane would also be faster. Thus, these X-ray luminosities should be considered as lower limits. Most disk hosting stars do not have high enough X-ray luminosities to destroy  $\text{CO}_2$  efficiently (Bustamante et al. 2016), but X-ray destruction of  $\text{CO}_2$  in the surface layers can be an explanation in some sources and lead to similar effects as for the case of UV, such as the  $\text{CO}_2$  IR lines becoming optically thick in the X-ray dominated region.

## 4.6 Summary and conclusions

We have presented a model for the transport of major gas and ice species. This model predicts that transport of ices from the outer disk towards the inner disk can have a significant effect on the abundance of species in the inner disk. Radial transport is predicted to be so efficient, that even in the case without any radial drift, the modelled  $\text{CO}_2$  abundance in the inner disk is orders of magnitude higher than the currently available observations of disks. As such  $\text{CO}_2$  cannot be directly used to trace the mass transport rate. The presence of dust in disks older than a Myr does imply that the mass transport rate of dust cannot be larger than  $10 \times \dot{M}_{\text{acc,gas}} / (\text{g/d})$ . This is inconsistent with the pebble-sized dust observed in disks.

To reconcile model and observation  $\text{CO}_2$  abundances, either the midplane  $\text{CO}_2$  needs to be destroyed by some physical or chemical mechanism, or the  $\text{CO}_2$  abundance in the upper layers needs to be decoupled from the  $\text{CO}_2$  abundance in the midplane. This can be achieved by preventing vertical  $\text{CO}_2$  cycling, hiding the  $\text{CO}_2$  under the dust IR photosphere or by the creating a low abundance  $\text{CO}_2$  column that is optically thick in a UV or X-ray dominated layer. We can summarize this work with the following conclusions.

- Accretion flow and diffusion equilibrate the inner disk  $\text{CO}_2$  gas abundance with the high outer disk  $\text{CO}_2$  ice abundance of  $\sim 10^{-5}$  in less than 1 Myr for  $\alpha > 10^{-3}$  (Sect. 4.4.1).
- For any disk that retains its dust on the same time-scale as it retains the gas, dust diffusion processes dominate over radial drift (Sect. 4.4.2 and App. 4.C).

- If dust can grow efficiently and drift inwards, both  $\text{CO}_2$  and  $\text{H}_2\text{O}$  will be enhanced above the outer disk ice abundance as long as the dust is drifting inwards with a mass flux more than 1% of that of the gas,  $\dot{M}_{\text{dust}} \gg 0.01 \dot{M}_{\text{gas}}$ . (Sect. 4.4.4)
- A physical or chemical process that would induce a vertically averaged  $\text{CO}_2$  destruction rate of at least  $10^{-11} \text{ s}^{-1}$  ( $< 10^3 \text{ yr}$ ) is necessary to produce  $^{12}\text{CO}_2$  fluxes that are consistent with the current observations of disks. (Sect. 4.4.5).
- Within the current chemical networks, there are no paths to destroy  $\text{CO}_2$  fast enough without invoking strong X-ray or UV-fluxes or elevated cosmic ray fluxes. Especially at temperatures between 60 and 150 K, destroying  $\text{CO}_2$  is extremely difficult in the current chemical networks since the formation of  $\text{CO}_2$  is strongly favoured over the production of  $\text{H}_2\text{O}$  in that temperature range. Above 300 K  $\text{CO}_2$  destruction pathways exists, but they only become efficient enough at temperatures above 750 K. (Sect. 4.3.2, 4.5.1 and App. 4.B).
- Shocks could raise temperatures enough to destroy  $\text{CO}_2$  efficiently, but effectively lowering the  $\text{CO}_2$  abundance would require the entire inner 10 AU of the disk to be processed by a shock every  $10^3$  years.
- Trapping  $\text{CO}_2$  in water ice seems unlikely and is not expected to lower the inner disk gaseous  $\text{CO}_2$  abundance significantly. Trapping the grains before they cross the iceline efficiently enough to lower  $\text{CO}_2$  abundances in the inner disk would quickly create a transition disk (Sect. 4.5.2 and 4.5.2).
- Deep penetration of UV and strong X-ray fluxes can lower the  $\text{CO}_2$  abundance in the  $^{12}\text{CO}_2$  emitting region. This can happen if grains in the disk atmosphere have grown to mm sizes and the central source has enough UV luminosity ( $> 10^{27} \text{ erg s}^{-1}$ , about 0.1% of the solar UV). Likewise sources that have an X-ray luminosity greater than  $10^{30} \text{ erg s}^{-1}$  efficiently destroy  $\text{CO}_2$  in a large part of the IR emitting region. If the UV or X-ray dominated region does not reach down to the dust  $15 \mu\text{m } \tau = 1$  surface,  $^{13}\text{CO}_2$  can still contain a information on the amount of sublimated  $\text{CO}_2$ .
- A high ratio of the  $^{13}\text{CO}_2$   $Q$ -branch flux over the  $^{12}\text{CO}_2$   $Q$ -branch flux ( $> 0.05$ ), can hint at an contribution of sublimating  $\text{CO}_2$  at the iceline. Sublimating  $\text{CO}_2$  is, however, not the only way to get high flux ratios. A more complete, source specific analysis would be needed to exclude other possibilities (Sect. 4.4.5).

In summary, to explain the discrepancy between our models and observations, we either need to invoke frequent shocks in the inner 10 AU, or need to hide the abundant midplane  $\text{CO}_2$  from our view. This can be due to very inefficient mixing or due to deep UV and/or X-ray penetration. In the case of UV penetration, this would imply efficient grain growth and settling, in the case of X-rays, this would be stronger than measured X-ray fluxes for most sources, or frequent X-ray flares. The key to hiding the mid-plane  $\text{CO}_2$  is that the low abundance  $\text{CO}_2$  in the upper layers has a high enough column density to become optically thick to its own IR radiation. Trapping the  $\text{CO}_2$  on the grains, or destroying it in the gas phase near the iceline at ambient temperatures is strongly disfavoured.

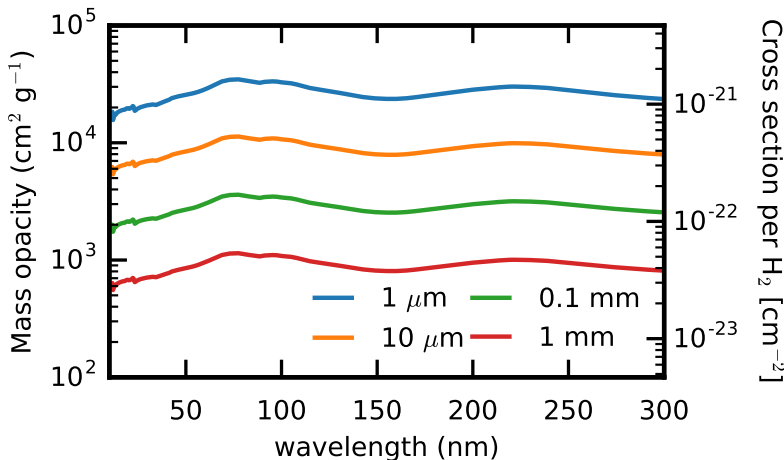


**Figure 4.14:** UV Opacities and cross section of the dust for different sizes of the largest grains. The MRN power law slope is 3.5 for all cases. Growing grains from  $1 \mu\text{m}$  to  $1 \text{mm}$  has more than an order of magnitude effect on the opacities.

Is  $\text{CO}_2$  a special case in terms of discrepancy between models and observations? Modelling and observations of other molecules abundant in ices, such as  $\text{NH}_3$  and  $\text{CH}_4$ , may be used to test whether a chemical or physical reason is the origin of the current discrepancy. Ultimately, such data can constrain the mass flow of solids if the chemical composition of the surface layers is sufficiently representative of that in the midplane.

## Appendix

### 4.A UV dust cross sections

Fig. 4.14 shows the UV opacities and cross sections for different grain size distributions used in Sect. 4.3.2.

### 4.B Chemical modelling

#### 4.B.1 Gas-phase only models

To test the main  $\text{CO}_2$  destruction and formation processes, a small grid of chemical models was run. The network from Walsh et al. (2014) was used as basis and modified. The gas-phase chemical network is based on the UMIST 2012 network (McElroy et al. 2013). The network includes freeze-out and desorption.  $\text{H}_2$  formation on grains following Cazaux & Tielens (2004), which includes  $\text{H}_2$  formation at high temperatures. The grain-surface reactions included in the network were removed for this test. As the main interest is in the midplane layers, the local UV and X-ray flux are assumed to be negligible. The cosmic ray rate is taken to be  $10^{-17} \text{s}^{-1}$ .

Four series of models were run, two starting from ‘atomic’ initial conditions (all species are in atomic form except for  $\text{H}_2$ , the other two from ‘molecular’ conditions (see Table 4.4, the atomic initial conditions use the same elemental abundances as the used for the molecular test). For each set of initial conditions one set of models was run with  $\text{H}_2$  formation happening only on grains according to Cazaux & Tielens (2004) leading to an atomic H abundance of  $10^{-4}$  with respect to  $\text{H}_2$ , while in the other set of models the additional  $\text{H}_2$  formation route at high temperature was added to keep the H abundance at  $10^{-12}$  ( $1 \text{ cm}^{-3}$ ). The density was kept constant at  $10^{12} \text{ cm}^{-3}$  and the temperature was varied between 150 and 800 K.

The  $\text{CO}_2$  abundances after 1 Myr of chemical evolution are presented in Fig. 4.15. From this plot it can be gathered that there is no efficient destruction mechanism in the current gas-phase network until a temperature of  $\sim 450$  K is reached.

For temperatures between 150 and 450 K, the different atomic H abundances do not significantly influence the results. The difference between the initial  $\text{CO}_2$  abundance and the  $\text{CO}_2$  abundance after 1 Myr in the molecular case can be explained by the destruction of  $\text{CO}_2$  and  $\text{H}_2\text{O}$  due to processes driven by cosmic rays, e.g. cosmic ray induced photo dissociation, and the reformation of  $\text{CO}_2$  from the fragments.

For models starting from atomic initial conditions the  $\text{CO}_2$  content decreases with increasing temperature as expected from the formation speeds of  $\text{CO}_2$  and  $\text{H}_2\text{O}$  in the model with a low H abundance, and this trend continues up to higher temperatures. The local minimum in the  $\text{CO}_2$  abundance at 350 K is due to reactions with atomic N before the nitrogen is locked up in other species. When the atomic nitrogen abundance is high,  $\text{CO}_2$  reacts with N to form CO and NO, NO is then further processed to  $\text{H}_2\text{O}$ , releasing a N in the process. This significantly slows down the build-up of  $\text{CO}_2$  when both O and OH are available in the gas-phase in high abundances.

In the models with a high H abundance, reactions with atomic hydrogen become important starting at 350 K. This process, which is slightly more efficient for  $\text{H}_2\text{O}$  than for  $\text{CO}_2$ , together with the reformation of  $\text{H}_2\text{O}$  and  $\text{CO}_2$  from the resulting OH, sets the equilibrium at high temperature. The abundance of  $\text{H}_2\text{O}$  as function of temperature is fairly constant, at  $10^{-4}$ , and thus the  $\text{CO}_2$  abundance decreases towards the highest temperature, as expected from the formation rate ratio given in Fig. 4.1. The difference between the  $\text{CO}_2$  abundance at high temperature in the case of atomic and molecular abundance can be explained by the lower CO abundance in the case of atomic initial conditions.

For the models with a low H abundance,  $\text{CO}_2$  is not efficiently destroyed by H at high temperatures so the  $\text{CO}_2$  abundance is nearly constant as function of temperature. From this parameter exploration we can conclude that  $\text{CO}_2$  can only be effectively destroyed by radicals like H and N and that this is only efficient if these are available at high abundances  $> 10^{-6}$ . For the model beginning with atomic abundances the low temperature dependence of the abundance is similar to the high H abundance case. Above temperatures of 400 K differences start to be noticeable. The  $\text{CO}_2$  abundance does not increase with temperature as it does in the case of high H abundance. This is due to a similar process as in the high H model around 350 K. All the  $\text{CO}_2$  that is formed when oxygen is not locked up in water is quickly destroyed by atomic H and N, when atomic H and N have settled to low enough abundances that  $\text{CO}_2$  can survive, all the O is already locked up in other species, mostly  $\text{H}_2\text{O}$  and CO leaving no extra O to form  $\text{CO}_2$ . The small amount of  $\text{CO}_2$  that is in the gas-phase is mostly created by cosmic ray induced destruction of  $\text{H}_2\text{O}$ . The decreasing abundance towards high



**Table 4.4:** Initial molecular abundances for the chemical models.

Abundances			
H <sub>2</sub>	5.0(-1)	H	0.0
He	1.4(-1)	CO	1.0(-4)
CO <sub>2</sub>	3.5(-5)	N <sub>2</sub>	1.1(-5)
N	2.1(-5)	H <sub>2</sub> O	1.2(-4)
Si	4.0(-10)	H <sub>2</sub> S	1.9(-9)

Notes.  $a(b) = a \times 10^b$

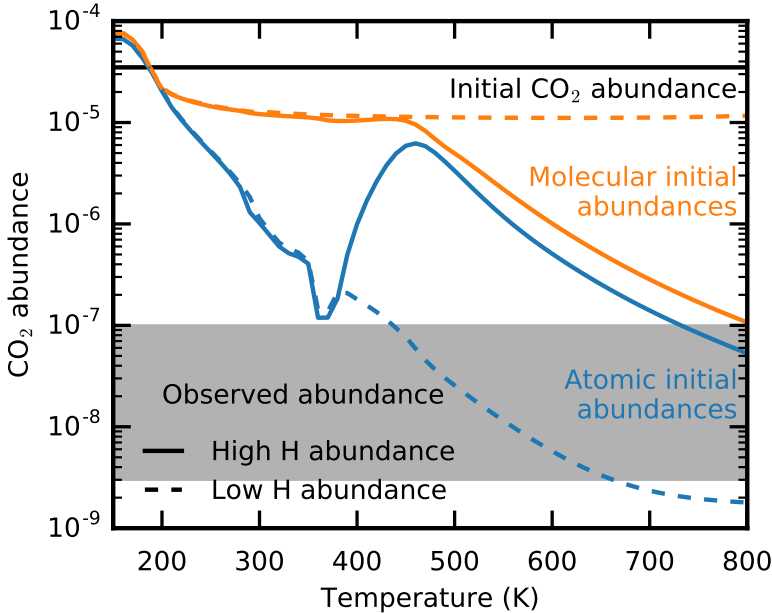


**Figure 4.15:** CO<sub>2</sub> abundance from a gas-phase chemical network as function of temperature after 1 Myr of evolution. The density is  $10^{12} \text{ cm}^{-3}$ .

temperatures is due to the increasingly efficient reformation of H<sub>2</sub>O after destruction due to cosmic rays.

#### 4.B.2 Grain surface chemistry between the H<sub>2</sub>O and CO<sub>2</sub> icelines

Section 4.B.1 investigates the gas-phase chemistry of CO<sub>2</sub> in the region within the H<sub>2</sub>O iceline, that is, above 150 K. In this region all species will be primarily in the gas-phase and grain surface chemistry is thus expected to be less important. Between the CO<sub>2</sub> and H<sub>2</sub>O icelines The efficiency of the destruction of gaseous CO<sub>2</sub> is estimated by investigating the chemical pathways in a full chemical model. The network from Walsh et al. (2014); Eistrup et al. (2016) was used. A point model representative for the conditions between the H<sub>2</sub>O and CO<sub>2</sub> iceline was run. The number density

**Table 4.5:** Chemical pathways from molecules possibly created by the destruction of CO<sub>2</sub>.

First generation molecule	Destruction efficiency	Stable resulting molecules
CO <sub>2</sub> <sup>+</sup> , HCO <sub>2</sub> <sup>+</sup>	0%	CO <sub>2</sub>
OH	27%	CO <sub>2</sub> , O <sub>2</sub> , H <sub>2</sub> O <sub>2</sub>
O <sup>+</sup> , OH <sup>+</sup> , H <sub>2</sub> O <sup>+</sup> , H <sub>3</sub> O <sup>+</sup>	100%	H <sub>2</sub> O
O, NO, HNO	82%	O <sub>2</sub> , CO <sub>2</sub> , H <sub>2</sub> O <sub>2</sub>
SO, SO <sub>2</sub>	100%	O <sub>2</sub>
OCN	0%	CO <sub>2</sub>
HCNO	100%	O <sub>2</sub>
SiO	100%	SiO

used is  $10^{13} \text{ cm}^{-3}$ , the temperature 100 K and the cosmic ray ionisation rate  $10^{-17} \text{ s}^{-1}$ . There was no external UV in our model. After running the model for 1 Myr to get equilibrium abundances of atomic and ionised species, the chemical pathways of oxygen carrying species are examined.

For each oxygen carrying molecule that could be created from a destruction of CO<sub>2</sub>, we define the destruction efficiency as the fraction the oxygen atoms that is incorporated into a stable molecule, for which we take that a cosmic ray induced process is needed to destroy the molecule. Here, pathways leading to incorporation of oxygen into CO are neglected, as these pathways are dominated by the availability of atomic C, which must originate from an other CO molecule. Pathways towards CO are generally very minor. Destruction efficiencies are tabulated in Table 4.5.

From the efficiencies it can be seen that direct ionisation or protonation of CO<sub>2</sub> is not an effective way to destroy it since CO<sub>2</sub> will be reformed from the products in most cases. Only if an oxygen atom can be removed from the central carbon, is there a chance that the oxygen will be locked up into something other than CO<sub>2</sub>. In these cases the efficiency is 27% (for OH) or higher.

## 4.C Viscous evolution and grain growth

Figures 4.16 through 4.24 show model results for the model with grain growth and radial drift, but without any destruction rate.  $\alpha$  values of  $10^{-2}$ ,  $10^{-3}$  and  $10^{-4}$  are shown, fragmentation velocities of 1, 10 and  $100 \text{ m s}^{-1}$  are used. The features seen in ice abundance for the higher fragmentation velocity models is due to a numerical instability in the grain growth algorithm, this does not influence our results.

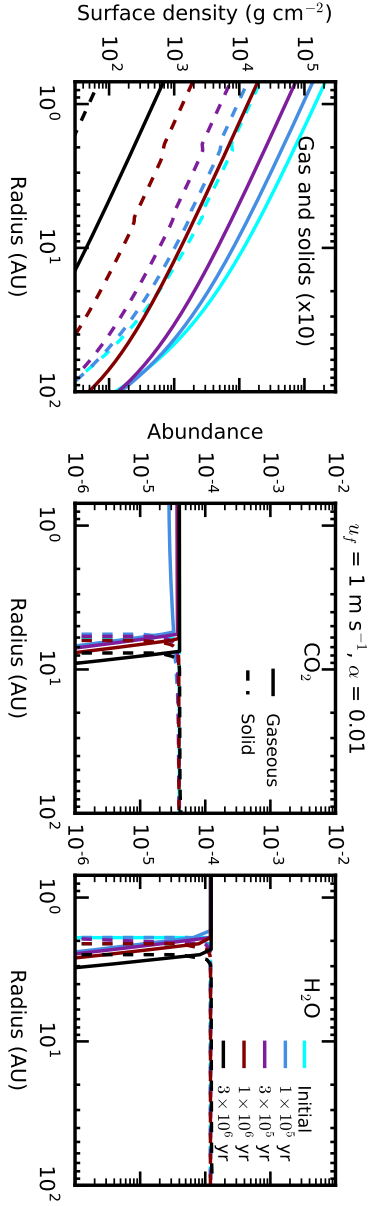


**Figure 4.16:** Time evolution series for a model with grain growth. This model assumes an  $\alpha$  of  $10^{-2}$ . The fragmentation velocity for this model is  $1 \text{ m s}^{-1}$ . Panels as in Fig. 4.3.

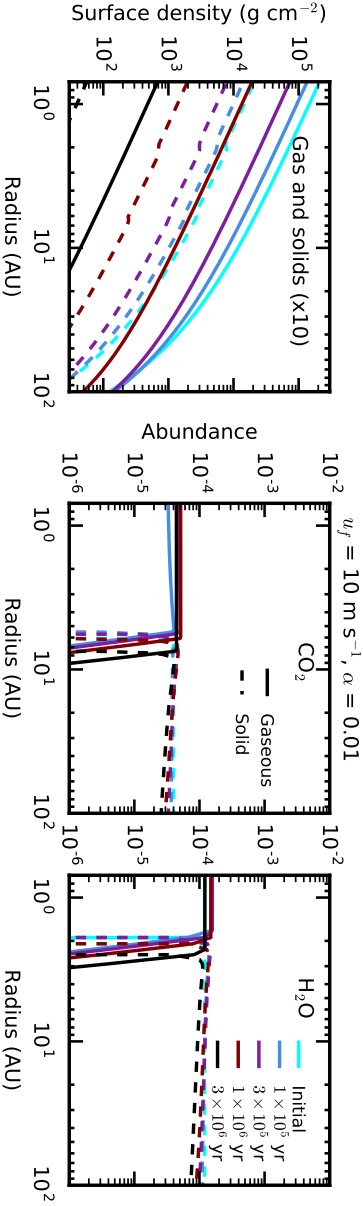


**Figure 4.17:** Time evolution series for a model with grain growth. This model assumes an  $\alpha$  of  $10^{-2}$ . The fragmentation velocity for this model is  $1 \text{ m s}^{-1}$ . Panels as in Fig. 4.3.

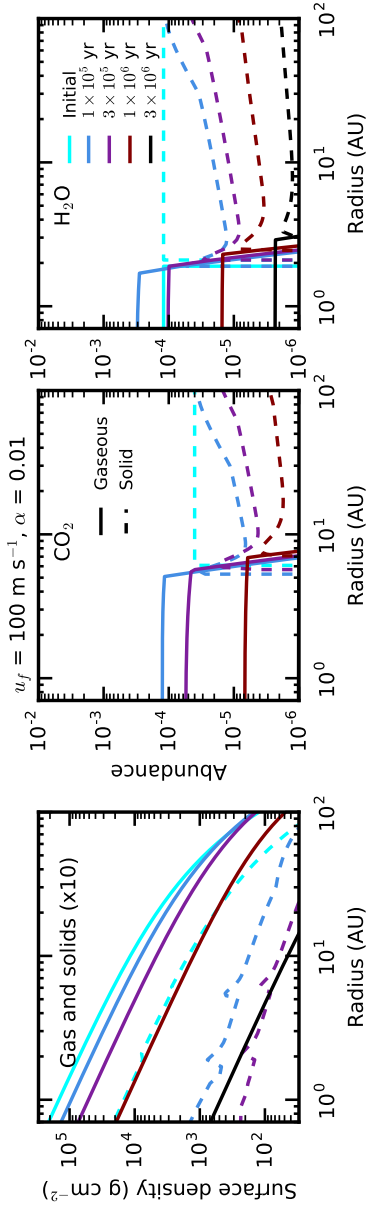


**Figure 4.18:** Time evolution series for a model with grain growth. This model assumes an  $\alpha$  of  $10^{-2}$ . The fragmentation velocity for this model is  $1 \text{ m s}^{-1}$ . Panels as in Fig. 4.3.

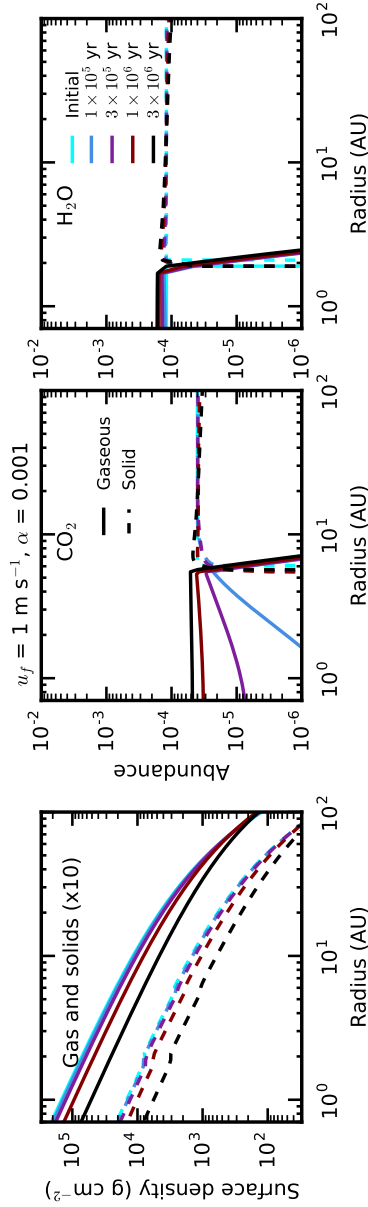


**Figure 4.19:** Time evolution series for a model with grain growth. This model assumes an  $\alpha$  of  $10^{-3}$ . The fragmentation velocity for this model is  $1 \text{ m s}^{-1}$ . Panels as in Fig. 4.3.

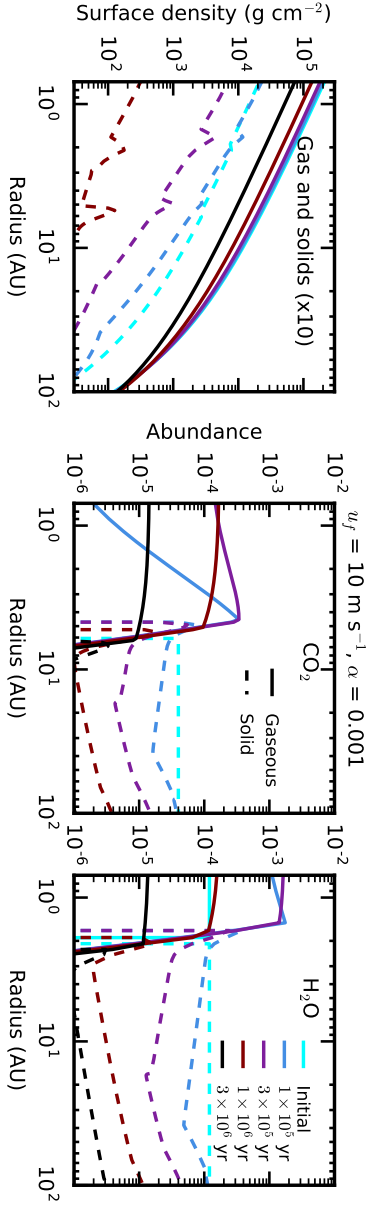


**Figure 4.20:** Time evolution series for a model with grain growth. This model assumes an  $\alpha$  of  $10^{-3}$ . The fragmentation velocity for this model is  $10 \text{ m s}^{-1}$ . Panels as in Fig. 4.3.

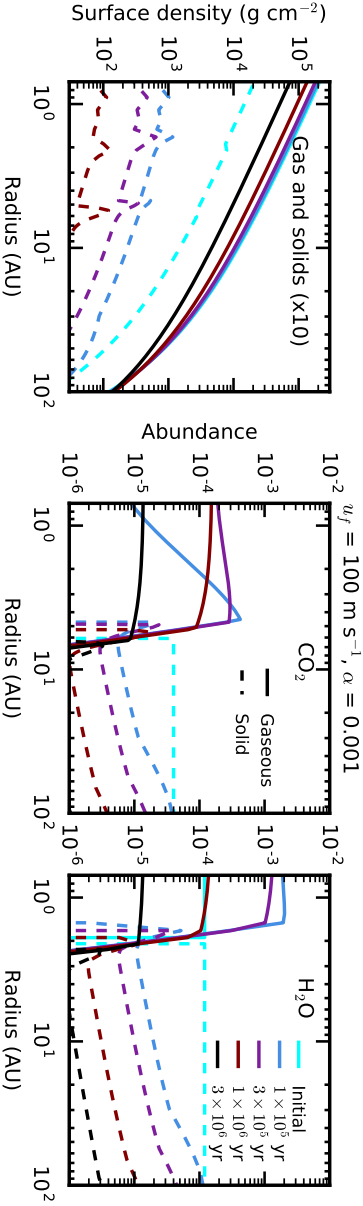


**Figure 4.21:** Time evolution series for a model with grain growth. This model assumes an  $\alpha$  of  $10^{-3}$ . The fragmentation velocity for this model is  $100 \text{ m s}^{-1}$ . Panels as in Fig. 4.3.

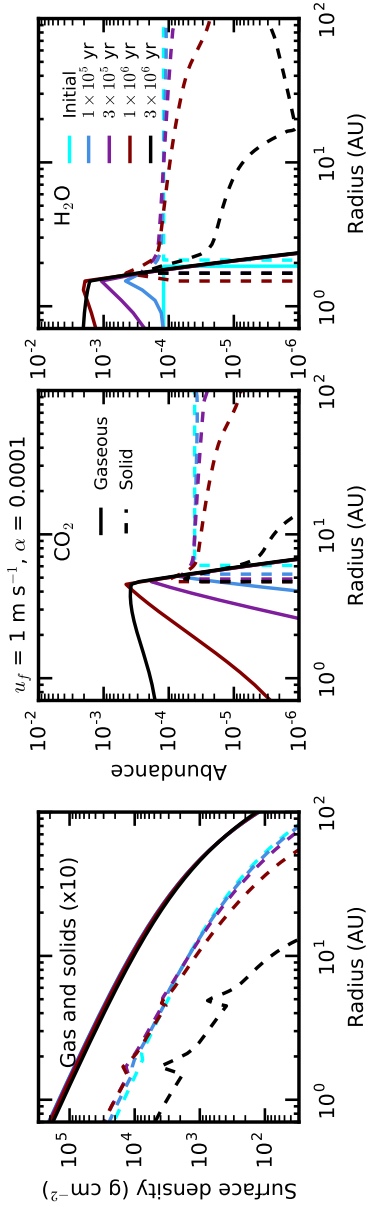


**Figure 4.22:** Time evolution series for a model with grain growth. This model assumes an  $\alpha$  of  $10^{-4}$ . The fragmentation velocity for this model is  $1 \text{ m s}^{-1}$ . Panels as in Fig. 4.3.

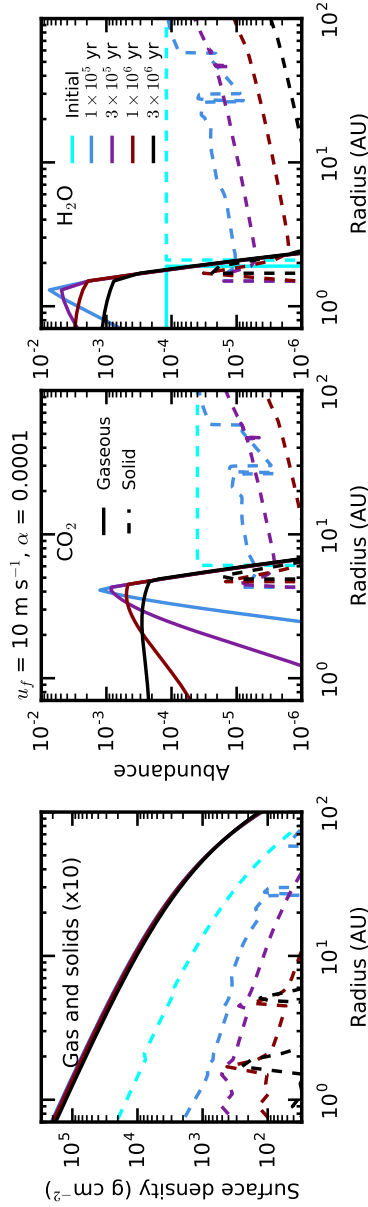


**Figure 4.23:** Time evolution series for a model with grain growth. This model assumes an  $\alpha$  of  $10^{-4}$ . The fragmentation velocity for this model is  $10 \text{ m s}^{-1}$ . Panels as in Fig. 4.3.

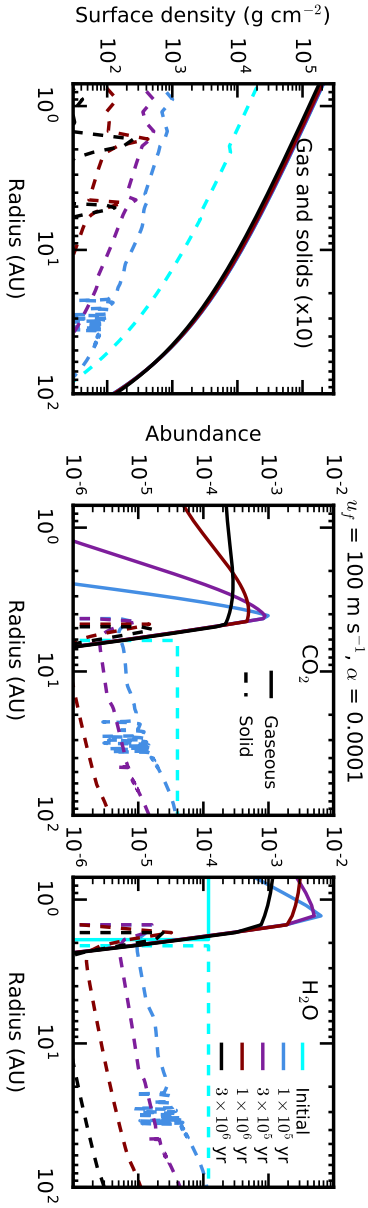
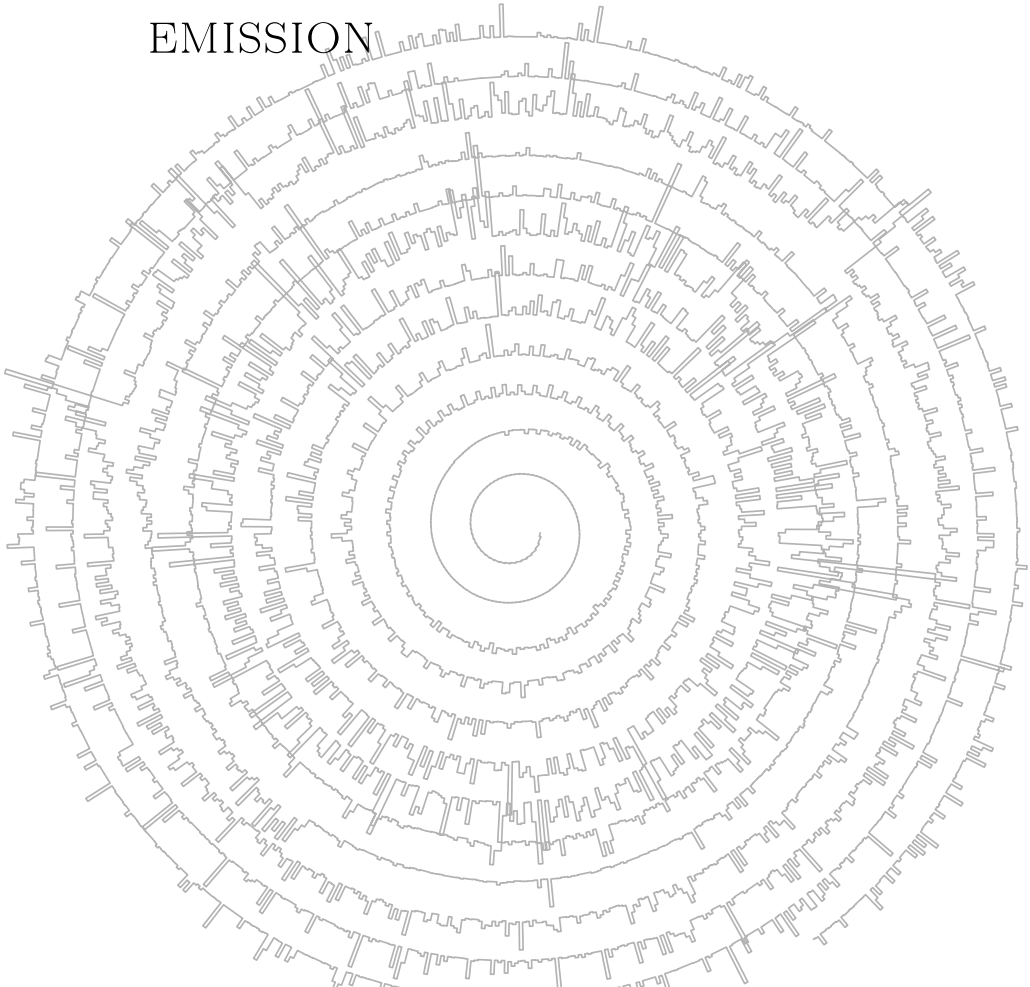


**Figure 4.24:** Time evolution series for a model with grain growth. This model assumes an  $\alpha$  of  $10^{-4}$ . The fragmentation velocity for this model is  $100 \text{ m s}^{-1}$ . Panels as in Fig. 4.3.

# 5

## PROBING PLANET FORMATION AND DISK SUBSTRUCTURES IN THE INNER DISK OF HERBIG AE STARS WITH CO ROVIBRATIONAL EMISSION



A.D. Bosman, A. Banzatti, S. Bruderer, G. A. Blake, A. G. G. M. Tielens and  
van E. F. van Dishoeck, 2019, A&A under revision



## Abstract

**Context:** CO rovibrational lines are efficient probes of warm molecular gas and can give unique insights into the inner 10 AU of proto-planetary disks, effectively complementing ALMA observations. Recent studies have found a relation between the ratio of lines originating from the second and first vibrationally excited state, denoted as  $v_2/v_1$ , and the Keplerian velocity or emitting radius of CO. Counter-intuitively, in disks around Herbig Ae stars the vibrational excitation is low when CO lines come from close to the star, and high when lines only probe gas at large radii (more than 5 AU). The  $v_2/v_1$  ratio is also counterintuitively anti-correlated with the near-IR (NIR) excess, which probes hot/warm dust in the inner disk.

**Aims:** We aim to find explanations for the observed trends between CO vibrational ratio, emitting radii, and NIR excess, and identify their implications in terms of the physical and chemical structure of inner disks around Herbig stars.

**Methods:** First, slab model explorations in LTE and non-LTE are used to identify the essential parameter space regions that can produce the observed CO emission. Second, we explore a grid of thermo-chemical models using the DALI code, varying gas-to-dust ratio and inner disk radius. Line flux, line ratios and emitting radii are extracted from the simulated lines in the same way as the observations and directly compared to the data.

**Results:** Broad CO lines with low vibrational ratios are best explained by a warm (400–1300 K) inner disk surface with gas-to-dust ratios below 1000 ( $N_{\text{CO}} < 10^{18} \text{ cm}^{-2}$ ); no CO is detected within/at the inner dust rim, due to dissociation at high temperatures. In contrast, explaining the narrow lines with high vibrational ratios requires an inner cavity of a least 5 AU in both dust and gas, followed by a cool (100–300 K) molecular gas reservoir with gas-to-dust ratios greater than 10000 ( $N_{\text{CO}} > 10^{18} \text{ cm}^{-2}$ ) at the cavity wall. In all cases the CO gas must be close to thermalization with the dust ( $T_{\text{gas}} \sim T_{\text{dust}}$ ).

**Conclusions:** The high gas-to-dust ratios needed to explain high  $v_2/v_1$  in narrow CO lines for a subset of group I disks can naturally be interpreted as due to the dust traps that have been proposed to explain millimeter dust cavities. The dust trap and the low gas surface density inside the cavity are consistent with the presence of one or more massive planets. The difference between group I disks with low and high NIR excess can be explained by gap opening mechanisms that do or do not create an efficient dust trap, respectively. The broad lines seen in most group II objects indicate a very flat disk in addition to inner disk substructures within 10 AU that can be related to the substructures recently observed with ALMA. We provide simulated ELT-METIS images to directly test these scenarios in the future.

## 5.1 Introduction

Planetary systems are thought to be built within proto-planetary disks of gas and dust around young stars. How these disks transition from the initial gas-rich remnants of star formation to the solid-body dominated debris disks and planetary systems is still an open question. While for most disks it seems that they go through a quick dispersal process (Cieza et al. 2007; Currie & Kenyon 2009), there is a subset of disks that goes through a prolonged period where dust and gas are (partially) depleted in the inner disk, but where there is a large reservoir of mass at larger radii, the so called transition disks (Maaskant et al. 2013; Garufi et al. 2017; van der Marel et al. 2018). It is thought that in these disks the cavity is formed either through giant planet formation or X-ray/UV photoevaporation (for reviews, see Owen 2016; Ercolano & Pascucci 2017). These processes cause different distributions of gas and dust in the inner disk.

To distinguish these scenarios, we have to study the inner disk. CO rovibrational lines are good tracers of the inner disk, because they are strong lines that originate only from warm, dense gas. The upper level energies for the first vibrationally excited level are around 3000 K so they will only be excited in environments with high temperatures ( $\gtrsim 300$  K). Furthermore CO is a very stable molecule and is thus expected to survive even in regions where there is little dust to shield the gas from UV photons (e.g. Bruderer 2013). Finally the transitions are strong so small columns of excited CO are needed to produce bright lines making CO columns as low as  $10^{16}$  cm $^{-2}$  easily detectable if the excitation conditions are right.

Observing the fundamental CO lines around  $4.7 \mu\text{m}$  allows for the simultaneous measurement of rovibrational line fluxes from the first ( $v1$ ) and second ( $v2$ ) excited states. The  $v2/v1$  line flux ratio carries information on the excitation conditions of the gas. The high resolving power on spectrographs such as Keck-NIRSPEC (McLean et al. 1998), VLT-CRIRES (Kaeuffl et al. 2004), IRTF-CSHELL and now iSHELL (Rayner et al. 2016) make velocity-resolved observations of CO line profiles possible (e.g. Najita et al. 2003; Blake & Boogert 2004; Thi et al. 2005; Brittain et al. 2007; Pontoppidan et al. 2008b; Salyk et al. 2011a; Brown et al. 2013; Banzatti & Pontoppidan 2015; Brittain et al. 2018). As the emission is expected to come from a Keplerian disk, the width of the line, once coupled with disk inclination and stellar mass, can be used to estimate the CO emitting radii for different gas velocities, thereby obtaining information on the spatial distribution of CO gas in inner disks.

For disks around T-Tauri stars, CO rovibrational lines have been used to probe molecular gas within inner disk dust cavities (Pontoppidan et al. 2008b, 2011a), and to propose an inside-out clearing scenario for gas and dust (Banzatti & Pontoppidan 2015). In their sample of T-Tauri disks, CO shows a lower vibrational temperature with decreasing linewidth (and hence increasing emitting radius). This fits well with the expectation that the gas temperature decreases as a function of distance from the star. Furthermore the variation in CO emitting radii can be explained by varying inner molecular gas disk radii, indicating that the inner edge of the molecular disk is not set by the sublimation of dust but carved by another process such as planet formation or photoevaporation.

Herbig disks, instead, behave very differently and show an inverse relation between linewidth and vibrational excitation (Banzatti & Pontoppidan 2015). This was attributed to UV-fluorescence becoming more important for stars with higher continuum UV fluxes when the thermal excitation becomes less efficient at larger disk radii

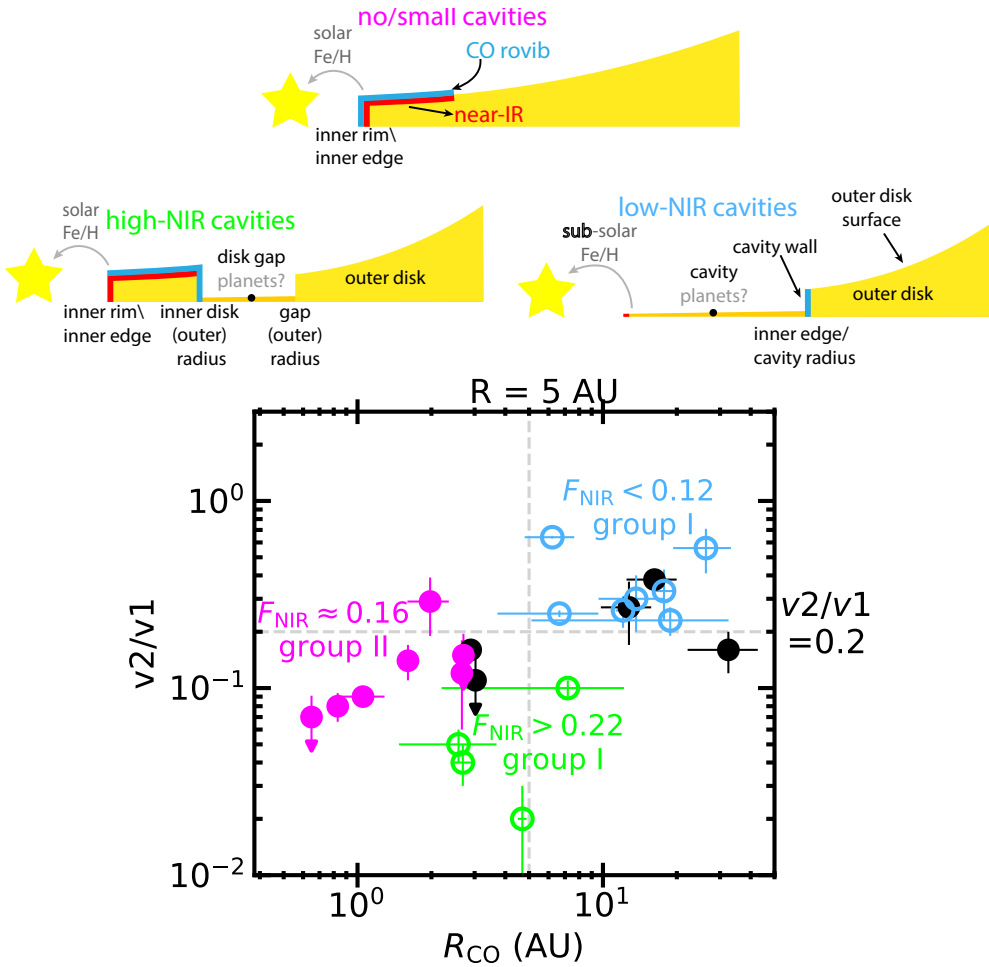


**Figure 5.1:** Disk structures as proposed by Banzatti et al. (2018) (left) and CO vibrational ratio  $v_2/v_1$  and emitting radius from near-infrared CO spectra of Herbig stars used for comparison to the models in this work (right), see details in Section 5.2). The three groups from Banzatti et al. (2018), are shown in different colors: group II in magenta, high-NIR group I in green, low-NIR group I in blue. Disks where  $F_{NIR}$  is not available are marked in black. We mark two regions that will be used for comparison with models: disks that have CO inside 5 AU, which show a low vibrational ratio (group II and high-NIR group I, *bottom left corner*), and disks that have CO only outside of 5 AU, which show high vibrational ratios (low-NIR group I, *top right corner*).

**Table 5.1:** Median values for Herbig groups from Banzatti et al. (2018), plus notes from imaging studies

Herbig group	$F_{\text{NIR}}$	$v2/v1$	$R_{\text{CO}}$ (AU)	$\log(\text{Fe}/\text{H})$	Dust structures from imaging	Refs
Group II	0.16	0.12	3	-4.4	no large inner cavities, some substructures < 5 AU	(1)
Group I (high-NIR)	0.27	0.05	5	-4.6	40–100 AU cavities, (misaligned) inner disks < 10 AU	(2)
Group I (low-NIR)	0.08	0.27	18	-5.2	15–50 AU cavities, no significant inner disks	(3)

**Notes.** References: (1) e.g. Menu et al. (2015); Huang et al. (2018); Isella et al. (2018); (2) e.g. Pinilla et al. (2018); Stolker et al. (2016); Avenhaus et al. (2017); Tang et al. (2017); di Folco et al. (2009); Boehler et al. (2018); Benisty et al. (2017); (3) van der Plas et al. (2017); Fedele et al. (2017); White et al. (2018); Pinilla et al. (2018)

(Brittain et al. 2007; Brown et al. 2013; Banzatti & Pontoppidan 2015). However, full thermo-chemical models suggest that UV fluorescence is not the dominant excitation mechanism for the  $v = 1$  and  $v = 2$  levels of CO (Thi et al. 2013; Hein Bertelsen et al. 2014). This is supported by the observed rovibrational excitation diagrams that only show a strong difference between rotational and vibrational temperatures for levels  $v = 3$  and higher, indicating that only for the higher vibrational levels, UV pumping is important (van der Plas et al. 2015).

Furthermore, based on their SEDs, Herbig disks are divided into two groups. Disks with strong far-infrared emission relative to their mid-infrared emission are classified as group I or "flared" disks. Disks with strong mid-infrared emission in comparison to their far infrared emission are classified as group II or "settled" disks (Meeus et al. 2001). An evolutionary sequence between these groups was inferred with group I disk being the precursors of group II disks (Dullemond & Dominik 2004). However it is the group I disk that are often observed to have a large ( $> 10$  AU) cavity in either scattered light or sub-mm imaging, implying that they are unlikely the precursors for the group II disks that are generally less massive and do not show any cavity (Maaskant et al. 2013; Garufi et al. 2017).

Inner disk ( $\lesssim 5$  AU) tracers of both gas and dust add interesting pieces to this puzzle. Table 5.1 reports median values for three inner disk tracers (near-infrared excess,  $F_{\text{NIR}}$ ; CO vibrational ratio,  $v2/v1$ ; CO emitting radius,  $R_{\text{CO}}$ ) as well as the median stellar surface Fe abundance (Kama et al. 2015) used to identify three groups of Herbig disks in Banzatti et al. (2018); here we also add notes on the presence of disk structures from imaging studies. Group II disks exhibit a narrow range of intermediate values for the near-infrared excess,  $F_{\text{NIR}} = L_{1.2-4.5\mu\text{m}}/L_{\star}$  (Garufi et al. 2017). All of the group II disks show broad CO 4.7  $\mu\text{m}$  rovibrational lines indicating that CO is emitting from small radii. These tracers together indicate that both molecular gas and dust are present and abundant at small distances from the star ( $\lesssim 5$  AU; van der Plas et al. 2015; Banzatti et al. 2018).

The group I disks, instead, remarkably split into two very distinct groups (Banzatti et al. 2018). Some of them have very high near-infrared excesses (high-NIR), higher than the group II sources, and only moderately broad CO rovibrational lines. The rest of the group I disks have low near-infrared excesses (low-NIR) and the narrowest CO rovibrational lines. Group I disks thus, while all having dust cavities imaged at larger radii, seem to show a marked dichotomy in their inner disks between those that have abundant gas and dust in the inner few AU, and those that do not, without a gradient of situations in between. While these groups do not show any segregation in terms of mass accretion rates (Banzatti et al. 2018), stellar elemental abundances show that the low-NIR group I disks are depleted in Fe compared to all of the other sources (Table 5.1), suggesting that the stars in low-NIR group I disks accrete gas that is depleted in dust compared to the 100:1 ISM dust ratio, suggesting that dust is trapped at larger radii in the disk (Kama et al. 2015).

In this work we focus on CO rovibrational emission, and in particular the observed trends between the radius and excitation of CO emission and the NIR excess (Fig. 5.1), to expand our growing understanding of inner disk structure and evolution in Herbig disks. Specifically, we aim to explain the dichotomy between low vibrational ratios coming from gas within  $< 5$  AU and the high vibrational ratios coming from larger radii. The observational dataset from Banzatti et al. (2017, 2018), briefly presented in Sec. 5.2, is used for comparison and validation of the models. In Sec. 5.3 the vibrational excitation

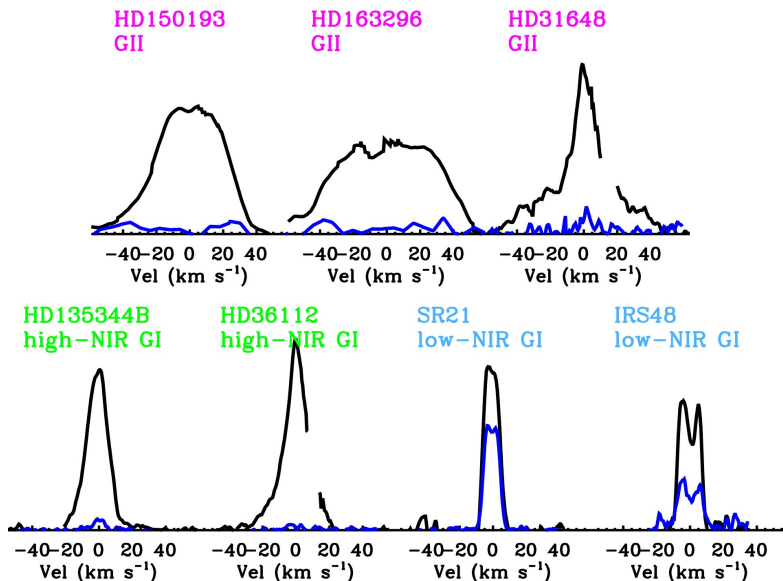


**Figure 5.2:** Selection of stacked CO line profiles from observed spectra (Section 5.2). The  $v_1$  lines are shown in black,  $v_2$  lines in blue. Gaps visible in some line profiles are due to telluric absorption. Disk inclinations are between 20 and 50 deg for all these objects. In HD 31648, the  $R_{\text{CO}}$  is taken for the broad component defined by the line wings.

of CO will be studied through simple slab models. Full thermo-chemical models using Dust And Lines (DALI, Bruderer et al. 2012; Bruderer 2013) for different physical structures will be presented and analysed in Sec. 5.4. The implications will be discussed in Sec. 5.5 and our conclusion will be summarized in Sec. 5.6.

## 5.2 Data overview

The CO emission lines adopted in this work for comparison to the models are taken from the compilation included in Banzatti et al. (2017, 2018), based on spectra originally presented in Pontoppidan et al. (2011b); Brown et al. (2012); Banzatti et al. (2015); van der Plas et al. (2015); Banzatti et al. (2018). The data consist of high resolution ( $R \sim 75,000\text{--}100,000$ ) spectra of CO rovibrational emission around  $4.7 \mu\text{m}$  for 20 Herbig Ae stars and 3 F stars, taken with the CRIRES instrument on the Very Large Telescope (VLT) of the European Southern Observatory (ESO; Kaeufel et al. 2004) and iSHELL on the NASA Infrared Telescope Facility (IRTF; Rayner et al. 2016). The spectrum of HD 142666 is taken from a previous survey (Blake & Boogert 2004; Salyk et al. 2011a) done with Keck-NIRSPEC ( $R \sim 25,000$ ; McLean et al. 1998). The two parameters we focus on in this work, the CO vibrational ratio,  $v_2/v_1$ , and a characteristic emitting radius, are measured from stacked line profiles as explained in Banzatti & Pontoppidan (2015).

In brief, the vibrational ratio  $v_2/v_1$  is measured from the line flux ratio between lines around the  $v_2 P(4)$  line ( $v' = 2, J' = 3 \rightarrow v'' = 1, J'' = 4$ ) and around the

$v1 P(10)$  line ( $v' = 1, J' = 9 \rightarrow v'' = 0, J'' = 10$ ). The choice of these specific lines is driven by the spectral coverage of the observations, and by the need to use unblended lines (see details in Banzatti & Pontoppidan 2015). The vibrational flux ratio between the  $v2 P(4)$  and  $v1 P(10)$  line is used as a proxy for the vibrational ratio between the  $v2$  and  $v1$  levels. The vibrational ratio depends on the lines that are used in the comparison, even lines of matching  $J$  level show a variation of up to 50% in the vibrational ratio. The  $v2 P(4)$  and  $v1 P(10)$  line ratio lies within the range of values obtained by using matching  $J$  levels and is thus a good proxy for the vibrational ratio (see Appendix A in Banzatti & Pontoppidan 2015). A characteristic emitting radius is estimated from the half width at half maximum (HWHM) of the line profile, assuming Keplerian rotation and using literature values for the disk inclination and the stellar mass. As better measurements of disk inclinations have become available over time for some disks, estimates of CO radii have changed accordingly; the error-bars in Fig. 5.1 reflect the uncertainties in the disk inclinations. Figure 5.1 shows these parameters and their trend as discussed above, namely that the vibrational ratio is larger when CO emission comes from larger disk radii.

Figure 5.2 shows a selection of CO line profiles, chosen to span the full range of CO emitting radii and vibrational ratios for the three groups of disks in Fig. 5.1. The broader lines (i.e. smaller CO emitting radii) have low  $v2/v1$ , and can have flat or double-peaked line profiles. HD 31648 is the only exception that clearly shows two velocity components, as commonly found for T-Tauri stars (Bast et al. 2011; Banzatti & Pontoppidan 2015). This combination of broad wings and strong peak indicates that the emitting area of the CO rovibrational lines spans a large range of radii (see more in Section 5.4). In this analysis, for HD 31648 we take the CO radius as indicated by the broad component, defined by the broad line wings. The narrower lines (i.e. larger CO emitting radii) often show a single peak profile indicative of a more extended emitting area, but in some cases they clearly show a double peak profile, indicative of an emitting region that is confined to a narrower ring.

In addition, we use CO line fluxes as measured in Banzatti et al. (2017), which we scale to a common distance of 150 pc for comparison with the model. The near-infrared excess is measured between 1.2 and 4.5  $\mu\text{m}$  (Garufi et al. 2017; Banzatti et al. 2018). Table 5.1 shows the median values for these parameters for the three groups of Herbig disks, as reported in Banzatti et al. (2018). Spectra and individual measurements can be found in the original references reported in this section.

### 5.3 Slab modelling of the vibrational ratio

To be able to infer the physical conditions of the CO emitting regions we have to look at the CO line formation process. To compute the strength of a line one needs to know both the chemical and physical state of the gas. Physics and chemistry are strongly intertwined with the temperature, density and radiation field influencing the chemistry and the chemical abundances influencing the heating and cooling of the gas, changing the temperature. Various thermo-chemical models have been developed to solve this coupled problem (e.g. Woitke et al. 2009; Bruderer et al. 2012; Bruderer 2013; Du & Bergin 2014), however, before we dive into the full problem, we will first study the line formation of CO in a more controlled setting.

The line formation of CO will be studied using two different types of slab models. First the behaviour of a slab of CO with fixed excitation will be studied analytically;

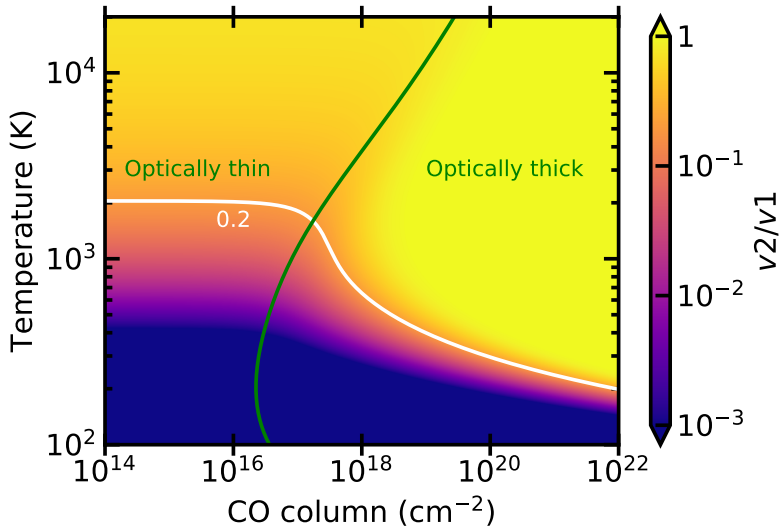


**Figure 5.3:** CO vibrational ratio,  $v_2/v_1$ , for different temperatures and columns from the analytic model. The green line shows the  $\tau = 1$  conditions for the  $v_1$  line. The white line shows  $v_2/v_1 = 0.2$ , which is the value that differentiates low and high vibrational ratio sources.

this will reveal the effects of the optical depth and excitation on the vibrational ratios. Afterwards RADEX models (van der Tak et al. 2007) will be used to study non-LTE effects. These RADEX models will be used to constrain the physical conditions of the CO rovibrational emitting regions.

### 5.3.1 Analytical line ratios

#### Methods

In the case of a mono-thermal slab of CO that is in LTE with an excitation temperature  $T_{\text{ex}}$ , the continuum subtracted peak surface brightness can be computed by:

$$I(u, l) = (B(T_{\text{ex}}, \nu(u, l)) - B(T_{\text{back}}, \nu(u, l))) \times (1 - e^{-\tau(u, l)}), \quad (5.1)$$

where

$$\tau(u, l) = \frac{g(u)}{g(l)} \frac{c^2 A(u, l)}{8\pi^2 \nu^2(u, l)} \frac{N_{\text{CO}} \left(1 - \exp\left[-\frac{h\nu(u, l)}{kT_{\text{ex}}}\right]\right)}{\sqrt{2\pi} \sigma_\nu Z(T_{\text{ex}})} g(l) \exp\left[-\frac{E(l)}{kT_{\text{ex}}}\right]. \quad (5.2)$$

In Eq. 5.1  $I(u, l)$  is the continuum subtracted line peak intensity,  $B(T, \nu)$  is the Planck function at temperature  $T$  and frequency  $\nu$ ,  $T_{\text{back}}$  is the radiation temperature of the background and  $\tau(u, l)$  is the line peak opacity. In Eq. 5.2  $g(n)$  is the degeneracy of rovibrational level  $n$ ,  $A(u, l)$  is the Einstein A coefficient of the transition between rovibrational levels  $u$  and  $l$ ,  $N_{\text{CO}}$  is the CO column,  $\sigma_\nu$  is the thermal linewidth,  $Z(T_{\text{ex}})$  is the rovibrational partition function of CO,  $E(n)$  is the energy above the rovibrational ground state of state  $n$  and  $c$ ,  $h$  and  $k$  are the speed of light, the Planck constant and the Boltzmann constant as usual.



The  $v1 P(10)$  and the  $v2 P(4)$  lines are used as proxy for the stacked  $v1$  and  $v2$  line from the observations (Section 5.2). Under the current assumptions the peak line intensity only depends on the excitation temperature, the total column and the background radiation temperature. This last parameter drops out when looking at line ratios (assuming that  $T_{\text{back}}$  does not vary significantly over the frequency range).

## Results

The peak line intensity ratio for the  $v1$  and  $v2$  lines are shown in Fig. 5.3 for a range of temperatures and CO columns. At columns smaller than  $10^{17} \text{ cm}^{-2}$  both lines are optically thin and as such there is no trend with column in the line ratio. At high column densities the line ratio converges to  $g_2(u)A_2(u, l)/g_1(u)A_1(u, l)$  which is  $\sim 1.01$  for the lines under consideration, for almost any temperature ( $T > 200 \text{ K}$ ).

The green line shows where the  $v1$  line becomes optically thick. An increase in CO column to the right of this line no longer elicits a linear response in the line flux. As the  $v2$  flux still increases linearly with the column, this increases the line ratio. If the column gets big enough the  $v2$  line also gets optically thick and the line ratio tends to unity. The speed at which this happens with increasing column strongly depends on the population of the upper level of the  $v2$  transition. At temperatures above, 2000 K the column at which the  $v1$  becomes optically thick increases due to the lower fractional population in the lower rotational levels of the  $v1$  line.

Observed line ratios coming from within 5 AU are generally below 0.2, so from Fig. 5.3 the conditions to match these observations can be easily read off. If both lines are optically thin, an excitation temperature less than  $\sim 2000 \text{ K}$  induces low line ratios. At columns above  $10^{17} \text{ cm}^{-2}$  a line ratio of 0.2 requires lower temperature with increasing column, to values as low as  $\sim 190 \text{ K}$  at a CO column of  $10^{22} \text{ cm}^{-2}$ .

All disks with  $R_{\text{CO}} > 5 \text{ AU}$  have line ratios between 0.2 and 0.5. For these high line ratios Fig. 5.3 shows that, as expected a high line ratio can be due to high temperature, or large columns. For low columns, temperatures between 2000 and 6000 K are needed to produce the right line ratios. Above a column of  $10^{17} \text{ cm}^{-2}$  progressively lower temperatures lead to the observed line flux ratios.

## Discussion

The vibrational ratio from these lines can be expressed as a vibrational excitation temperature. However, this only represents the excitation of the gas if both lines are optically thin. CO rovibrational lines get optically thick at CO columns of  $10^{16}$ – $10^{18} \text{ cm}^{-2}$  (Fig. 5.3). Assuming a dust mass opacity of  $2 \times 10^3 \text{ cm}^2 \text{ g}^{-1}$  (Bruderer et al. 2015, small grains), and a gas-to-dust ratio of 100 gives a H column of  $\sim 10^{22} \text{ cm}^{-2}$  before the dust gets optically thick at  $4.7 \mu\text{m}$ . This allows for CO columns up to  $10^{18} \text{ cm}^{-2}$  that can be detected for a canonical CO abundance of  $10^{-4}$ , and thus the generation of optically thick lines above the dust photosphere. Higher CO columns are possible if grains have grown beyond  $1 \mu\text{m}$  or if the dust is depleted with respect to the gas in the emitting layer. Analysis of  $^{13}\text{CO}$  lines suggest that columns of  $10^{19} \text{ cm}^{-2}$  are not uncommon for the sources with a high vibrational ratio (van der Plas et al. 2015). For these columns the high  $v2/v1$  ratios can be explained with a temperature between 300 and 500 K.

Equation (5.1) does not include the absorption of the line by dust grains nor the emission of hot dust in the region were  $\tau_{\text{dust}} < 1$ . These contributions would lower the

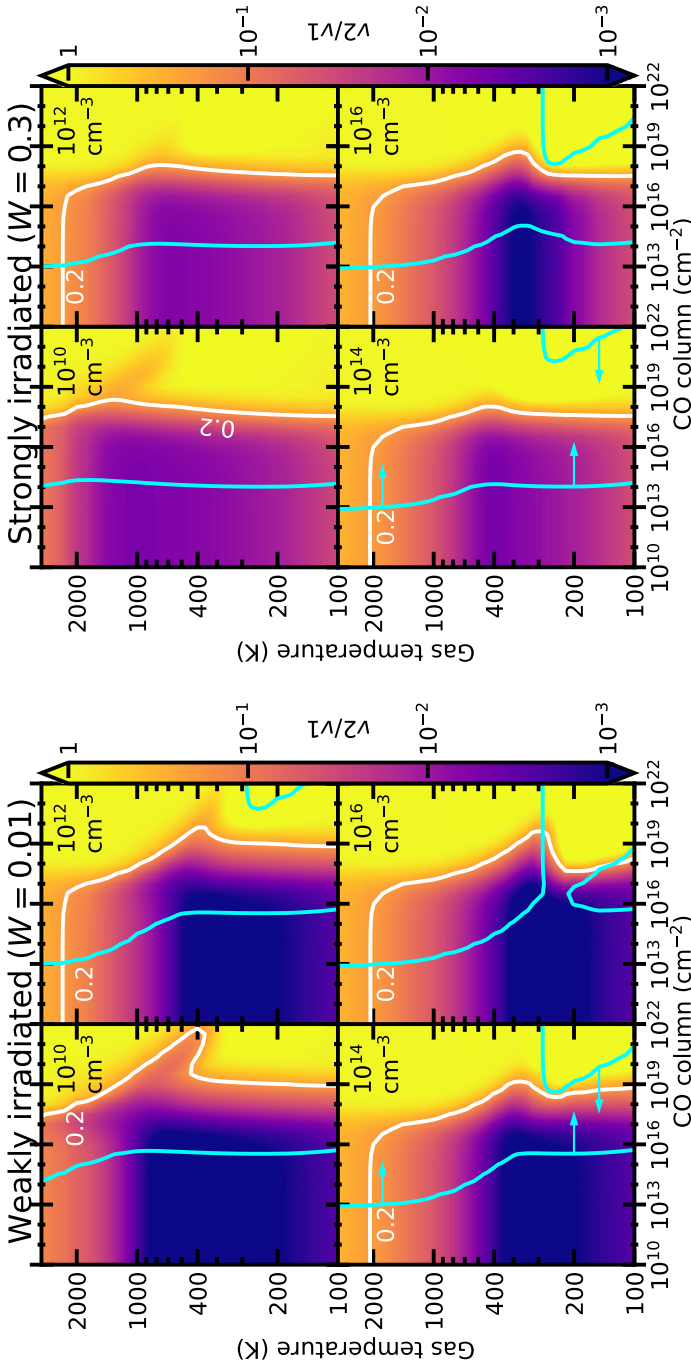


**Figure 5.4:** CO vibrational ratio,  $v_2/v_1$ , for different temperatures and columns from the RADEX models using a 750 K radiation field with a dilution factor  $W$  of 0.01 (*left*) and 0.3 (*right*). The area between the blue and white lines shows where both the vibrational ratio and the  $v_1$  flux of the low vibrational ratio sources are reproduced. For the  $v_1$  flux an emitting area with a radius of 5 AU is assumed. If a smaller emitting area is assumed the blue lines would shift in the direction of the blue arrows. High vibrational ratio sources can either be explained by gas with a high column ( $N \gtrsim 10^{18} \text{ cm}^{-2}$ ) or a high temperature ( $T > 2000 \text{ K}$ ).

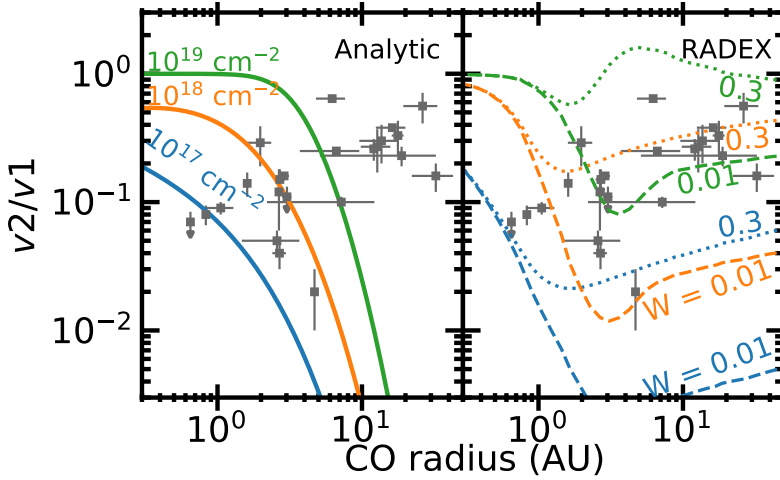


**Figure 5.5:** CO vibrational ratio versus the inferred radius of emission for observational data (grey points) and analytic (*left*) and RADEX (*right*) model results (coloured lines). For the RADEX models, two different assumption for the radiation field are shown weakly irradiated ( $W = 0.01$ , *dashed*) and strongly irradiated ( $W = 0.3$ , *dotted*) cases. For the highest column only the LTE model and the weakly irradiated RADEX model are shown. The density for the RADEX models is  $10^{12} \text{ cm}^{-3}$ .

line flux, by absorbing line photons and increasing the continuum level. These effects are more pronounced at low line opacities, and so affect the  $v2$  line stronger than the  $v1$  lines. As such, the line ratios are overestimated.

In the case of an added dust contribution, the dust opacity sets a maximum to the CO column that can be seen, while the dust emission sets the background temperature. The CO column under consideration is thus only the CO column above the dust photosphere ( $\tau_{\text{dust},4.7\mu\text{m}} \lesssim 1$ ).

One critical assumption of this analysis is that both lines are formed in the same region of the disk, either under one set of conditions or under a range of conditions each of which gives rise to a similar line ratio as the region average. The idea being that if the  $v1$  and  $v2$  lines would be coming from different regions of the disk, this would be seen as a significantly different line shape. As the line ratios are determined on the broad component that is seen in both the  $v2$  and  $v1$  lines we can be sure that this assumption holds.

### 5.3.2 RADEX models

Previously we have assumed a fixed excitation, parametrised by an excitation temperature. Here the excitation processes will be included explicitly by calculating the level populations from the balance between collisions, spontaneous emission and vibrational pumping. If no continuum opacity is assumed, the parameter space is four dimensional: the CO gas column, the kinetic temperature of the gas, the collision partner density (for this purpose assumed to be  $\text{H}_2$  (Yang et al. 2010)<sup>1</sup>) and the radiation field. For

<sup>1</sup>Results for H as collision partner are similar, but as the collisional rate coefficients are about an order of magnitude larger than the  $\text{H}_2$  collisional rate coefficients, the results for similar densities are

the geometry, a slab that is illuminated from one side is assumed. This configuration is representative for the surface layers of proto-planetary disks, where the infrared continuum photons interacting with the gas are not along the same line of sight as the observations are taken. The pumping radiation intensity is parametrized using a 750 K black body diluted by a factor ( $W$ ) between 0.0001 and 0.3, representative of a region at  $\sim 100$  times the radius of the  $4.7 \mu\text{m}$  continuum emitting region and of a region very close to the continuum emitting region.

Figure 5.4 shows the line ratio for the  $v2$  and  $v1$  lines from the RADEX models for different densities. This shows that for columns below  $10^{17} \text{ cm}^{-2}$  line ratios below 0.1 are the norm. Only at high density ( $> 10^{14} \text{ cm}^{-3}$ ) and high temperature ( $> 1300 \text{ K}$ ) is the ratio boosted above 0.1, this is similar to the results from the analytic analysis. For  $W = 0.01$ , the low density results show the expected subthermal excitation of CO leading to lower line ratios compared to the LTE case. In contrast, in the  $W = 0.3$  case there is a stronger contribution from excitation by infrared photons. This contribution is strongest at low temperatures where collisional excitation rates for the vibrational transitions are lowest.

### 5.3.3 LTE vs non-LTE

The line ratios for CO columns of  $10^{17}$ ,  $10^{18}$  and  $10^{19} \text{ cm}^{-2}$  are plotted in Fig. 5.5 for both the analytical and RADEX models. For these curves the temperature is assumed to scale as:

$$T(R_{\text{CO}}) = 1500 \left( \frac{0.4 \text{ AU}}{R_{\text{CO}}} \right)^2 \quad (5.3)$$

which is approximately the dust equilibrium temperature around a star of  $30 L_{\odot}$ . It is clear that, for these conditions the LTE models can only explain the vibrational ratios at small radii, and those only at columns  $< 10^{18} \text{ cm}^{-2}$ .

The non-LTE RADEX models do somewhat better. With a  $\text{H}_2$  density of  $10^{12} \text{ cm}^{-3}$ , the RADEX models can reproduce the relatively low line ratios at radii smaller than 5 AU at larger columns than the analytical model. The RADEX models can also reproduce the trend in the observed data points in Figure 5.5, and with a strong enough radiation field, or high enough column, it can also reproduce the absolute line ratios. This indicates that high temperatures or a strongly out of LTE excitation is causing the high vibrational ratio at  $R_{\text{CO}} > 5 \text{ AU}$ .

Taking into account that the infrared radiation field decreases with radius, Fig. 5.5 implies that the CO column responsible for the emission needs to increase with  $R_{\text{CO}}$ .

### 5.3.4 Absolute fluxes

#### Low vibrational ratios in the inner disk

To further constrain the conditions of the emitting gas, it is useful to compare the absolute fluxes to the observations. First the sources with low vibrational ratios and small CO emitting radii in the lower left corner of Fig. 5.1 are investigated. Rescaling the Herbig line fluxes from Banzatti et al. (2017) to a common distance of 150 pc leads to a range in fluxes between  $4 \times 10^{-15}$  and  $2 \times 10^{-12} \text{ erg s}^{-1} \text{ cm}^{-2}$  for the  $v1$  line and  $3 \times 10^{-16}$  and  $4 \times 10^{-13} \text{ erg s}^{-1} \text{ cm}^{-2}$  for the  $v2$  line.

---

shifted to more towards LTE (Song et al. 2015; Walker et al. 2015).

For these sources, the line width implies an emitting radius smaller than 5 AU. Assuming, as a conservative case, that the flux comes from the full inner 5 AU, it is possible to select conditions that are able to produce both the correct  $v_1$  line flux and the correct line ratio. These conditions are confined between the blue and white lines in Fig. 5.4.

The low vibrational ratios and line fluxes can be reproduced with CO columns between  $10^{14}$ – $10^{19}$   $\text{cm}^{-2}$ . More confined emitting areas would increase the lower limit of the possible columns. Temperatures between 400 and 1300 K are most likely if the CO excitation is dominated by collisions. If IR vibrational pumping dominates, higher gas temperatures are still consistent with the low vibrational ratios.

### High vibrational ratios at larger radii

To extract the physical conditions in the emitting regions for the disks with a high vibrational ratio at large radii (low NIR group I disks), the observed fluxes and vibrational ratios were compared with the predicted fluxes from a grid of RADEX models. As the emitting area for these disks is harder to estimate than for sources with a low vibrational ratio at small radii, the emitting area was left as free parameter. As CO is coming from large radii it is expected that the near-infrared radiation field will be weak in the CO emitting area for these sources. Therefore, weaker radiation fields ( $W = 0.0001$  and  $0.01$ ) are used in the RADEX modelling. Figure 5.6 shows the conditions that lead to a vibrational ratio between 0.2 and 0.5 and total integrated  $v_1$  fluxes between  $3 \times 10^{-15}$  and  $5 \times 10^{-14}$   $\text{erg s}^{-1} \text{cm}^{-2}$  (normalized to 150 parsec), the range of observed values for low NIR group I sources.

Within the RADEX models there are two families of solutions. For clarity these solution families have been split in Fig. 5.6. One solution family is characterised by low temperatures ( $< 300$  K) and very high column densities ( $> 10^{18}$   $\text{cm}^{-2}$ ), the other solution has high temperatures ( $> 2000$  K) and low column densities ( $< 10^{14}$   $\text{cm}^{-2}$ ). In the low temperature family of solutions, the high line ratio comes primarily from the large columns of gas. The density is virtually unconstrained at small emitting areas and the lowest radiation fields. To allow for a large emitting area, very high densities are needed ( $> 10^{13}$   $\text{cm}^{-3}$ ), these densities are not reasonable at 10 AU, especially not in the disk surface. In the  $W = 0.0001$  case, the radiation field does not dominate the excitation. The low temperature branch is also sensitive to the IR continuum radiation field. A stronger IR field moves the solutions to smaller emitting surface areas and higher densities as excitation conditions are more easily met and the line surface brightness increases. Strong IR radiation fields are not expected to be produced by local dust so a local pumping field with  $W = 0.0001$  is preferred over  $W = 0.01$ .

In the high temperature family the excitation of CO is dominated by the collisions with the gas. At these high temperatures both vibrational states are easily populated by collisions and the ratio in which they are populated is similar to the line ratios that is seen. As long as the density is above  $10^{11}$   $\text{cm}^{-3}$ , the result is density independent. Because the lines are optically thin, the line flux is given by the total amount of CO molecules giving rise to a surface area, column degeneracy. The solution is independent of the radiation field assumed.

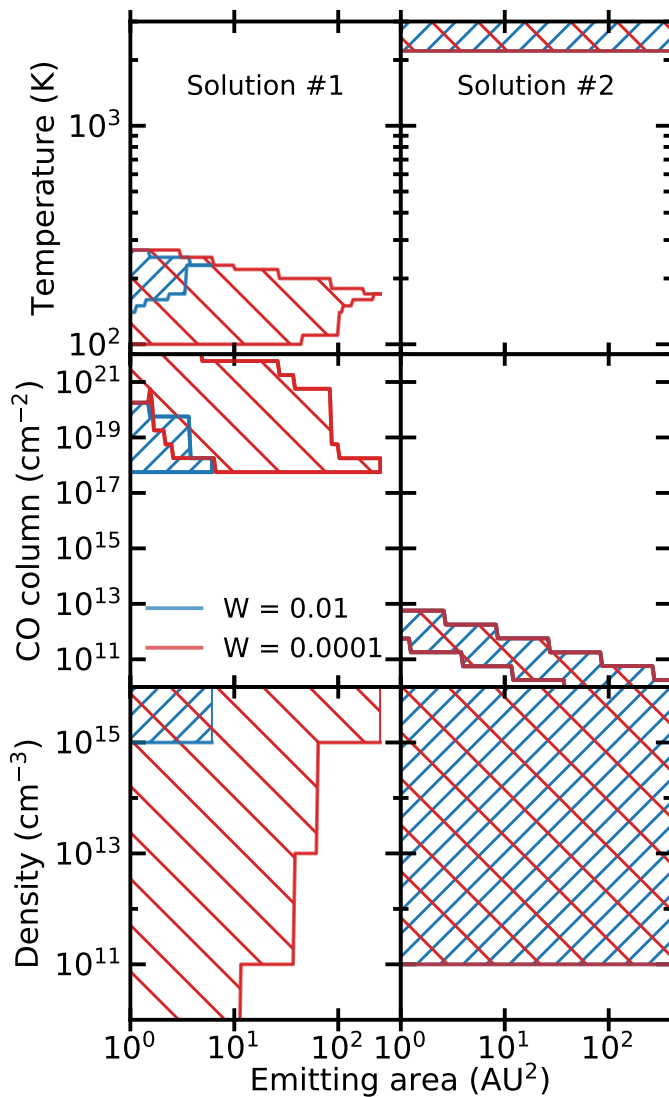


**Figure 5.6:** Parameters that can reproduce the observed CO rovibrational fluxes and line ratios for sources with  $R_{\text{CO}} > 5$  AU as function of assumed emitting area. Two solution branches are found, a low temperature (*left*) and a high temperature (*right*) branch. Different colours show models with different strengths of the infrared radiation field. In the second solution branch, the radiation field does not impact the solutions significantly.

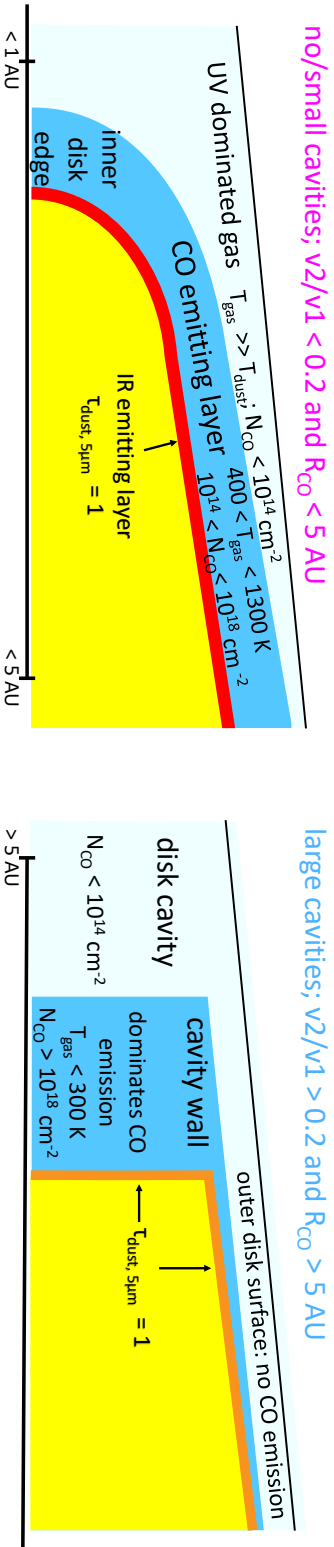


**Figure 5.7:** Summary of physical condition constraints from the RADEX models on the emitting regions of the CO rovibrational lines. Fig. 5.14 shows a version of this figure updated with the results of the full disk modelling. The constraints derived here are used to guide the DALI modelling. Regions are not shown to scale. The right panel shows solution #1 from Fig. 5.6 as observations of  $^{13}\text{CO}$  ro-vibrational lines indicate the presence of large columns of CO (van der Plas et al. 2015).

### 5.3.5 Physical conditions in the CO emitting region

The slab models provide important constraints on the physical conditions of gas producing the observed CO rovibrational emission. In Fig. 5.7 these constraints have been put in the context of simple disk geometries. Modest temperatures ( $\lesssim 1000$  K) and columns below  $10^{18}$   $\text{cm}^{-2}$  are needed to explain the low vibrational ratios at small  $R_{\text{CO}}$ . These columns are most likely present in the surface layers of a dust rich inner disk and imply gas-to-dust ratios smaller than 1000, assuming that the dust is optically thick at  $4.7$   $\mu\text{m}$ . The modest temperatures needed indicate that at these small radii, the temperature of the CO emitting gas cannot be more than a factor  $\sim 2$  higher than the dust temperature, as gas that is hotter than twice the dust temperature would easily reach 1500 K, especially within the inner AU. This would create higher vibrational ratios than measured. In the next Section, the constraints from the slab models will be used as guidance for the thermo-chemical modelling, and the constraints will be updated with the results from the full disk modelling.

To explain the high vibrational ratios coming from large radii a large gap in molecular gas is needed. As these sources also have low near-infrared continuum emission and gaps have been imaged in many of them (e.g. Garufi et al. 2017), a gap devoid of most of the gas and all the dust is assumed. In the case of a large dust gap, the CO column in the cavity needs to be very low, on average lower than  $10^{14}$   $\text{cm}^{-2}$ . If the column were higher, then the  $v1$  flux from within 5 AU would be strong enough to be detected. Alternatively, it can be estimated that the surface area of optically thick CO gas within the cavity needs to be  $\lesssim 0.25\text{AU}^2$ .

Two families of solutions have been found from the RADEX models to fit both the line strengths and the line ratios. The first solution is shown in the left panel in Fig. 5.7 and needs low temperatures and high columns. This solution is preferred as fits of the rotational diagram of rovibrational lines of  $^{12}\text{CO}$  and  $^{13}\text{CO}$  for disks with a high vibrational ratio (van der Plas et al. 2015) prefer large columns  $N_{\text{CO}} \approx 10^{19}$   $\text{cm}^{-2}$  and moderate temperatures (300 – 500 K). To be able to probe these large columns, local gas-to-dust ratios in the CO emitting regions above 100 are necessary, with many solutions needing gas-to-dust ratios of 10000.

The increase in vibrational line ratio with emitting radius seems thus to be an effect of the increase in gas-to-dust ratio of the CO emitting area, with CO coming from gas with a temperature that is coupled to the dust for both the low  $v2/v1$  and the high  $v2/v1$  sources. This indicates that the process that clears out the inner disk of gas in the high  $v2/v1$  sources, clears out the dust as well and confines it to larger radii than the gas. This is what would be expected for a dust trap and in line with the low metallicity measured in the accreting material in these sources (Kama et al. 2015). We will discuss these scenarios in Section 5.5.

## 5.4 DALI modelling

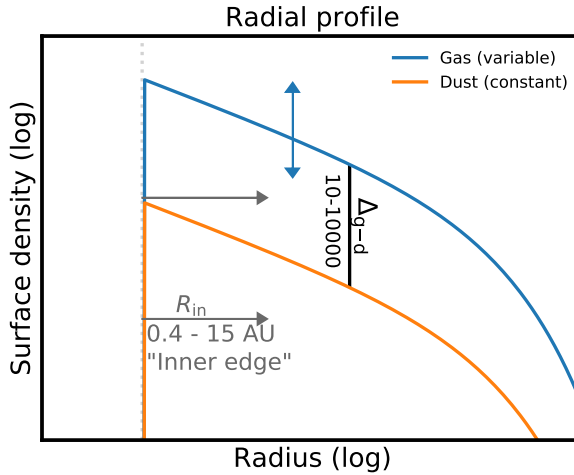
### 5.4.1 Model setup

Armed with an understanding of which conditions reproduce the observations we now run a set of DALI models. Different sets of Herbig disks is modelled with the inner edge, that is, innermost radius at which gas and dust is present ( $R_{\text{in}}$ ), varied from the classical sublimation radius at 0.4 AU up to 15 AU (see Fig. 5.8). Table 5.2 shows the



**Table 5.2:** Fiducial parameters

Parameter	Symbol	Value
Stellar Luminosity		$30 L_{\odot}$
Stellar Mass		$2.5 M_{\odot}$
Effective Temperature		10000 K
Sublimation radius	$R_{\text{subl}}$	0.4 AU
Critical radius	$R_c$	50 AU
Disk outer radius	$R_{\text{out}}$	500.0 AU
Gas surface density at $R_c$	$\Sigma_c$	$60 \text{ g cm}^{-2}$
Surface density power law slope	$\gamma$	1
Disk opening angle	$h_c$	0.1
Disk flaring angle	$\psi$	0.25
PAH abun. rel. to ISM	$x_{\text{PAH, ISM}}$	$10^{-20}$
Large dust fraction		0.9
Large dust settling		0.1
Disk inner radius	$R_{\text{in}}$	0.4 – 15 AU
Gas-to-dust ratio	$\Delta_{\text{g-d}}$	10 – 10000

**Figure 5.8:** Schematic representation of the surface density in the monolithic models.  $R_{\text{in}}$  is the same for gas and dust and is varied between 0.4 and 15 AU, while  $\Delta_{\text{g-d}}$  is varied between 10 and 10000.

parameters assumed for the model disks. The gas and dust surface densities are given by:

$$\begin{aligned}\Sigma_{\text{gas}} &= \Delta_{\text{g-d}} \Sigma_{\text{dust}} \\ \Sigma_{\text{dust}} &= \frac{\Sigma_c}{100} \left( \frac{R}{R_c} \right)^{-\gamma} \exp \left[ - \left( \frac{R}{R_c} \right)^{2-\gamma} \right],\end{aligned}\tag{5.4}$$

where the gas-to-dust ratio is varied between 10 and 10000. The thermo-chemical modelling is done with the code DALI (Bruderer et al. 2012; Bruderer 2013). The standard setup is used except for a few changes that will be highlighted where relevant. Dust temperature is calculated using Monte Carlo radiative transfer. Gas temperature, chemical composition and molecular excitation are self-consistently calculated. For the thermo-chemical calculation both the CO and H<sub>2</sub>O molecular models have been expanded. For CO five vibrational levels, up to  $v = 4$  each with 41 rotational levels, up to  $J = 40$  are included, with level energies, line positions and Einstein A coefficients taken from the HITRAN database (Rothman et al. 2013). Collision rate coefficients for collisions between CO and H<sub>2</sub> (Yang et al. 2010) and H (Song et al. 2015; Walker et al. 2015) are included. The full molecule model is described in Appendix 5.A. The molecule model for H<sub>2</sub>O has been expanded to include vibrational lines, as these could be important for cooling in the regions that CO is emitting. For H<sub>2</sub>O the rovibrational datafiles from LAMDA<sup>2</sup> are used (Tennyson et al. 2001; Barber et al. 2006; Faure & Josselin 2008). The line profiles are extracted for the CO  $v_2$  and  $v_1$  transitions using the raytracer as described in Bruderer et al. (2012). For the ray tracing a disk inclination of 45° and distance of 150 parsec is used.

The extracted line profiles are then convolved to match a resolving power of  $R = 100000$ , and noise is added to achieve a similar signal-to-noise as in the observations ( $\sim 200$ ). From these line profiles the emitting radius (from the line width) and vibrational line ratio are extracted using the same method as used for observational data by Banzatti & Pontoppidan (2015).

For some models the gas temperature and chemistry are not calculated self consistently. These are the LTE models in Fig. 5.9 and the  $T_{\text{gas}} = T_{\text{dust}}$  model in Appendix 5.B. In these models the gas temperature is set equal to the dust temperature as calculated by the dust radiative transfer and the CO abundance is parametrised by:

$$x_{\text{CO}} = 10^{-4} \times \frac{A_V}{1 + A_V},\tag{5.5}$$

with  $A_V$  the visual extinction as calculated from the continuum radiative transfer. For large  $A_V$  the CO abundance converges to the canonical value of  $10^{-4}$ , at  $A_V < 1$  the CO abundance is decreased from the canonical value to mimic the effects of photo-dissociation. The CO abundance globally agrees well with the CO abundance from the thermo-chemical model. These simplified models have been run in LTE conditions and in non-LTE by explicitly calculating the excitation ( $T_{\text{gas}} = T_{\text{dust}}$  model).

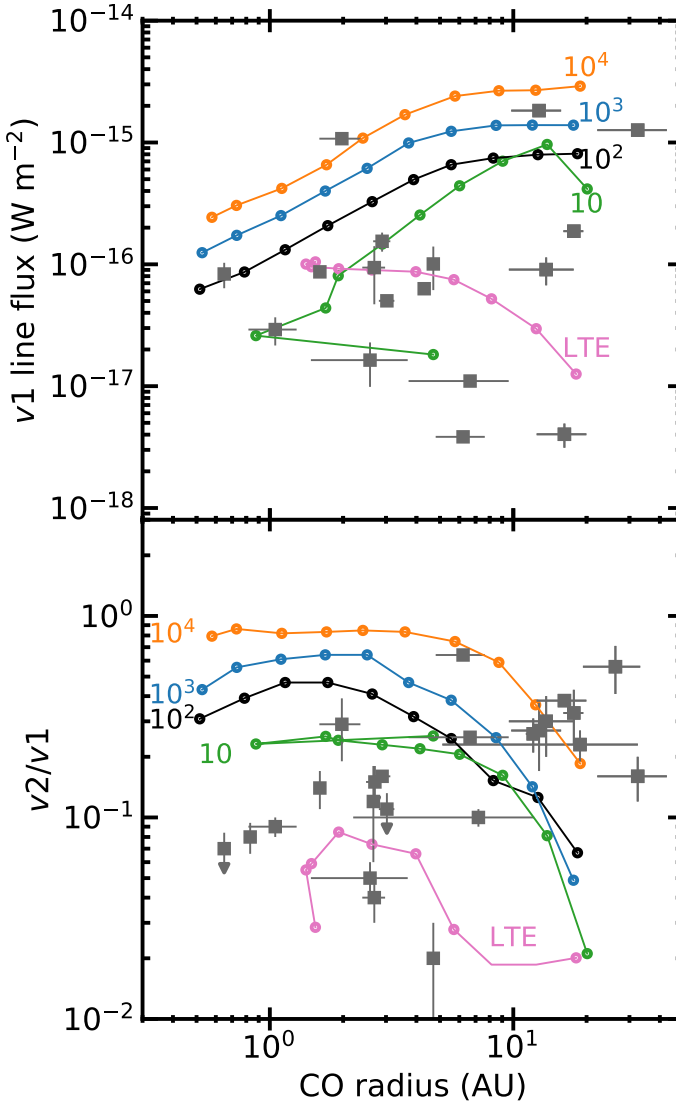


**Figure 5.9:**  $v_1$  line flux (*top*) and vibrational ratio of CO (*bottom*) versus the inferred radius of emission for observational data and DALI model results. Lines connect the dots in order of inner model radius. Labels indicate the gas-to-dust ratio for the thermo-chemical models, the LTE model also has a gas-to-dust ratio of 100. The model with the largest cavity has the largest CO radius. The dust surface density is kept constant for models of different gas-to-dust ratios. Due to missing data, not every source with a vibrational ratio in the lower panel also has a line flux in the upper panel. Clearly none of these models reproduce the trends in the data.

## 5.4.2 Model results

### $v1$ line flux and $v2/v1$ ratio

Results of our fiducial model, with a gas-to-dust ratio of 100, are plotted in Fig. 5.9 as the black points. The vibrational ratio from these models shows exactly the opposite trend from the data. The model vibrational ratio is roughly flat with a value around 0.4 for CO radii less than 2 AU, while at larger radii the line ratio decreases. The line-to-continuum ratios and line fluxes for the models are generally too high (Fig. 5.9, top). At small CO emitting radii line fluxes are consistent with the highest observed fluxes, at large CO emitting radii the model line fluxes are a factor  $\sim 10$  higher than the average flux.

The flux is dominated by optically thick lines coming from the inner edge of the model. The gas temperature in the emitting region is higher than  $\sim 600$  K in all models. This means that the CO rovibrational lines are emitted at wavelengths longer than peak of the relevant Planck function. As a result, the line flux of these optically thick lines scales linearly with the gas temperature. The gas temperature in the emitting regions decreases slowly with increasing inner model radius and is almost constant for models with  $R_{\text{in}}$  between 1.4 and 10 AU. While the total area of the inner edge scales as  $A \propto R_{\text{in}}^{2+\psi}$ , not all of this area contributes to the emission. The emission is dominated by two rings, at the top and bottom of the inner edge wall. These rings are situated in the region where the dust temperatures are higher than the midplane dust temperature and the CO excitation is still thermalized with the gas. In the models the vertical extend of this region increases slightly with radius, leading to faster than linear growth of the emitting area. Coupled with the constant or slowly declining temperature with radius leads to a roughly linear relation between inner model radius and CO  $v1$  flux.

The effect of the gas-to-dust ratio on the vibrational ratio is also shown in Fig. 5.9 (bottom). All models show a similar trend: with increasing CO radius, the  $v2/v1$  drops. Models with an increased gas-to-dust ratio produce higher  $v2/v1$  line ratios. This is due to the larger column of gas that can emit, leading to more optically thick lines, driving up the  $v2$  lines compared to the  $v1$  lines. Even so, the models with the lowest gas-to-dust ratio still have a  $v2/v1$  ratio larger than most of the observed disks for emitting radii of less than  $\sim 4$  AU. For models with the smallest cavities the line becomes undetectable at gas-to-dust ratios lower than 10. With increasing gas-to-dust ratio, there is also an increasing  $v1$  line flux, indicating that the emitting area is getting larger.

The LTE models in Fig. 5.9 show a very different behaviour to the thermo-chemical models. This is fully due to the LTE assumption because the parametrisation of the CO abundances and the assumption of coupled gas and dust temperature have only very small effects of the line ratios (see Appendix 5.B). The LTE models consistently have lower vibrational ratios than the fiducial models, due to the fact that neither the IR pumping nor excitation due to self-absorption are included. Together these processes explain the different vibrational ratios between the fiducial and LTE models. The LTE models with small cavities have vibrational ratios and CO emitting radii that are consistent with with observations. For the disks with larger cavities, the LTE models cannot come close to the observations, indicating that non-LTE processes

---

<sup>2</sup>Leiden Atomic and Molecular DAtabase <http://home.strw.leidenuniv.nl/~moldata/> (Schöier et al. 2005)

are definitely important for gas at large radii. The effect of infrared pumping and UV pumping has also been studied in Appendix 5.B but removing IR pumping and including UV pumping only has marginal effects on the excitation and neither can explain the discrepancy between the data and the models. The LTE models consistently show line fluxes that are in good agreement with the data.

That the LTE models seem to do so well, certainly for the low  $v_2/v_1$  sources, is puzzling. The LTE assumption only holds for the CO rovibrational lines if the local gas density is above  $\sim 10^{16} \text{ cm}^{-3}$ . These high densities are only expected near the disk midplane and not at the disk surface.

Beyond 5 AU there are non-LTE models that overlap with the data and there is a suggestion that higher gas-to-dust ratios are needed to explain the increase in vibrational ratio with increasing CO emitting radius. However, fluxes are high for these models,  $10^{-15} \text{ W m}^{-2}$  at 150 parsec, about a factor of 300 higher than most observed high vibrational line ratio sources. The DALI models do not show a hot, tenuous layer of CO such as would be needed for solution #2 of Fig. 5.6. They show instead that with high gas-to-dust ratios, and thus high CO columns the right vibrational ratios can be reproduced, consistent with solution #1 of Fig. 5.6.

### Line profiles

As shown in Fig. 5.9, the extracted line ratios and emitting areas of most models are not able to explain the observed behaviour, especially the low line ratios in the inner disk. It is thus necessary to take a closer look at the predicted line profiles, and compare those with the observed line profiles (Fig. 5.2) for an explanation for this mismatch. The line profiles for subsets of DALI models are shown in Fig. 5.10 (line profiles for all models are shown in App. 5.C).

The models with small holes ( $< 2 \text{ AU}$ ) show a clear difference between the full thermo-chemical models and the LTE models. The full DALI models consistently show a two component line structure. There is a broad, nearly top hat, component of the line which is present in both the  $v_1$  and the  $v_2$  lines, and a more strongly peaked line profile that is very weak in the  $v_2$  line. This second component compares well to the line profile of HD 31648 in Fig. 5.2.

The total line flux and the line ratio are seen to increase with increasing gas-to-dust ratio. Furthermore, the  $v_1$  line profile gets narrower with increasing gas-to-dust ratio, consistent with the emitting area getting larger for higher gas-to-dust ratios.

None of the observations show the broad plateau-like feature that is in our model line profiles with small  $R_{\text{in}}$  ( $< 2 \text{ AU}$ ). This indicates that the inner rim of the model disk needs to be adapted to fit the data. Mostly, the  $v_2$  flux from the inner disk wall needs to be strongly reduced. The LTE models show that low vibrational ratios are produced if the gas, dust and CO excitation are thermalised. To thermalise the CO excitation densities in the emitting area of more than  $\sim 10^{16} \text{ cm}^{-3}$  are necessary, this is an increase in density of about 4 orders of magnitude compared to the current density of the inner disk wall. Another option would be to lower the CO abundance from the inner rim regions by at least 4 orders of magnitude, removing most of the contribution of the inner rim to both the  $v_1$  and  $v_2$  lines.

The line profiles from models with an inner radius of 10 AU generally show a narrow double peaked profile in both lines, indicating that the directly irradiated inner edge is contributing most of the flux in both transitions. This is consistent with the very steep line profiles without low-level wings seen from disks with a high vibrational ratio (e.g.

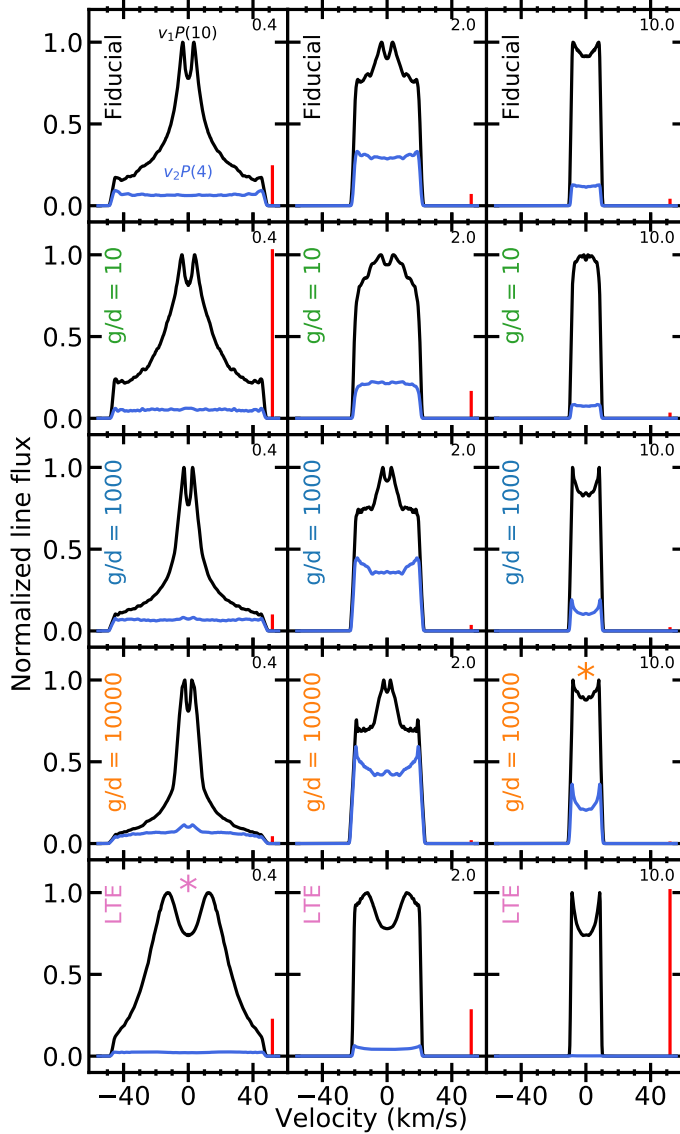


**Figure 5.10:** Normalised model line profiles for the  $v_1$  (black) and the  $v_2$  (blue) lines for a subset of the models at the native resolution of the model,  $R = 10^6$ . The text on the left of each panel denotes the model set. The top right corner of each panel denotes the inner radius of the model. The vertical bar in the bottom right of each panel shows 0.03 (top two rows) or 0.3 (bottom row) of the continuum flux density. Two models with a "\*" match both  $R_{CO}$  and  $v_2/v_1$  for a subset of the data. All lines are modelled assuming a 45 degree inclination. No noise has been added to these lines, noise-like features in the line profiles are due to the sampling of the DALI grid.

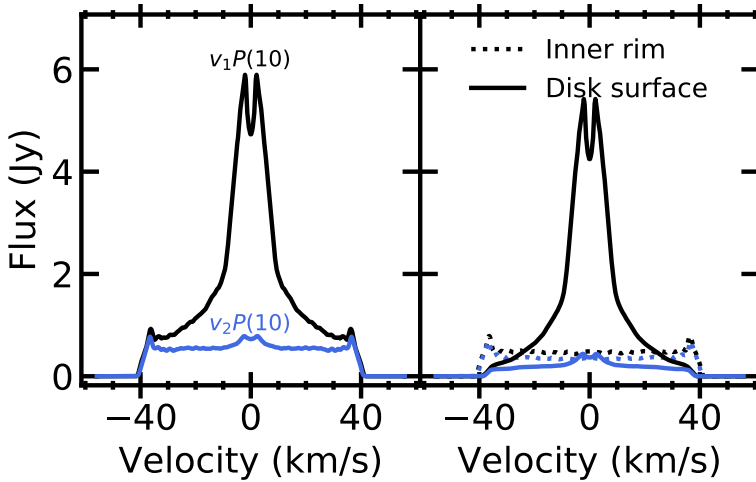


**Figure 5.11:** Line profiles for the models with an inner cavity of 0.6 AU and a gas-to-dust ratio of 10000. In the right hand plot contributions from the inner rim and disk surface are separated.

IRS 48, Fig. 5.2). The line ratio strongly depends on the gas-to-dust ratio in the disk surface: high gas-to-dust ratios lead to higher vibrational ratios as the  $v_1$  line opacity increases. Higher gas-to-dust ratios also lead to larger  $v_1$  fluxes. The LTE models with large cavities have no detectable  $v_2$  emission. It is, however the only model  $v_1$  line for which the flux is within the observed range; the non-LTE models overpredict the flux.

Comparison of the line profiles in Fig. 5.2 and Fig. 5.10 indicates that for observed disks with low vibrational ratios, the line profiles can be well reproduced by models that have a small cavity radius except that these models have a plateau-like contribution to the line profile in the inner disk. This indicates that emission from the disk surface agrees with the observed line profiles and line ratios. This is consistent with the analytical and RADEX analysis which predict low vibrational ratios for disk surface conditions.

Using the spatial information in the model image cube, the emission was decomposed into a disk surface and a disk inner rim component. Fig. 5.11 shows the original (continuum subtracted) and decomposed line profile for the model. The line profile cleanly separates into a broad, high line ratio component coming from within 0.63 AU and a narrowly peaked, low line ratio component from the rest of the disk. This suggest that the models strongly overestimate the flux coming from the inner rim. The implications of this will be discussed in Sec. 5.5.1.

### 5.4.3 Disk surface emission

The removal of the line contribution from the inner rim makes it possible to make a direct comparison between observations and the flux from the disk surface. We restrict ourselves to model disks with a small inner cavity size ( $< 1.5$  AU) as for these radii the vibrational ratio is most strongly over predicted in the models. The inner rim region from which the line emission is removed originally produces  $\sim 40\%$  of the  $v_1$  flux and

**Table 5.3:** Model variations for the models with subtracted edge contributions.

Inner radius variation		$g/d = 100$		$g/d = 1000$		$g/d = 10000$	
$R_{\text{in}}$ (AU)	$F_{\text{NIR}}$	$v2/v1$	$R_{\text{CO}}$ (AU)	$F_{v1}^a$	$v2/v1$	$R_{\text{CO}}$ (AU)	$F_{v1}^a$
# 1.	0.14	0.03	2.3	4.6	0.05	2.4	9.7
# 2.	0.16	0.02	2.8	4.9	0.04	3.2	10.4
# 3.	0.18	0.04	15.2	5.5	0.03	20.7	12.1
Outer radius variation		$g/d = 100$		$g/d = 10000$		$g/d = 10000$	
$R_{\text{out}}$ (AU)	$F_{\text{NIR}}$	$v2/v1$	$R_{\text{CO}}$ (AU)	$F_{v1}^a$	$v2/v1$	$R_{\text{CO}}$ (AU)	$F_{v1}^a$
# 1.	0.13	0.18	1.4	2.0	0.32	1.5	7.0
# 2.	0.13	0.12	2.5	2.6	0.25	2.3	9.0
# 3.	0.14	0.07	3.2	3.0	0.42	1.1	10.4
# 4.	0.14	0.03	2.3	4.6	0.33	3.7	20.9
Flaring variation		$g/d = 100$		$g/d = 10000$		$g/d = 10000$	
h (rad)	$\psi$	$v2/v1$	$R_{\text{CO}}$ (AU)	$F_{v1}^a$	$v2/v1$	$R_{\text{CO}}$ (AU)	$F_{v1}^a$
# 1.	0.02	0.0	0.8	0.2	0.35	0.7	1.4
# 2.	0.1	0.0	1.4	3.5	0.67	0.80	16.6
# 3.	0.02	0.25	12.2	0.4	0.03	2.5	5.9
# 4.	0.1	0.25	2.3	4.6	0.33	3.7	20.9

**Notes.** <sup>(a)</sup>  $v1$  line flux ( $\times 10^{-14}$  erg cm<sup>-2</sup> s<sup>-1</sup>)



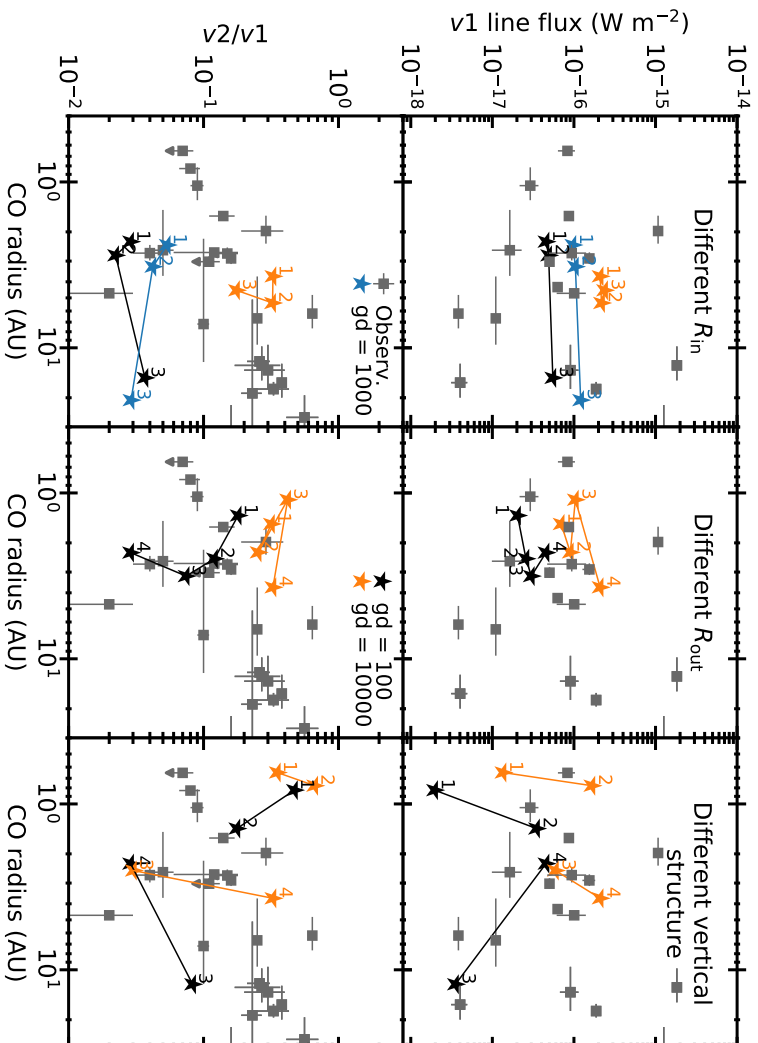


**Figure 5.12:**  $v_1$  flux (top) and CO vibrational ratio (bottom) versus the inferred radius of emission for observational data and model results.

The contribution from the inner edge has been subtracted from the models spectra before analysis. Models show variation in inner radius (left panel), variation in outer radius (middle panel) and variation in flaring and disk height (right panel). In the left and middle panels lines connect points in increasing order of the parameter varied. In the right panels, lines connect models with the same flaring angle and thus the difference between connected points show the effect of a change in thickness of the disk. Table 5.3 lists the parameters varied for these models. Models with a gas-to-dust ratio of 100 and 1000 are better at reproducing the vibrational ratio than the models with gas-to-dust ratios of 10000. Variation in the vibrational ratio can be reproduced by variations in the disk structure, but no single parameter explain all the variation.

$\sim 90\%$  of the  $v_2$  flux. This region also accounts for  $\sim 90\%$  of the  $4.7 \mu\text{m}$  continuum flux in the model. As before, different inner disk radii and gas-to-dust ratios are studied. On top of that, for models with an inner radius of 0.4 AU and gas-to-dust ratios of 100 and 10000, the outer radius and vertical scale height and flaring are also varied. Table 5.3 gives an overview of the varied parameters and model results. Figure 5.12 compares results of the DALI models without a contribution of the inner rim to the observed data.

By isolating the emission from the disk surface, low vibrational ratios can be obtained at small CO radii. Increasing the gas-to-dust ratio increases the vibrational ratio and the  $v_1$  line flux, while only slightly increasing the CO emitting radius. Increasing the inner cavity radius to more than 1 AU causes the CO emitting radius to increase beyond 10 AU for gas-to-dust ratios of 100 and 1000. No sources with such a narrow CO line and a low vibrational ratio are seen.

Truncating the outer disk, by removing all material beyond a radius of 8, 5 or 3 AU moves the emission inward and generally increases the vibrational ratio, because the emission has less contribution from larger radii and colder gas. The more truncated disks also have lower  $v_1$  fluxes, while the NIR continuum emission is not reduced compared to their full disk counterparts. As expected, a more flared disk has emission from further out, and is vibrationally colder, than a geometrically flatter disk. Lowering the scale height moves the emission further out for a non-flared disk, while for flared disks the emitting radius is reduced.

Overall, figure 5.12 shows that emission from the disk surface, especially with gas-to-dust ratios of 100 or 1000, can match the observed CO line fluxes and vibrational ratios at small radii. Different inner radii disk cannot explain the full extent of the data. Restricting the emitting region, in this case by truncating the disk, or changing the vertical structure of the inner disk helps in reproducing the spread in vibrational ratio and CO radius. This indicates that rovibrational CO emission is tracing substructures in the inner disk surface.

Comparing the model line profiles (Fig. 5.10) with the observed line profiles (Fig. 5.2) reveals that there is only one disk that is matched well with a full, flared disk (HD 31648, also known as MWC 480). All other line profiles are better matched with a very flat or even truncated model. The ubiquity of emission at large radii in the models, but not in the data, implies that the inner disk structure of the observed disks is different from the smooth, flared geometry assumed in the model.

#### 5.4.4 $T_{\text{gas}} \approx T_{\text{dust}}$

The removal of the inner rim for the small  $R_{\text{in}}$  models (Sec. 5.4.3) and the lower temperatures in the rounded models with large  $R_{\text{in}}$  (Appendix 5.E) allow us to reproduce line widths, line strengths and vibrational ratios. All these models have in common that the gas and dust temperature in the emitting area are similar, with 20% temperature differences in the surface layers of the disks with small holes and difference below 50% for the inner walls of disks with large cavities. Conversely, models that over predicted the flux or vibrational ratio generally had gas temperatures that were at least twice as high as the dust temperature.

These results seem contradictory with results from Bruderer et al. (2012) who modelled the pure rotational high  $J$  CO lines in HD 100546, a low-NIR group I source in our sample. Bruderer et al. find that they need a gas temperature that is significantly

higher than the dust temperature to explain the  $v = 0$  high  $J$  CO rotation diagram. However, the emitting area for the high  $J$  and rovibrational CO lines is not the same. The high  $J$  lines come from the surface of the outer disk, while the rovibrational CO lines come from the cavity wall. This difference in emitting region is due to the difference in critical density of the transitions. The critical density of the CO rovibrational lines is around  $10^{15} \text{ cm}^{-3}$  while the  $v = 0, J = 32 - 31$  transition has a critical density around  $10^7 \text{ cm}^{-3}$ . The CO rovibrational lines are thus coming from denser ( $\sim 10^{10} \text{ cm}^{-3}$ ), better thermalised gas than the high  $J$  CO lines that can be effectively emitted from the more tenuous, thermally decoupled surface layers.

The thermo-chemical models by Thi et al. (2013) show a slightly stronger gas-dust temperature decoupling in the inner 10 AU at the CO emitting layer with the gas temperature being 2-3 times higher than the dust temperature. The temperature of the CO emitting layer in Thi et al. (2013) is still within the 400–1300 K range. Further testing will have to be done to see if this hotter layer can also reproduce the low vibrational ratios that are observed.

In T-Tauri disks, models of the  $\text{H}_2\text{O}$  mid-infrared observations have invoked a decoupling of gas and dust temperatures high in the disk atmosphere to explain *Spitzer* observations (e.g. Meijerink et al. 2009). In these models this decoupling happens at densities below  $10^9 \text{ cm}^{-3}$ , which is lower than the density of the gas that produces most of the CO rovibrational lines of  $> 10^{10} \text{ cm}^{-3}$ . Our models also show a strong decoupling of gas and dust temperatures ( $T_{\text{gas}} > 3 \times T_{\text{dust}}$ ) in this layer, but no CO rovibrational lines are emitted from there.

Observations of optically thin CO ro-vibrational lines, i.e. high  $J$   $^{12}\text{CO}$  and CO isotopologue lines, can be used to directly probe the gas temperatures predicted here. The high  $J$   $^{12}\text{CO}$  will most likely be more sensitive to the hotter, upper or inner layers of the disk atmosphere and so a higher gas temperature would be inferred from these lines compared to the  $^{13}\text{CO}$  and possibly  $\text{C}^{18}\text{O}$  ro-vibrational lines.

## 5.5 Discussion

Our modelling results show that we can reproduce the observed CO emission with low vibrational ratios at small radii versus high vibrational ratios at large radii (Fig. 5.1) under different and separate conditions. Low vibrational ratios measured at small disk radii require a CO column below  $10^{18} \text{ cm}^{-2}$  and a temperature between 400–1300 K. These conditions naturally occur in the denser  $> 10^9 \text{ cm}^{-3}$  surface layers of the disk. Emission from a dust-free inner region, and from an inner disk rim directly irradiated from the star, are ruled out based on the high  $v_2/v_1$  that would be produced under these conditions which are not observed. Line velocity profiles indicate that most group II disks have an emitting area that is radially narrower than what a flared disk model produces. Thus, flared group II disks should be rare, in agreement with the currently accepted paradigm.

High vibrational ratios measured at large disk radii require instead an inner disk region strongly devoid in CO ( $N_{\text{CO}} < 10^{14} \text{ cm}^{-2}$ ), i.e. the region that would otherwise produce the high-velocity CO line wings that are not observed in these spectra. In the emitting region at larger radii, where CO is still present, the gas must be cold ( $< 300$  K) and CO columns must be high ( $> 10^{20} \text{ cm}^{-2}$ ). To provide these conditions, a high gas-to-dust ratio is necessary ( $> 10000$ ) coupled with a density structure that allows for efficient cooling. Models with midplane number density and column density

**Table 5.4:** Summary of physical constraints from modelling results.

CO emission	Conditions	Model	Comments
$v_2/v_1 < 0.2$ and $R_{\text{CO}} < 5$	$T < 1500$ K, $N_{\text{CO}} < 10^{18}$ cm $^{-2}$ $T = 400 - 1300$ K, $10^{14} < N_{\text{CO}} < 10^{18}$ cm $^{-2}$ No CO in dust free gas $g/d \lesssim 1000$ No CO at the inner rim Radially constrained emitting area	Slab LTE RADEX Slab LTE, RADEX DALI DALI DALI	Fig. 5.3 Fig. 5.4 Sec. 5.3.5 Fig. 5.12 Sec. 5.4.3 and Fig. 5.12 Sec. 5.4.3 and Figs. 5.2, 5.18 and 5.10
$v_2/v_1 > 0.2$ and $R_{\text{CO}} > 5$	$T \lesssim 300$ K, $N_{\text{CO}} > 10^{18}$ cm $^{-2}$ <b>or</b> $T \gtrsim 1000$ K, $N_{\text{CO}} < 10^{14}$ cm $^{-2}$ $g/d > 10000$ Rounded edge, $T_{\text{gas}} < 300$ K, $N_{\text{CO}} > 10^{20}$ cm $^{-2}$	Slab LTE, RADEX DALI DALI	Figs. 5.3, 5.4 and 5.6 Figs. 5.9 and 5.23 Sec. 5.E

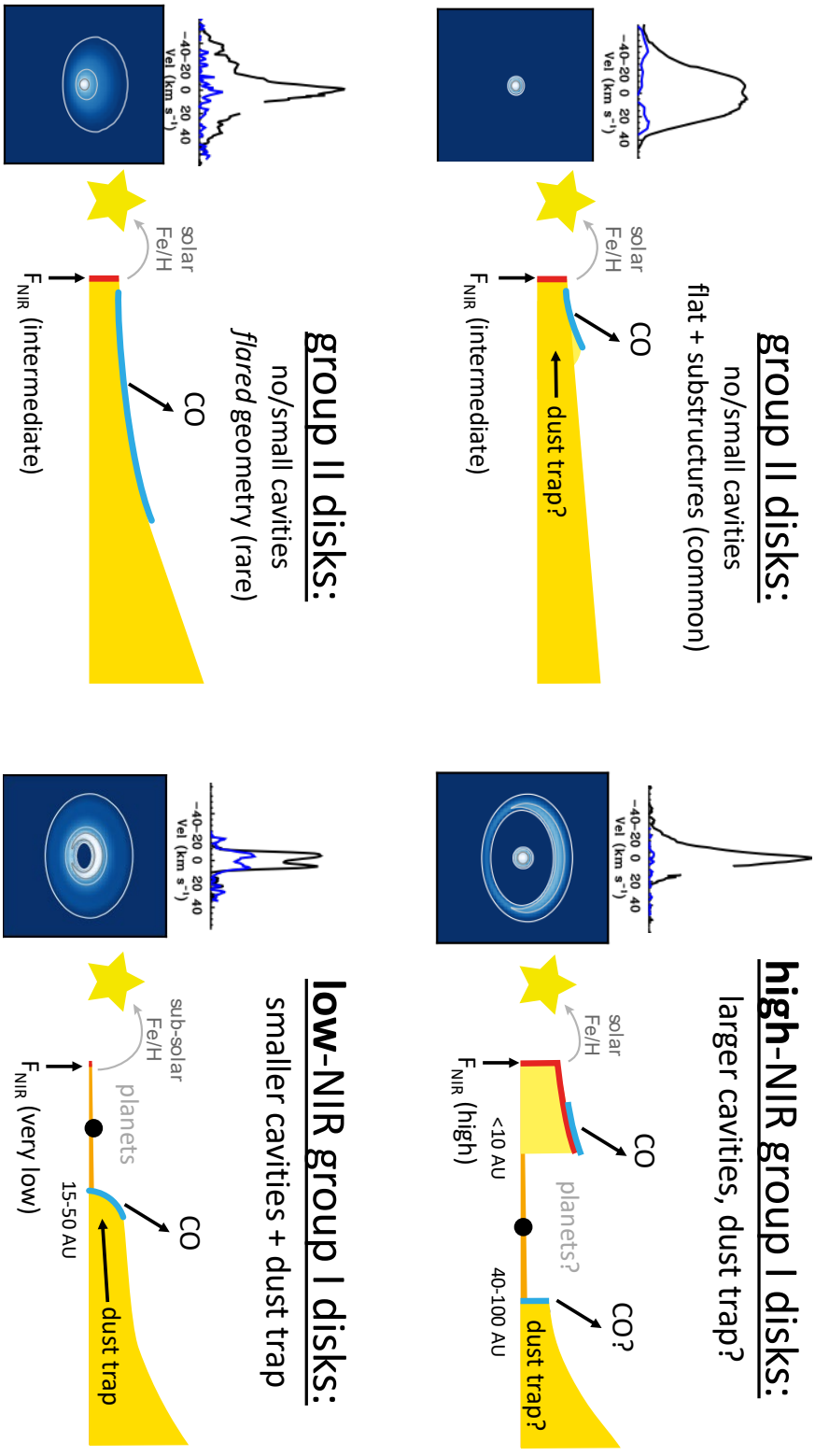


**Figure 5.13:** Typical line profiles, simulated images and inferred disk proposed disk structures for four types of disks identified in the Herbig sample. Near-infrared continuum and CO emitting areas are shown in red and blue respectively. The simulated images show the velocity integrated CO  $v_1$  line flux. These images are discussed in more detail in Sec. 5.5.4. The disk structures are updated versions of those shown in Fig. 5.1.

that increase with radius are able to match the line flux, vibrational ratio and  $R_{\text{CO}}$ . The large columns and low gas temperatures are consistent with  $^{13}\text{CO}$  observations (van der Plas et al. 2015). These constraints on the disk physical structure, and their relative models, are summarized in Table. 5.4.

Figure 5.13 shows four representative CO line profiles, simulated images, and cartoons of the disk structures proposed to produce the observed emission as based on the combination of this and previous analyses. In Sec. 5.5.1 and Sec. 5.5.2 we will link these structures to the physical and chemical processes proposed to produce them.

Three different disk structures for the low vibrational ratios at small radii are shown in Figure 5.13. Two of these apply to group II disks. They are divided into structures with a compact (upper left) and extended (lower left) rovibrational CO emitting area. CO line profiles and infrared excess show that abundant gas and dust is present within  $\sim 5$  AU, so any existing disk cavities must be smaller or the dust extends to the sublimation radius. The stellar abundances for these sources are consistent with solar Fe abundances, so transport of dust to the star is relatively unhindered (Kama et al. 2015). The NIR and CO flux are not emitted from the same region: the IR flux mostly comes from the inner dust edge that is directly irradiated by the star, while the CO must only be emitted from the disk surface. The major difference between the two group II structures is that those with compact CO emission must have a non-flared geometry confining the CO emitting region, possibly with inner disk substructures shadowing the rest of the disk, further confining the emission. The one group II disk with extended CO emission (HD 31648) needs to have a more flared geometry or have a slow molecular disk wind, analogous to those seen in T-Tauris (Pontoppidan et al. 2011a; Brown et al. 2013). Based on this sample we conclude that both molecular disk winds, as well as flared group II disks should, be very rare. In the case of a flared disk, the size of the emission is measurable is by spectro-astrometry on 8-meter class or IFU spectroscopy on 30-meter class telescopes.

The third structure giving rise to low vibrational ratios at small radii is that of the high-NIR group I disks (upper right). These disks have large cavities (typically the largest found in Herbig, see Table 5.1), but they have a residual inner dust disk/belt that produces the high near-infrared flux. These disks therefore have a gap between inner and outer disk. CO emission comes from the inner disk, again from the disk surface in order to produce the very low vibrational ratios measured in the data. The high near-infrared flux instead, higher than the group II disks, must have come from a larger emitting area than in the group II disks, possibly from both the inner edge and surface of the inner disk. The solar Fe abundance in the surface layers of the star is an independent indicator of accretion from a still gas- and dust-rich inner disk (Kama et al. 2015), possibly implying efficient filtration of small dust from the outer disk to the inner disk.

The high vibrational ratios at large radii can all be explained with a single structure (bottom right in Figure 5.13). These disks have an inner cavity that is strongly reduced in CO surface density. These inner cavities seem to be on average smaller in size than those imaged in high-NIR group I disks (see Table 5.1). The rovibrational CO emission comes from the cavity wall, i.e. the inner edge of the outer disk, which must be rich in molecular gas but strongly depleted in dust. This structure combined with the low metallicity of the material that is accreted on the stellar surface (Kama et al. 2015), indicates that the dust is efficiently trapped at some radii larger than  $R_{\text{CO}}$  for these disks. The most appropriate explanation for these deep gas cavities and

dust traps currently seems to be that they are caused by giant planets and not by photo-evaporation or dead-zones (see also van der Marel et al. 2016).

### 5.5.1 Implications for sources with low $v_2/v_1$ at small radii

#### No CO at the inner rim

The good match between the line profiles of disks without a contribution from the inner disk edge (Sec. 5.4.3) indicates that CO is not present within or around the dust sublimation radius in any of these disks. The left plot in Figure 5.14 shows the proposed structure of the inner disk of a group II source as inferred from the data. The dust disk in this case reaches to the dust sublimation radius, forming an inner dust rim. Our modelling suggests that, for Herbig disks, the gas gets heated to high enough temperatures ( $> 3000$  K) near the sublimation radius to keep the gas atomic (see App. 5.F for a discussion on the chemistry), at least until the gas is hidden under the dust infrared photosphere. This is not seen in the thermo-chemical models, however, the gas and dust temperature in this region are very uncertain. Dust sublimation impacts both the dust temperature structure, as well as the gas temperature by changing the composition of the gas.

At larger radii the gas can cool enough to become molecular above the dust infrared photosphere. The expectation is that the phase change from atomic to molecular gas also induces a strong extra cooling effect, lowering the gas temperature to the dust temperature. This seems to be the most appropriate scenario to produce the low vibrational ratios measured at such inner disk radii.

This scenario assumes that the dust disk extends all the way to the dust sublimation radius. However, even if there is a small inner hole in the dust disk, the radiation field should still be strong enough to heat the gas to temperatures above 3000 K and keep the gas atomic at the inner edge of the dust cavity, at least within the small inner cavities that have been explored above in Fig.5.12.

The CO abundance structure proposed in our modelling, with the low columns and temperatures and the absence of molecular gas within the inner dust rim, also naturally produces very weak or no CO overtone ( $\Delta\nu = 2$ ) emission. This is consistent with a large survey of  $2 \mu\text{m}$  CO emission towards Herbig AeBe stars, with detection rates as low as 7% (Ilee et al. 2014).

The dissociation of  $\text{H}_2$  and CO as proposed here, should leave a large ( $N_{\text{H}} \gtrsim 10^{18} \text{ cm}^{-2}$ ), hot ( $T > 3000$  K) atomic or ionised reservoir around the dust inner radius. Velocity or spatially resolved atomic lines, such as can now be measured with near-IR interferometry (e.g. Eisner et al. 2014; Garcia Lopez et al. 2015, and with VLTI-GRAVITY, Gravity Collaboration et al. (2017)), can thus be used to test if CO and  $\text{H}_2$  are indeed being dissociated around the inner edge of the disk.

#### Group II disks have more mass within 5 AU than group I high-NIR sources

Both the group II disks and the high-NIR group I disks show low vibrational ratios at small radii, with the latter showing larger radii and lower vibrational ratios on average (Table 5.1). At the same time these group I disks have a higher NIR excess than the group II disks: this is thought to be due to a vertically more extended dust structure in the inner disk (see e.g. discussions in Maaskant et al. 2013; Banzatti et al. 2018). A vertically more extended structure will lead to lower gas densities in the

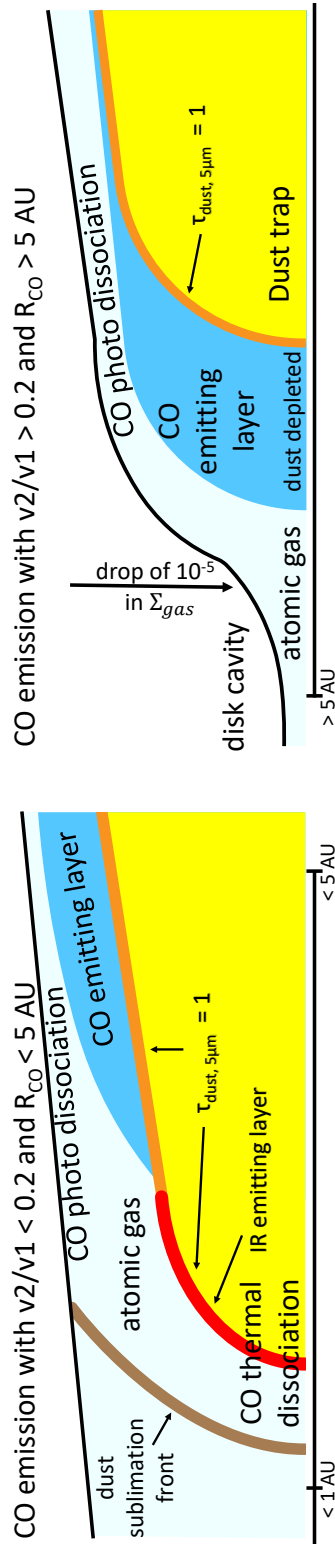


**Figure 5.14:** Sketches of the upper right quartile of a disk cross section of the preferred configuration of the CO emitting region in the case of low  $R_{CO}$  and low  $v_2/v_1$  (group II and group I high NIR, *left*) and large  $R_{CO}$  and high  $v_2/v_1$  (group I low NIR, *right*). This figure is an update to Fig. 5.7 including the DALI results. Relevant radial scales for the inner and outer edge are shown on the bottom left and right corner of each sketch.



surface layers of the disk. A large population of small grains is needed to populate the tenuous surface layers and convert stellar flux into the observed bright NIR flux. These conditions naturally lead to larger  $R_{\text{CO}}$  and lower vibrational ratios. In fact, low densities slow down the chemical formation of CO and observable abundances of CO are thus only produced at lower UV fluxes, further from the star. Furthermore, a larger population of small grains has a higher NIR opacity per unit mass of gas, so the visible column of CO is smaller than for group II disks. A lower gas density also helps in lowering the excitation in the  $v = 2$  state (Fig. 5.4), thereby lowering the vibrational ratio and providing a good explanation for the measured difference from the group II disks.

Source specific modelling of the rovibrational lines of CO and its isotopes, fitting the full rovibrational sequence using non-LTE models can be used to further constrain the density in the inner regions of these disks. Furthermore if the grains are indeed small, and the dust mass in the inner disk is low, the continuum might be optically thin at ALMA wavelengths, allowing for inner disk mass and grain size measurements.

The radial extent of CO emission in the high-NIR group I objects is harder to estimate than for the group II objects as the observed CO lines are intrinsically narrower. Spectro-astrometric measurements of HD 142527 indicate that the CO emission extends up to  $\sim 5$  AU, twice the measured emitting radius (Pontoppidan et al. 2011a), and nicely matching an inner dust belt detected by Avenhaus et al. (2017). A narrow emitting region would imply that CO only emits in the inner dust disk and is absent in the disk gap. None of the high NIR group I sources show the double peak structure expected from such a narrow emitting ring. This could be due to emission from the outer disk cavity wall and surface filling up the centre of the observed spectral line, but higher spectral and spatial resolution observations are needed to confirm this scenario.

### Inner disk CO emission is confined by substructures

One disk in this sample provides exceptional insight into the inner dust and gas structures: HD 142666. Its  $R_{\text{CO}}$  of  $\sim 3$  AU is relatively large for a group II object, and a bright ring at  $\sim 6$  AU has recently been found in sub-millimeter dust continuum images taken at very high angular resolution with ALMA (Andrews et al. 2018; Huang et al. 2018). Figure 5.15 shows the comparison of the inner part of the sub-millimeter radial continuum intensity profile with the CO radial emission profile. The CO radial emission profile was derived by fitting a flat Keplerian disk intensity model to the observed line profile. The observed line profile and the flat disk fit can be seen in the inset in Fig. 5.15. The CO rovibrational emission is confined within the inner edge of the sub-millimeter dust ring, indicating that the process that is producing this sub-millimeter ring also confines the CO rovibrational emission. This could happen if the bright sub-millimeter ring traces a vertically extended dust structure that shadows the disk beyond, preventing CO emission from larger radii.

Our fit to the CO line profile for HD 142666 shows that the inner 1 AU of the disk is devoid of emission (Figure 5.15). This would be consistent with IR interferometric observations that report an inner disk radius of 1 AU (Schegerer et al. 2013), significantly larger than the dust sublimation radius expected at 0.3 AU as based on the stellar luminosity. This indicates that a small cavity has formed in this disk; similar cavities could also be present in the other group II disks that have  $R_{\text{CO}} \gtrsim 2R_{\text{subl}}$ . These small cavities should still allow for efficient transport of both gas and dust (in a  $\sim 100$ –1 ratio) from the inner disk edge to the star, as the accretion rates are normal

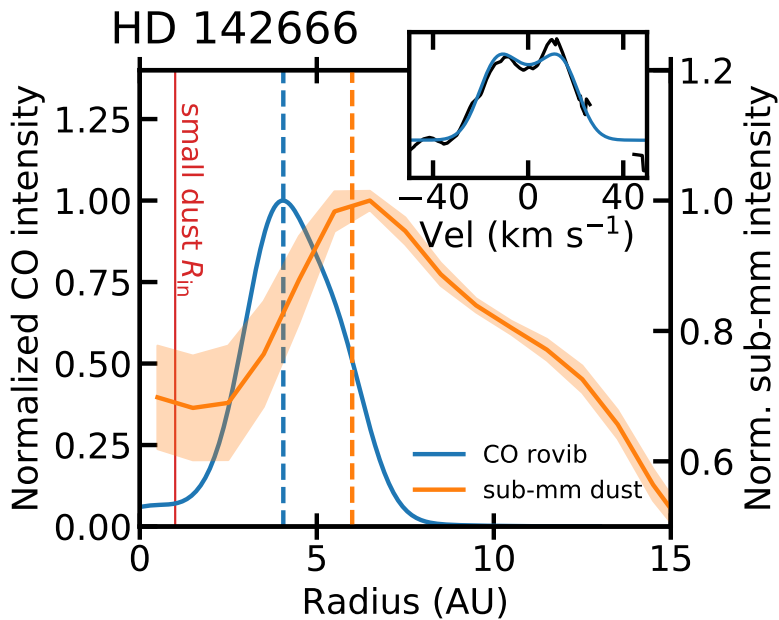


**Figure 5.15:** Radial intensity cuts for the sub-millimeter dust from Huang et al. (2018) and the radial intensity as inferred from the CO rovibrational line profile of HD 142666. Vertical dashed lines show the maximum of the CO and sub-millimeter dust intensity. The CO emission is clearly contained within the bright sub-millimeter ring at 6 AU. The inset on the top right shows the observed line profile (black) and the fitted profile (blue). The vertical red line shows the inner edge of the dust disk at  $\sim 1$  AU as inferred from IR interferometry (Schegerer et al. 2013).

and the stellar abundances for these sources close to solar (Kama et al. 2015; Banzatti et al. 2018). The lower sub-mm intensity implies a lower dust surface density at 1 AU. If we assume there is no continuous build up of material around the sub-millimeter ring, then the lower surface density in the inner disk gap should be accompanied with an increase in the velocity of the accretion flow. This would be consistent with an inner dead-zone edge, possibly due to the thermal ionisation of alkali metals (Umebayashi & Nakano 1988). Another option would be the presence of a giant planet within the small cavity with a saturated or leaky dust trap. In either case there would be a dust trap or traffic jam. This raises the tantalizing possibility that all group II disks with  $R_{\text{CO}} \gtrsim 1$  AU could have a bright sub-millimeter ring in the inner regions as found in HD 142666 and HD 163296 (Huang et al. 2018; Isella et al. 2018).

### 5.5.2 Implications for high $v_2/v_1$ at large radii

#### High gas-to-dust ratios by dust trapping

The large CO columns needed to produce a high vibrational ratio at large radii indicate that around  $R_{\text{CO}}$  the gas surface density does not deviate strongly from what would be expected in absence of an inner cavity. To get the  $v_2$  lines bright enough, CO columns larger than  $10^{20}$  cm $^{-2}$  and thus total H columns larger than  $10^{24}$  cm $^{-2}$  are needed. This necessitates a drop in gas surface density that is less than two orders of magnitude at  $R_{\text{CO}}$  if CO is at the canonical abundance of  $10^{-4}$  alternatively, a CO abundance of more than  $\sim 10^{-6}$  is needed if the gas surface density is continuous within the dust cavity. The large CO column also implies that dust is under abundant by at least two orders of magnitude at  $R_{\text{CO}}$ . The high gas-to-dust ratios necessary are likely not due to strong settling as ALMA images of millimeter dust show cavities that are consistently larger than  $R_{\text{CO}}$  indicating that there is a indeed a radial segregation (e.g. HD 100546, HD 97048, IRS 48, HD169142; van der Marel et al. 2016; van der Plas et al. 2017; Fedele et al. 2017; Pinilla et al. 2018). This is consistent with ALMA gas observations of transition disks, showing that also in the sub-millimeter, CO cavities are smaller than dust cavities (van der Marel et al. 2013, 2016).

The steep line profiles and the lack of high velocity CO emission indicates that the CO column within  $R_{\text{CO}}$  is at least six orders of magnitude lower than the column at  $R_{\text{CO}}$  for the observed disks. As CO is hard to photodissociate, a drop in the total gas surface density in the cavity is necessary. A total gas surface density drop of 5 orders of magnitude between the dust ring and the CO poor cavity is needed to produce CO columns below  $10^{14}$  cm $^{-2}$  (Bruderer 2013). Observations of atomic oxygen or carbon could be used to measure gas depletion factors directly, constraining the depth of the cavity and thus the mass of a possible cavity-forming planet. Fig. 5.14, right, illustrates the disk structure as reconstructed from modelling the CO rovibrational lines in low-NIR group I disks.

The combination of a large cavity in both gas and dust and of a radial segregation between gas and dust at the disk cavity wall fits well with what is expected for a giant planet carving an inner disk hole. A sufficiently massive planet can explain the gas depletion in the cavity together with the different cavity sizes in dust and gas, as a gas pressure maximum is created that traps dust at a slightly larger radius. Both photo-evaporation and dead zone models, instead, have problems creating transition disks that have an inner region rich in gas, but depleted in micron-sized grains (Pinilla et al. 2012a; Gorti et al. 2015; van der Marel et al. 2015, 2016; Pinilla et al. 2016).

### Not all dust traps are equal

In Sec. 5.5.1 we compared the high NIR group I disks to the group II disks on the basis of inner disk structures. However, at long wavelengths and larger radii these high NIR disks appear more similar to the rest of the group I sources showing cavities in sub-millimeter and scattered light imaging (e.g. Garufi et al. 2017). One notable difference is that the inner disk in the high NIR group I sample seems to be misaligned with respect to the outer disk (e.g. Benisty et al. 2017; Banzatti et al. 2018). Due to this misalignment, perhaps the inner disk cannot shadow the cavity wall in the outer disk and thus CO emission in high NIR group I sources could in principle include a component similar to what observed in low NIR group I disks. If so, there should be a narrow emission component with large  $v2/v1$  at the center of the line. This could be the origin of the narrower  $v2$  emission line observed in HD 135344B (Fig. 5.2), but even at the current high spectral resolution it is not possible to distinguish a narrower central peak in the  $v1$  line. Part of the problem may also be due to flux filtration by the narrow slit (0.2" for VLT-CRIRES), where the signal from the outer disk will be diluted by any slit that includes a bright inner disk but excludes part of the outer disk (Hein Bertelsen et al. 2014).

Another possibility is that the outer disk in the high NIR group I systems may not have as high a gas-to-dust ratio as the rest of the group I systems. A normal gas-to-dust ratio would quench the  $v2$  emission, with  $v1$  emission from the gap outer edge filling in the line center and producing a narrow single peak. A close to ISM gas-to-dust ratio would imply that dust is not efficiently trapped at the gap outer edge. This could fit with a scenario in which the dusty inner disk and near solar abundances in the stellar atmosphere are replenished by dust from the outer disk. Mapping of the CO emission, either with multiple slit positions with VLT/CRIRES+ or observations with ELT/METIS integral field unit can determine the brightness and nature of the CO emission from the outer disk in high NIR group I sources (see Sec. 5.5.4).

### 5.5.3 Comparison to T-Tauri disks: distribution of UV flux matters

Under several aspects, disks around Herbig AeBe stars are analogous to T-Tauri disks. However, in CO rovibrational emission they exhibit a very different behaviour (Banzatti & Pontoppidan 2015; Banzatti et al. 2018). While the T-Tauri disks have a decreasing  $v2/v1$  with increasing  $R_{CO}$ , the Herbig disks show the opposite trend. This implies a significant difference in the distribution of molecular gas between Herbig and T-Tauri inner disks. This is also seen in the line profiles, since many of the T-Tauri disks have a two component CO profile: if both components originate from the Keplerian disk, it means that the CO emitting region is more radially extended than in the Herbig disks. This can be explained if the T-Tauri disks have CO emission from the inner rim (and from within the inner rim), while in Herbig disks CO is dissociated by high temperatures in these regions as explained above.

Both Herbig and highly accreting T-Tauris have strong UV fields. The energy distribution as function of wavelength is very different, however. The UV field of Herbig stars is dominated by the continuum coming from the stellar surface. For T-Tauri stars, on the other hand, most of the UV comes from the accretion shocks and is emitted in emission lines, especially Lyman- $\alpha$  (e.g. France et al. 2014). Both CO and H<sub>2</sub> cannot be photo-dissociated by Lyman- $\alpha$  photons. As such the photo-dissociation

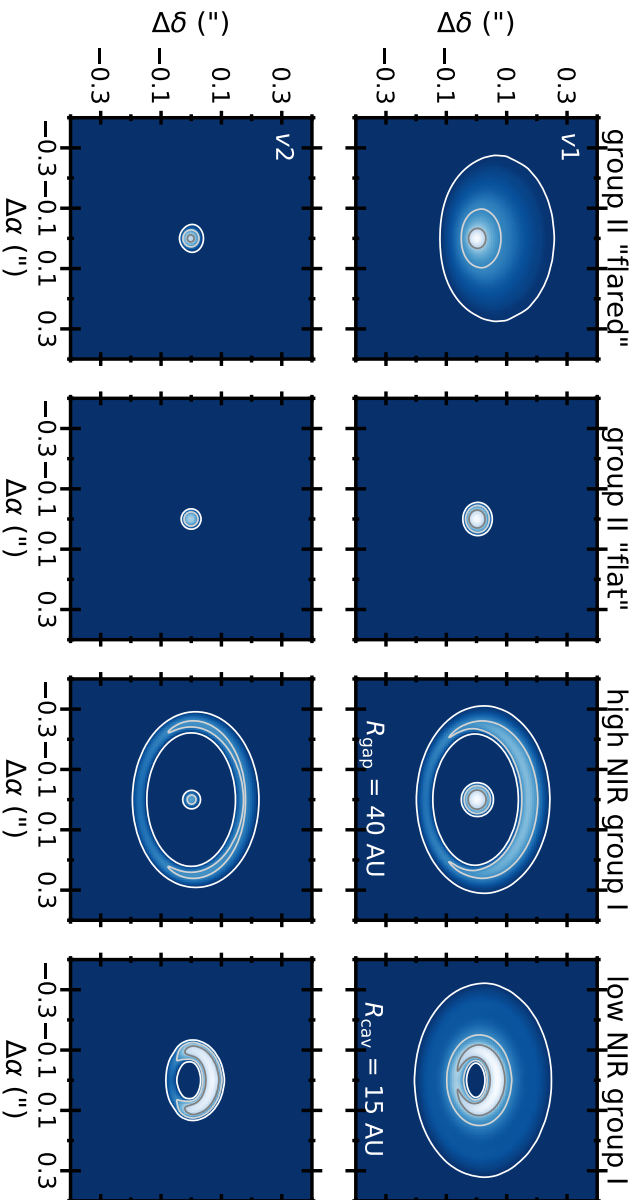


**Figure 5.16:** Simulated velocity integrated  $v1P(10)$  (top) and  $v2P(4)$  (bottom) line maps convolved to METTIS resolution (Brandl et al. 2014). The colour scale is log-stretched between 0.1% and 100% of the maximum of the  $v1$  line flux. The continuum has been subtracted before velocity integration. The contours show 0.1%, 1% and 10% of the peak surface brightness. The disk geometries refer to those presented in Fig. 5.13. The distance is assumed to be 150 parsec and the inclination is 45 degrees, the far side of the disk is in the north. For the "flat" geometry, a truncated gas disk (5 AU outer radius) is used. The high NIR group I image is composed by combining two models, a truncated disk model, with an inclination of 30 degrees and a disk with a 40 AU hole and a strong dust trap (so strong  $v2$  emission) with an inclination of 45 degrees. No interactions between the inner and outer disk have been taken into account.

of CO and H<sub>2</sub> is much more efficient around Herbig stars. If hydrogen is mainly in atomic form, formation of other molecules such as CO<sub>2</sub> and H<sub>2</sub>O is significantly slowed down as molecules both need the OH radical for their formation. This radical forms from H<sub>2</sub> + O → OH + H and can be destroyed by OH + H → H<sub>2</sub> + O. Only with abundant H<sub>2</sub> can enough OH be produced and can OH survive long enough to form CO<sub>2</sub> and H<sub>2</sub>O. This could explain the lack of H<sub>2</sub>O and CO<sub>2</sub> emission towards Herbig AeBe disks in comparison to T-Tauri disks (e.g. Pontoppidan et al. 2010; Banzatti et al. 2017).

The higher broad-band optical-UV flux in Herbig systems can have a larger impact on the gas temperature compared to the line dominated T-Tauri spectrum as more power can be absorbed by atomic and molecular electronic transitions before the dust absorbs the radiation. Finally, a larger fraction of the stellar flux can generate photo-electrons upon absorption by the dust (Spaans et al. 1994). All these effects will heat the gas more in Herbig than in T-Tauri disks, increasing CO dissociation in the former.

#### 5.5.4 Predictions for future observations

ELT-METIS will be a generation I instrument on the ELT (Brandl et al. 2014). It will be able to do diffraction limited imaging and IFU spectroscopy at 3–5 μm. The 39 meter mirror allows for a spatial resolution of ~ 0.03'' at 4.7 μm in a 0.5'' by 1'' field of view. IFU spectroscopy will be possible at a resolving power of  $R = 100000$ . With these capabilities, ELT-METIS will be able to resolve CO rovibrational emission both spatially and in velocity in nearby Herbig disks. Fig. 5.16 shows continuum subtracted, velocity integrated maps of the  $v1P(10)$  line. The four different disk structures proposed in Fig. 5.13 can be clearly distinguished in these images. Spatially resolving the emission will enable to study asymmetries in the spatial distribution of CO and will help in explaining the single peaked nature of CO lines observed in the high-NIR group I disks.

The CO rovibrational ratio is a good tracer of large cavities in Herbig disks, with high ratios (> 0.2) only coming from low-NIR group I disks, intermediate ratios (0.05 – 0.2) coming from group II disks and very low ratios (< 0.05) coming from the high-NIR group I disks. This could be exploited in more distant and more massive star forming regions, for instance by observing multiple Herbig stars within the field of view of the *JWST*-NIRSPEC multi object spectrograph, providing an efficient classification of large numbers of Herbig sources, either for more detailed follow-up or for population studies.

In the shorter term, ground based, high sensitivity observations can be used to constrain densities in the inner disk. In all disk models, CO emission is not in LTE. This results in strongly decoupled vibrational and rotational excitation temperatures. On top of this, most of the  $v1$  lines are also optically thick so there should be a break in the  $v1$  rotational diagram. This is the point where the lines become optically thin. The position and sharpness of the break critically depends on the density of the emitting area. A source by source modelling of the CO rovibrational lines over a large number of  $J$  levels ( $J > 30$ ) can derive this density and from that the mass in the inner few AU can be constrained. The same should apply to T-Tauri disks, but as the CO line flux can have contribution from within the sublimation radius it will not be straightforward to measure the mass in the dust rich inner disk.

## 5.6 Conclusions

The goal of this work has been to find the physical conditions that can reproduce trends observed in inner disks of Herbig stars, in terms of the CO vibrational ratio  $v_2/v_1$ , the radius of CO emission (from the HWHM of the lines) and the NIR excess (Fig. 5.1). We have studied the excitation and line profiles of CO rovibrational emission from disks around Herbig Ae stars using LTE and non-LTE slab models, as well as using the thermo-chemical model DALI. Our findings are collected in Figs. 5.13 and 5.14 and our conclusions can be summarised as follows:

- *Emission from the inner disk surface:* CO emission with  $v_2/v_1 < 0.2$  at  $R_{\text{CO}} < 5$  AU is reproduced by conditions found in the inner disk surface. CO columns must be  $\lesssim 10^{18} \text{ cm}^{-2}$  and gas-to-dust ratios  $< 1000$ . Gas and dust temperatures must be coupled and between 400 and 1300 K. Emission from and within the inner disk rim is ruled out on basis of the measured low vibrational ratios. A scenario in which the gas around the dust sublimation radius is hot,  $> 3000$  K, is preferred to explain the absence of CO at the inner rim. At these temperatures, reactions between CO and atomic H should produce a primarily atomic gas that could be observed by IR interferometry.
- *Emission from the cavity wall:* CO emission with  $v_2/v_1 > 0.2$  at  $R_{\text{CO}} > 5$  AU is reproduced by conditions found in a cavity wall at large disk radii. CO columns must be  $> 10^{18} \text{ cm}^{-2}$  and gas-to-dust ratios  $> 10000$ . Gas and dust temperatures must be coupled and below 300 K, indicating efficient cooling of the gas. Within  $R_{\text{CO}}$  the gas surface density drops by at least 5 orders of magnitude. A high gas surface density, rather than UV pumping, is the most likely reason for the bright  $v_2$  lines providing high  $v_2/v_1$  ratios.
- *Substructures in inner disks:* The broad, flat topped or double peaked line profiles that most group II sources exhibit cannot be explained by a smooth, flared disk. The radial extent of the CO emission in these sources is restricted. Flat disk models work better in matching these line profiles, but they generally still have too much flux at large radii. The outermost radius that emits in these sources thus most likely traces some variation in vertical scale-height. This could be the case for HD 142666, where all the CO emission arises from within the first resolved sub-millimeter dust ring at 6 AU.
- *Dust trapping:* Small cavities in gas and dust are possible in the group II objects. The low vibrational ratios observed indicate that dust-free and molecular gas rich cavities are not present. If there are small cavities formed by planets in the sample, then they apparently do not create a very efficient dust trap. This is in contrast with the low NIR group I disks that have high vibrational ratios. The large gas surface density drop and the dust poor gas necessary in these disks fit very well with predictions of giant planets producing a cavity and a strong dust trap. High NIR group I disks, instead, may have dust traps that allow for dust filtration from the outer to the inner disk, sustaining normal elemental accretion onto the star.
- *CO as a tracer of disk cavities and inner dust belts/disks:* rovibrational CO emission can be used to identify dust cavities also in absence of direct imaging,

especially when disks are further away than 200 pc; the difference in CO lines as observed in high- and low-NIR group I disks moreover shows that, in disks with large cavities, CO emission is a good tracer for residual inner dust belts/disks that may be unseen in direct imaging.

- *Molecular gas within the sublimation radius*: The lack of broad, high vibrational ratio, CO emission in many of the observed sources puts strong constraints on the amounts of dust free molecular gas within the sublimation radius:  $N_{\text{CO}} < 10^{18} \text{ cm}^{-2}$ . This upper limit is consistent with the non-detection of the CO overtone ( $v = 2-0$ ) emission towards most Herbig AeBe disks.
- *Future METIS observations*: ELT-METIS will be able to resolve the emitting area of the CO rovibrational lines. These observations can further constrain the emitting area in group II disks. For low NIR group I disks METIS should find CO rovibrational rings within the scattered light and sub-millimeter dust cavities, while for high NIR group I disks the extent of molecular gas in the inner disk as well as the gas-to-dust ratio, and thus efficiency of dust trapping, in the outer disk can be measured.

## Appendix

### 5.A CO molecule model

#### 5.A.1 Rovibrational

The CO molecule model used in this work contains 205 energy levels distributed over five vibrational states ( $J = 0 - 40, v = 0 - 5$ ). Energy levels and line strengths have been extracted from the HITRAN database Rothman et al. (2013). Collisional excitation by  $\text{H}_2$  and H was included. For the CO- $\text{H}_2$  collisional de-excitation rates the collisional rates from Bruderer et al. (2012), based on Yang et al. (2010) have been used. The collisional rate matrix was expanded using the formalisms in Chandra & Sharma (2001).

For the H-CO collisions, the pure rotational rate coefficients were taken from Walker et al. (2015) while the rovibrational rate coefficients were taken from Song et al. (2015). The rates from Walker et al. (2015) were used for all  $\Delta v = 0$  transitions.

#### 5.A.2 Electronic

The electronic excitation of CO has been done in post processing. From the model output the total rate into and out of each vibrational state due to collisions and photon absorption and emission was calculated. To these vibrational band-to-band rates the electronic rates are added and a new vibrational equilibrium is calculated. Using the rotational distribution from the model, a new rovibrational level distribution is calculated. This is then used for ray tracing.

The electronic transitions and Einstein A coefficients were taken from Beegle et al. (1999). The Einstein A coefficients were used to calculate a transition probability matrix for an absorption and subsequent emission of a UV photon. It is assumed that electronic relaxation into a vibrational level of the ground state with  $v'' > 4$  will



further cascade into  $v'' = 4$  and will be treated as if the relaxation directly goes into  $v'' = 4$ . By construction the rotational distribution of the molecules was assumed to be unaffected by the electronic excitation.

## 5.B Excitation tests

To increase our understand of the CO line formation processes in DALI, a few variations on the standard temperature and excitation calculations have been done. In one set of models, the thermo-chemistry has been skipped and  $T_{\text{gas}} = T_{\text{dust}}$  has been assumed. The CO abundance in these models is parameterized according to Eq. (5.5). The excitation has been tested without IR pumping and with UV pumping. Results have been plotted in Fig. 5.17.

Assuming equal gas and dust temperature lowers the vibrational ratio somewhat for the models with small inner radii and has slightly increased vibrational ratios for models with 5 to 10 AU gaps. For models with gaps smaller than 5 AU the vibrational ratio is still higher than the data. The models with equal gas and dust temperature also predict very low ( $> 0.05$ ) vibrational ratios for models with gaps larger than 10 AU. Fig. 5.17 shows that the thermo-chemical balance does influence the line fluxes and line flux ratios for CO.

A returning topic of discussion for vibrational excitation of molecules is the treatment and relative importance of pumping by radiation of different wavelengths. In DALI the radiation that pumps the lines, radiation that is absorbed by the molecules increasing their excitation, is always assumed to come from either radially inward, or vertically upward, whichever has the lowest line optical depth. This could, depending on the situation, both over- and under-predict the effective pumping flux. For CO there are two possible ways to excite vibrational levels through the absorption of a photon. The first is the absorption of an infrared photon through the rovibrational lines around 4.7 or 2.3  $\mu\text{m}$  raising the vibrational excitation by one or two quanta directly. In Fig. 5.17 a comparison is made between models with and without infrared pumping, but otherwise using the same abundance and temperature structure. The general trend is that the infrared pumping lowers the vibrational ratio, especially in the inner regions of the disk. Infrared pumping increases the excitation in the  $v = 1$  state more strongly than the  $v = 2$  state. This greatly increases the vertical and radial extent of the emitting region of the  $v1$  lines increasing line flux. Although the  $v = 2$  state can be directly pumped from the ground state, the Einstein  $A$  coefficient for these lines is small, contributing little to the overall excitation of the second vibrationally excited state.

The inclusions of UV pumping has a small effect of the line fluxes. However it mostly effects the disks with cavities smaller than 10 AU and in these models the vibrational ratio is lowered. The regions where the UV field is strongest is in the cavity wall near the star. These regions show emission with a vibrational ratio close to unity. UV pumping and the vibrational cascade would create a vibrational ratio of  $\sim 0.6$  thus lowering the contribution of the  $v2$  line in the inner region in favour of the  $v1$  line. At radii larger than 10 AU the UV field is so diluted that it can no longer affect the vibrational ratio. Fig. 5.17 shows UV pumping without taking into account the self-absorption of UV photons by CO molecules. Including self-absorption only changes the vibrational ratios by a few percent.

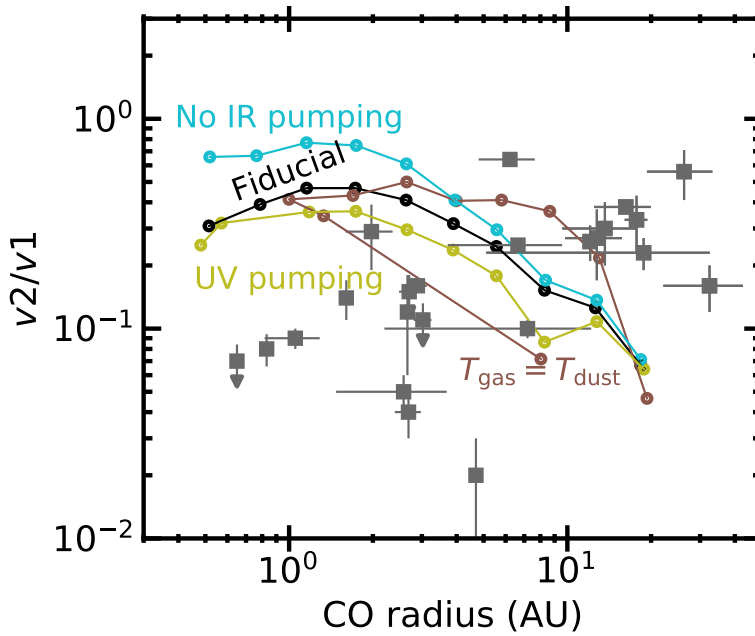


**Figure 5.17:** Ratio of the flux from the  $v = 2$  and  $v = 1$  levels of CO versus the inferred radius of emission for observational data and DALI model results. Line connect the dots in order of inner model radius. Labels indicate the different assumptions for the excitation calculation. All models have a gas-to-dust ratio of 100. The model with the largest cavity is always at the largest CO radius. Different assumptions on the excitation are tested.

## 5.C Line profiles

Figure 5.18 shows the line profiles for the disks with the smaller inner holes. Most line profiles show two components, a broad component that is present in both the  $v_2$  and the  $v_1$  line and a narrow component, that is mostly seen in the  $v_1$  line. The velocity of the broad component is the component used in the flux ratio extraction and radius determination. This component is consistent with emission dominated by the inner wall of the model. The narrow component is more extended and thus has to come from the disk surface.

Figure 5.19 shows the line profiles for the disks with larger holes. Almost all of the emission in these models is dominated by the inner wall. The lines are very strong with respect to the continuum, in some cases line-to-continuum ratios reach over 100. Part of this is the NIR excess, which is almost non-existent, but even taking that into account, some of the line fluxes are a factor of 10 above the brightest lines observed.

Figure 5.20 shows the line profiles for the disks with emission from the inner rim subtracted. Many of these models show very low  $v_2/v_1$  emission. Variations in outer radius and vertical structure redistribute the CO emission over the disk surface, creating a large assortment of line profiles.

## 5.D Near-infrared excess

The near-infrared continuum is another good probe of the inner disk. As all of the models discussed above have the same dust structure, they show identical near-infrared excesses, only depending on the inner edge radius of the disk in the model. Fig. 5.21 shows the near-infrared excess as function of  $R_{\text{CO}}$  for the gas-to-dust = 100 model and the data. The gas-to-dust 1000 and 10000 overlap almost exactly, the LTE and gas-to-dust 10 models deviate at small inner model radii.

The models match the near-infrared excess range for most of the observations, except for the four observed disks with  $F_{\text{NIR}}/F_{\star}$  around 0.3. These disks have been shown to require very vertically extended dust structures to fit the NIR SED (Maaskant et al. 2013). The good match between the model and the observational near-infrared excesses indicate that the vertical extent,  $h_c$ , used in the model is reasonable for most of the observed sources. Up to  $R_{\text{CO}} = 5$  AU there is only very little variation in the NIR-excess in both the models and the group II objects, indicating that up to 5 AU the NIR excess is a bad discriminator of gap size.

### 5.D.1 CO as tracer of the inner disk radius

The half width half maximum of the  $v_1$  lines, or of their broad component where present (see Section 5.2), is used to estimate a characteristic emitting radius for the inner molecular gas in the disk (e.g. Salyk et al. 2008; Brown et al. 2013; Banzatti & Pontoppidan 2015). Using the results from our thermo-chemical models we can infer how well the relation between CO emission radius and inner (molecular) disk radius holds. Figure 5.22 shows that  $R_{\text{CO}}$  is always larger than the model inner radius. For the fiducial thermo-chemical models the deviations are around 50%, if the inner rim of the disk is detected. If the inner rim is too weak to be detected, or in cases where it is artificially removed, the relation between  $R_{\text{CO}}$  and  $R_{\text{in}}$  breaks down as the disk surface far beyond the inner disk radius can dominate the emission.

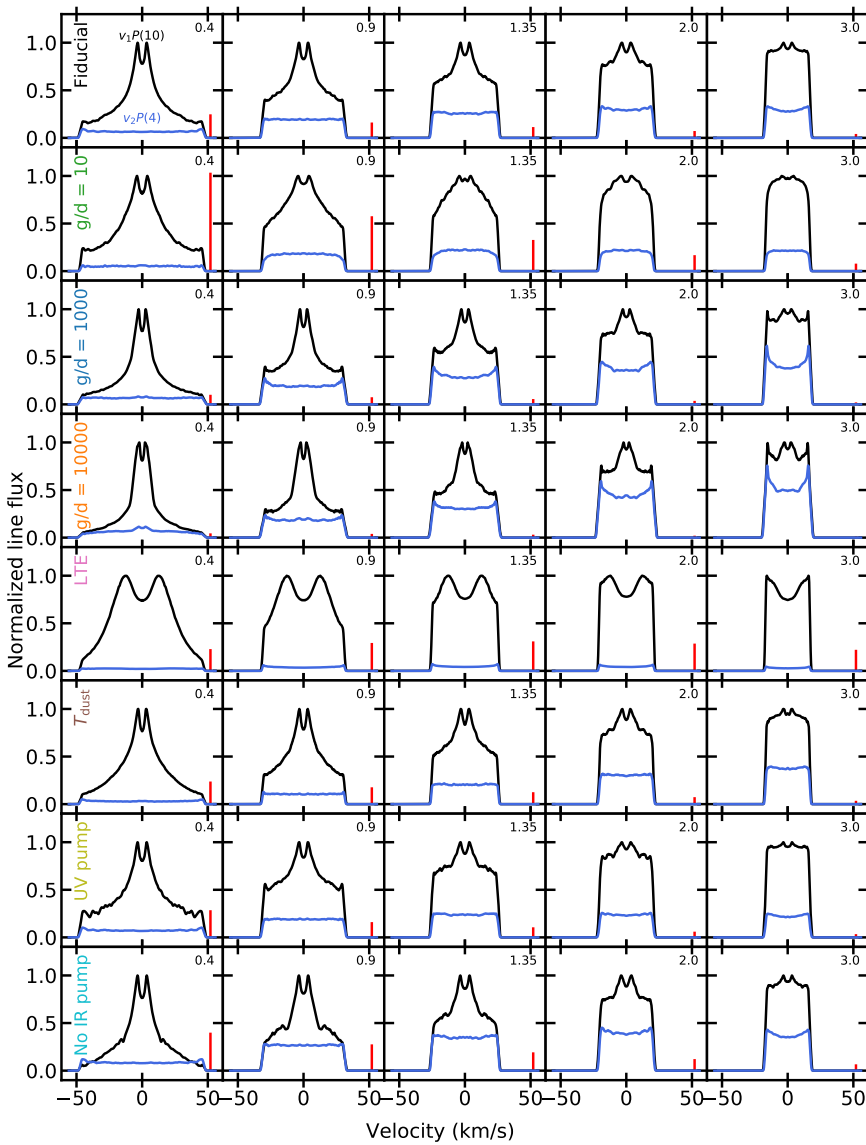


**Figure 5.18:** Normalised model line profiles for the  $v_1$  (black) and the  $v_2$  (blue) lines for a subset of the models at the native resolution of the model,  $R = 10^6$ . The text on the left of each panel denotes the model set. The top right corner of each panel denotes the inner radius of the model. The vertical bar in the bottom right of each panel shows 0.03 of the continuum flux density. All lines are modelled assuming a 45 degree inclination. No noise has been added to these lines, features in the line profiles are due to the sampling of the DALI grid.

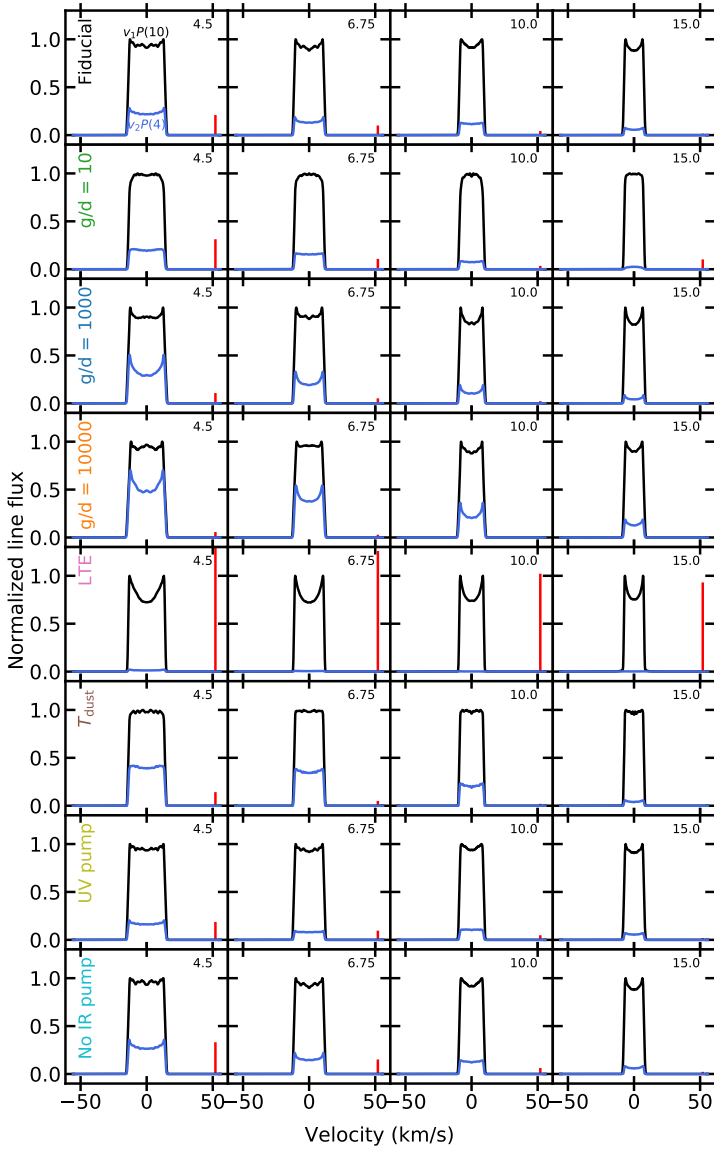


**Figure 5.19:** Same as Fig. 5.18, but for models with inner radii  $> 4.5$  AU. The right bar in the bottom right of each panel shows 0.3 times the continuum.

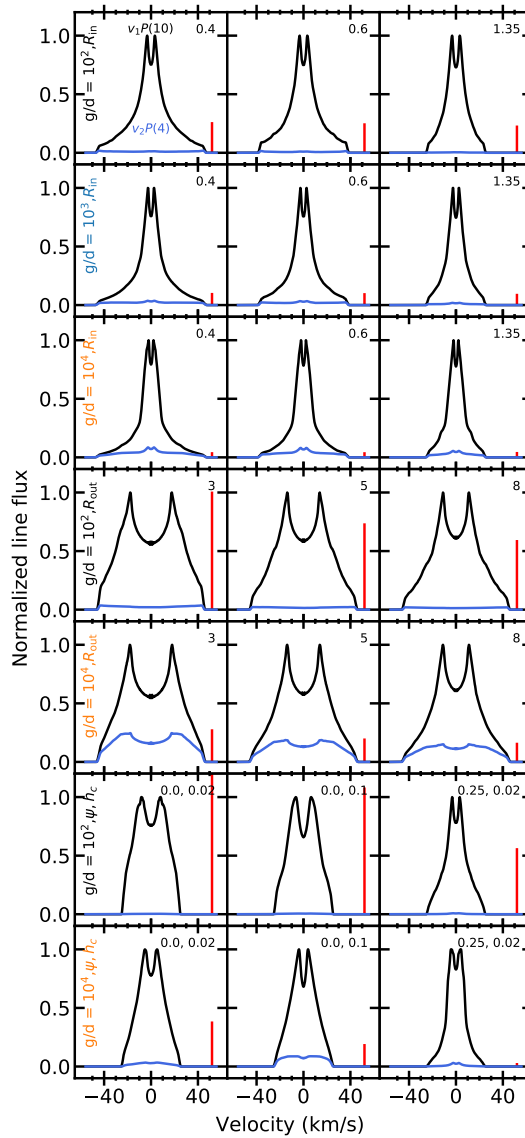


**Figure 5.20:** Same as Fig. 5.18, but for models where the inner rim contribution has been subtracted.

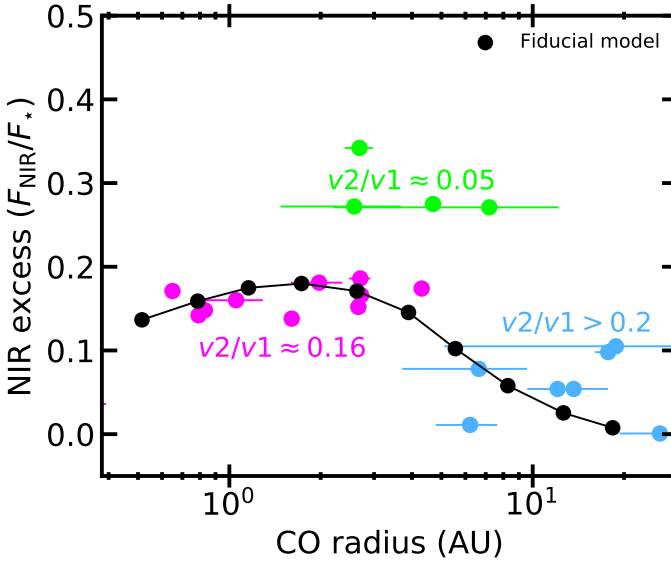


**Figure 5.21:** CO emitting radius versus the near-infrared excess flux as fraction of the total stellar flux. Black circles show the inner model radius against the near-infrared excess for the fiducial,  $g/d=100$ , model (see Sec. 5.4 for details). The data are shown following the same color coding as in Fig. 5.1.

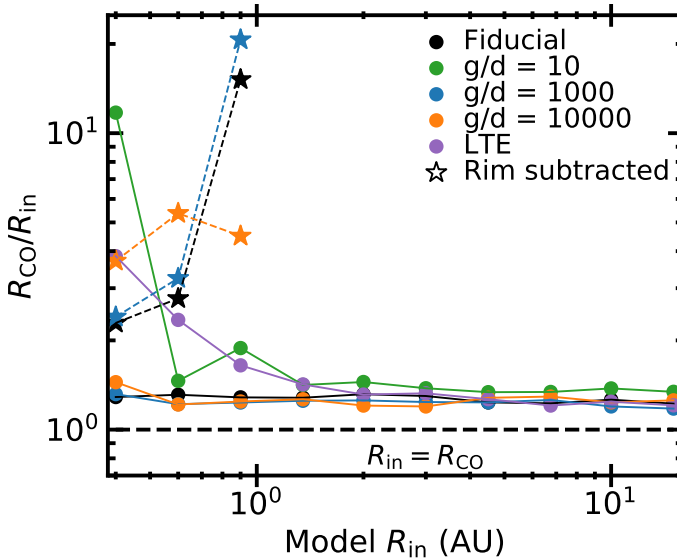


**Figure 5.22:** Model radius versus the deviation of  $R_{\text{CO}}$  from the inner model radius. Filled circles correspond to the normal DALI models, the stars correspond to the DALI models with the contribution of the inner rim removed. Only the models sets with varying inner rim location are shown.

The low vibrational ratios at small  $R_{\text{CO}}$  can only be matched by disk surface emission. It is thus for these sources that the largest discrepancy is expected between the measured  $R_{\text{CO}}$  and the innermost radius where dust or molecular gas is actually present. The model explorations in Sec. 5.4.3 show that a single inner model radius can lead to a spread in measured CO radii. In these cases the line profiles give a clear sign of CO emission within  $R_{\text{CO}}$ .

The high vibrational ratios at large  $R_{\text{CO}}$  are best matched by emission from an inner cavity wall. As such  $R_{\text{CO}}$  tightly traces the inner most radius at which CO is present. This is also clearly seen in the observed line profiles for these sources which have very steep sides.

## 5.E Lowering the flux of the outer disk

The fiducial, high gas-to-dust ratio models that can match both  $R_{\text{CO}}$  and the high line ratios have  $v1$  fluxes that are around a factor 50 higher than that of the average source. Comparisons between the RADEX model predictions in Fig. 5.6 and the emitting area in the DALI models with 10 and 15 AU cavities showed that both the emitting area and the temperature of the gas had to be reduced. Reducing the models scale height from 0.1 to 0.03, in line with van der Marel et al. (2016) lowered the fluxes by about a factor of 3 (e.g. HD 142527, HD 135344B, HD 36112 and HD 31293). The emitting area was further reduced by putting  $\chi_{\text{set}} = 1$ . This lowered the flux from the disk surface. To lower the gas temperature at the inner wall of the disk we considered a different structure of the inner wall than the step-function we had. It turned out that a structure with an decreasing density inwards of the inner radius worked well. The gas density within the inner radius ( $R_{\text{in}}$ ) was parameterized by:

$$n_{\text{gas}}(r, z) = n_{\text{gas}}(R_{\text{in}}, 0) \frac{1}{\sqrt{2\pi}H(R_{\text{in}})} \exp \left[ -\frac{1}{2} \frac{(r - R_{\text{in}})^2 + z^2}{H^2(R_{\text{in}})} \right], \quad (5.6)$$

where  $n_{\text{gas}}(R_{\text{in}}, 0)$  is the midplane density at the inner disk edge from the fiducial model.  $H(r) = h_c r \left( \frac{r}{R_c} \right)^\psi$ , with the parameters as defined in Table 5.2.  $R_{\text{in}}$  was taken to be either 10 or 15 AU. Within the cavity radius, it was assumed that there were only small grains and the dust density was decreased to reach gas-to-dust ratios of 20000 and 100000. The CO lines from these models were calculated and are shown in Fig. 5.23.

The high gas-to-dust ratios are necessary to reach get the vibrational ratios to the observed values. At these gas-to-dust ratios the dust is nearly transparent to the CO lines and varying the gas-to-dust ratio has little effect on the line ratios. To further increase the line ratios, larger gas columns would be needed.

These structures are probably not the only structures that can explain the CO rovibrational observables. Modelling of other observations of CO such as high resolution ALMA images or *Herschel* observations of high  $J$  CO lines would be able to differentiate between different structures. This modelling will have to be done on a source by source basis and is left to future work.



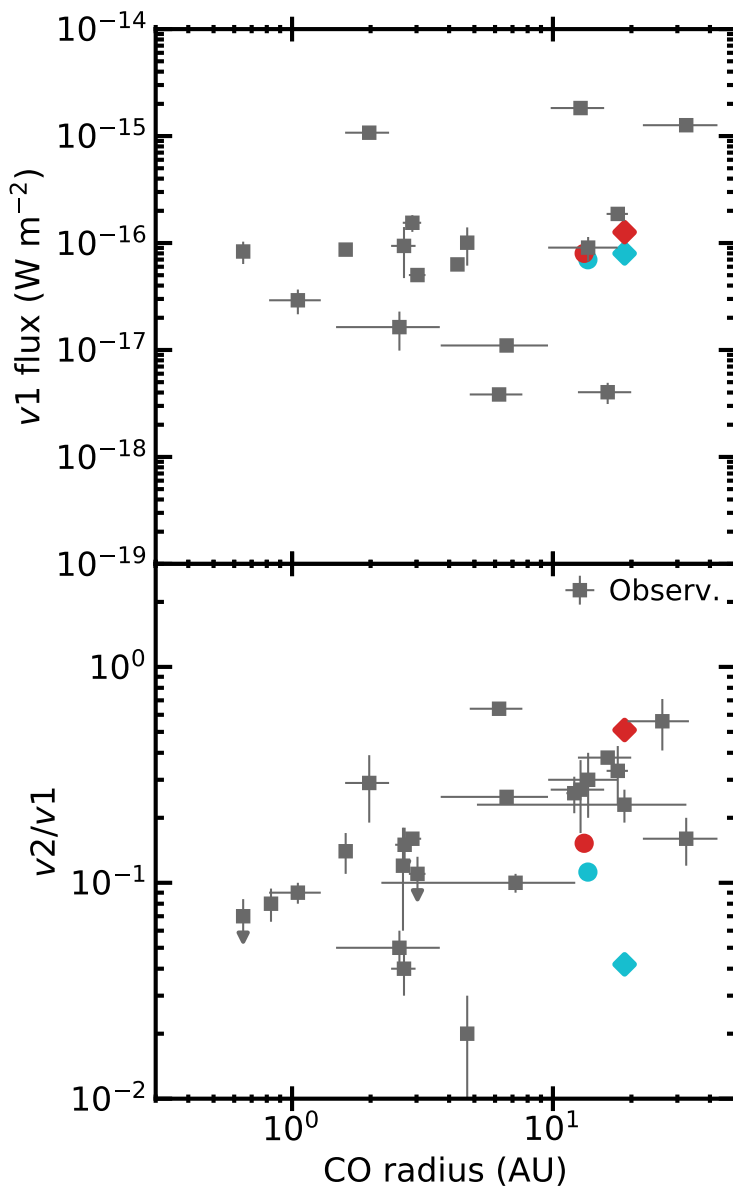


**Figure 5.23:**  $v_1$  line flux (*top*) and vibrational ratio of CO (*bottom*) versus the inferred radius of emission for observational data and DALI model results. Cyan and red markers show models with a gas-to-dust ratio of 20000 and 100000 respectively. Circles show models with  $R_{\text{in}} = 10$  AU, squares show models with with  $R_{\text{in}} = 15$  AU

## 5.F Thermal dissociation of CO

As mentioned before dissociating CO is difficult. The CO photo-dissociation rate is an order of magnitude lower than the dissociation rate for CO<sub>2</sub> or H<sub>2</sub>O for a 10000 K black body radiation field. Furthermore, most reactions destroying CO have a large barrier (e.g.  $\text{CO} + \text{H} \longrightarrow \text{C} + \text{OH}$ , 77000K Hollenbach & McKee 1979; Mitchell 1984) or create products that dissociate back into CO (e.g.  $\text{CO} + \text{OH} \longrightarrow \text{CO}_2 + \text{H}$ ).

The strong UV fields near a Herbig star, especially when coupled with a low dust opacity, can photo-dissociate CO. This is most effective at lower densities. At higher densities ( $10^{12} - 10^{14} \text{ cm}^{-3}$ ), the chemical model in DALI shows that the CO production rate is faster than the UV radiation field expected at the sublimation radius. The high radiation field could however increase the gas temperature to far above the dust temperature.

At temperatures above 3000 K Gibbs free energy minimisers find CO abundances lower than the canonical  $10^{-4}$  (Fig. 5.24). Around this temperature, the kinetical network also shows a decrease in the CO abundance as the endothermic  $\text{CO} + \text{H} \longrightarrow \text{C} + \text{OH}$  and  $\text{OH} + \text{H} \longrightarrow \text{O} + \text{H}_2$  reactions coupled with collisional dissociation of H<sub>2</sub> push the gas towards a fully atomic state.

Figure 5.24 clearly shows that the molecular to atomic transition happens slower and at higher temperatures than in the equilibrium models. The kinetic model does not have all the reaction pathways included that could be important for the production and destruction of CO and H<sub>2</sub> at high temperatures. Between the uncertainty in the gas temperature and the uncertainty in the chemistry, it is thus not unlikely that the CO abundance in the inner disk rim is overestimated by DALI.

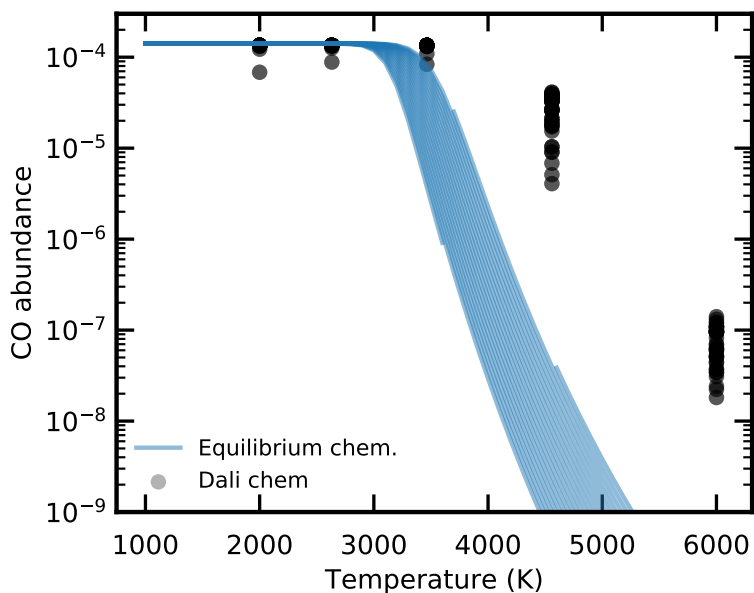
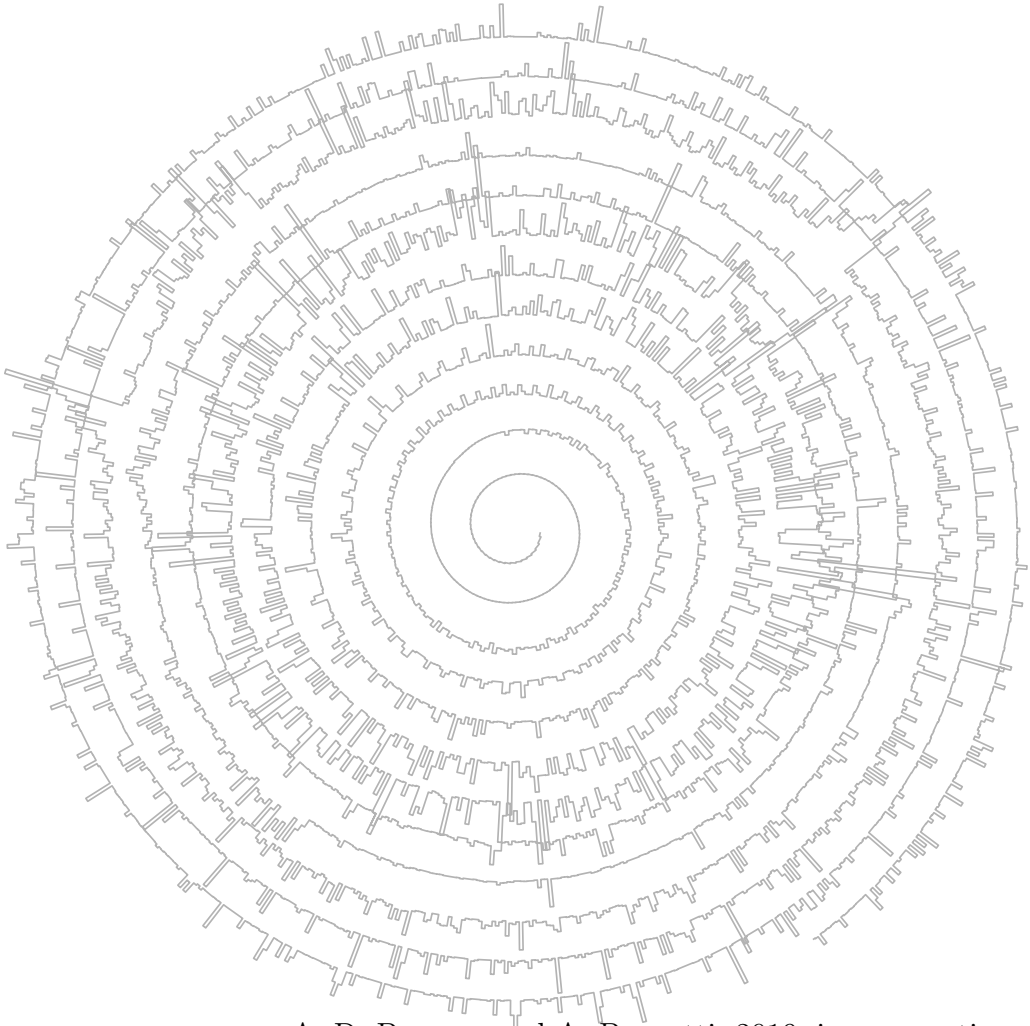


**Figure 5.24:** CO abundance as function of temperature under inner disk conditions. Black points show the results from the chemical model in DALI under conditions relevant for the inner disk ( $n = 10^{12}$ – $10^{14} \text{ cm}^{-3}$ ,  $10^4$ – $10^{10} G_0$  radiation field). Blue line show the results from equilibrium chemistry for the same range of densities (Chemical Equilibrium with Applications, Gordon & McBride 1994; McBride & Gordon 1996).

# 6

## THE DRY AND CARBON POOR INNER DISK OF TW HYA: EVIDENCE FOR A GIGANTIC ICY DUST TRAP



A. D. Bosman and A. Banzatti, 2019, in preparation

## Abstract

**Context:** Gas giants accrete their envelopes from the gas and dust of protoplanetary disks, so it is important to determine the composition of the inner few AU, where most giant planets are expected to form.

**Aims:** We aim to constrain the elemental carbon and oxygen abundance in the inner disk of TW Hya and compare with the outer disk where carbon and oxygen appear underabundant by a factor of  $\sim 50$ .

**Methods:** Archival *Spitzer*-IRS and VLT-CRIRES observations of TW Hya are compared with a detailed thermo-chemical model, DALI. The inner disk gas mass and elemental C and O abundances are varied to fit the mid-infrared  $\text{H}_2$  and  $\text{H}_2\text{O}$  line fluxes as well as the near-infrared CO line flux.

**Results:** Best fitting models have an inner disk that has a gas mass of  $2 \times 10^{-4} M_\odot$  with  $\text{C}/\text{H} \approx 3 \times 10^{-6}$  and  $\text{O}/\text{H} \approx 6 \times 10^{-6}$ , that is, 50 times underabundant compared to the ISM. The elemental oxygen and carbon abundances of the inner disk are consistent with those found in the outer disk.

**Conclusions:** The uniformly low volatile abundances imply that dust transport is inefficient, with both the carbon and oxygen being locked in solids at radii larger than 2.4 AU. If CO is the major carbon carrier in the ices, dust needs to be trapped efficiently outside the CO snowline of  $\sim 20$  AU. This would imply that the shallow sub-millimeter rings in the TW Hya disk at 20 AU correspond to very efficient dust traps. Otherwise conversion of CO into more volatile species, e.g.  $\text{CO}_2$  and  $\text{CH}_3\text{OH}$ , has been fast, converting more than 98% of the CO. A giant planet forming in the inner disk is accreting very low metallicity gas with very little icy dust, potentially leading to a planet atmosphere with a substellar metallicity.

## 6.1 Introduction

The elemental abundances of carbon and oxygen in proto-planetary disks are a vital input to planet formation models and, combined with characterization of exoplanets, can tell us about the formation history of those planets. Observations and modelling have shown that the picture, as proposed by Öberg et al. (2011), with elemental abundances only changing at the icelines is too simplistic. Chemical evolution can be efficient in changing the composition of the disk gas, changing the major carriers of carbon and oxygen (e.g. Eistrup et al. 2016; Schwarz et al. 2018; Bosman et al. 2018a). Furthermore, disk dynamics and dust evolution can efficiently transport the volatile component of the disk, changing the elemental composition of the gas and ice (Kama et al. 2016; Booth et al. 2017; Bosman et al. 2018a; Krijt et al. 2016a, 2018).

As the interplay of the physical and chemical processes is complex, observations are needed to benchmark the disk models and provide the much needed input for planet formation models. CO and H<sub>2</sub>O observations focussing on the outer regions of proto-planetary disks show that their abundances are up to two orders of magnitude lower than expected, implying that chemical and physical processes are indeed modifying the abundances of these species (Hogerheijde et al. 2011; Favre et al. 2013; Bergin et al. 2013; Miotello et al. 2017; Du et al. 2017). Planet formation models, however, primarily need the composition around and within the H<sub>2</sub>O iceline, as this is where we expect giant planets to form and accrete their atmospheres (Cridland et al. 2017; Dawson & Johnson 2018).

Therefore we aim to constrain the elemental abundances in the inner disk of TW Hya. The outer disk of TW Hya has been well studied and the elemental composition of the gas has been constrained from a variety of observations, including HD to trace the total disk mass, allowing for the measurement of absolute abundances (Hogerheijde et al. 2011; Bergin et al. 2013; Kama et al. 2016; Schwarz et al. 2016; Trapman et al. 2017; Zhang et al. 2017). These efforts have shown that both the volatile carbon and oxygen abundance in the outer disk are lowered by a factor of  $\sim 50$  compared to the interstellar medium (ISM).

The physical and chemical structure of the inner disk of TW Hya has also been studied in detail. It is the disk that has been resolved at the highest physical resolution with ALMA (Andrews et al. 2016). Together with abundant photometry and infrared interferometry, there is a good picture of the inner disk structure of TW Hya (Andrews et al. 2012; Menu et al. 2014; Kama et al. 2016). In the infrared, high signal-to-noise, *Spitzer*-IRS and VLT-CRIRES spectra have been taken. These observations include 3.2 km s<sup>-1</sup> resolution observations of the CO  $v = 1 - 0$  rovibrational band at 4.7  $\mu\text{m}$ , and detections of the CO<sub>2</sub> 15 $\mu\text{m}$   $Q$ -branch, pure rotational lines of H<sub>2</sub>, H<sub>2</sub>O and OH, as well as a number of atomic hydrogen lines (Najita et al. 2010; Pontoppidan et al. 2008a). Modelling efforts have further constrained the inner disk gas mass using H<sub>2</sub> (Gorti et al. 2011) as well as the H<sub>2</sub>O content of the inner disk (Zhang et al. 2013). These studies hint at depleted CO and H<sub>2</sub>O in the inner disk, respectively.

Here we will build on these studies, using the better constrained outer disk structure and composition from Trapman et al. (2017), with an updated inner disk gap from ALMA observations (Andrews et al. 2016). Using this disk structure and the thermo-chemical code DALI we constrain the elemental carbon and oxygen abundance in the inner disk of TW Hya.

**Table 6.1:** H<sub>2</sub>, CO and H<sub>2</sub>O fluxes from observations and modelling

Molecular line	Observed flux <sup>1</sup>	Model flux <sup>1</sup>	$E_{\text{up}}$ (K)
H <sub>2</sub> S(1)	1.57±0.05	1.7	1015
H <sub>2</sub> S(2)	1.21±0.20	0.75	1681
CO v1 P(10)	0.64 ± 0.05	0.72	3330
H <sub>2</sub> O 17.12 μm	< 0.17	0.03	3243
H <sub>2</sub> O 17.22 μm	< 0.29	0.05	2473
H <sub>2</sub> O 17.36 μm	< 0.32	0.11	2396
H <sub>2</sub> O 21.85 μm	2.8 ± 0.2	6.7	1730
H <sub>2</sub> O 28.23 μm	2.1 ± 0.1	1.3	1929, 2122
H <sub>2</sub> O 28.43 μm	1.6 ± 0.2	1.2	2031
H <sub>2</sub> O 28.6 μm	1.7 ± 0.1	1.2	2006
H <sub>2</sub> O 30.87 μm	2.7 ± 0.2	1.8	1806
H <sub>2</sub> O 33 μm	3.96 ± 0.46	4.0	1504

**Notes.** Observed CO line flux is taken from Banzatti et al. (2017), H<sub>2</sub> and H<sub>2</sub>O fluxes are extracted from the *Spitzer*-IRS spectra using the method in Banzatti et al. (2012). The H<sub>2</sub> S(2) line is contaminated by an OH line; the contribution of the OH line was estimated by taking the average flux of two adjacent OH lines.

<sup>(1)</sup> In units of  $10^{-14}$  erg s<sup>-1</sup> cm<sup>-2</sup>

## 6.2 Methods

The lines and features and their fluxes that we consider for our modelling comparison are tabulated in Table 6.1. The CO flux for TW Hya is taken from Banzatti et al. (2017) based on VLT-CRIRES (Kaeufl et al. 2004) spectra presented in Pontoppidan et al. (2008a) (program ID 179.C-0151). The fluxes for H<sub>2</sub> and H<sub>2</sub>O are extracted from the *Spitzer*-IRS spectrum obtained from program GO 30300 using the method described in Banzatti et al. (2012). The spectrum has been published in Najita et al. (2010) and Zhang et al. (2013).

We start with the Dust and Lines (DALI) (Bruderer et al. 2012; Bruderer 2013) model of Trapman et al. (2017) for TW Hya (see also Kama et al. 2016, model parameters are given in Table 6.2). This model fits the SED, many far-infrared and sub-millimeter lines as well as the ALMA <sup>12</sup>CO  $J = 3 - 2$  image. The most important lines are the HD 112 and 56 μm lines, constraining the outer disk mass, and many CO (isotopologue) lines constraining the carbon abundance. On top of these some atomic carbon and oxygen fine-structure lines have also been fit, which constrain the elemental carbon and oxygen abundances in the outer disk at C/H =  $2.7 \times 10^{-6}$  and O/H =  $5.8 \times 10^{-6}$  a factor 50 lower than expected for the interstellar medium (ISM). In this work we update the inner disk structure moving the outer edge of the gap from 4 to 2.4 AU in accordance with the bright sub-millimeter ring seen by Andrews et al. (2016) at this radius (assuming a distance of 54 parsec).

Figure 1 shows the surface density structure in the inner disk. The inner disk mass is varied by varying  $\delta_{\text{gas}} = \delta_{\text{dust}}$  in the inner disk using a model that has constant, low elemental abundances. The predicted H<sub>2</sub> lines for DALI are compared to the observed fluxes. The model that fits best is then used to constrain the elemental C and O abundances. We make the simplifying assumptions that the CO abundance

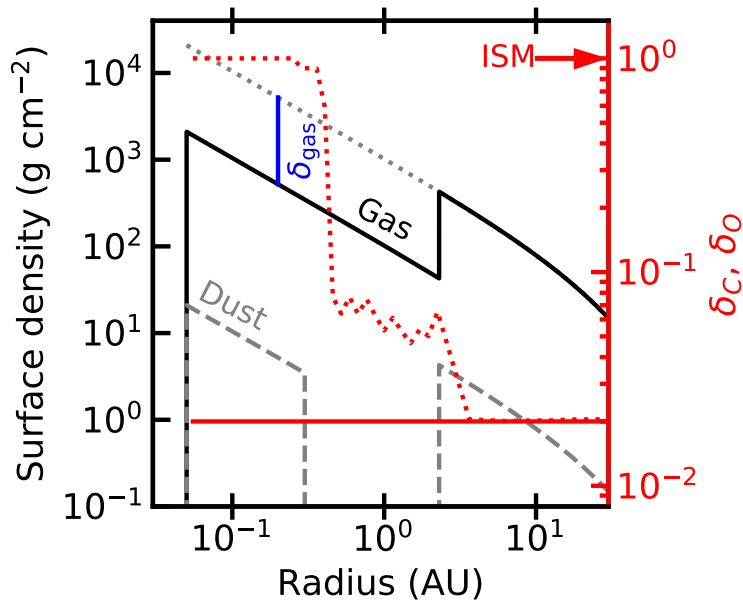


**Figure 6.1:** Surface density structure in inner regions of the TW Hya model.  $\delta_{\text{dust}}$  is the inner disk drop in gas surface density. The value  $\delta_{\text{gas}} = 0.1$  used here best fits the  $\text{H}_2$  observations. The red curves show the column averaged oxygen and carbon depletion factors in TW Hya. The red solid line shows a model with constant depletion. The dotted line shows the depletion profile assuming that carbon and oxygen return to the ISM values above  $T_{\text{gas}} = 150$  K.

in the inner disk scales linearly with the total elemental carbon abundance, that the  $\text{H}_2\text{O}$  abundance scales with the elemental oxygen that is not locked in CO and that changing the CO and  $\text{H}_2\text{O}$  abundances do not significantly alter the gas temperatures. The abundances of CO and  $\text{H}_2\text{O}$  multiplied by a factor  $\delta_C$  and  $\delta_O$ , respectively, above gas temperatures of  $T_{\text{step}} = [70, 150, 500]$  K. The excitation is recalculated for these new abundance structures and the CO v1 P(10) line flux as well as the full  $\text{H}_2\text{O}$  spectrum between 12 and 34  $\mu\text{m}$  are extracted.

The excitation for  $\text{H}_2$  is done in LTE, while for  $\text{H}_2\text{O}$  and CO the local excitation, de-excitation balance is calculated explicitly. For CO, collision rate coefficients from Yang et al. (2010) for  $\text{H}_2$  and Song et al. (2015); Walker et al. (2015) for H are used (See also Bosman et al. *subm.*). For  $\text{H}_2\text{O}$ , the data file from the LAMDA database<sup>1</sup> (Schöier et al. 2005) is used.

### 6.3 Results

Figure 6.2 compares the emitting regions of the different species in the constant abundance model with  $\delta_{\text{gas}} = 0.1$ . There is a large overlap in the emitting areas, especially in the inner disk ( $< 2.4$  AU).  $\text{H}_2\text{O}$  has the most confined emitting area and only probes

<sup>1</sup><http://strw.leidenuniv.nl/~moldata>



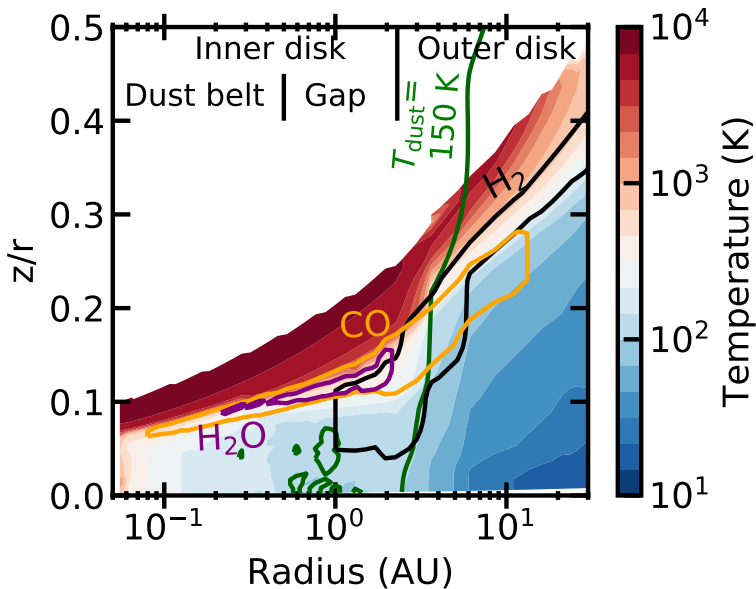


**Figure 6.2:** Map of the gas temperature in the inner region of the model together with the emitting areas of the  $\text{H}_2$   $S(1)$  line (black) the CO  $v_1$  vibrational lines (orange) and the strongest line of the  $\text{H}_2\text{O}$   $33\ \mu\text{m}$  feature (purple). The green line shows  $T_{\text{dust}} = 150\ \text{K}$ , the approximate location of the  $\text{H}_2\text{O}$  iceline. The emitting areas radially overlap in the inner disk.

the inner disk while CO and  $\text{H}_2$  both also probe the outer disk, where the composition of the gas is already strongly constrained (Bergin et al. 2013; Kama et al. 2016; Trapman et al. 2017; Zhang et al. 2017).

Figure 6.3 compares the results of the DALI modelling with the observed fluxes. The  $\text{H}_2$  fluxes constrain the inner disk gas mass to be around  $1.7 \times 10^{-4} M_{\odot}$  ( $\delta_{\text{gas}} \approx 0.1$ ), comparable to the value found in (Gorti et al. 2011). The observations show a lower  $S(1)/S(2)$  line ratio compared to the models, this indicates that the average gas temperature in the inner disk of the model is too low. The upper level energies of the CO ( $\sim 3000\ \text{K}$ ) and  $\text{H}_2\text{O}$  ( $\sim 1500\ \text{K}$ ) are similar or higher than the upper level energies of the  $\text{H}_2$  lines ( $\sim 1000$  and  $\sim 1700\ \text{K}$ ), therefore a higher temperature in the inner disk would lead to even lower inferred values for C/H and O/H.

The CO  $4.7\ \mu\text{m}$  lines fit well to an inner disk carbon abundance that is equal to the abundance found in the outer disk, that is, a factor 50 depleted compared to the ISM. Even a jump of a factor of 2 in the elemental carbon abundance above  $500\ \text{K}$  can be ruled out based on the observed fluxes.

The water lines tell a similar story to the CO rovibrational lines. A canonical elemental oxygen abundance of  $\sim 3 \times 10^{-4}$  is firmly ruled out and the data and models are consistent with an inner disk that is depleted by a factor  $\sim 50$ , the same value as found for the outer disk. The fluxes in Table 6.1 show that this model underpredicts the  $\text{H}_2\text{O}$  detections between  $20$  and  $31\ \mu\text{m}$  by a factor  $\sim 2$ , this is in line with the gas temperature in the model being too low.

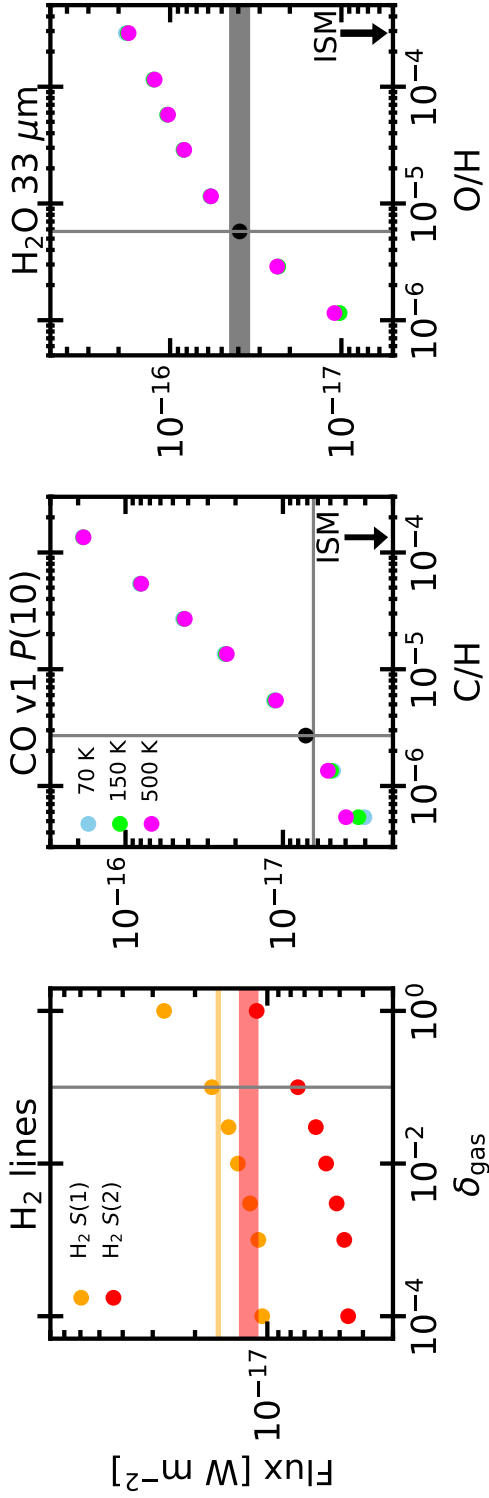


**Figure 6.3:** Comparison of the H<sub>2</sub> line fluxes (*left*), CO rovibrational line flux (*middle*) and the H<sub>2</sub>O 33  $\mu\text{m}$  feature flux (*right*) between models and data. For the left panel the amount of gas within 2.4 AU is varied. For the *middle* and *right* panels  $\delta_{\text{gas}} = 0.1$  is used and C/H and O/H are varied respectively. Horizontal bands show the  $1\sigma$  variation of the observed fluxes. The different coloured points denote different values for  $T_{\text{step}}$ . The temperature threshold above which the abundances are varied. The vertical lines in the middle and right panel show the volatile carbon and oxygen abundances assumed for the ISM (Meyer et al. 1998; Lacy et al. 2017).

## 6.4 Discussion

### 6.4.1 Constraining the inner disk chemical structure

Here, using a more complete physical and chemical structure of both the inner and the outer disk, we can quantify the total H<sub>2</sub> mass, as well as the volatile carbon and oxygen abundance in the inner disk, confirming that the inner disk of TW Hya is both oxygen and carbon poor by a factor  $\sim 50$ . Furthermore, our modelling shows that there is no significant (factor 2) increase in volatile carbon or oxygen in the inner disk up to 500 K. Thus, there is no sign of volatile release at the CO<sub>2</sub> or H<sub>2</sub>O icelines nor is there evidence of carbonaceous or silicate grain destruction at  $T < 500$  K.

Both Gorti et al. (2011) and Zhang et al. (2013) have studied the inner region of TW Hya using detailed modelling. They note that they overproduce the CO rovibrational lines by a factor of  $\sim 2$ . Furthermore, Gorti et al. (2011) assume LTE excitation for CO, which generally underpredicts fluxes compared to models that include the non-LTE effects (Bruderer et al. 2015; Bosman et al. 2017). These two factors together explain why our models need a CO or elemental carbon abundance that is almost two orders lower than ISM to fit the CO rovibrational line.

Zhang et al. (2013) use a low abundance in the inner disk  $x_{\text{H}_2\text{O}} < 10^{-6}$  with a ring of high abundance H<sub>2</sub>O at 4 AU, their ice line, to produce the *Spitzer* lines. Including such a ring and fitting the 33  $\mu\text{m}$  ( $E_{\text{up}} = 1504$  K) feature would lead to inferring lower oxygen abundances in the inner disk, however, it would also move the H<sub>2</sub>O emission to colder gas, increasing the discrepancy between model and observations for the 22 and 28  $\mu\text{m}$  features. A constant abundance model, thus fits the data better than a ring model.

### 6.4.2 Hiding C and O carriers?

The DALI models predict that CO and H<sub>2</sub>O are the dominant gas-phase oxygen and carbon carriers in the inner disk. However, it is possible that carbon and oxygen are locked in other gaseous species. There are a few obvious candidates for hiding more carbon and oxygen in molecular gas: CO<sub>2</sub>, C<sub>2</sub>H<sub>2</sub>, HCN and CH<sub>4</sub>. There is a CO<sub>2</sub> feature detected in the *Spitzer* spectrum of TW Hya. Applying the model results from Bosman et al. (2017) to the detected feature, retrieves a CO<sub>2</sub> abundance lower than  $10^{-9}$  w.r.t. H<sub>2</sub>. The models in Bosman et al. (2017) do not have a gap, which, if included would only increase the strength of the CO<sub>2</sub> lines. As such the CO<sub>2</sub> abundance  $< 10^{-9}$  is a stringent upper limit and it is not an abundant carrier of either carbon or oxygen.

C<sub>2</sub>H<sub>2</sub> and HCN are detected in many proto-planetary disks (Salyk et al. 2011b), however, neither are detected in the spectrum of TW Hya. As the Q-branches of HCN and C<sub>2</sub>H<sub>2</sub> around 14  $\mu\text{m}$  have similar upper level energies and Einstein A coefficients to the 15  $\mu\text{m}$  Q-branch of CO<sub>2</sub>, both HCN and C<sub>2</sub>H<sub>2</sub> should have been detected if they are as abundant as CO<sub>2</sub>. The lack of observed features implies that both HCN and C<sub>2</sub>H<sub>2</sub> contain less than 1% of the volatile carbon. The final possible gaseous carbon carrier is CH<sub>4</sub>. This molecule has only been observed towards one disk (Gibb & Horne 2013), and is not expected to be abundant in inner disk atmospheres (Walsh et al. 2015; Agúndez et al. 2018). As such, with CO and H<sub>2</sub>O we trace the bulk of carbon and oxygen in the inner disk.

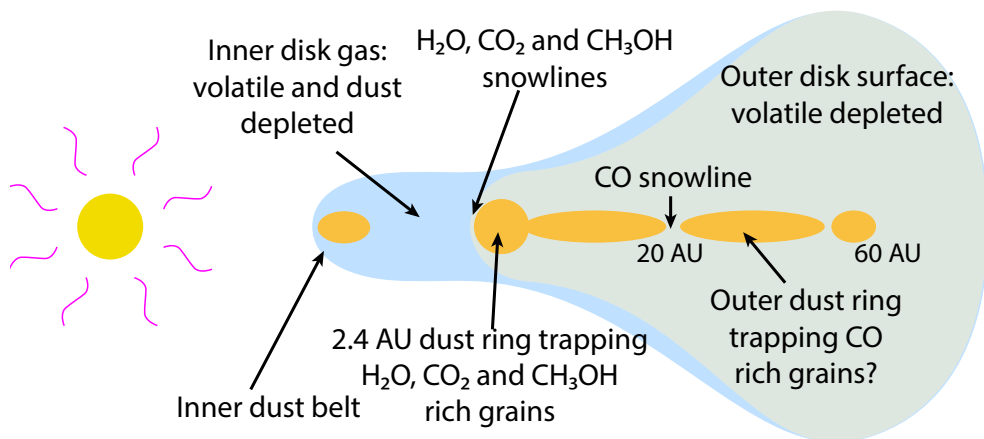


**Figure 6.4:** Schematic of the TW Hya disk showing the locations that should trap the oxygen and carbon bearing molecules. Oxygen needs to be trapped outside of 2.4 AU and is most likely trapped in the dust ring at that location. Carbon can either be trapped at the same location, with  $\text{CO}_2$  as most probable carrier, or at larger radii outside the CO snowline, with CO as the most probable carrier.

### 6.4.3 Implications of uniform depletion

The low elemental abundances in the inner disk imply one of two things: either the entire disk is depleted in volatiles, implying dust grains with almost no ices, or volatiles are efficiently locked in ices on solids that are not transported through the disk.

To deplete the entire disk in volatiles, a period of very strong radial drift, coupled with strong radial mixing is necessary (e.g. Booth et al. 2017). In such a scenario, the icy grains drift from the mass reservoir in the outer disk, into the regions of the disk where the ices desorb. This leads to enhancements in C/H and O/H in the inner regions of the disk. After a few Myr all of this high C/H and O/H material is accreted onto the star and the disk is left depleted in carbon and oxygen. However, a disk like this will also be strongly depleted in solid material as the grains that transport the ices inward, will continue to drift into the star leading to dust depletions at least as high as the volatile element depletion. This scenario is thus very unlikely for TW Hya, which has a massive dust component, and a gas-to-dust ratio of around 100 (Bergin et al. 2013).

This leaves the locking of 98% of the carbon and oxygen in solids that are not efficiently transported. Assuming that CO and  $\text{H}_2\text{O}$  are the dominant oxygen and carbon carriers in the outer disk, it is necessary to stop CO from being transported over the CO iceline, this would imply that the shallow millimeter continuum ring of TW Hya at 20 AU correspond to an efficient dust trap. An efficient dust trap at  $\sim 20$  AU should result in a disk with a large cavity. As dust is abundant down to 2.4 AU, a second dust trap would be necessary at that location, which would trap  $\text{H}_2\text{O}$  rich grains.

In this scenario  $\text{H}_2\text{O}$  would be far more efficiently locked in large grains than CO as the former is frozen out in a larger fraction of the disk. However, if gaseous CO is efficiently converted into less volatiles species, especially  $\text{CO}_2$  and  $\text{CH}_3\text{OH}$ , then the

CO and H<sub>2</sub>O depletion fractions are likely to be more similar and an efficient dust trap around 20 AU is no longer strictly necessary. The age of TW Hya, 10 Myr, is long enough to convert large amounts of CO into other species (Donaldson et al. 2016; Bosman et al. 2018b). In this case, the dust should not be allowed to pass the CO<sub>2</sub> or CH<sub>3</sub>OH snowlines. These snowlines are at nearly the same location as the H<sub>2</sub>O snowline, at the inner edge of the outer disk. A dust trap at the innermost sub-millimeter ring would trap all of the icy CO<sub>2</sub>, CH<sub>3</sub>OH and H<sub>2</sub>O in the outer disk. A schematic representation of this is given in Fig. 6.4.

In summary, we find that the elemental carbon and oxygen abundance in the inner disk are lower by a factor  $\sim 50$  compared to the ISM. Even at temperatures of 500 K, the gaseous carbon or oxygen elemental abundances cannot have increased by a factor of 2, strongly constraining the release of volatiles and grain destruction up to 500 K. This is interpreted as a lack of transport of solids from the outer disk ( $R > 2.4$  AU) to the inner disk ( $R < 2.4$  AU), trapping all the icy solids outside of 2.4 AU. A planet currently accreting gas in the gap will accrete very low amounts of carbon and oxygen, while possibly accreting ISM concentrations of nitrogen and noble gasses. Depending on the accretion history this planet could have a substellar C/H and O/H abundance.

## Appendix

### 6.A DALI model

**Table 6.2:** Parameters of the TW Hya model

Stellar parameters	
Stellar mass	$0.74 M_{\odot}$
Stellar luminosity	$1 L_{\odot}$
X-ray luminosity	$10^{30} \text{ erg s}^{-1}$
Disk parameters	
Disk mass	$0.025 M_{\odot}$
Critical radius ( $R_c$ )	35 AU
Surface density slope ( $\gamma$ )	1
scale-height at $R_c$ ( $h_c$ )	0.1 rad
Flaring angle ( $\psi$ )	0.3
Inner radius	0.05 AU
Gap inner radius	0.3 AU
Gap outer radius	2.4 AU
Inner disk gas-to-dust	100
Inner disk gas depletion	$[10^{-5} - 1]$
Small dust size	0.005–1 $\mu\text{m}$
Small dust fraction	0.01
Large dust size	0.005–1000 $\mu\text{m}$
Large dust fraction	0.99
Large dust settling factor	0.2

# BIBLIOGRAPHY

- Acharyya, K., Fuchs, G. W., Fraser, H. J., van Dishoeck, E. F., & Linnartz, H. 2007, *A&A*, 466, 1005
- Adams, N. G. & Smith, D. 1976, *Journal of Physics B: Atomic and Molecular Physics*, 9, 1439
- Agúndez, M., Cernicharo, J., & Goicoechea, J. R. 2008, *A&A*, 483, 831
- Agúndez, M., Roueff, E., Le Petit, F., & Le Bourlot, J. 2018, *A&A*, 616, A19
- Aikawa, Y. & Herbst, E. 1999, *A&A*, 351, 233
- Aikawa, Y., Umabayashi, T., Nakano, T., & Miyama, S. M. 1999, *ApJ*, 519, 705
- Aikawa, Y., van Zadelhoff, G. J., van Dishoeck, E. F., & Herbst, E. 2002, *A&A*, 386, 622
- Akimkin, V., Zhukovska, S., Wiebe, D., et al. 2013, *ApJ*, 766, 8
- Alcalá, J. M., Manara, C. F., Natta, A., et al. 2017, *A&A*, 600, A20
- Alcalá, J. M., Natta, A., Manara, C. F., et al. 2014, *A&A*, 561, A2
- Ali-Dib, M., Mousis, O., Petit, J.-M., & Lunine, J. I. 2014, *ApJ*, 785, 125
- Allègre, C., Manhès, G., & Lewin, É. 2001, *Earth and Planetary Science Letters*, 185, 49
- Allen, D., Scragg, T., & Simpson, C. 1980, *Chemical Physics*, 51, 279
- ALMA Partnership, Brogan, C. L., Pérez, L. M., et al. 2015, *ApJ*, 808, L3
- Andersson, S., Goumans, T. P. M., & Arnaldsson, A. 2011, *Chemical Physics Letters*, 513, 31
- André, P., Di Francesco, J., Ward-Thompson, D., et al. 2014, in *Protostars and Planets VI*, ed. H. Beuther, R. S. Klessen, C. P. Dullemond, & T. Henning, 27
- Andrews, S. M., Huang, J., Pérez, L. M., et al. 2018, *ApJ*, 869, L41
- Andrews, S. M., Rosenfeld, K. A., Kraus, A. L., & Wilner, D. J. 2013, *ApJ*, 771, 129
- Andrews, S. M., Wilner, D. J., Hughes, A. M., Qi, C., & Dullemond, C. P. 2009, *ApJ*, 700, 1502

- Andrews, S. M., Wilner, D. J., Hughes, A. M., et al. 2012, *ApJ*, 744, 162
- Andrews, S. M., Wilner, D. J., Zhu, Z., et al. 2016, *ApJ*, 820, L40
- Anicich, V. G., Laudenslager, J. B., Jr., W. T. H., & Futrell, J. H. 1977, *The Journal of Chemical Physics*, 67, 4340
- Ansdell, M., Williams, J. P., van der Marel, N., et al. 2016, *ApJ*, 828, 46
- Antonellini, S., Kamp, I., Lahuis, F., et al. 2016, *A&A*, 585, A61
- Antonellini, S., Kamp, I., Riviere-Marichalar, P., et al. 2015, *A&A*, 582, A105
- Arasa, C., van Hemert, M. C., van Dishoeck, E. F., & Kroes, G. J. 2013, *Journal of Physical Chemistry A*, 117, 7064
- Armitage, P. J. 2011, *ARA&A*, 49, 195
- Asplund, M., Grevesse, N., Sauval, A. J., & Scott, P. 2009, *ARA&A*, 47, 481
- Avenhaus, H., Quanz, S. P., Schmid, H. M., et al. 2017, *AJ*, 154, 33
- Avramenko, L. I. & Krasnen'kov, V. M. 1967, *Bull. Acad. Sci. USSR Div. Chem. Sci. (Engl. Transl.)*, 16, 501
- Bachiller, R. & Tafalla, M. 1999, in *NATO Advanced Science Institutes (ASI) Series C*, ed. C. J. Lada & N. D. Kylafis, Vol. 540, 227
- Bai, X.-N. & Stone, J. M. 2013, *ApJ*, 769, 76
- Banzatti, A., Garufi, A., Kama, M., et al. 2018, *A&A*, 609, L2
- Banzatti, A., Meyer, M. R., Bruderer, S., et al. 2012, *ApJ*, 745, 90
- Banzatti, A. & Pontoppidan, K. M. 2015, *ApJ*, 809, 167
- Banzatti, A., Pontoppidan, K. M., Bruderer, S., Muzerolle, J., & Meyer, M. R. 2015, *ApJ*, 798, L16
- Banzatti, A., Pontoppidan, K. M., Salyk, C., et al. 2016, *ArXiv e-prints* [[arXiv:1611.06230](https://arxiv.org/abs/1611.06230)]
- Banzatti, A., Pontoppidan, K. M., Salyk, C., et al. 2017, *ApJ*, 834, 152
- Barber, R. J., Tennyson, J., Harris, G. J., & Tolchenov, R. N. 2006, *MNRAS*, 368, 1087
- Baruteau, C., Crida, A., Paardekooper, S.-J., et al. 2014, *Protostars and Planets VI*, 667
- Bast, J. E., Brown, J. M., Herczeg, G. J., van Dishoeck, E. F., & Pontoppidan, K. M. 2011, *A&A*, 527, A119
- Baulch, D. L., Cobos, C. J., Cox, R. A., et al. 1992, *Journal of Physical and Chemical Reference Data*, 21, 411

- Beegle, L. W., Ajello, J. M., James, G. K., Dzikczek, D., & Alvarez, M. 1999, *A&A*, 347, 375
- Benisty, M., Stolker, T., Pohl, A., et al. 2017, *A&A*, 597, A42
- Bergin, E. A., Blake, G. A., Ciesla, F., Hirschmann, M. M., & Li, J. 2015, *Proceedings of the National Academy of Science*, 112, 8965
- Bergin, E. A., Cleeves, L. I., Gorti, U., et al. 2013, *Nature*, 493, 644
- Bergin, E. A., Melnick, G. J., Gerakines, P. A., Neufeld, D. A., & Whittet, D. C. B. 2005, *ApJ*, 627, L33
- Bergin, E. A. & Williams, J. P. 2017, in *Astrophysics and Space Science Library*, Vol. 445, *Astrophysics and Space Science Library*, ed. M. Pessah & O. Gressel, 1
- Bertin, M., Romanzin, C., Doronin, M., et al. 2016, *ApJ*, 817, L12
- Birnstiel, T., Dullemond, C. P., & Brauer, F. 2010, *A&A*, 513, A79
- Birnstiel, T., Klahr, H., & Ercolano, B. 2012, *A&A*, 539, A148
- Bisschop, S. E., Fuchs, G. W., van Dishoeck, E. F., & Linnartz, H. 2007, *A&A*, 474, 1061
- Blake, G. A. & Boogert, A. C. A. 2004, *ApJ*, 606, L73
- Blum, J. & Wurm, G. 2008, *ARA&A*, 46, 21
- Boehler, Y., Ricci, L., Weaver, E., et al. 2018, *ApJ*, 853, 162
- Bolatto, A. D., Wolfire, M., & Leroy, A. K. 2013, *ARA&A*, 51, 207
- Boogert, A. C. A., Gerakines, P. A., & Whittet, D. C. B. 2015, *ARA&A*, 53, 541
- Boonman, A. M. S., van Dishoeck, E. F., Lahuis, F., & Doty, S. D. 2003a, *A&A*, 399, 1063
- Boonman, A. M. S., van Dishoeck, E. F., Lahuis, F., et al. 2003b, *A&A*, 399, 1047
- Booth, R. A., Clarke, C. J., Madhusudhan, N., & Ilee, J. D. 2017, *MNRAS*, 469, 3994
- Bosman, A. D., Bruderer, S., & van Dishoeck, E. F. 2017, *A&A*, 601, A36
- Bosman, A. D., Tielens, A. G. G. M., & van Dishoeck, E. F. 2018a, *A&A*, 611, A80
- Bosman, A. D., Walsh, C., & van Dishoeck, E. F. 2018b, *A&A*, 618, A182
- Brandl, B. R., Feldt, M., Glasse, A., et al. 2014, in *Proc. SPIE*, Vol. 9147, *Ground-based and Airborne Instrumentation for Astronomy V*, 914721
- Brauer, F., Dullemond, C. P., & Henning, T. 2008, *A&A*, 480, 859
- Brinch, C. & Hogerheijde, M. R. 2010, *A&A*, 523, A25
- Brittain, S. D., Carr, J. S., & Najita, J. R. 2018, *PASP*, 130, 074505



- Brittain, S. D., Simon, T., Najita, J. R., & Rettig, T. W. 2007, *ApJ*, 659, 685
- Brown, J. M., Herczeg, G. J., Pontoppidan, K. M., & van Dishoeck, E. F. 2012, *ApJ*, 744, 116
- Brown, J. M., Pontoppidan, K. M., van Dishoeck, E. F., et al. 2013, *ApJ*, 770, 94
- Brown, W. A. & Bolina, A. S. 2007, *MNRAS*, 374, 1006
- Bruderer, S. 2013, *A&A*, 559, A46
- Bruderer, S., Doty, S. D., & Benz, A. O. 2009, *ApJS*, 183, 179
- Bruderer, S., Harsono, D., & van Dishoeck, E. F. 2015, *A&A*, 575, A94
- Bruderer, S., van Dishoeck, E. F., Doty, S. D., & Herczeg, G. J. 2012, *A&A*, 541, A91
- Bustamante, I., Merín, B., Bouy, H., et al. 2016, *A&A*, 587, A81
- Cami, J., Yamamura, I., de Jong, T., et al. 2000, *A&A*, 360, 562
- Carney, M. T., Yıldız, U. A., Mottram, J. C., et al. 2016, *A&A*, 586
- Carr, J. S. & Najita, J. R. 2008, *Science*, 319, 1504
- Carr, J. S. & Najita, J. R. 2011, *ApJ*, 733, 102
- Cassen, P. & Moosman, A. 1981, *ICARUS*, 48, 353
- Cazaux, S. & Tielens, A. G. G. M. 2004, *ApJ*, 604, 222
- Cazzoletti, P., van Dishoeck, E. F., Pinilla, P., et al. 2018, *A&A*, 619, A161
- Chambers, J. E. 2009, *Annual Review of Earth and Planetary Sciences*, 37, 321
- Chandra, S. & Sharma, A. K. 2001, *A&A*, 376, 356
- Charnley, S. B. & Kaufman, M. J. 2000, *ApJ*, 529, L111
- Chen, Y.-J., Chuang, K.-J., Muñoz Caro, G. M., et al. 2014, *ApJ*, 781, 15
- Chiang, E. I. & Goldreich, P. 1997, *ApJ*, 490, 368
- Chuang, K. J., Fedoseev, G., Qasim, D., et al. 2017, *MNRAS*, 467, 2552
- Ciesla, F. J. 2010, *ApJ*, 723, 514
- Ciesla, F. J. & Cuzzi, J. N. 2006, *ICARUS*, 181, 178
- Cieza, L., Padgett, D. L., Stapelfeldt, K. R., et al. 2007, *ApJ*, 667, 308
- Clarke, C. J. & Pringle, J. E. 1988, *MNRAS*, 235, 365
- Cleeves, L. I., Bergin, E. A., Öberg, K. I., et al. 2017, *ApJ*, 843, L3
- Cleeves, L. I., Bergin, E. A., Qi, C., Adams, F. C., & Öberg, K. I. 2015, *ApJ*, 799, 204
- Collings, M. P., Anderson, M. A., Chen, R., et al. 2004, *MNRAS*, 354, 1133

- Collings, M. P., Dever, J. W., Fraser, H. J., & McCoustra, M. R. S. 2003, *AP&SS*, 285, 633
- Cooke, I. R., Öberg, K. I., Fayolle, E. C., Peeler, Z., & Bergner, J. B. 2018, *ApJ*, 852, 75
- Cridland, A. J., Pudritz, R. E., Birnstiel, T., Cleeves, L. I., & Bergin, E. A. 2017, *MNRAS*, 469, 3910
- Cuppen, H. M. & Herbst, E. 2007, *ApJ*, 668, 294
- Cuppen, H. M., Ioppolo, S., Romanzin, C., & Linnartz, H. 2010, *Physical Chemistry Chemical Physics (Incorporating Faraday Transactions)*, 12, 12077
- Cuppen, H. M., van Dishoeck, E. F., Herbst, E., & Tielens, A. G. G. M. 2009, *A&A*, 508, 275
- Cuppen, H. M., Walsh, C., Lamberts, T., et al. 2017, *Space Sci. Rev.*, 212, 1
- Currie, T. & Kenyon, S. J. 2009, *AJ*, 138, 703
- Cyr, K. E., Sears, W. D., & Lumine, J. I. 1998, *ICARUS*, 135, 537
- Dalgarno, A. 2006, *Proceedings of the National Academy of Science*, 103, 12269
- Dawson, R. I. & Johnson, J. A. 2018, *ARA&A*, 56, 175
- de Graauw, T., Whittet, D. C. B., Gerakines, P. A., et al. 1996, *A&A*, 315, L345
- Debes, J. H., Jang-Condell, H., Weinberger, A. J., Roberge, A., & Schneider, G. 2013, *ApJ*, 771, 45
- Desch, S. J. & Connolly, Jr., H. C. 2002, *Meteoritics and Planetary Science*, 37, 183
- Desch, S. J., Estrada, P. R., Kalyaan, A., & Cuzzi, J. N. 2017, *ApJ*, 840, 86
- Desch, S. J., Morris, M. A., Connolly, H. C., & Boss, A. P. 2012, *Meteoritics and Planetary Science*, 47, 1139
- di Folco, E., Dutrey, A., Chesneau, O., et al. 2009, *A&A*, 500, 1065
- Donaldson, J. K., Weinberger, A. J., Gagné, J., et al. 2016, *ApJ*, 833, 95
- Draine, B. T. 1978, *ApJS*, 36, 595
- Draine, B. T. 2003, *ApJ*, 598, 1017
- Draine, B. T. & Lee, H. M. 1984, *ApJ*, 285, 89
- Drozdovskaya, M. N., Walsh, C., van Dishoeck, E. F., et al. 2016, *MNRAS*, 462, 977
- Du, F. & Bergin, E. A. 2014, *ApJ*, 792, 2
- Du, F., Bergin, E. A., Hogerheijde, M., et al. 2017, *ApJ*, 842, 98
- Du, F., Bergin, E. A., & Hogerheijde, M. R. 2015, *ApJ*, 807, L32

- Dubrulle, B., Morfill, G., & Sterzik, M. 1995, *ICARUS*, 114, 237
- Dullemond, C. P. & Dominik, C. 2004, *A&A*, 417, 159
- Dullemond, C. P., Juhasz, A., Pohl, A., et al. 2012, *RADMC-3D: A multi-purpose radiative transfer tool*, *Astrophysics Source Code Library*
- Dunham, M. M., Stutz, A. M., Allen, L. E., et al. 2014, in *Protostars and Planets VI*, ed. H. Beuther, R. S. Klessen, C. P. Dullemond, & T. Henning, 195
- Dutrey, A., Guilloteau, S., & Guelin, M. 1997, *A&A*, 317, L55
- Eisner, J. A., Hillenbrand, L. A., & Stone, J. M. 2014, *MNRAS*, 443, 1916
- Eistrup, C., Walsh, C., & van Dishoeck, E. F. 2016, *A&A*, 595, A83
- Eistrup, C., Walsh, C., & van Dishoeck, E. F. 2018, *A&A*, 613, A14
- Endres, C. P., Schlemmer, S., Schilke, P., Stutzki, J., & Müller, H. S. P. 2016, *Journal of Molecular Spectroscopy*, 327, 95
- Ercolano, B. & Pascucci, I. 2017, *Royal Society Open Science*, 4, 170114
- Espaillet, C., Muzerolle, J., Najita, J., et al. 2014, in *Protostars and Planets VI*, ed. H. Beuther, R. S. Klessen, C. P. Dullemond, & T. Henning, 497
- Faure, A. & Josselin, E. 2008, *A&A*, 492, 257
- Favre, C., Cleaves, L. I., Bergin, E. A., Qi, C., & Blake, G. A. 2013, *ApJ*, 776, L38
- Fayolle, E. C., Öberg, K. I., Cuppen, H. M., Visser, R., & Linnartz, H. 2011, *A&A*, 529, A74
- Fedele, D., Carney, M., Hogerheijde, M. R., et al. 2017, *A&A*, 600, A72
- Fedele, D., Pascucci, I., Brittain, S., et al. 2011, *ApJ*, 732, 106
- Feigelson, E. D., Broos, P., Gaffney, III, J. A., et al. 2002, *ApJ*, 574, 258
- Fleyfel, F. & Devlin, J. P. 1991, *The Journal of Physical Chemistry*, 95, 3811
- France, K., Schindhelm, E., Bergin, E. A., Roueff, E., & Abgrall, H. 2014, *ApJ*, 784, 127
- Fraser, H. J., Collings, M. P., McCoustra, M. R. S., & Williams, D. A. 2001, *MNRAS*, 327, 1165
- Fuchs, G. W., Cuppen, H. M., Ioppolo, S., et al. 2009, *A&A*, 505, 629
- Furuya, K. & Aikawa, Y. 2014, *ApJ*, 790, 97
- Furuya, K., Aikawa, Y., Hincelin, U., et al. 2015, *A&A*, 584, A124
- Furuya, K., van Dishoeck, E. F., & Aikawa, Y. 2016, *A&A*, 586, A127
- Galli, D. & Shu, F. H. 1993, *ApJ*, 417, 220

- Gammie, C. F. 1996, *ApJ*, 457, 355
- Garcia Lopez, R., Tambovtseva, L. V., Schertl, D., et al. 2015, *A&A*, 576, A84
- Garrod, R. T. & Herbst, E. 2006, *A&A*, 457, 927
- Garrod, R. T. & Pauly, T. 2011, *ApJ*, 735, 15
- Garrod, R. T., Widicus Weaver, S. L., & Herbst, E. 2008, *ApJ*, 682, 283
- Garufi, A., Meeus, G., Benisty, M., et al. 2017, *A&A*, 603, A21
- Gibb, E. L. & Horne, D. 2013, *ApJ*, 776, L28
- Gibb, E. L., Van Brunt, K. A., Brittain, S. D., & Rettig, T. W. 2007, *ApJ*, 660, 1572
- Gibb, E. L., Whittet, D. C. B., Boogert, A. C. A., & Tielens, A. G. G. M. 2004, *ApJS*, 151, 35
- González-Alfonso, E. & Cernicharo, J. 1999, in *ESA Special Publication*, Vol. 427, *The Universe as Seen by ISO*, ed. P. Cox & M. Kessler, 325
- Gordon, S. & McBride, B. J. 1994, *Computer Program for Calculation of Complex Chemical Equilibrium Compositions and Applications. Part 1: Analysis* (Washington, DC: NASA)
- Gorti, U. & Hollenbach, D. 2008, *The Astrophysical Journal*, 683, 287
- Gorti, U., Hollenbach, D., & Dullemond, C. P. 2015, *ApJ*, 804, 29
- Gorti, U., Hollenbach, D., Najita, J., & Pascucci, I. 2011, *ApJ*, 735, 90
- Gravity Collaboration, Abuter, R., Accardo, M., et al. 2017, *A&A*, 602, A94
- Gredel, R., Lepp, S., & Dalgarno, A. 1987, *ApJ*, 323, L137
- Gundlach, B. & Blum, J. 2015, *ApJ*, 798, 34
- Haisch, Karl E., J., Lada, E. A., & Lada, C. J. 2001, *ApJ*, 553, L153
- Han, E., Wang, S. X., Wright, J. T., et al. 2014, *PASP*, 126, 827
- Harries, T. J., Haworth, T. J., Acreman, D., Ali, A., & Douglas, T. 2019, *Astronomy and Computing*, 27, 63
- Harsono, D., Bruderer, S., & van Dishoeck, E. F. 2015, *A&A*, 582, A41
- Hartmann, L., Calvet, N., Gullbring, E., & D'Alessio, P. 1998, *ApJ*, 495, 385
- Hasegawa, T. I., Herbst, E., & Leung, C. M. 1992, *ApJS*, 82, 167
- Hässig, M., Altwegg, K., Balsiger, H., et al. 2015, *Science*, 347
- He, J. & Vidalí, G. 2014, *ApJ*, 788, 50
- Heays, A. N., Bosman, A. D., & van Dishoeck, E. F. 2017, *A&A*, 602, A105
- Heays, A. N., Visser, R., Gredel, R., et al. 2014, *A&A*, 562, A61

- Hébrard, E., Dobrijevic, M., Pernot, P., et al. 2009, *Journal of Physical Chemistry A*, 113, 11227
- Hein Bertelsen, R. P., Kamp, I., Goto, M., et al. 2014, *A&A*, 561, A102
- Henning, T. & Semenov, D. 2013, *Chemical Reviews*, 113, 9016
- Hewins, R. H., Connolly, Jr., H. C., Lofgren, G. E., & Libourel, G. 2005, in *Astronomical Society of the Pacific Conference Series*, Vol. 341, *Chondrites and the Protoplanetary Disk*, ed. A. N. Krot, E. R. D. Scott, & B. Reipurth, 286
- Hincelin, U., Chang, Q., & Herbst, E. 2015, *A&A*, 574, A24
- Hindmarsh, A. C., Brown, P. N., Grant, K. E., et al. 2005, *ACM Transactions on Mathematical Software (TOMS)*, 31, 363
- Hiraoka, K., Sato, T., Sato, S., et al. 2002, *ApJ*, 577, 265
- Hogerheijde, M. R., Bergin, E. A., Brinch, C., et al. 2011, *Science*, 334, 338
- Hollenbach, D. & McKee, C. F. 1979, *ApJS*, 41, 555
- Horne, K. & Marsh, T. R. 1986, *MNRAS*, 218, 761
- Huang, J., Andrews, S. M., Dullemond, C. P., et al. 2018, *ApJ*, 869, L42
- Husain, D. & Norris, P. E. 1978, *Chemical Physics Letters*, 53, 474
- Ikoma, M., Nakazawa, K., & Emori, H. 2000, *ApJ*, 537, 1013
- Ilee, J. D., Fairlamb, J., Oudmaijer, R. D., et al. 2014, *MNRAS*, 445, 3723
- Ioppolo, S., Fedoseev, G., Lamberts, T., Romanzin, C., & Linnartz, H. 2013, *Review of Scientific Instruments*, 84, 073112
- Isella, A., Huang, J., Andrews, S. M., et al. 2018, *ApJ*, 869, L49
- Jacobs, R. R., Pettipiece, K. J., & Thomas, S. J. 1975, *Phys. Rev. A*, 11, 54
- Jacquinet-Husson, N., Crepeau, L., Armante, R., et al. 2011, *Journal of Quantitative Spectroscopy and Radiative Transfer*, 112, 2395
- Johansen, A., Blum, J., Tanaka, H., et al. 2014, in *Protostars and Planets VI*, ed. H. Beuther, R. Klessen, C. Dullemond, & T. Henning (University of Arizona Press, Tucson), 547–570
- Johansen, A. & Lambrechts, M. 2017, *Annual Review of Earth and Planetary Sciences*, 45, null
- Jones, A., Noll, S., Kausch, W., Szyszka, C., & Kimeswenger, S. 2013, *A&A*, 560, A91
- Jonkheid, B., Faas, F. G. A., van Zadelhoff, G. J., & van Dishoeck, E. F. 2004, *Astronomy and Astrophysics*, 428, 511
- Kaeufl, H.-U., Ballester, P., Biereichel, P., et al. 2004, in *Proc. SPIE*, Vol. 5492, *Ground-based Instrumentation for Astronomy*, ed. A. F. M. Moorwood & M. Iye, 1218–1227

- Kama, M., Bruderer, S., van Dishoeck, E. F., et al. 2016, *A&A*, 592, A83
- Kama, M., Folsom, C. P., & Pinilla, P. 2015, *A&A*, 582, L10
- Kamp, I. & Dullemond, C. P. 2004, *The Astrophysical Journal*, 615, 991
- Kamp, I., Thi, W. F., Woitke, P., et al. 2017, *A&A*, 607, A41
- Kastner, J. H., Huenemoerder, D. P., Schulz, N. S., Canizares, C. R., & Weintraub, D. A. 2002, *ApJ*, 567, 434
- Kley, W. & Nelson, R. P. 2012, *ARA&A*, 50, 211
- Kratter, K. & Lodato, G. 2016, *ARA&A*, 54, 271
- Krijt, S. & Ciesla, F. J. 2016, *ApJ*, 822, 111
- Krijt, S., Ciesla, F. J., & Bergin, E. A. 2016a, *ApJ*, 833, 285
- Krijt, S., Ormel, C. W., Dominik, C., & Tielens, A. G. G. M. 2016b, *A&A*, 586, A20
- Krijt, S., Schwarz, K. R., Bergin, E. A., & Ciesla, F. J. 2018, *ApJ*, 864, 78
- Lacy, J. H., Sneden, C., Kim, H., & Jaffe, D. T. 2017, *ApJ*, 838, 66
- Lahuis, F., van Dishoeck, E. F., Boogert, A. C. A., et al. 2006, *ApJ*, 636, L145
- Lamberts, T., Cuppen, H. M., Ioppolo, S., & Linnartz, H. 2013, *Physical Chemistry Chemical Physics (Incorporating Faraday Transactions)*, 15, 8287
- Lambrechts, M. & Johansen, A. 2012, *A&A*, 544, A32
- Lauck, T., Karssemeijer, L., Shulenberger, K., et al. 2015, *ApJ*, 801, 118
- Le Roy, L., Altwegg, K., Balsiger, H., et al. 2015, *A&A*, 583, A1
- Lee, H.-H., Herbst, E., Pineau des Forets, G., Roueff, E., & Le Bourlot, J. 1996, *A&A*, 311, 690
- Levison, H. F., Kretke, K. A., & Duncan, M. J. 2015, *Nature*, 524, 322
- Li, X., Heays, A. N., Visser, R., et al. 2013, *A&A*, 555, A14
- Lissauer, J. J., Dawson, R. I., & Tremaine, S. 2014, *Nature*, 513, 336
- Long, F., Herczeg, G. J., Pascucci, I., et al. 2017, *ApJ*, 844, 99
- Lopez, E. D. & Fortney, J. J. 2014, *ApJ*, 792, 1
- Lynden-Bell, D. & Pringle, J. E. 1974, *MNRAS*, 168, 603
- Maaskant, K. M., Honda, M., Waters, L. B. F. M., et al. 2013, *A&A*, 555, A64
- Madhusudhan, N., Knutson, H., Fortney, J. J., & Barman, T. 2014, in *Protostars and Planets VI*, ed. H. Beuther, R. Klessen, C. Dullemond, & T. Henning (University of Arizona Press, Tucson), 739–762
- Manara, C. F., Fedele, D., Herczeg, G. J., & Teixeira, P. S. 2016a, *A&A*, 585, A136

- Manara, C. F., Rosotti, G., Testi, L., et al. 2016b, *A&A*, 591, L3
- Mandell, A. M., Bast, J., van Dishoeck, E. F., et al. 2012, *ApJ*, 747, 92
- Markwick, A. J., Ilgner, M., Millar, T. J., & Henning, T. 2002, *A&A*, 385, 632
- Mathis, J. S., Rumpl, W., & Nordsieck, K. H. 1977, *ApJ*, 217, 425
- Mauclaire, G., Derai, R., & Marx, R. 1978, *International Journal of Mass Spectrometry and Ion Physics*, 26, 289
- McBride, B. J. & Gordon, S. 1996, *Computer Program for Calculation of Complex Chemical Equilibrium Compositions and Applications II. User's Manual and Program Description*, Vol. 19 (Washington, DC: NASA), 178
- McClure, M. K., Bergin, E. A., Cleeves, L. I., et al. 2016, *ApJ*, 831, 167
- McElroy, D., Walsh, C., Markwick, A. J., et al. 2013, *A&A*, 550, A36
- McLean, I. S., Becklin, E. E., Bendiksen, O., et al. 1998, in *Society of Photo-Optical Instrumentation Engineers (SPIE) Conference Series*, Vol. 3354, *Infrared Astronomical Instrumentation*, ed. A. M. Fowler, 566–578
- Meeus, G., Waters, L. B. F. M., Bouwman, J., et al. 2001, *A&A*, 365, 476
- Meijerink, R., Pontoppidan, K. M., Blake, G. A., Poelman, D. R., & Dullemond, C. P. 2009, *ApJ*, 704, 1471
- Menu, J., van Boekel, R., Henning, T., et al. 2014, *A&A*, 564, A93
- Menu, J., van Boekel, R., Henning, T., et al. 2015, *A&A*, 581, A107
- Meyer, D. M., Jura, M., & Cardelli, J. A. 1998, *ApJ*, 493, 222
- Milam, S. N., Savage, C., Brewster, M. A., Ziurys, L. M., & Wyckoff, S. 2005, *ApJ*, 634, 1126
- Miotello, A., Bruderer, S., & van Dishoeck, E. F. 2014, *A&A*, 572, A96
- Miotello, A., van Dishoeck, E. F., Kama, M., & Bruderer, S. 2016, *A&A*, 594, A85
- Miotello, A., van Dishoeck, E. F., Williams, J. P., et al. 2017, *A&A*, 599, A113
- Mitchell, G. F. 1984, *Astrophysical Journal Supplement Series*, 54, 81
- Molyarova, T., Akimkin, V., Semenov, D., et al. 2017, *ApJ*, 849, 130
- Morbidelli, A. & Raymond, S. N. 2016, *Journal of Geophysical Research (Planets)*, 121, 1962
- Muñoz Caro, G. M., Chen, Y.-J., Aparicio, S., et al. 2016, *A&A*, 589, A19
- Muñoz Caro, G. M., Jiménez-Escobar, A., Martín-Gago, J. Á., et al. 2010, *A&A*, 522, A108
- Mumma, M. J. & Charnley, S. B. 2011, *ARA&A*, 49, 471

- Najita, J., Carr, J. S., & Mathieu, R. D. 2003, *ApJ*, 589, 931
- Najita, J. R. & Ádámkóvics, M. 2017, *ApJ*, 847, 6
- Najita, J. R., Ádámkóvics, M., & Glassgold, A. E. 2011, *ApJ*, 743, 147
- Najita, J. R., Carr, J. S., Pontoppidan, K. M., et al. 2013, *ApJ*, 766, 134
- Najita, J. R., Carr, J. S., Salyk, C., et al. 2018, *ApJ*, 862, 122
- Najita, J. R., Carr, J. S., Strom, S. E., et al. 2010, *ApJ*, 712, 274
- Neufeld, D. A. 2012, *ApJ*, 749, 125
- Nevdakh, V., Orlov, L., & Leshenyuk, N. 2003, *Journal of Applied Spectroscopy*, 70, 276
- Noble, J. A., Congiu, E., Dulieu, F., & Fraser, H. J. 2012, *MNRAS*, 421, 768
- Noll, S., Kausch, W., Barden, M., et al. 2012, *A&A*, 543, A92
- Notsu, S., Nomura, H., Ishimoto, D., et al. 2016, *ApJ*, 827, 113
- Oba, Y., Watanabe, N., Kouchi, A., Hama, T., & Pirronello, V. 2010, *ApJ*, 712, L174
- Öberg, K. I. & Bergin, E. A. 2016, *ApJ*, 831, L19
- Öberg, K. I., Boogert, A. C. A., Pontoppidan, K. M., et al. 2011, *ApJ*, 740, 109
- Öberg, K. I., Fuchs, G. W., Awad, Z., et al. 2007, *ApJ*, 662, L23
- Öberg, K. I., Garrod, R. T., van Dishoeck, E. F., & Linnartz, H. 2009a, *A&A*, 504, 891
- Öberg, K. I., Linnartz, H., Visser, R., & van Dishoeck, E. F. 2009b, *ApJ*, 693, 1209
- Öberg, K. I., van Dishoeck, E. F., & Linnartz, H. 2009c, *A&A*, 496, 281
- Ormel, C., Liu, B., & Schoonenberg, D. 2017, *ArXiv e-prints* [[arXiv:1703.06924](https://arxiv.org/abs/1703.06924)]
- Ormel, C. W. & Cuzzi, J. N. 2007, *A&A*, 466, 413
- Ormel, C. W. & Klahr, H. H. 2010, *A&A*, 520, A43
- Owen, J. E. 2016, *PASA*, 33, e005
- Paardekooper, D. M., Fedoseev, G., Riedo, A., & Linnartz, H. 2016, *A&A*, 596, A72
- Paardekooper, S.-J. & Johansen, A. 2018, *Space Sci. Rev.*, 214, 38
- Paardekooper, S. J. & Mellema, G. 2006, *A&A*, 459, L17
- Pascucci, I., Apai, D., Luhman, K., et al. 2009, *ApJ*, 696, 143
- Pascucci, I., Herczeg, G., Carr, J. S., & Bruderer, S. 2013, *ApJ*, 779, 178
- Pascucci, I., Testi, L., Herczeg, G. J., et al. 2016, *ApJ*, 831, 125



- Penteado, E. M., Walsh, C., & Cuppen, H. M. 2017, *ApJ*, 844, 71
- Pérez, L. M., Carpenter, J. M., Chandler, C. J., et al. 2012, *ApJ*, 760, L17
- Pickett, H. M., Poynter, R. L., Cohen, E. A., et al. 1998, *JQSRT*, 60, 883
- Pinilla, P., Benisty, M., & Birnstiel, T. 2012a, *A&A*, 545, A81
- Pinilla, P., Birnstiel, T., Ricci, L., et al. 2012b, *A&A*, 538, A114
- Pinilla, P., Klarmann, L., Birnstiel, T., et al. 2016, *A&A*, 585, A35
- Pinilla, P., Tazzari, M., Pascucci, I., et al. 2018, *ApJ*, 859, 32
- Piso, A.-M. A., Öberg, K. I., Birnstiel, T., & Murray-Clay, R. A. 2015, *ApJ*, 815, 109
- Pontoppidan, K. M. 2016, *CHIP: Caltech High-res IRS Pipeline*, Astrophysics Source Code Library
- Pontoppidan, K. M., Blake, G. A., & Smette, A. 2011a, *ApJ*, 733, 84
- Pontoppidan, K. M., Blake, G. A., van Dishoeck, E. F., et al. 2008a, *ApJ*, 684, 1323
- Pontoppidan, K. M. & Blevins, S. M. 2014, *Faraday Discussions*, 169, 49
- Pontoppidan, K. M., Boogert, A. C. A., Fraser, H. J., et al. 2008b, *ApJ*, 678, 1005
- Pontoppidan, K. M., Dullemond, C. P., van Dishoeck, E. F., et al. 2005, *ApJ*, 622, 463
- Pontoppidan, K. M., Meijerink, R., Dullemond, C. P., & Blake, G. A. 2009, *ApJ*, 704, 1482
- Pontoppidan, K. M., Salyk, C., Blake, G. A., et al. 2010, *ApJ*, 720, 887
- Pontoppidan, K. M., van Dishoeck, E., Blake, G. A., et al. 2011b, *The Messenger*, 143, 32
- Prasad, S. S. & Tarafdar, S. P. 1983, *ApJ*, 267, 603
- Procaccia, I. & Levine, R. D. 1975, *The Journal of Chemical Physics*, 63, 4261
- Rayner, J., Tokunaga, A., Jaffe, D., et al. 2016, in *Proc. SPIE*, Vol. 9908, *Ground-based and Airborne Instrumentation for Astronomy VI*, 990884
- Reboussin, L., Wakelam, V., Guilloteau, S., Hersant, F., & Dutrey, A. 2015, *A&A*, 579, A82
- Rieke, G. H., Wright, G. S., Böker, T., et al. 2015, *PASP*, 127, 584
- Rigliaco, E., Pascucci, I., Duchene, G., et al. 2015, *ApJ*, 801, 31
- Robitaille, T. P. 2011, *A&A*, 536, A79
- Rothman, L., Gordon, I., Babikov, Y., et al. 2013, *Journal of Quantitative Spectroscopy and Radiative Transfer*, 130, 4

- Rothman, L., Gordon, I., Barbe, A., et al. 2009, *Journal of Quantitative Spectroscopy and Radiative Transfer*, 110, 533
- Ruffle, D. P. & Herbst, E. 2001, *MNRAS*, 324, 1054
- Ruzicka, A., Floss, C., & Hutson, M. 2008, *Geochimica et Cosmochimica Acta*, 72, 5530
- Salyk, C., Blake, G. A., Boogert, A. C. A., & Brown, J. M. 2011a, *ApJ*, 743, 112
- Salyk, C., Pontoppidan, K. M., Blake, G. A., et al. 2008, *ApJ*, 676, L49
- Salyk, C., Pontoppidan, K. M., Blake, G. A., Najita, J. R., & Carr, J. S. 2011b, *ApJ*, 731, 130
- Sandford, S. A. & Allamandola, L. J. 1990, *ICARUS*, 87, 188
- Scheegerer, A. A., Ratzka, T., Schuller, P. A., et al. 2013, *A&A*, 555, A103
- Schöier, F. L., van der Tak, F. F. S., van Dishoeck, E. F., & Black, J. H. 2005, *A&A*, 432, 369
- Schoonenberg, D. & Ormel, C. W. 2017, *A&A*, 602, A21
- Schwarz, K. R., Bergin, E. A., Cleeves, L. I., et al. 2016, *ApJ*, 823, 91
- Schwarz, K. R., Bergin, E. A., Cleeves, L. I., et al. 2018, *ApJ*, 856, 85
- Semenov, D. & Wiebe, D. 2011, *ApJS*, 196, 25
- Senevirathne, B., Andersson, S., Dulieu, F., & Nyman, G. 2017, *Molecular Astrophysics*, 6, 59
- Shakura, N. I. & Sunyaev, R. A. 1973, *A&A*, 24, 337
- Shen, C. J., Greenberg, J. M., Schutte, W. A., & van Dishoeck, E. F. 2004, *A&A*, 415, 203
- Shu, F. H. 1977, *ApJ*, 214, 488
- Sing, D. K., Fortney, J. J., Nikolov, N., et al. 2016, *Nature*, 529, 59
- Singleton, D. L. & Cvetanovic, R. J. 1988, *Journal of Physical and Chemical Reference Data*, 17, 1377
- Smith, I. W. M., Herbst, E., & Chang, Q. 2004, *MNRAS*, 350, 323
- Song, L., Balakrishnan, N., Walker, K. M., et al. 2015, *ApJ*, 813, 96
- Spaans, M., Tielens, A. G. G. M., van Dishoeck, E. F., & Bakes, E. L. O. 1994, *ApJ*, 437, 270
- Stammler, S. M., Birnstiel, T., Panić, O., Dullemond, C. P., & Dominik, C. 2017, *A&A*, 600, A140
- Stammler, S. M. & Dullemond, C. P. 2014, *ICARUS*, 242, 1

- Stäuber, P., Doty, S. D., van Dishoeck, E. F., & Benz, A. O. 2005, *A&A*, 440, 949
- Stevenson, D. J. & Lunine, J. I. 1988, *ICARUS*, 75, 146
- Stolker, T., Dominik, C., Avenhaus, H., et al. 2016, *A&A*, 595, A113
- Swings, P. & Rosenfeld, L. 1937, *ApJ*, 86, 483
- Takeuchi, T. & Lin, D. N. C. 2002, *ApJ*, 581, 1344
- Talbi, D. & Herbst, E. 2002, *A&A*, 386, 1139
- Tan, J. C., Chatterjee, S., Hu, X., Zhu, Z., & Mohanty, S. 2016, *IAU Focus Meeting*, 29, 6
- Tang, Y.-W., Guilloteau, S., Dutrey, A., et al. 2017, *ApJ*, 840, 32
- Taquet, V., Ceccarelli, C., & Kahane, C. 2012, *A&A*, 538, A42
- Tashkun, S., Perevalov, V., Gamache, R., & Lamouroux, J. 2015, *Journal of Quantitative Spectroscopy and Radiative Transfer*, 152, 45
- Taylor, R. L. & Bitterman, S. 1969, *Rev. Mod. Phys.*, 41, 26
- Tazzari, M., Testi, L., Ercolano, B., et al. 2016, *A&A*, 588, A53
- Tennyson, J., Zobov, N. F., Williamson, R., Polyansky, O. L., & Bernath, P. F. 2001, *Journal of Physical and Chemical Reference Data*, 30, 735
- Terebey, S., Shu, F. H., & Cassen, P. 1984, *ApJ*, 286, 529
- Testi, L., Birnstiel, T., Ricci, L., et al. 2014, *Protostars and Planets VI*, 339
- Thi, W. F., Kamp, I., Woitke, P., et al. 2013, *A&A*, 551, A49
- Thi, W.-F., van Dalen, B., Bik, A., & Waters, L. B. F. M. 2005, *A&A*, 430, L61
- Tielens, A. G. G. M. & Hagen, W. 1982, *A&A*, 114, 245
- Tielens, A. G. G. M., Tokunaga, A. T., Geballe, T. R., & Baas, F. 1991, *ApJ*, 381, 181
- Trapman, L., Miotello, A., Kama, M., van Dishoeck, E. F., & Bruderer, S. 2017, *A&A*, 605, A69
- Tsang, W. & Hampson, R. F. 1986, *J. Phys. Chem. Ref. Data*, 15, 1087
- Turner, N. J., Fromang, S., Gammie, C., et al. 2014, *Protostars and Planets VI*, 411
- Turner, N. J., Sano, T., & Dziourkevitch, N. 2007, *ApJ*, 659, 729
- Udry, S. & Santos, N. C. 2007, *ARA&A*, 45, 397
- Umebayashi, T. & Nakano, T. 1981, *PASJ*, 33, 617
- Umebayashi, T. & Nakano, T. 1988, *Progress of Theoretical Physics Supplement*, 96, 151

- Umebayashi, T. & Nakano, T. 2009, *ApJ*, 690, 69
- van der Marel, N., van Dishoeck, E. F., Bruderer, S., et al. 2016, *A&A*, 585, A58
- van der Marel, N., van Dishoeck, E. F., Bruderer, S., et al. 2013, *Science*, 340, 1199
- van der Marel, N., van Dishoeck, E. F., Bruderer, S., Pérez, L., & Isella, A. 2015, *A&A*, 579, A106
- van der Marel, N., Williams, J. P., Ansdell, M., et al. 2018, *ApJ*, 854, 177
- van der Plas, G., van den Ancker, M. E., Fedele, D., et al. 2008, *A&A*, 485, 487
- van der Plas, G., van den Ancker, M. E., Waters, L. B. F. M., & Dominik, C. 2015, *A&A*, 574, A75
- van der Plas, G., Wright, C. M., Ménard, F., et al. 2017, *A&A*, 597, A32
- van der Tak, F. F. S., Black, J. H., Schöier, F. L., Jansen, D. J., & van Dishoeck, E. F. 2007, *A&A*, 468, 627
- van Dishoeck, E. F. & Black, J. H. 1987, in *NATO ASIC Proc. 210: Physical Processes in Interstellar Clouds*, ed. G. E. Morfill & M. Scholer, 241–274
- van Dishoeck, E. F. & Black, J. H. 1988, *ApJ*, 334, 771
- van Dishoeck, E. F., Helmich, F. P., de Graauw, T., et al. 1996, *A&A*, 315, L349
- van 't Hoff, M. L. R., Tobin, J. J., Harsono, D., & van Dishoeck, E. F. 2018, *A&A*, 615, A83
- van 't Hoff, M. L. R., Walsh, C., Kama, M., Facchini, S., & van Dishoeck, E. F. 2017, *A&A*, 599, A101
- van Terwisga, S. E., van Dishoeck, E. F., Cazzoletti, P., et al. 2019, *A&A*, 623, A150
- van Zadelhoff, G.-J., Aikawa, Y., Hogerheijde, M. R., & van Dishoeck, E. F. 2003, *A&A*, 397, 789
- van Zadelhoff, G.-J., van Dishoeck, E. F., Thi, W.-F., & Blake, G. A. 2001, *A&A*, 377, 566
- Viala, Y. P., Letzelter, C., Eidelsberg, M., & Rostas, F. 1988, *A&A*, 193, 265
- Visser, R., Bruderer, S., Cazzoletti, P., et al. 2018, *A&A*, 615, A75
- Visser, R. & Dullemond, C. P. 2010, *A&A*, 519, A28
- Visser, R., van Dishoeck, E. F., & Black, J. H. 2009, *A&A*, 503, 323
- Wakelam, V., Herbst, E., Loison, J.-C., et al. 2012, *ApJS*, 199, 21
- Wakelam, V., Loison, J. C., Herbst, E., et al. 2015, *ApJS*, 217, 20
- Wakelam, V., Ruaud, M., Hersant, F., et al. 2016, *A&A*, 594, A35
- Walker, K. M., Song, L., Yang, B. H., et al. 2015, *ApJ*, 811, 27

- Walsh, C., Loomis, R. A., Öberg, K. I., et al. 2016, *ApJ*, 823, L10
- Walsh, C., Millar, T. J., & Nomura, H. 2010, *ApJ*, 722, 1607
- Walsh, C., Millar, T. J., Nomura, H., et al. 2014, *A&A*, 563, A33
- Walsh, C., Nomura, H., Millar, T. J., & Aikawa, Y. 2012, *ApJ*, 747, 114
- Walsh, C., Nomura, H., & van Dishoeck, E. 2015, *A&A*, 582, A88
- Ward-Thompson, D. 2002, *Science*, 295, 76
- Watanabe, N. & Kouchi, A. 2002, *ApJ*, 571, L173
- Watanabe, N., Mouri, O., Nagaoka, A., et al. 2007, *ApJ*, 668, 1001
- Weidenschilling, S. J. 1977, *MNRAS*, 180, 57
- Weingartner, J. C. & Draine, B. T. 2001, *ApJ*, 548, 296
- Wells, M., Pel, J.-W., Glasse, A., et al. 2015, *PASP*, 127, 646
- White, J. A., Boley, A. C., MacGregor, M. A., Hughes, A. M., & Wilner, D. J. 2018, *MNRAS*, 474, 4500
- Willacy, K., Klahr, H. H., Millar, T. J., & Henning, T. 1998, *A&A*, 338, 995
- Williams, J. P. & Best, W. M. J. 2014, *ApJ*, 788, 59
- Wilson, T. L. & Rood, R. 1994, *ARA&A*, 32, 191
- Winn, J. N. & Fabrycky, D. C. 2015, *ARA&A*, 53, 409
- Winston, E., Megeath, S. T., Wolk, S. J., et al. 2010, *AJ*, 140, 266
- Woitke, P., Kamp, I., & Thi, W.-F. 2009, *A&A*, 501, 383
- Woitke, P., Min, M., Thi, W. F., et al. 2018, *A&A*, 618, A57
- Wolf, S. & Voshchinnikov, N. V. 2004, *Computer Physics Communications*, 162, 113
- Woon, D. E. 2002, *ApJ*, 569, 541
- Yang, B., Stancil, P. C., Balakrishnan, N., & Forrey, R. C. 2010, *ApJ*, 718, 1062
- Youdin, A. N. & Goodman, J. 2005, *ApJ*, 620, 459
- Youdin, A. N. & Lithwick, Y. 2007, *ICARUS*, 192, 588
- Yu, M., Willacy, K., Dodson-Robinson, S. E., Turner, N. J., & Evans, II, N. J. 2016, *ApJ*, 822, 53
- Zhang, K., Bergin, E. A., Blake, G. A., Cleeves, L. I., & Schwarz, K. R. 2017, *Nature Astronomy*, 1, 0130
- Zhang, K., Pontoppidan, K. M., Salyk, C., & Blake, G. A. 2013, *ApJ*, 766, 82
- Zhang, S., Zhu, Z., Huang, J., et al. 2018, *ApJ*, 869, L47
- Zubko, V., Dwek, E., & Arendt, R. G. 2004, *ApJS*, 152, 211

# SAMENVATTING

De grond onder onze voeten is iets waar de meeste mensen vaker stil óp staan, dan stil bij staan. Als stil wordt gestaan bij de Aarde, vooral bij de Aarde als planeet, roept dit vragen op als, waarvan is de Aarde gemaakt, zijn er andere planeten zoals de Aarde en hoe is de Aarde gevormd?

De samenstelling van de Aarde is redelijk nauwkeurig gemeten. Deze samenstelling is vastgesteld door het analyseren van vulkanisch gesteente en het meten van de echo's van aardbevingen. Het aardoppervlak en de mantel bestaan voornamelijk uit (gesmolten) silicaten en de aardkern bestaat voornamelijk uit metalen zoals, ijzer en nikkel. Om de andere vragen te beantwoorden moeten we verder kijken dan de Aarde. Onze twee naaste buurplaneten, Venus en Mars, hebben een samenstelling die veel lijkt op die van de Aarde, vooral in de ogen van een astronoom. Mercurius lijkt al minder op de Aarde met meer ijzer en nikkel, maar lijkt genoeg op de Aarde om tot de aardse planeten gerekend te worden. De andere vier planeten, Jupiter, Saturnus, Uranus en Neptunus, lijken zelfs in de verste verte niet op de Aarde. Deze planeten zijn vele malen massiever dan de Aarde en bestaan voornamelijk uit waterstof- en heliumgas.

Dit laat zien dat er meerdere uitkomsten van het planeetvormingsproces zijn. Als exoplaneten, planeten rond andere sterren, meegenomen worden, is er een nog grotere variëteit aan planeetgroottes en samenstelling dan er is in ons eigen zonnestelsel. Zo zijn er waarnemingen die suggereren dat science-fictionwaardige waterwerelden, die bestaan uit meer dan 50% water, en koolstofplaneten, die voornamelijk uit koolstof bestaan, daadwerkelijk voorkomen rond andere sterren.

Om deze verscheidenheid aan planeten te verklaren, is het noodzakelijk zowel de fysische als chemische processen tijdens het planeetvormingsproces te volgen. Veel van het planeetvormingsproces gebeurt tijdens het vormen van de ster. Daarom is enig begrip van het stervormingsproces noodzakelijk om planeetvorming in context te plaatsen. Stervorming vindt plaats in enorme wolken van gas en stof. Deze moleculaire wolken zijn in de Melkweg zichtbaar als donkere banden, doordat het stof het licht van de achterliggende sterren absorbeert (zie Figuur 1).

Stervorming begint als een deel van een moleculaire wolk onder zijn eigen zwaartekracht samentrekt. Dit vormt een "prestellaire kern" waaruit één of meerdere sterren gevormd zullen worden. Het dichtste deel van de prestellaire kern trekt steeds verder samen en verzamelt meer en meer materiaal van de rest van de kern. Dit is het begin van een ster, een protoster genaamd. De kern draait een klein beetje rond. Hierdoor zal het, door behoud van hoekmoment, voor de protoster niet meer mogelijk zijn om direct materiaal van de kern in te vangen. Het gas en stof valt nog steeds in de richting van de protoster, maar vormt een schijf om de protoster heen. Daarna verplaatsen processen in deze schijf het gas en stof langzaam, in een periode van tien miljoen jaar, in de richting van de ster.



**Figuur 1:** 360 graden panorama van de Melkweg in zichtbaar licht. De donkere banden zijn wolken van gas en stof die de sterren erachter verhullen. Credit: ESO/S. Brunier

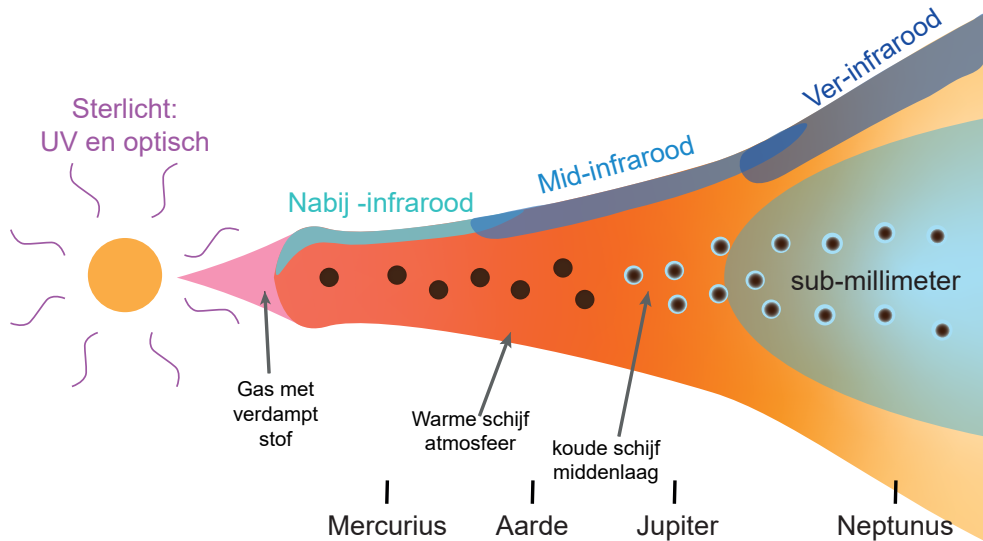
Het is in deze “protoplanetaire schijf” van gas en stof dat een nieuw planetair systeem zal ontstaan. Figuur 2 geeft een schets van een protoplanetaire schijf weer. Het licht dat de jonge ster uitstraalt zorgt ervoor dat het gas en stof dicht bij de ster warmer is dan verder weg van de ster, en dat het in de atmosfeer van de schijf warmer is dan in de middenlaag.

Bij zeer lage temperaturen zullen veel moleculen in het gas vastvriezen op het stof. Hoe kouder, en hoe dus verder van de ster, hoe meer moleculen aangevoren zijn. Dit zorgt voor grote verschillen in de samenstelling van het gas. In de middenlaag van de schijf zijn de dichtheden hoog genoeg dat de stofdeeltjes kunnen botsen en groeien, van 0.001 millimeter tot 1 centimeter grootte. Dit is de eerste stap richting de vorming van planeten van duizenden tot tienduizenden kilometers groot.

Hoe het stof verder groeit is nog onbekend. Experimenten in laboratoria voorspellen dat als deeltjes van centimeter grootte met elkaar botsen in de schijf, dit leidt tot verbrijzeling van beide deeltjes. Dit stopt de groei van het stof. Er zijn waarschijnlijk processen die een grote hoeveelheid deeltjes van centimeter grootte kunnen laten samen klonteren tot planetesimalen, rotsen groter dan 100 kilometer. Deze planetesimalen kunnen daarna verder groeien door botsingen met elkaar, of door het opvegen van stofdeeltjes in de schijf.

Afhankelijk van hoe snel de planetesimaal groeit, worden verschillende planeten gevormd. Als de planetesimaal snel groeit, terwijl er nog veel gas in de schijf is, kan deze het gas van de schijf invangen. Dit resulteert in een gasreus zoals Jupiter. Als de groei niet snel genoeg is, of te laat begint, is het gas in de schijf verdwenen voordat de planeet groot genoeg is om gas in te vangen. In dit geval blijft er een veel kleinere aardachtige planeet over.

Deze schets van de fysische processen is slechts de helft van het verhaal van planeetvorming. In principe is de Aarde, volgens deze processen, niets anders dan een opeenhoping van een enorme hoeveelheid stofdeeltjes, en zou de samenstelling van de Aarde dus hetzelfde moeten zijn als van deze stofdeeltjes. Dit is niet het geval. Alhoewel stof deeltjes, net als de aarde, grote hoeveelheden silicaten en metalen bevatten, bevatten de stofdeeltjes ook veel koolstof, ongeveer 25% van hun massa. Dit betekent



**Figuur 2:** Schematische representatie van een jonge ster met daaromheen een protplanetaire schijf. De gekleurde gebieden geven aan met welke golflengte van licht de verschillende delen van de schijf kunnen worden waargenomen. Onderaan wordt ruwweg de schaal in de schijf aangegeven met de planeten in ons eigen zonnestelsel. Omdat het sterlicht de schijf opwarmt is het in het binnenste delen en de hogere lagen van de schijf warmer. Dit zorgt ervoor dat hoe dichterbij de ster komt hoe minder ijs (blauw) het bevat.

dat ergens in de reis van de moleculaire wolk naar de net gevormde planeet, chemische processen de samenstelling van het stof hebben aangepast.

Dit betekent dat ook de samenstelling van het gas is aangepast, het koolstof uit de stofdeeltjes moet immer ergens heen. Het vastvriezen van verschillende moleculen in de schijf verandert ook de samenstelling van het gas. Dit zorgt voor grote chemische veranderingen rond “ijslijnen”, locaties in de schijf waarbinnen het warm genoeg is voor een molecuul om zich in de gasfase te bevinden, maar waarbuiten het zo koud is dat dat molecuul uitvriest en zich voornamelijk op het ijs bevindt.

Dit heeft niet alleen gevolgen voor de samenstelling van de Aardachtige planeten maar ook voor de samenstelling van de gasreuzen. Dit is handig voor astronomen omdat de samenstelling van gas op afstand makkelijker te meten is dan de samenstelling van vaste deeltjes. Verder, omdat een gasreus het gas uit een schijf invangt, zou de samenstelling van de atmosfeer gelijk moeten zijn aan de samenstelling van het gas op de plaats in de schijf waar die gevormd is. Als de samenstelling van zowel de planeten, als de schijven bekend is, is het mogelijk te herleiden in wat voor schijven de planeten gevormd zijn.

Elk molecuul laat een unieke vingerafdruk achter in het licht dat het absorbeert of uitzendt, het spectrum. Hoe meer van een molecuul aanwezig is, hoe sterker deze vingerafdruk is. Veel moleculen hebben deze vingerafdrukken niet in het zichtbaar licht, maar in het UV of het infrarood.

Voor het bepalen van de compositie van warm gas, dat wil zeggen ergens tussen 300 and 1000 K ( $\sim 0-700^\circ\text{C}$ ), wordt vaak infraroodspectroscopie gebruikt. Gas en stof van



deze temperaturen zenden veel infrarood licht uit. Verder hebben deze waarneming het voordeel ze qua temperatuur ongeveer het gebied beslaan waar we verwachten dat de meeste planeten gevormd worden, en in ons eigen zonnestelsel zijn zowel de Aarde als Jupiter in dit gebied gevormd.

Het zijn moleculen als water ( $\text{H}_2\text{O}$ ), koolstofmonoxide ( $\text{CO}$ ), koolstofdioxide ( $\text{CO}_2$ ), methaan ( $\text{CH}_4$ ), ethyn ( $\text{C}_2\text{H}_2$ ) en blauwzuur ( $\text{HCN}$ ) die iets kunnen vertellen over de samenstelling van het gas. Veel van deze gassen zijn broeikasgassen, en aanwezig in de atmosfeer van de Aarde. Hierdoor is vanaf de grond de vingerafdruk van deze moleculen uit de ruimte niet meer zichtbaar.

Hierdoor is het noodzakelijk om waarnemingen te doen vanuit de ruimte. Verschillende ruimtetelescopen zijn in staat geweest om te zoeken naar het signaal van deze moleculen in de ruimte, waaronder het “*Infrared Space Observatory*” (*ISO*) en de “*Spitzer Space Telescope*”. Het was *Spitzer* die voor het eerst aantoonde dat  $\text{H}_2\text{O}$ ,  $\text{CO}_2$ ,  $\text{HCN}$  en  $\text{C}_2\text{H}_2$  in bijna alle protoplanetaire schijven voorkwamen. In de nabije toekomst wordt de “*James Webb Space Telescope*” (*JWST*) gelanceerd. Met een grotere spiegel en nieuwe detectoren zal *JWST* vele malen gevoeliger zijn dan *Spitzer*. De waarnemingen die *JWST* gaat doen, zullen ons dichterbij het antwoord brengen op de vraag, hoe de Aarde gevormd is.

## Dit proefschrift

Er is veel nog onbekend over de lange weg van moleculaire wolk tot ster en planetenstelsel. Dit proefschrift bestudeert de fysische en chemische processen die de samenstelling van het gas en het ijs in de protoplanetaire schijf kunnen aanpassen en, andersom, hoe waarnemingen van verschillende moleculen gebruikt kunnen worden om te bepalen welke fysische en chemische processen daadwerkelijk van belang zijn.

In Hoofdstuk 2 van dit proefschrift wordt de chemie van  $\text{CO}$  in de koudere delen van de schijf bestudeerd.  $\text{CO}$  wordt veel gebruikt als maatstaf voor de totale hoeveelheid moleculair gas. In protoplanetaire schijven lijkt  $\text{CO}$  alleen veel lagere massa's te geven dan andere methoden om de massa te meten. Hoofdstuk 2 bestudeert de chemische processen die  $\text{CO}$  omvormen in andere moleculen en de tijdschalen die daarmee gemoeid zijn.

Hoofdstukken 3 en 4 bestuderen  $\text{CO}_2$  in het binnenste deel van een protoplanetaire schijf.  $\text{CO}_2$  is een belangrijk component van warm moleculair gas, maar is niet waar te nemen vanaf de grond. Hoofdstuk 3 bestudeert de interactie van  $\text{CO}_2$  met infrarood licht in protoplanetaire schijven. Met gebruik van computermodellen wordt de relatie tussen de hoeveelheid  $\text{CO}_2$  in de schijf en de sterkte van de spectrale vingerafdruk geïjkt. Deze relatie wordt gebruikt om de hoeveelheid  $\text{CO}_2$  te bepalen uit waarnemingen van *Spitzer*. Verder worden voorspellingen gedaan voor de waarnemingen met *JWST*. In hoofdstuk 4 wordt het effect van gas en stof transport in de schijf op de hoeveelheid  $\text{CO}_2$  in het binnenste deel van de schijf gemodelleerd.

Hoofdstuk 5 houdt zich bezig met infrarood emissie van  $\text{CO}$  rond jonge sterren die ongeveer twee keer zo massief zijn als de Zon. Deze objecten zien er heel anders uit in  $\text{CO}$  infrarood emissie dan lichtere sterren. Door het gebruik van modellen die de emissie van  $\text{CO}$  kunnen voorspellen wordt de structuur van het binnenste deel van de schijven rond deze zwaardere sterren bepaald.

Hoofdstuk 6 bestudeert het binnenste deel van de dichtstbijzijnde protoplanetaire schijf, die rond de jonge ster TW Hya. Dit is het best bestudeerde ster-schijf sys-

teem. Gebruikmakend van modellen, in combinatie met archiefdata met spectra van  $\text{H}_2\text{O}$ ,  $\text{CO}$  en  $\text{H}_2$ , wordt de totale hoeveelheid zuurstof en koolstof in het gas in de planeetvormende zone van TW Hya bepaald.

De conclusies van dit proefschrift kunnen als volgt worden samengevat:

- Chemische processen in de koude delen van de schijf kunnen  $\text{CO}$  omvormen tot andere moleculen, voornamelijk  $\text{CO}_2$ ,  $\text{CH}_3\text{OH}$  en  $\text{CH}_4$ . Onder standaard omstandigheden duurt dit proces enkele miljoenen jaren. Een verklaring voor de grote hoeveelheid verdwenen  $\text{CO}$  is dat de hoeveelheid energetische straling groter is dan meestal wordt aangenomen. De chemische modellen voorspellen dat het ijs in de buitenste delen van de schijf rijk is aan  $\text{CO}_2$  en  $\text{CH}_3\text{OH}$ .
- De gasfase abundantie van  $\text{CO}_2$  in de binnenste delen van de schijf is een factor 100 lager dan in interstellair ijs. De samenstelling van het gas dat uit de moleculaire wolk wordt geërfd, is dus aangepast door chemische processen in het binnenste van de schijf. Met het hogere spectrale onderscheidingsvermogen van *JWST* wordt het mogelijk om uit het spectrum van  $\text{CO}_2$  niet alleen de totale hoeveelheid, maar ook de radiale verdeling van  $\text{CO}_2$  te bepalen.
- Transport van met ijs bedekt stof vanuit de buitenste delen van de schijf naar de binnenste delen van de schijf is efficiënt. Dit proces kan dus een grote impact hebben op de abundantie van gasfase  $\text{CO}_2$  in het binnenste deel van de schijf. De modellen voorspellen een  $\text{CO}_2$  abundantie minstens 100 keer groter dan gemeten. Chemische processen in het binnenste van de schijf zijn te langzaam om  $\text{CO}_2$  af te breken. Een mogelijke oplossing voor dit probleem is het bestaan van een sterke verticale gradiënt in de  $\text{CO}_2$ -abundantie. Door de lage abundantie in schijfatmosfeer lijkt de hoeveelheid  $\text{CO}_2$  laag, terwijl er een groot reservoir van  $\text{CO}_2$  onder verstopt zit. Dit geeft een waarschuwing af: de gemeten hoeveelheid in de bovenste lagen is niet noodzakelijk een maat voor de totale hoeveelheid van een molecuul.
- Infraroodspectra van  $\text{CO}$  bevatten een schat aan informatie over de binnenste delen van schijven. Zo blijkt dat voor zwaardere sterren, in het deel van de schijf waar het zo heet is dat zelfs het stof verdampt, het gas niet meer moleculair is, maar atomair. Dit is een significant verschil tussen schijven rond sterren die meer dan anderhalf keer zo zwaar zijn als de zon, en schijven rond sterren die lichter zijn dan anderhalf zonsmassa. Verder duidt de  $\text{CO}$ -emissie erop dat veel schijven structuren hebben op relatief kleine schalen<sup>2</sup>. In schijven waarin het binnenste deel van de schijf geen stof bevat is ook zeer weinig gas, honderdduizend keer zo weinig als in schijven die daar wel stof hebben. Dit komt waarschijnlijk door een net gevormde gasreus die het gas en stof in de schijf verstoord heeft.
- Het binnenste deel van de schijf van TW Hya lijkt, net als de rest van de schijf, zeer arm in moleculen die zuurstof of koolstof bevatten. Dit betekent dat de schijf zeer veel stof bevat dat rijk is aan ijs. Dit stof zit in een stof val en wordt dus niet naar het binnenste deel van de schijf getransporteerd. Dit heeft waarschijnlijk te maken met een gas reus in het binnenste deel van de schijf rond TW Hya.

---

<sup>2</sup>één tot vijf keer de afstand tussen de Aarde en de Zon, zo'n 150 miljoen kilometer.

## Toekomstperspectief

Met de komst van de *James Webb Space Telescope* zal het onderzoek naar de compositie van schijven een grote stap voorwaarts nemen. Zo zal het mogelijk worden om niet alleen de relatieve samenstelling van het gas te meten (bijvoorbeeld: hoeveel CO<sub>2</sub> er is in verhouding met H<sub>2</sub>O), maar wordt het ook mogelijk om de absolute hoeveelheden te meten. Daarnaast wordt het ook mogelijk iets te zeggen over de distributie van verschillende moleculen over het binnenste deel van de schijf. Dit kan dan weer gebruikt worden om te vergelijken met de samenstellingen van planeten om zo hun vormingsgeschiedenis te ontrafelen.

Voordat deze stappen gemaakt kunnen worden moet er nog wel een hoop werk gedaan worden. Het nauwkeurig bepalen van de samenstelling van het gas vereist een goed begrip van de chemische processen en het effect van de fysische structuur op de spectra. Hiervoor moet vanuit de modeleerkant nog een hoop werk gedaan worden. Daarnaast zal de distributie van de moleculen ons iets vertellen over de fysische processen die belangrijk zijn in de schijf. Als we alles willen halen uit de vijf tot tien jaar dat *JWST* waarnemingen zal doen, is het noodzakelijk dat, voordat de waarnemingen binnen komen, de eerste modellen al doorgerekend zijn. Hierdoor kunnen de waarnemingen sneller geïnterpreteerd worden en kunnen de nodige vervolgwarnemingen snel daarna worden ingepland.

# LIST OF PUBLICATIONS

## Refereed publications

1. *Probing planet formation and disk substructures in the inner disk of Herbig Ae stars with CO rovibrational emission*  
**Bosman, A. D.**, Banzatti, A., Bruderer, S., Tielens, A. G. G. M., Blake, G. A., van Dishoeck, E. F. *Astronomy and Astrophysics* in press
2. *CO destruction in protoplanetary disk midplanes: Inside versus outside the CO snow surface*  
**Bosman, A. D.**, Walsh, C., van Dishoeck, E. F., (2018), *Astronomy and Astrophysics* 618, 182
3. *Efficiency of radial transport of ices in protoplanetary disks probed with infrared observations: the case of CO<sub>2</sub>*  
**Bosman, A. D.**, Tielens, A. G. G. M., van Dishoeck, E. F., (2018), *Astronomy and Astrophysics* 611, 80
4. *Photodissociation and photoionisation of atoms and molecules of astrophysical interest*  
Heays, A. N., **Bosman, A. D.**, van Dishoeck, E. F., (2017), *Astronomy and Astrophysics* 602, 105
5. *CO<sub>2</sub> infrared emission as a diagnostic of planet-forming regions of disks*  
**Bosman, A. D.**, Bruderer, S., van Dishoeck, E. F., (2017), *Astronomy and Astrophysics* 601, 36

## Submitted publications

1. HCN/HNC luminosity ratio: a new chemical thermometer for the molecular ISM  
Hacar, A., **Bosman, A. D.**, van Dishoeck, E. F., (2017), *Astronomy and Astrophysics* submitted



# CURRICULUM VITAE

I was born on March 21<sup>nd</sup> in The Hague to Theo Bosman and Thea Hagemeyer. With a father working as a naval engineer and a mother teaching English at a secondary school, it should not have been a big surprise when the pediatrician remarked that my development seemed to be more cognitively focussed than physically focussed. This clearly indicated that a career in sports was not for me. Even so my parents kept investing in my physical development, and decided that korfbal would be a good sport for me, which I have been playing for most of the past 20 years. During primary school, I had a video game fuelled interest in ancient, classical and medieval history. Clearly pointing me to a career in archaeology.

This started to shift around the time I went to the Dalton Den Haag, for my secondary education. My interests started to shift from the relics themselves to the ground these relics are in: Geology. I still picked up Latin and Greek in my second and third year as my interest in classical history was still strong. I've always had a knack and a interest for math, physics and chemistry and the more the focus of these courses shifted for memorizing to figuring out and understanding, the more my interest was piqued. At the end of the third year I thus chose to follow this path and picked a program with math, physics, chemistry, biology and Latin. Although the latter was partially motivated by the fact that it allowed me not having to continue German or French.

During the next two years, chemistry became my primary interest. I decided to partake in the "Scheikunde Olympiade", where I did well enough to join 19 other students for a one week master class and the national final. It was only in my last year that my interest in astronomy was solidified after taking part in the "Sterrenkunde Olympiade" and joining the master class in Amsterdam.

Partially unsure of my choice, partially looking for a challenge, I enrolled in the dual program of astronomy and mathematics in Leiden in the fall of 2010. As the big expanse was pulling on me, I decided to focus on Astronomy after the first year taking a few interesting math courses on the side. During my Bachelor project I worked with Sierk van Terwisga, under the supervision of David Sobral and Huub Röttgering. Together we dove into the joys of optical data reduction, looking for the brightest and largest blobs of gas in the universe.

I was torn between my ever resurfacing interest in chemistry and the physics of the early universe. As a compromise, I took the cosmology stream of the Leiden astronomy master program but started my first research project in astrochemistry. My project was on the photo-dissociation on molecules under various UV radiation fields in space in the group of Ewine van Dishoeck under Alan Heays and Catherine Walsh. For my second project I worked under Marijn Franx on the evolution of galaxies and how this influences the total observed population of galaxies at a set

age. During the five years of my bachelors and masters I have done various teaching related activities, including training secondary school students for their final economics exams at “Stichting Studiebegeleiding Leiden” and working as a teaching assistant for calculus.

When the time came for the PhD interviews in Leiden, I had mostly made my choice so when Ewine offered me a position within the astrochemistry group I did not think long before I took it.

During the four years of my PhD thesis I have worked on many of the theoretical aspects of astrochemistry, especially those important within proto-planetary disks. I have looked at molecular physics, the energy states of molecules and transitions between them to predict emission line strengths. I have studied the chemistry in warm gas as well as on cold grains surface with the help of kinetic chemical models. I have also considered the impact of physical processes, especially the transport of gas and dust through the disk on the chemical composition. All to explain the current observations of different chemical tracers and make predictions for the next big generation of instruments. The results of the work can be found in this thesis. During these four years I helped organise the “Sterrenkunde Olympiade”, the contest that got me into astronomy years ago, as well as taught master students as teaching assistant for the course Star and Planet formation. In November 2019 I will start a post-doc position at the University of Michigan.

# ACKNOWLEDGMENTS

The writing of any PhD thesis is a far cry from the “ff een boekie doen”, or “just doing a booklet”, that my dad jokingly refers to, and this one was no different. This thesis contains the results of four years of work, including many deadline crunches, coding frustrations, exhausting meetings and the occasional sleepless night. Luckily, it also contains the results of four years of lively discussions, the attitude that there is always time to help a colleague, laughter and an awful lot of horrible puns without which this thesis would not have been finished. Thanks to all who have made this possible.

I would like to start by thanking the boss, Ewine, for giving me the opportunity to take this journey and all the support during it. You have always been able to get a bit more out of me than I thought was possible. Then there is Xander, who, besides handing out great advice, acted as counter balance by telling me to stick with good enough. Furthermore, Tim, thanks for teaching the life lessons of the less talkative. Here I would also like to thank Andrea Banzatti, who challenged my theoretical mind with the scientific reality of observations.

While the group’s composition has been in constant flux during the past four years, it has always been a great environment to work in. A big thanks to all of you who have made it this way. I would like to thank Anna, Mihkel, Catherine and Alan for getting me started on this journey and teaching me many of the things I needed to finish it. A special shout out to the two that have sat at the other side of my screen, Leon, for being there to share all the technical difficulties with, and Alex, for sharing your truly stellar (or rather planetary) optimism and enthusiasm. Sierk, thanks for all the help, from statistics to imaging. Alvaro, thanks for broadening my scientific horizons. Nadia, thanks for all the great baked goods that I could actually eat. Benoît, Giovanni, I’ve always enjoyed our intense discussions. Martijn, it has been good to have a fellow Hagenaar in the group, best of luck the next years. Niels, Ko-Ju, Kirstin, Vincent, Jeroen, Donna and Michał, I’ve always greatly enjoyed the more down to earth discussions. Niels and Jeroen, thanks for your great contribution to the atmosphere in our corridor. Paolo and Stefano, thanks for always making me feel at home when I came to visit Garching. The biggest thanks to my (travel) buddies that have always been at my side. Łukasz, your relaxed and open attitude is something I can still learn a lot from, thanks for all the good times, and I hope there will be more great coffee in the future. Merel, you’ve always been there when I needed you, from the organisational stuff (that you had already figured out) to the big questions (where your insights are always useful), thank you for everything.

I would also like to thank all my friends outside of work, for your support, keeping me connected to the rest of the world and of course, all the boardgames. Special thanks to Kai and Bram for making sure my summary is readable and Anouk for the great cover illustration. Finally, I would like to thank my parents for their unwavering support.